Doctoral Dissertation
Doctoral Program in Chemical Engineering ($XXXV$cycle)

Molecular Modeling of Supramolecular Systems with Controllable Stimuli-Responsive Properties

By

Chiara Lionello

******

Supervisor(s):
Prof. Giovanni M. Pavan, Supervisor

Doctoral Examination Committee:
Prof. Tibor Kudernác, Referee, University of Groningen
Prof. Giulia Rossi, Referee, University of Genoa
Prof. Marta Corno, University of Turin
Prof. Daniele Marchisio, Politecnico di Torino
Prof. Anđela Šarić, Institute of Science and Technology Austria

Politecnico di Torino
2023

Declaration

I hereby declare that, the contents and organization of this dissertation constitute my own original work and does not compromise in any way the rights of third parties, including those relating to the security of personal data.

Chiara Lionello
2023

* This dissertation is presented in partial fulfillment of the requirements for **Ph.D. degree** in the Graduate School of Politecnico di Torino (ScuDo).

Acknowledgements

I would like to express my sincere gratitude to everyone that supported me throughout my PhD journey.

First and foremost, I would like to express my deepest gratitude to my esteemed PhD supervisor, Prof. Giovanni M. Pavan, whose guidance and insightful feedback have been fundamental in helping me achieve significant milestones in my research.

I extended my utmost gratitude to Dr. Anđela Šarić and her research group at Institute of Science and Technology Austria for their warm hospitality and unwavering belief in me. The six months I spent with them were truly enriching.

I am also indebted to Prof. Tibor Kudernác and Prof. Giulia Rossi for their invaluable feedback on my thesis.

Special thanks go to Dr. Annalisa Cardellini and Dr. Claudio Perego for their valuable advice and constant support throughout my studies. And of course, I am grateful to all the current and former members of the CPC and CMS labs whose collaboration and encouragement were crucial in making this journey possible.

Lastly, I would like to express my heartfelt thanks to my family, my boyfriend, and all my friends for their unconditional support during the entire academic journey.

Part of the research reported in this work has received funding from the European Research Council (ERC) under the European Union's Horizon 2020 research and innovation program (Grant Agreement no. 818776 - DYNAPOL), Swiss National Science Foundation (SNSF Grants 200021_175735, IZLIZ2_183336), U.S. Army Research Office (Grants W911NF-18-1-0355 and W911NF-15-1-0568). Computational resources were provided by the Swiss National Supercomputing Center (CSCS), CINECA and HPC@POLITO (http://www.hpc.polito.it).

Abstract

Self-assembly allows obtaining materials with stimuli-responsive properties, offering a highly attractive alternative for new designing strategies and material engineering. However, the rational design of self-assembled materials with programmable properties requires a deep knowledge of the physical-chemical features controlling them. A detailed comprehension of the mechanism governing the material's response to a single stimulus or a combination of them may be particularly challenging solely through experimental results. In this view, molecular models and simulations may be useful to understand these mechanisms.

The aim of this thesis is to explore the internal dynamics of new self-assembled materials in relation to their responsiveness to various stimuli by using molecular dynamics (MD) simulations. In addition, molecular simulations are also used to support experimental evidences, enabling the observation of phenomena at the molecular level.

In the light of this perspective, this thesis starts presenting a first work exploring the dynamics of supramolecular self-assembled soft nanoparticles (NPs) scanning surfaces functionalized with chemical gradients of receptors. In particular, the utilization of coarse-grained (CG) molecular models give us the possibility to control the fate of the nanoparticle by adjusting the chemical and physical properties of the single assembling units. As a result, the combination of classical MD and enhanced sampling simulations provides valuable insights into the design of nanoparticles with controlled disassembly and cargo release.

Subsequently, we investigated the emergence of relevant physical behaviors in response to external stimuli, such as the addition of second components in self assembled micelles, or the application of electric fields on colloidal lattices by employing CG-MD simulations. The second part of the thesis highlights the effects of introducing second components, with different intermolecular interactions, on the

rearrangement and self-organization of surfactants in self-assembled micelles. While, in the third part of the thesis, the same model resolution enables us to explore the semiconductive properties of a lattice of positively charged nanoparticles that self-assemble in the presence of multivalent counterions, where the application of electric fields promotes ion conduction within the lattice. In both cases, the combination of MD simulations with machine learning approaches permits the observation of these phenomena with a local point of view.

The fourth part of the thesis presents a work where simulations are used to examine, from a submolecular perspective, thermo-responsive amphiphilic assemblies that undergo phase transition in correspondence to the lower critical solution temperature. In particular, CG molecular models allow for the observation of the monomer-monomer and monomer-solvent interactions at different temperatures. The final case study focuses on the realization of a tubulin-based nanocapsule stabilized by glue molecules. In this case, all-atom models lead to the quantification of the effects of the glue molecules adhering on the surface of the nanocapsule.

In conclusion, the results discussed in this thesis show how molecular dynamics simulations may provide a fundamental support for the development of new self-assembled stimuli-responsive materials, starting through a deeper understanding of the intermolecular interactions that characterize the macroscopic properties of the aggregate.

Contents

List of Figures

List of Tables

Chapter 1

State of the Art

Supramolecular chemistry enables the realization of self-assembled materials with unique dynamic properties by manipulating the individual building blocks. Stimuli-responsive polymers can be used to obtain self-assembled materials that adapt their macroscopic properties in response to physical or chemical signals. This Chapter provides an overview of state-of-the-art experimental approaches to characterize self-assembling materials and their limitation. Finally, computational approaches are presented as a tool to facilitate the development of new smart materials obtained via self-assembled principles.

1.1 Self-assembly

As suggested by the Nobel Prize Jean-Marie Lehn, chemistry can be divided into two branches: molecular chemistry, which focuses on covalent bonds, and supramolecular chemistry, which considers the chemistry of molecular assemblies and intermolecular bonds.[1] Supramolecular chemistry, also referred to as "chemistry beyond the molecule", [2] thus concerns the study of molecular aggregates which are held together by intermolecular interactions [1]. Examples of non-covalent interactions are hydrogen bonding, dipole-dipole interactions, π-π stacking, and hydrophobic effects. In particular, these interactions play a fundamental role in several biological processes, such as protein aggregation, enzymatic reactions, antigen-antibody association, cellular recognition, and the transmission of signals *via* neurotransmitters. Inspired by these biological mechanisms, researchers have sought to develop

new supramolecular materials with applications in various fields, including biology, chemistry, and physics.

In the field of supramolecular chemistry, two different types of entities can be identified: the molecular building blocks, also named constituent units or monomers, and the supramolecular assemblies, which instead refer to the molecular aggregates that can be formed by more or less ordered structures. The spontaneous non-covalent association of the monomers, resulting into the formation of higher scale supramolecular objects, is known as self-assembly.[1] Supramolecular chemistry also encompasses the concept of molecular recognition, which describes the energy and the information involved in the selective binding between a substrate and receptor molecules. The monomer-monomer interaction is influenced by several factors such as the shape and size of the molecules, the dimensions of the contact surfaces, the affinity between them, as well as the interaction with the environment (e.g. solvent) and the external conditions (e.g. temperature).[1] The processes of molecular recognition and self-assembly can then occur in two ways: either in a spontaneous manner, when the formation of the final aggregate occurs directly (self-assembly), or in a directed manner, when it is guided by external species such as templates, substrates, or additional entities [3].

The realization of supramolecular systems requires a precise design of their building blocks, which must possess specific structural, conformational, thermodynamic, and bonding characteristics. Non-bonded interactions that contribute to the formation of supramolecular systems include *van der Waals* interactions originated from the dispersive or inductive forces, *electrostatic* interactions among different charged ions or dipoles, *charge transfer* between energy-rich and energy-poor components (such as π-π stacking, or metals and ligands attractions), *hydrogen bonding*, *metal coordination*, and *reversible bonds* like imine or disulfide formation (see Figure 1.1).[4] However, it should be noted that non-covalent interactions are generally weaker than covalent bonds, resulting in supramolecular structures that are thermodynamically less stable and thus more dynamical than covalent (macro)molecular systems.

Although intermolecular interactions are generally considered weak, they can form stable assemblies when present in large numbers due to the multivalency effect. In fact, after the onset of a first non-covalent bond between two monomers, the probability of aggregation with other building blocks might increase.[5] The balance of multiple concerted interactions thus determines the shape and function of the final

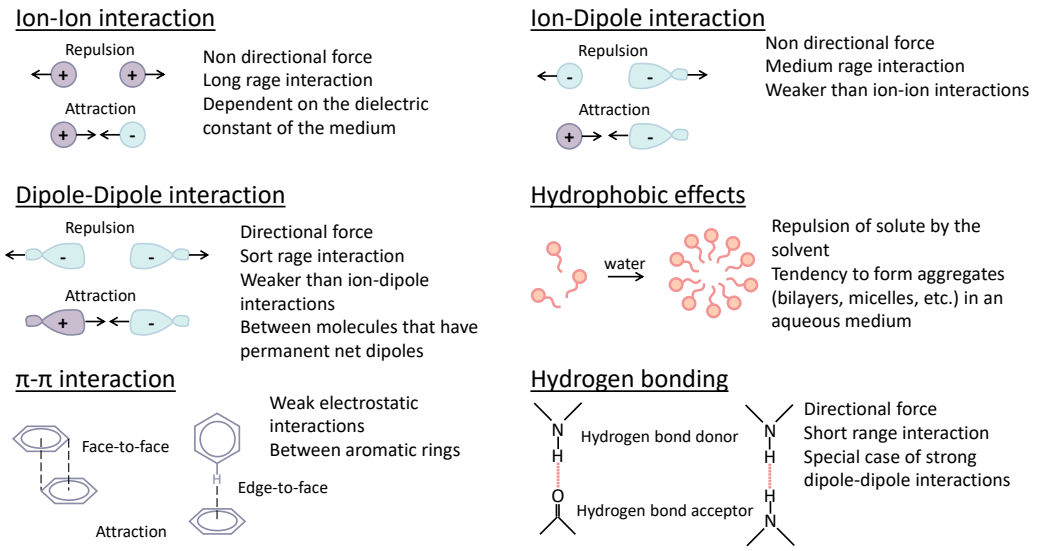

Fig. 1.1 Examples of non-covalent interactions in supramolecular materials.

assembly.[6, 7] Additionally, the reversibility of non-covalent interactions allows for self-organization of structures that, for example, self-heal when damaged, adapt to respond when stimulated, etc. [1, 4, 8–10]. The stability of the final structure depends on the balance between the enthalpic and entropic terms of the Gibbs-Helmholz equation ($\Delta G = \Delta H - T\Delta S$). Ideally, the change in enthalpy should result from the aggregation of the building blocks and the release of energy associated to the formation of new bonds, while entropy should disfavor the formation of an organized architecture. However, in practice, influences from the external environment may encourage the assembly, making the evaluation of the difference between the two energies difficult.[4]

The final self-assembled architectures typically reach the thermodynamic equilibrium state (Figure 1.2, #1) of the energy landscape associated to the considered chemical system and the relative environmental parameters such as temperature, pressure, and surrounding solvent. However, under certain conditions, as the presence of strong non-covalent interactions, the aggregate may reach a kinetically trapped metastable state, which resides in local rather than global minima (Figure 1.2, #2 and #3). Additionally, systems that occupy dissipative non-equilibrium states (Figure 1.2, #4), such as living supramolecular polymers, are maintained in such non-equilibrium states by constant influx of energy or matter. With the removal of

the energy supply, the system moves toward the closest non-dissipative equilibrium state or disintegrates.

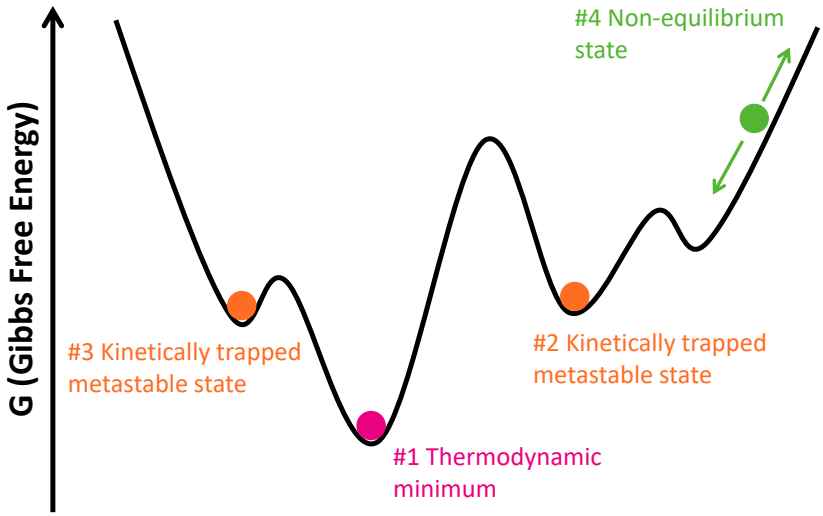

Fig. 1.2 Example of a free energy profile showing the thermodynamic states in supramolecular self-assembly.

Researchers have always been interested in utilizing supramolecular materials to replicate the self-assembling features present in nature, such as the aggregation of phospholipids in the formation of lipid membranes or the stacking of tubulin monomers in the formation of microtubules. As a result, self-assembly has become a widely used technique for creating a variety of materials with different properties by customizing the constituent building blocks. In particular, such an approach lays the foundation of modern material design to create "bottom up" materials that assemble molecule-by-molecule to form complex supramolecular architectures.

However, when designing the monomeric subunits, it is important to consider all the factors influencing the self-assembling process and, in that, the final structure [11]. There have been various studies conducted to understand how to properly design the single subunits based on the desired outcome. For example, in the formation of a vesicle from the self-assembly of amphiphilic monomers, the shape and size of the aggregate strongly depend on the relative size of the hydrophobic part compared to the hydrophilic one, as well as the relative composition and geometry of the single monomers (see Figure 1.3) [12]. On the other hand, the thermodynamic equilibrium among the amphiphilic monomers depends on the interfacial energy

of the hydrophobic/hydrophilic interfaces and the entropy loss required for the amphiphiles to fit into the aggregate. When the interfacial energy is high and the entropy loss is low, the formation of a vesicle is favored, while the formation of a bilayer is more probable with stiff monomers. The shape persistence also depends on the ability of monomers to arrange [12].

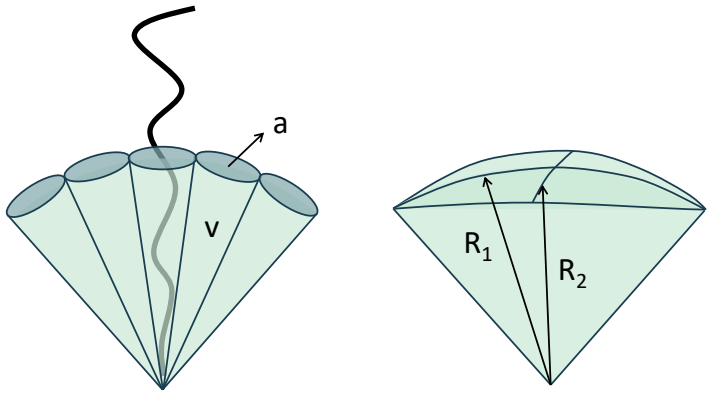

Fig. 1.3 Schematic representation of a vesicle portion obtained from the self-assembly of surfactants (cones). Considering the vesicle curvature H and the Gaussian curvature K, the surfactant packing parameter related to the curvature by $\frac{v}{al} = 1 + Hl + \frac{Kl^2}{3}$, where v is the hydrophobic volume of the monomer, a the interfacial area, and l the chain length normal to the interface. Thus, by varying the dimension of the hydrophobic head or the hydrophilic tail of the subunit, it is possible to obtain, for example, a bilayer, a cylinder or a sphere [12].

1.2 Examples of natural self-assembled materials

Self-assembly is widely employed by nature to build materials that are fundamental for living organisms. In the field of biology, most of the systems that constitute the foundation of life are composed of units that aggregate to form high-scale complex structures with specific shapes, sizes, and spatial distributions. [7] Examples of such structures include protein filaments, double-stranded nucleic acids, microtubules, cell membranes, viruses capsid, to cite a few.

Protein folding is one of the most explicative examples involving a self-assembling mechanism. Proteins are made up of covalently linked amino acids, where intramolecular interactions play a crucial role in the formation of secondary and tertiary conformations, while intermolecular interactions are responsible for the quaternary structure, such as in the formation of fibrils. On the other hand, the

configuration of DNA is strongly influenced by non-covalent interactions between the two strands, namely hydrogen bonds and π-π stacking interactions between nucleotides, resulting in a stable structure that contributes to the stability of DNA helices.[13]

Alternatively, silk is composed by silk fibroin protein that is approximately 1 μm in length, and silkworms are able to spin fibers up to 2 km of in length [14, 15]. The production of silk by spiders is also noteworthy, as it involves the replication of spidroins and the creation of silk with specific strength and elasticity based on the type of intermolecular connection between repeating regions [16]. This property has potential application, such as the production of sutures. Other two examples of self-assembled fibers include collagen and keratin. Collagen, the most abundant protein in vertebrates, helps to maintain the integrity of tissues and cells. There are various types of collagen that self-assemble into different complex structures, such as tendons, which are able to convert elastic energy into kinetic energy during muscle and tendon stretching [17, 18]. Keratin is an insoluble filament that self-assembles into helices to form hairs and wool, and has potential applications in tissue engineering and regenerative medicine.[19]

In many cases, the resulting self-assembled material is almost static, meaning that once the building blocks have self-assembled into a final structure, the material does not change its structural properties. However, there are examples of dynamic self-assemblies, which continuously change their shape and properties. Microtubules, for instance, are composed of tubulin subunits that continuously self-assemble into tubules and disassemble at the charged ends of the protofilament (see Figure 1.4a).[20] This dynamic process involves three different steps: nucleation, elongation, and depolymerization, and the dynamics will vary based on the number of nucleation sites and on the number of tubulin subunits present in the system.[21] A more complex example of a dynamic self-assembled system is the cytoplasmic membrane, which is a phospholipid bilayer that separates the cell from the external environment. The arrangement of phospholipids in the membrane is based on hydrophilic-hydrophobic interactions, specifically, the polar ends are exposed to the solvent while the non-polar ends facing the inner part of the membrane.[22] Phospholipids are able to continuously rearrange within the membrane, allowing the cell to change shape and to move, permitting for example the transport of water-soluble ions and molecules, the motion, and the fusion and subdivision of the cells.

Viruses can also be considered as self-assembled architectures. Their shell is typically composed of self-assembled proteins. There are two types of viruses: enveloped viruses, which have a capsid surrounded by a phospholipid membrane, and non-enveloped viruses, which do not. The latter are the simplest type of viruses and are composed by a self-assembled layer of proteins called capsid that encloses the genomic material. The tobacco mosaic virus is an example of a non-enveloped virus whose self-assembly process has been explored well *in vitro* [23]. It is a rod-shaper virus, meaning that it consists of a helical array of identical protein subunits, with the RNA embedded in each molecule. The self-assembling process of this virus is complex and begins with the nucleation of a starting protein disk, through which the RNA strand can insert.[24] From this point, the proteins self-assemble and the helical can be formed (see Figure 1.4b).

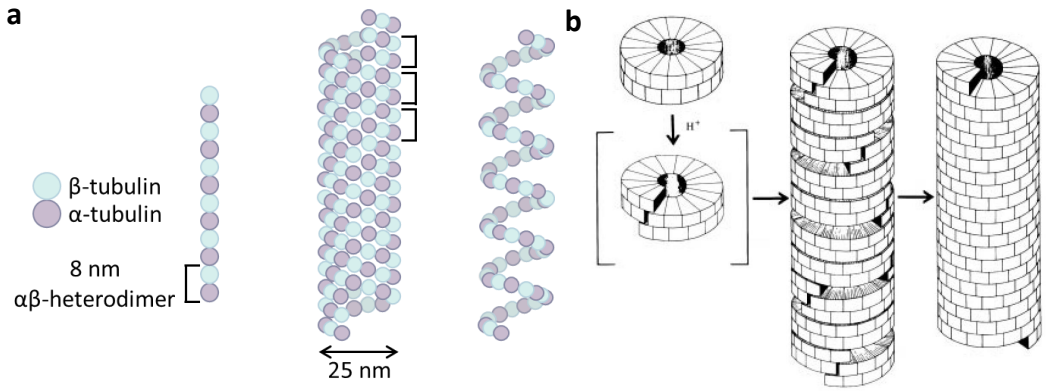

Fig. 1.4 Examples of natural soft self-assembled systems. **a** Schematic representation of the microtubule structure. **b** Schematic representation of the tobacco mosaic virus from Ref. [23] and reproduced under the permission of *Royal Society*.

1.3 Synthetic self-assembling systems

Inspired by such natural materials, many researchers have been focusing on the design of synthetic self-assembling systems. As a first example of building blocks, peptides are frequently utilized to design self-assembled materials due to their various advantages, such as the possibility to utilize the 20 distinct amino acids as monomers or to synthesize new peptides with specific functional groups. Additionally, the use of peptides facilitates the compatibility of the final aggregate with the biological

environment and its relative applications.[25] By utilizing peptides, and exploiting the multiple non-covalent interactions among them, it is possible to create a range of self-assembling architectures, from one-dimensional structures such as fibers [26] (Figure 1.5a) to three-dimensional aggregates such as nanospheres [27]. Additionally, complex configurations can also be achieved, as demonstrated by Kornmueller *et al.* [28], who observed a double-helix-like structure through the aggregation of an amphiphilic peptide at varying concentrations (Figure 1.5c). Similarly, Pan *et al.* [29] designed amphiphilic surfactants that self-assemble into a bilayer under appropriate conditions, while Khoe *et al.* [30] observed a donut-shaped nanostructure resulting from a properly cone-shaped designed peptide (Figure 1.5b).

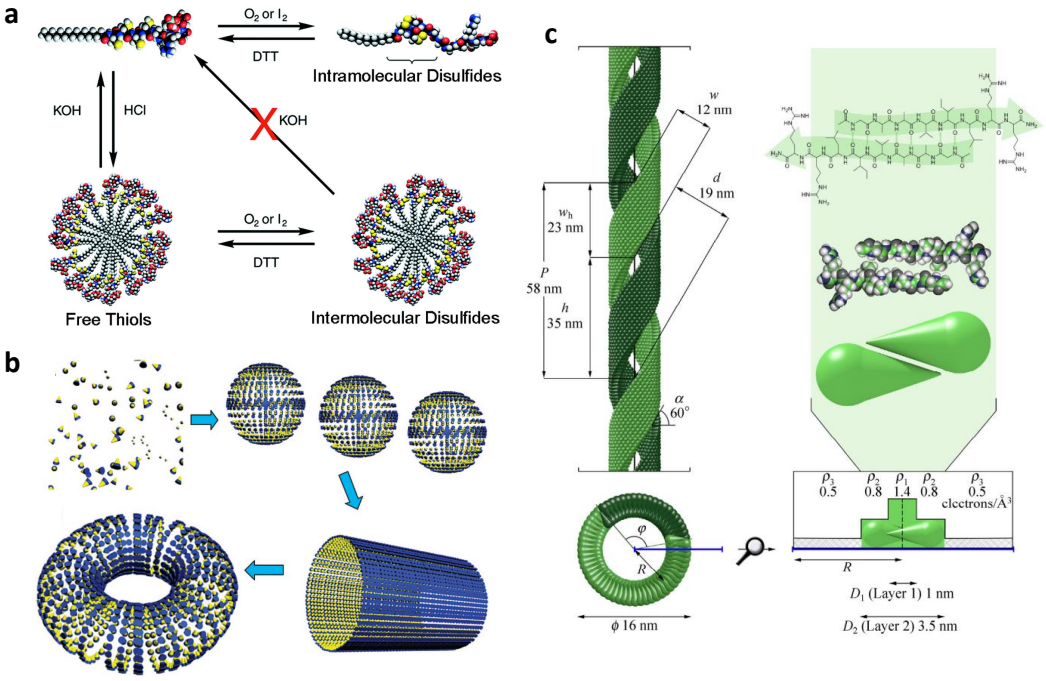

Fig. 1.5 Examples of bioinspired synthetic self-assembled systems. **a** Schematic illustration of the process of peptide-amphiphile units into supramolecular fibers. Figure from Ref. [26] replicated under the permission of *The National Academy of Sciences* (Copyright 2002). **b** Scheme of the assembling process of peptides into a nanodonut shape. Reprinted with permission from [30], *American Chemical Society* (Copyright 2008). **c** Structural parameters of the double-helical model from Ref. [28], replicated with the permission of *Creative Commons license*.

As previously mentioned, the design of appropriate building blocks is closely finalized to achieve specific self-assembled structures with *ad-hoc* properties. In this regard, researchers are making significant efforts to engineer new complex

supramolecular materials by using different approaches. One strategy is to use amphiphilic polymers, which upon contact with aqueous solutions, self-assemble into a supramolecular structure where the hydrophilic tails are in direct contact with the solvent while the hydrophobic moieties constitute the core of the assembly. The size of the final structure increases as the hydrophobicity of the polymer increases.[31] A prominent example are benzene-1,3,5-tricarboxamide (BTA) monomers, characterized by a hydrophobic core and hydrophilic branches, which form 1D fibers via core-core stacking and three-fold hydrogen bonding between amide groups.[32] In particular, the use of BTA monomers allows obtaining supramolecular fibers with a number of properties based on the chemical structure of the BTA functional groups [32]. One example is the BTA-fiber helices that can increase order and stability over time [33] (Figure 1.6a). Alternatively, BTA monomers can be functionalized with metal ions to get stable cylinders through the coordination bonds added by the metals [34]. Further amphiphilic polymer-based systems have been designed by Ouyang *et al.* [35] who obtained various types of Möbius strips by half-twisting, an odd number of times, an amphiphilic-based band and then fixing the ends together (Figure 1.6b). The utilization of amphiphilic polymers permits the realization of more complex structures, such as 2D membranes or 3D micelles. For instance, Imai *et al.* [8] discovered that by mixing two different amphiphilic copolymers in an aqueous solution, the self-assembled micelles are initially formed but then they self-correct by exchanging copolymers until they finally reach the thermodynamic equilibrium.

Another option to synthesize supramolecular materials is combining organic polymers with metals, where metal-organic coordination bonds control the self-assembling process. Self-assembled coordination cages, for instance, can be considered as nanoscale containers for performing reactions, encapsulating and transporting, or stabilizing reactive molecules [36]. As the confined space inside a cage must be recognized by a specific molecule, the design of the assembled structure is crucial. Specifically, cages are composed of metal centers acting as nodes, and synthesized organic ligands which bridge the nodes into a 3-dimensional structure [37, 38]. However, during the design process one has to consider the host-guest equilibrium in solution and the interaction between the cage and the guest as, in some cases, the disassembly of the cage may occur [39]. These host-guest systems can then be used to design novel synthetic receptors, sensors, and molecular transporters [36]. For example, the optical properties of chromophore dimers can be modulated through

the interaction within the cage [39] (Figure 1.6c) or different acid-mediated reactions can be catalyzed through different cationic intermediates [40].

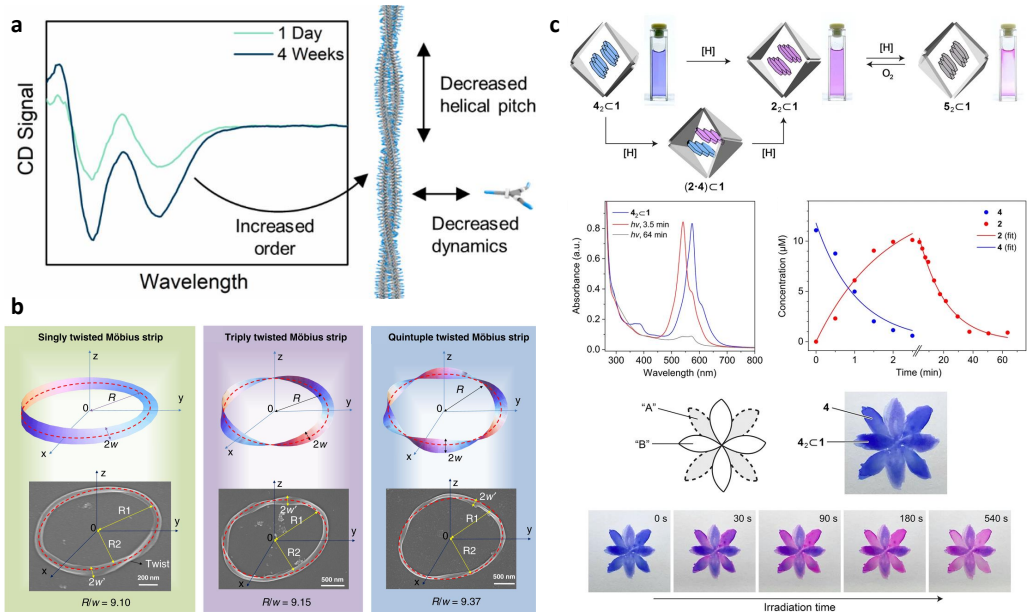

Fig. 1.6 Examples of synthetic self-assembled systems. **a** Stability of the BTA fiber helices over time, from Ref. [33]. **b** Theoretical parameters and experimental observation of the Möbius strips. Figure adapted from Ref. [35] under the permission of *Creative Commons license*. **c** Example of supramolecular cages utilized to control the optical properties of two different cromophores. Figure adapted from Ref. [39] under the permission of *Creative Commons license*.

1.4 Dynamic self-assembled architectures

All the applications discussed so far involve self-assembled units that aggregate in accordance with thermodynamic processes. As a result, the final structure represents the equilibrium state of the system, in which the only considered dynamics involve the continuous exchange of monomers between the assembled and disassembled states in solution in order to reach the most stable configuration (as illustrated in Figure 1.2).[41] Nonetheless, most self-assembled architectures posses an intrinsic dynamics of molecular exchange between the structures that characterizes their equilibrium configuration. Moreover, processes such as translation, replication, and chemical transport that are fundamental to living organisms possess dynamic features.[42, 43] Most of self-assembled materials can then be considered dynamics

in certain conditions (temperature, pressure, etc.), especially the ones that exist in a dissipative state, as living materials. Dynamic self-assembled structures can adapt and transform in response to the external environment.[44] Imparting the dynamic properties to the static self-assembled architectures, such as self-healing or stimuli-responsive features, would necessitate obtaining materials with dynamic properties.

Living materials are capable to self-heal and regenerate, at both microscopic and macroscopic levels, such as DNA repairing the healing of a wound on a finger.[45] Supramolecular assemblies, and especially their dynamic non-covalent interactions, are well-suited for the development of self-healing artificial materials with applications in material coatings. As an example, conductive stretchable materials, such as metal nanowires, have potential for various applications, including skin sensors and artificial muscles. Song *et al.* designed a stretchable conductor based on silver nanowire hydrogels and backfilling polymers, which preserve their conductive capability at strains from 100 to 800% within 500 cycles (see Figure 1.7a).[46] Another potential application for self-healing materials includes their use as coatings to prevent corrosion of aluminum alloys commonly employed in aircraft structures, which can repair damaged areas on their own. A recent study [47] proposed an eco-friendly pH-responsive coating composed of a molecular sieve containing pH-sensitive substances and ions capable to stop corrosion, and to recover when damaged up to 3.5 wt%. The self-healing mechanism is illustrated in Figure 1.7b.

1.4.1 Stimuli-responsive assemblies

Other examples of dynamic self/assembled materials are the stimuli-responsive materials. The ability to sense and react to changes in the external environment is a feature common to all living systems. For example, the Mimosa pudica plant is able to change the leaf orientation in response to different stimuli such as light, touch and temperature [48], while some Cephalopods are able to change their skin tone to mimic their surroundings as defense from predators [49]. The realization of active materials capable of responding to stimuli in a controllable and predictable fashion presents significant but fascinating challenges, especially because mimicking of biological systems requires controlling structural and compositional features at different length scales.[50] Self-assembled materials offer a well-suited platform to this purpose, as the non-covalent interactions characterizing them are sensitive

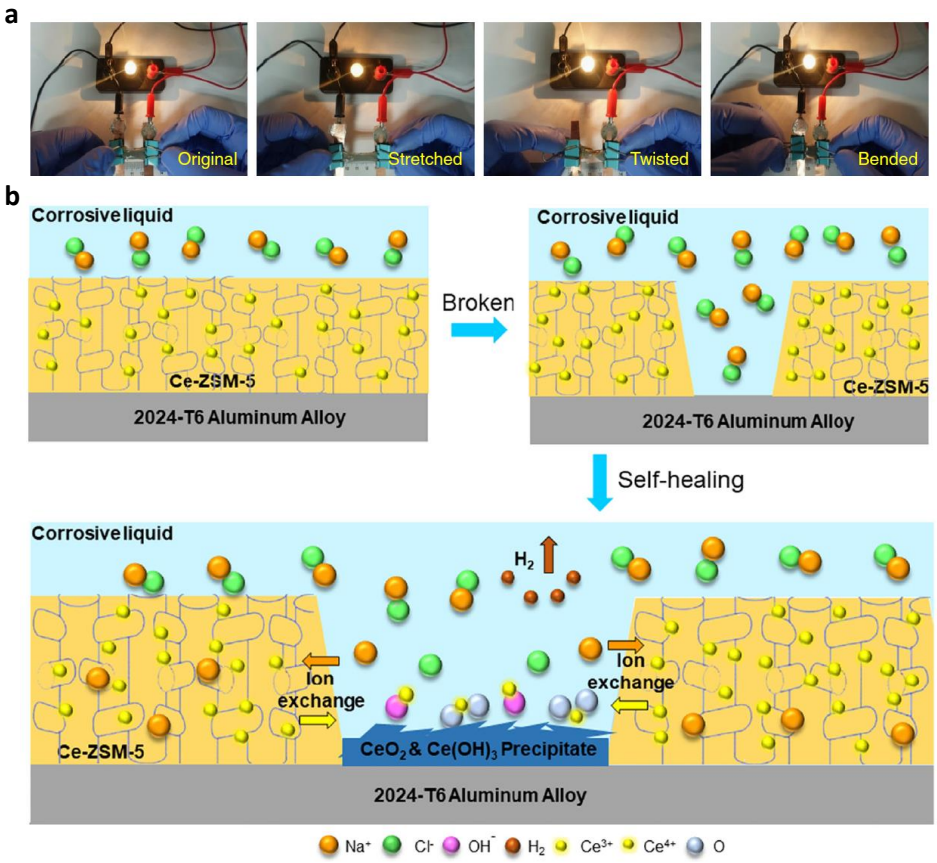

Fig. 1.7 Examples of self-healing assemblies. **a** Photographs demonstrating good electrical conductivity of silver nanowires hydrogel when stretched, twisted and bent. Figure from Ref. [46] replicated under the permission of *Creative Commons license*. **b** The self-healing mechanism of Ce-ZSM-5 self-healing coating. Figure from Ref. [47], and replicated under the permission of *Elsevier*

.

to variations of the external environment. Self-assembled materials, thanks to their dynamical supramolecular nature, are for example capable to react to single stimuli (such as pH, chemical gradients, light, magnetic field, or ultrasounds), or a combination of them, modifying their intrinsic chemical or physical properties. The adaptivity and self-regulation capabilities of these materials make them well suited to builds smart and responsive materials in a variety of fields.

Thermo-responsive polymers are the most used as the weak non-covalent interactions are particularly sensible to thermal stimuli which are indeed easy to be applied [52]. In particular, thermo-responsiveness is considered for those polymers able to

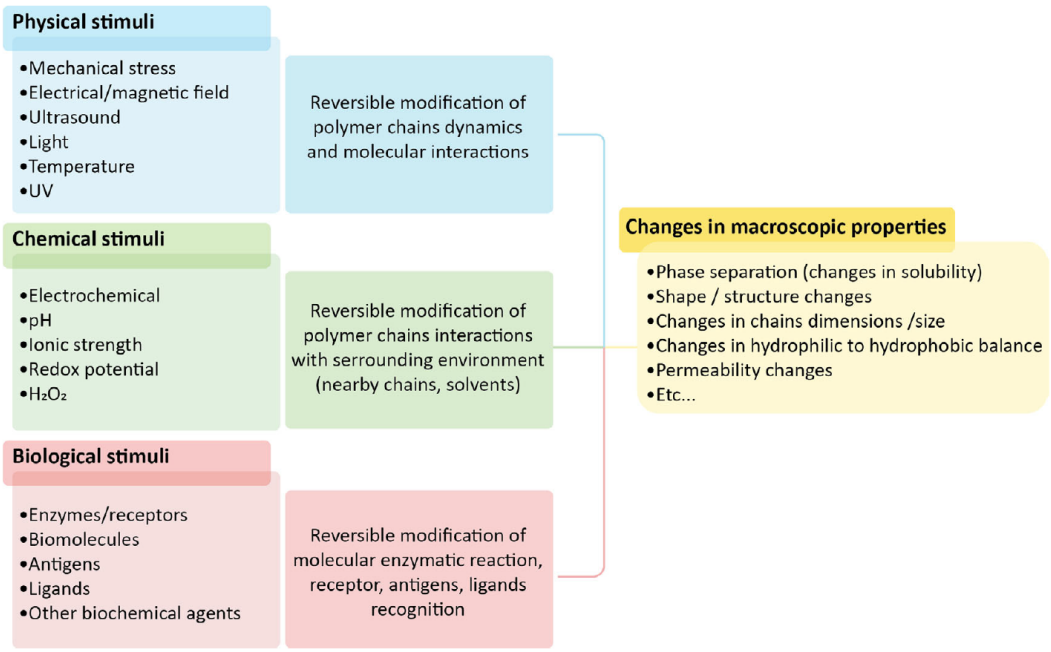

Fig. 1.8 Examples of external stimuli. Figure from Ref. [51] and reproduced under the permission of *John Wiley and Sons license*.

exhibit a lower critical solution temperature (LCST) or an upper critical solution temperature (UCST). In the first case, polymers are completely miscible in water for temperature below the LCST, while, in the other case, polymers are miscible in water for temperatures above the UCST [53]. Therefore, the behavior of the polymers depends on the balance between polymer-polymer interactions and polymer-aqueous solution interactions. One interesting application is in the field of building energy efficiency, where windows represent the main source of energy loss. In this context, Zhou *et al.* [54], proposed a different model of window, which contains a hydrogel within the glasses, and is able to block the solar energy transmission when the temperature is above the LCST (see Figure 1.9).

Alternatively, external fields can be applied to activate responsive materials. The usage of external field entails various advantages, such as, remote and non-invasive control, but also they can be modulated by varying different parameters, as duration, intensity, and frequency. Under the application of light, photo-responsive polymers are able to suddenly convert the energy into a chemical reaction, or into other forms of energy, such as heat, sound, light, or electricity [55, 56]. For example, photo-reponsive polymers patched with microneedles can be used to efficiently localize

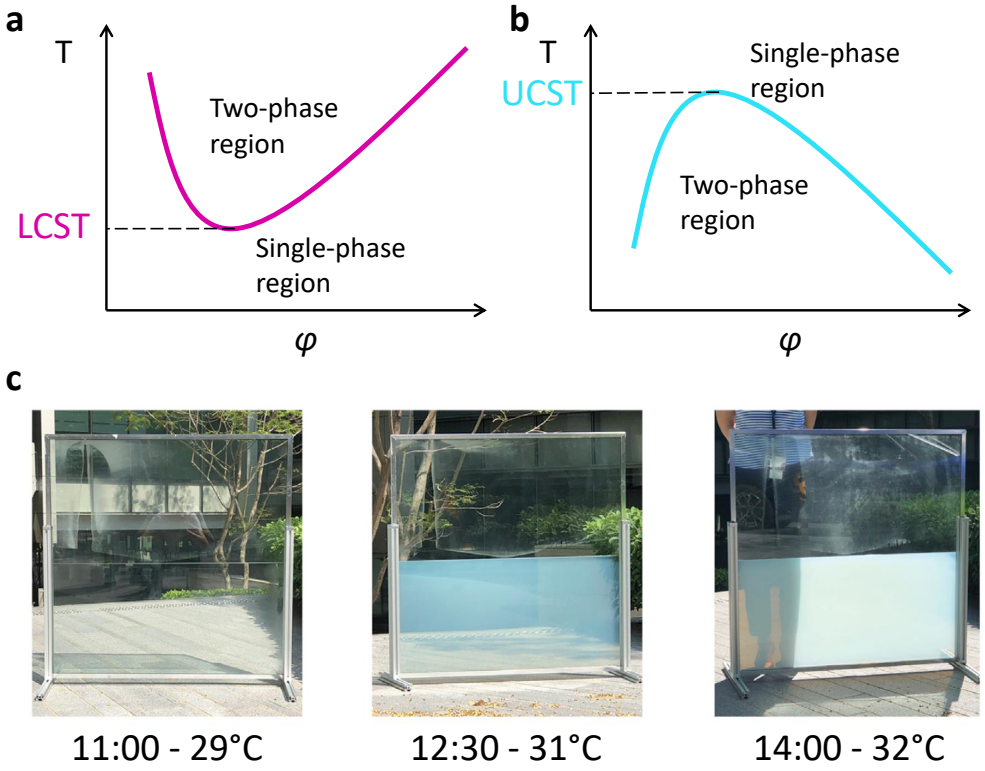

Fig. 1.9 Thermo-responsive polymers. Definition of **a** lower critical solution temperature (LCST) and **b** upper critical solution temperature (UCST). **c** Temperature-responsive windows tested at different time of a day from ref [54], reproduced under the permission of *Elsevier*.

and treat tumors, or wound healing [57]. Magneto- or electro-responsive polymers are normally composed of a soft polymer matrix which includes magneto or electro-responsive particles, and can be used to realize a broad range of materials, with applications from tissue engineering to actuators [58]. Among others, Ma *et al.* [59] realized a soft robot incorporating hard magnetic particles into a shape memory polymer.

Among the chemical stimuli, the variation of pH is generally adopted with those polymers composed of weak acid or basis and characterized by functional groups that protonate or deprotonate in specific chemical condition solutions. pH-responsive polymers can then undergo hydrophobic, conductive or morphological changes [60]. Zeng *et al.* [61], for instance, obtained a functionalized cotton fabric which exhibits a superhydrophobic or superhydrophilic behavior based on the pH thereby helping the separation of oil and water. Alternatively, both pH and temperature perturbation

can be combined, especially in peculiar cases such as the oral therapy for colon disease: due to the long transportation route along the gastrointestinal tract, there is a high possibility for the drug to be decomposed by other organs; thus the hydrogels can be employed as delivery systems, since they load a large quantity of drug, they are alkaline-pH responsive, and shrink at 37 °C [62].

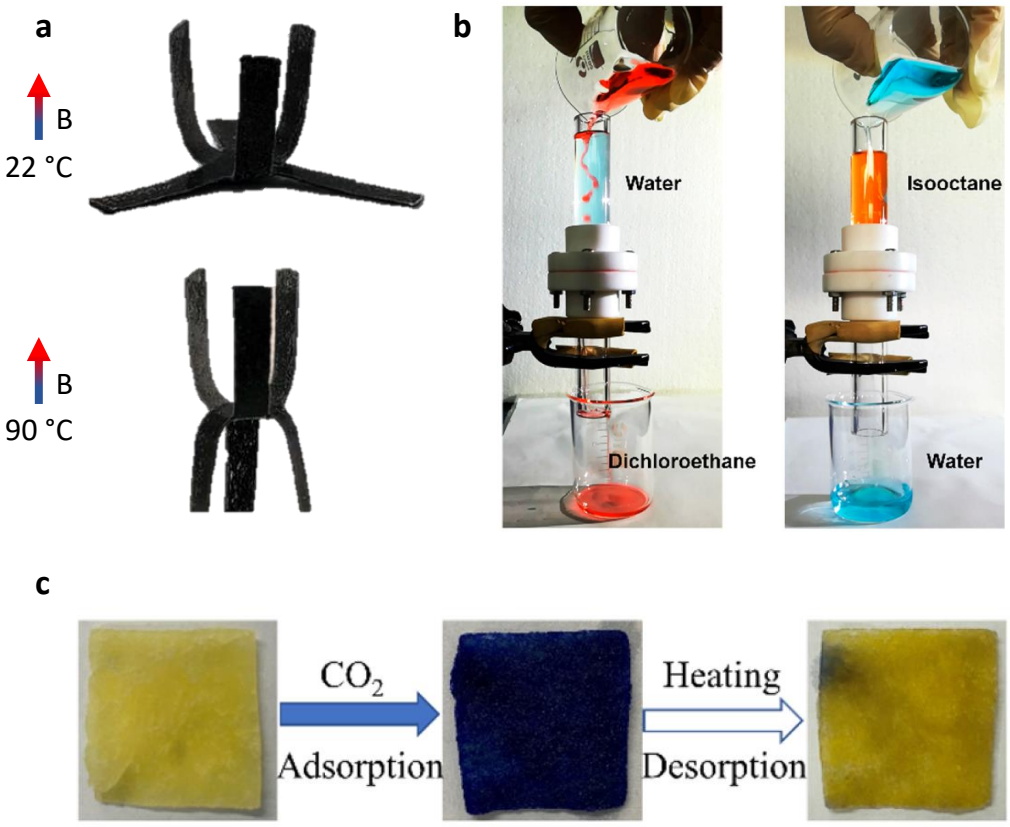

Fig. 1.10 Applications of stimuli-responsive materials. **a** Magneto-responsive soft robots from Ref. [59]. **b** pH responsive cotton fabric from Ref. [61]. **c** CO_2 responsive cotton of Ref. [63]. All the figures were reproduced with the permission from the *American Chemical Society*.

The development of stimuli-responsive molecular systems opens up the possibility to design various type of materials, therefore, recent research is moving toward the design of eco-friendly and reusable materials. CO_2 responsive materials are widely studied as CO_2 is considered a "green" chemical trigger, obtaining responsive absorbents of heavy atoms from polluted water [64], or of anionic dyes from wastewater (see Figure 1.10c) [63].

1.5 Characterization of stimuli-responsive materials

Based on the preceding discussion, supramolecular materials, particularly stimuli-responsive materials, exhibit internal dynamics that enable the aggregate to adapt its chemical or physical properties as a response to stimuli. Therefore, comprehending and regulating the dynamic response of these materials is fundamental for designing supramolecular materials capable of adapting to external stimuli. Despite the advanced experimental techniques that are currently available, studying these systems is not trivial as the dynamics occurs at the molecular level and on short time-scales. Thus, a combination of various techniques is typically required for characterization purposes.

One approach for detecting the dynamics of individual building blocks involves labeling them with fluorescent molecules, chiral centers, or molecules with higher mass to facilitate better characterization and observation of the aggregate. Spectroscopy techniques provide valuable structural and morphological information at the atomic and molecular level, enabling insight into the stability of the final assembly. Nuclear magnetic resonance (NMR) spectroscopy, for instance, can provide information on specific species and functional groups under various conditions, allowing then for the study of the effects of different stimuli, such as changing solvents or variation of temperature.[65–67] Raman spectroscopy, on the other hand, reveals the crystallinity of the aggregate [68, 69]. Similarly, absorption techniques, such as UV-vis and FT-IR, can be used to obtain information related to the composition of the aggregate.[70, 71] Circular dichroism (CD) is also used to detect intermolecular interactions and is capable of revealing the presence of $\pi - \pi$ stacking.

Microscopy, on the other hand, allows for imaging of materials at nanoscale resolution, revealing structural and morphological details. Electron microscopy, such as transmission electron microscopy (TEM) and scanning electron microscopy (SEM) (Figure 1.11a), allows for the estimation of the size of fibrils and micelles, while fluorescence microscopy enables the observation of dynamic processes.[70, 72] Stochastic optical reconstruction microscopy (STORM) permits the detection of dynamic mechanisms, as, for example, BTA fibers exchange pathways with a resolution $\sim$20-50 nm (Figure 1.11b).[73]

Diffraction techniques are useful for detecting the arrangement of molecules in the assemblies. For example, x-ray diffraction can describe the atomic arrangement

in powder, thin films, or bulks, but requires drying the sample. These techniques are usually utilized to characterize the final aggregate by its size, thickness, and shape. Small-angle x-ray scattering (SAXS), on the other hand, permits the study of complex structures in real-time with a resolution up to 15 $\dot{A}$. It is commonly used to detect structural changes during the experiments.[69]

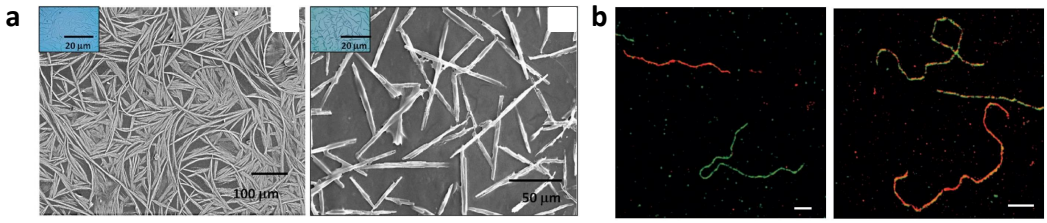

Fig. 1.11 Examples of experimental characterization. **a** SEM images of cationic dyes in different solvents. From Ref. [70]. **b** STORM experiments show exchange along the BTA fibers from the beginning of the observation (left) to the end of the observation (right). From Ref. [73].

Despite all these techniques partially satisfy the necessity to observe and describe the structure of supramolecular materials, they have some limitations. For instance, the requirement to utilize dried materials, as in TEM and SEM, provides structural information at high resolution but does not reveal any information related to the supramolecular dynamics. The usage of fluorescent molecules to label the individual monomers can also impact the final structure of the aggregate, influencing its internal dynamics. Finally, most of these approaches do not reach molecular resolution, which is fundamental for investigating the molecular processes involved in the stimuli-responsiveness. As a result, the utilization of molecular models and molecular simulations is crucial for deepening the understanding of these supramolecular processes.

1.6 The role of molecular models and simulations

Despite the numerous experimental techniques developed to characterize the microscopic features of the self-assembled structures, the observation of their internal dynamic is still challenging. The use of molecular modeling and simulations permits (i) to develop a model of the system considered, which contains information related to the interactions between the different species, such as the different monomers

and the solvent. In this way, (ii) molecular models allow simulating the system *via* different methods as Monte Carlo (MS) or molecular dynamics (MD), from which the physical observable specific to the model can be obtained. MD simulations permit to follow the dynamics of the system, which depend on its equation of motion, while in MC the study is exclusively statistic and the system is governed by its potential energy and statistical mechanics. Molecular modeling and simulations are crucial to enrich the investigation of dynamic mechanisms underlying these phenomena. Molecular modelling finds wide applications in various fields such as biology, chemistry and physics for exploring and predicting the behavior of molecules and molecular systems [74]. Molecular models can also be used to design delivery systems, create new materials, characterize their structure and properties, and to investigate the interactions between single building blocks in self-assembled materials. Molecular models also support and help interpret experimental data by analyzing molecules with higher resolution and by controlling the atoms, bonds, angles and dihedrals in the studied molecular structure [75]. The resolution of a model allows investigating different aspects of chemical structures, ranging from atomistic resolution where every particle represents a single atom, or coarse-grained (CG), in which a particle (bead) represents a small group of atoms. Since atomistic models limit the time- and space-scales that can be explored, enhanced sampling techniques and CG models are usually employed to improve the exploration of the energy landscape while maintaining a certain chemical detail, despite the reduction of the molecular resolution. Different representations of molecular systems permit the observation of different aspects of the self-assembling materials. Therefore, a proper combination of finer CG models and minimalistic representations of molecular systems allows merging of macroscopic evidence with more detailed sub-molecular observations.

As a representative case, the dynamic behavior of benzene-1,3,5-tricarboxamide (BTA)-based supramolecular polymers is highly dependent on monomer-monomer interactions, and the study of the polymerization process in water is experimentally inaccessible (Figure 1.12a). To understand this complex process, the utilization of molecular models can help to understand this complex process. As mentioned before, the choice of the appropriate level of resolution is fundamental to simulate the appropriate space and time scales, as the atomistic model does not allow simulating the self-assembling process of this system (Figure 1.12b). A first solution to accelerate the simulations is the use of coarse-grained (CG) models, which permit the observation of the self-assembling process and the dynamics internal to the aggre-

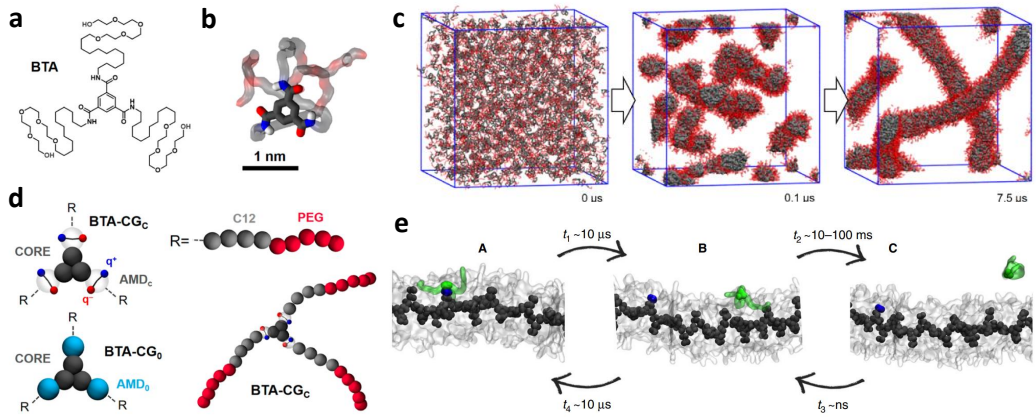

Fig. 1.12 Molecular simulations of BTA fiber formation. **a** Chemical structure of a BTA monomer and **b** its atomistic model. Figure adapted from Ref. [76] **c** Snapshots reporting the different steps in the self-assembling process from BTA monomers to the assembled fibers. Figure adapted from Ref. [77] **d** Examples of CG models of BTA monomer. Figure adapted from Ref. [76] **e** Monomer exchange in BTA water-soluble fiber. Figure adapted from Ref. [78], replicated under the permission of *Creative Commons license*

.

gate. One case is the use of MARTINI-based models, where every bead represents three to five heavy atoms of the chemical structures (Figure 1.12d). Bochicchio *et al.* demonstrated that MARTINI-based CG-MD simulations, developed from the atomistic model, not only confirm the behavior observed with experimental evidences, but also provide information about the dynamics at the supramolecular level.[76] Additionally, by developing a MARTINI-based CG model in implicit solvent, Bochicchio *et al.* observed the self-assembling process of different monomers in different concentrations (Figure 1.12c).[77] However, in some cases, the resolutions dictated by the MARTINI force field is too detailed. Minimalistic models can then be useful to explore general aspects of the self-assembling process.[79] Another approach to accelerate the simulations is to employ enhanced sampling techniques, such as metadynamics, which allows, for example, studying the free-energy differences and barriers associated to the monomer exchange process in BTA fibers.[78] The application of these techniques leads then to the observation of the dynamic adaptivity of supramolecular systems, and their dynamic response to the application of external stimuli. For example, still considering the self-assembling of BTA monomers, Torchi *et al.* tested the dynamic adaptivity of the BTA monomers in a self-assembled fiber containing few charged monomers that selectively interact with an oppositely charged recruiter molecule (DNA strand) dispersed in solution

(Figure 1.12e).[80] With MD simulations they observe the reorganization of the BTA charged monomers to interact with the DNA recruiter. Furthermore, they tested the responsivity of this charged BTA structure to external electrostatic field.

Analogously, the same approaches can be applied to every complex supramolecular system. For example, CG models and metadynamics simulations revealed that the responsiveness to UV-light in supramolecular tubules is strictly related to the presence of defects on the structure, leading to the monomers the possibility to allow the *trans-to-cis* isomerization.[81] MD simulations have played a crucial role also in understanding the potential precursor of the hydrochloride salt of fampridine and predicting the formation of their crystal in the study by Montis *et al.* [82]. In the latter case, the simulations also opened up new possibilities in the design of new organic crystalline materials. In the work of Datta *et al.*, focused on the study of self-assembled poly-catenanes composed of single building blocks, MD simulations, along with enhanced sampling techniques, explore the free-energy associated to the secondary nucleation of a catenane onto the surface of an existing one, deemed responsible for the formation of these topologically interlocked structures (Figure 1.13a-c).[83] Lochenie *et al.* [84] have demonstrated the importance of combining experimental approaches with MD simulations in order to fully understand the physical-chemical phenomena involved in their system. In particular, using all-atom simulations, the authors calculated the number of hydrogen bonds between Pt-PyAG monomers in different solvents, while by employing CG models, they observed the formation of fibers from Pt-PyAG monomers and the assembly of these fibers in different solvents (Figure 1.13d-f).

It is worth noting that the results obtained from MD simulations are strongly dependent on the quality of the molecular model employed. In order to efficiently optimize the CG model based on the MARTINI force field, there are various tools available, such as Swarm-CG that exploits an automatic multi-porpose scheme based on swarm particle optimization.[85]

Once the simulations have been carried out different analysis may be conducted on the final trajectory, starting from standard calculations, such as number of contacts, gyration radius, and radial distribution functions, or utilizing advanced techniques of analysis, such as machine learning algorithms. In the study of Gasparotto *et al.* [86], the use of a machine learning approach allowed the authors to characterize the internal dynamics of a self-assembled BTA fiber. This approach also enabled

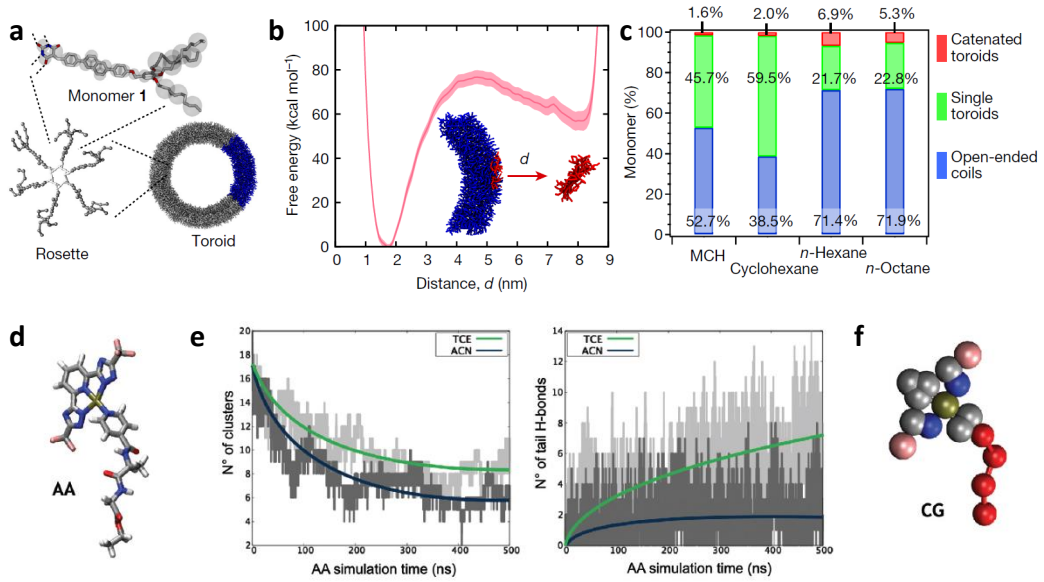

Fig. 1.13 Examples of molecular dynamics simulations results. **a-c** (a) All-atom and, in transparency, coarse-grained model of one monomer, (b) free-energy profile, (c) histogram showing the dependency of the choice of the solvent on catenanes, toroids and open-ended coils. Figure adapted from Ref. [83], replicated under the permission of *Springer Nature Limited* **d-f** (d) All-atom model of one monomer, (e) monitoring of the assembling process through the calculation of the number of cluster and the calculation of the number of hydrogen bonds, (f) coarse-grained model of the same monomer. Figure adapted from Ref. [84], replicated under the permission of *Creative Commons license*

.

the classification of self-assembled materials based on their structure, stability and dynamics. Gardin *et al.* [87], in their recent work, demonstrated the applicability of this approach to all types of self-assembled material.

In summary, molecular models and simulations are important tools for gaining a deep understanding of the behavior of supramolecular materials. They allow predicting molecular behavior and the analysis of molecular structures at various resolutions.

1.7 Aim of the thesis

Supramolecular chemistry offers a wide range of valuable examples to guide the design of dynamic self-assembled materials with advanced properties. By manipulat-

ing the constituent building blocks and the interaction between them, it is possible to produce new materials with unexpected properties and a number of applications in biotechnology, chemistry, and material science. The use of stimuli-responsive materials as constituent units in self-assemblies has introduced the unique prospect to tailor the macroscopic properties of supramolecular architectures in response to external stimuli or signals. In particular, I focused on physical or chemical signals, such as, chemical gradients, electrostatic fields, and variation of temperature. However, the ability to design these fundamental units to control the properties of such assemblies remains an open challenge. The use of molecular models allows predicting the behavior of supramolecular materials, facilitating their design and functionalization. Furthermore, molecular simulations provide a comprehensive understanding of the physical-chemical mechanisms embedded into the self-assembling process, thereby giving a molecular-level insight into the behavior of these complex systems which is not accessible through experimental methods.

The aim of this PhD work is to investigate the dynamic behavior of self-assembled structures in response to various external stimuli. To overcome the limitations in the experimental resolution, the study utilizes molecular dynamics simulations. However, classical molecular simulations can access only restricted time-scales, and therefore CG molecular models and enhanced sampling techniques like metadynamics have been employed to capture rare molecular events, which play a crucial role in controlling the dynamic adaptivity of supramolecular structures.

This Thesis contains a description of the methods utilized in the studies (**Chaper 2**) and the presentation of the case studies explored during my PhD career. In particular, the results include examining multivalent interactions on dynamic nanoparticles with bioinspired chemotactic properties (**Chapter 3**), exploring the impact of mixing different surfactants on the internal dynamics of micelles (**Chapter 4**), studying the effects of electrostatic stimuli on co-assembled nanoparticles forming a colloidal lattice structure (**Chapter 5**), investigating the influence of temperature variations on soft polymeric assemblies (**Chapter 6**), and exploring the formation of GTP-responsive nanocapsules using microtubules (**Chapter 7**).

Chapter 3. In nature, various systems exhibit the ability to release chemical species in response to external stimuli. For instance, leukocytes can bind the surfaces of blood capillaries, roll and scan surface markers, slow down, stop, and then release inflammatory signals. Consequently, replicating such abilities in synthetic

materials would be a significant advancement in many fields, including biomedicine, sensing, and adaptive materials. As a case study, we investigated the use of various amphiphilic monomers to design a supramolecular nanoparticle that manifests autonomous chemotactic behavior.

Chapter 4. Micelles are characterized by an innate dynamics, which determine the properties of the aggregate. However, a clear understanding of their internal dynamics is non-trivial. The reorganization and compartmentalization of the monomers in the aggregate are influenced by changes in the shape and chemical structure of the self-assembling units. To gain insight into the dynamics of micelles, we selected three surfactants and examined their dominant molecular environments and the movement and exchange of self-assembling monomers.[88, 89]

Chapter 5. The self-assembly of nanoparticles into more complex structures provides excellent controllability, which has resulted in increasing interest in colloidal superlattices based on self-assembled nanoparticles. Recent studies have demonstrated that, when small species are dispersed in the lattice, the supramolecular structure is analogue to the one of atomic crystals, in which the nanoparticles represent the atoms analogues, while the smaller specie act as electron equivalents.[90–99] Inspired by these observations and a previous work [100] that involved gold nanoparticles functionalized with positively charged ligands self-assembling in the presence of multivalent anions, we investigated the supramolecular semi-conductive properties of a lattice composed of these nanoparticles and the mediating anion species when subjected to different electrostatic fields.

Chapter 6. Soft stimuli-responsive materials are attractive due to their adaptability and suitability for a wide range of applications. In particular, the intermolecular interactions that charaterize the supramolecular polymers are extremely sensible to the variations of temperature. In correspondence to the lower critical solution temperature, thermo-responsive polymers undergo a phase transition, from complete miscibility to phase separation, when the temperature overcomes a certain threshold. To gain insight into how self-assembled aggregates are affected by temperature fluctuations, we examined a nanoparticle composed by amphiphilic oligomers.

Chapter 7. Guanosine triphosphate (GTP) is known to be over-expressed in certain diseased cells, therefore, the realization of GTP-responsive nanocarriers can be a potential solution for the treatment of cancer and RNA-virus-induced diseases. The interaction within α- and β-tubulin with GTP results in the formation of a

leaf-like nanosheets, which transform into spherical nanocapsules in the presence of a glue molecule. In this study, simulations were utilized to gain insights into the positioning of the glue molecules on the tubulin heterodimer and their interaction with it.

Chapter 2

Methods

In order to gain further insights in the internal mechanisms of stimuli-responsive self-assembled materials, it is essential to observe these materials at a molecular resolution. In this regard, molecular modeling and simulations are crucial to enrich the investigation of dynamic mechanisms underlying these phenomena. The purpose of this Chapter is to give a general overview of the theory behind molecular dynamics simulations, coarse-graining approaches, enhanced sampling techniques, and machine-learning based approaches for analyzing the resulting trajectories.

2.1 Molecular models

A molecular model is a three-dimensional representation of chemical or biological molecules that is used to observe their structure, investigate their physical and chemical properties, compare different molecules, visualize their dynamics, and predict their behavior. This is achieved by solving the equations of quantum and classical physics.[101, 102] The resolution of the molecular models defines the type of phenomena that can be observed.

Molecular modeling techniques can be classified into several categories based on their resolution and, as a consequence, on the achievable timescale, such as *ab initio* quantum mechanics, molecular dynamics (MD), coarse-graining (CG), mesoscale, and continuum approaches. Quantum mechanics offers the highest accuracy and is primarily used to study electronic structures. Molecular dynamics and coarse-grained dynamics are based on classical mechanics and are often utilized

to study the conformation of complex molecules with a sub-molecular or molecular resolution and to observe dynamic processes as self-assembling processes.[102] The level of detail in molecular model also influences the time-scale that can be simulated, ranging from 10^{-15} seconds for quantum mechanics to seconds or hours with continuum approaches, where, however, the chemical structure of molecules is not considered.

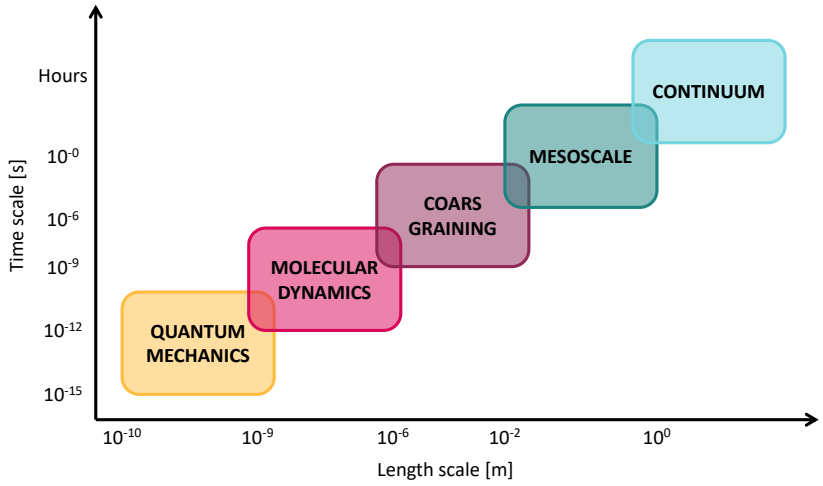

Fig. 2.1 Schematic representation of multiscale modeling. The choice of the spatial resolution allows for the observation of phenomena that occurs at specific timescales.

The theory that describes the molecular models influences the phenomena that can be observed with the simulations. The models considered in this Thesis relied on molecular mechanics, which are represented as interacting spheres connected by springs.

2.2 Force fields

The motion of the particles in a system is determined by the interactions between and within molecules. The description of these inter- and intra- molecular interactions depends on the definition of the potential energy function, which in turn depends on the force field considered. Therefore, a force field is the mathematical description of the energy of a system, which depends on the coordinates of its particles.[103] Generally, the potential energy function defines both intra- and inter-molecular interactions:

$$\mathscr{V} = \mathscr{V}_{bonded} + \mathscr{V}_{non-bonded} \tag{2.1}$$

The terms used to describe intra- and inter- molecular interactions can vary in complexity based on the chosen force field. One of common method for describing bonded interactions is:

$$\mathscr{V}_{bonded} = \sum_{bonds} \frac{k_i}{2}(l_i - l_{i,o})^2 + \sum_{angles} \frac{k_i}{2}(\theta_i - \theta_{i,0})^2 + \sum_{torsions} \frac{V_n}{2}(1 + cos(n\omega - \gamma)) \tag{2.2}$$

The first two terms in the equation are harmonic potentials that describe bond stretching and angle bending, while the third term is a torsional potential that models the ability of a bond to rotate. Differently from bond and angle description, the torsional terms can be modeled with different potential functions. Additionally, improper torsional parameters are necessary to maintain the planarity of certain structures, such as aromatic rings. On the other hand, non-bonded interaction are calculated between all pairs of atoms (i and j) that are in different molecules or in the same molecule but separated by at least three bonds. Non-bonded interactions consider both the short- and long-range interactions, where the former ones decay faster than the latter ones. Specifically, short-range interactions are highly sensitive to the local environment and can be influenced by adjacent particles, while long-range interactions are more influenced by the global distribution of particles in the system. The definition of the non-bonded interactions typically includes two terms, one for the electrostatic interactions (acting on a long-range) and the other for van der Waals interactions (acting on short distances):

$$\mathscr{V}_{non-bonded} = \sum_{i=1}^{N} \sum_{j=i+1}^{N} \left(4\varepsilon_{ij} \left[\left(\frac{\sigma_{ij}}{r_{ij}} \right)^{12} - \left(\frac{\sigma_{ij}}{r_{ij}} \right)^{6} \right] + \frac{q_i q_j}{4\pi\varepsilon_0 r_{ij}} \right) \tag{2.3}$$

Where, r_{ij} is the distance between the two interacting particles i and j, σ is the distance at which the in interaction between the two particles is zero, ε is the well depth that indicate how strong is the attraction, q_i and q_j are the charges of the two particles, and ε_0 is the dielectric constant (ε_0 = 1 in all atom MD in explicit solvent). In a simple force field, the electrostatic interactions are described by the

Coulomb potential and the van der Waals interactions by the Lennard-Jones (LJ) 12-6 potential. In particular, van der Waals interactions are usually truncated at a certain cutoff distance, while the electrostatic interactions can be considered exclusively in a certain cutoff, or can be calculated using the particle-mesh Ewald algorithm or Ewald summation. However, calculating the interaction energies is the most time-consuming part of an MD simulation. To reduce the computational time, it is necessary to restrict the pairs of particles for which the interactions are calculated by choosing a cut-off radius.

2.3 Multiscale modeling

Molecular models are essential to explore systems at molecular level. Atomistic models describe with high fidelity the chemical structure of the system studied. These models are usually employed to explore the interactions between different molecules, that occur at time-scales of $\sim 10^{-9}$ s. Since the aim of this Thesis is to explore the stimuli-responsivness dynamics of self-assembled systems, which occurs at higher time-scales (from $\sim 10^{-6}$ s up to seconds or minutes), atomistic models cannot be considered. In this regard, this Thesis focuses mainly on the use of fine or minimalistic coarse-grained (CG) models, which represent a good compromise in terms of spacial and time resolution.

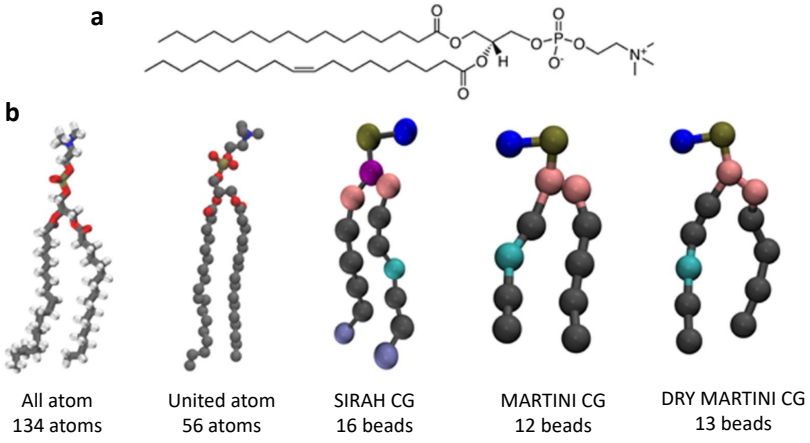

Fig. 2.2 Examples of multiscale models. **a** Chemical structure of a POPC molecule. **b** Examples of models at different resolution. Figure adapted from Ref. [104], replicated under the permission of *American Chemical Society*

Two different approaches can be used to develop a CG model: a top-down approach, if the non-bonded interactions between the different chemical building blocks are tuned from the experimental results, and a bottom-up approach, if the atomistic models are used as a reference. [105–108]. In this view, bottom-up CG models reproduce exclusively certain structural details at specific energy states, while top-down CG models are more general and can be utilized to study different systems without the need to re-parametrize the force field every time. Bottom-up models are based on the definition of force fields, such as the MARTINI force field, which is an effective solution to study self-assembled supramolecular materials without losing the definition of the chemical structure of the system studied.

2.3.1 Explicit solvent MARTINI force field

The MARTINI force field [105, 109] is based on a four-to-one mapping, in which four heavy atoms and their associated hydrogens are typically represented by a single interaction site (CG-bead). This allows for a fairly accurate representation of the chemical structure of the system being studied. However, the mapping rule is not strict, and it is sometimes possible to group three, five, or more atoms in a single interaction center. The interaction sites can be classified into four types: polar, nonpolar, apolar, and charged. Each type has various subtypes, allowing for the fine-tuning of interactions for different chemical structures. Like all-atom models, the MARTINI force field defines both non-bonded and bonded interactions. The non-bonded interactions are described by the LJ 12-6 potential, which is divided into different levels to represent different interactions, such as strong polar interactions in water or various degrees of hydrophobic repulsion between polar and non-polar phases. If the CG-beads are charged, the electrostatic interactions are described by the Coulomb potential. Bonded interactions are modelled using weak harmonic potential for bonds, angles, and dihedrals, as in all-atom models.

Thanks to the stability of the MARTINI force field and the reduction in degrees of freedom, it is possible to increase the integration time step and therefore increase the number of steps simulated. However, since the CG energy landscape is smoother than the atomistic one, the dynamics observed cannot be directly compared to those observed in all-atom simulations. To compare the results from AA and CG simulations, a conversion factor of 4 should be applied [105, 106].

All the CG models described by the MARTINI force field utilized in the works reported in this Thesis are created following a three steps process: i) grouping the chemical structure into small chemical building blocks, each of which is preferably composed of four heavy atoms (though sometimes a smaller or larger number may be used), ii) selecting bonded interactions, with the standard bond length ($0.47nm$) and force constant (K_{bond} = 1250 kJ mol^{-1} nm^{-2}) able to be adjusted to better describe the chemical structure, and iii) optimizing the model by comparing it to the finer models (such as all-atom models) to optimize bonded and non-bonded interactions and match the free energy landscape, allowing for results that can be compared to real systems. In all the CG models discussed in this thesis, steps ii) and iii) were implemented using the tool published in reference [85].

It is important to note that, as this is a CG model, the results are subject to certain approximations such as a decrease in entropy due to reduced fluctuations. As a result, the entropy loss is compensated by a reduction in the enthalpy term, and all results should therefore be considered qualitative rather than quantitative.

2.3.2 Implicit solvent (dry) MARTINI force field

The MARTINI force field significantly accelerates the sampling of the phase space by approximately three orders of magnitude compared to the all-atoms model. However, CG-MD simulations are still slow for those systems characterized by a high number of water molecules. One method of reducing the number of molecules in molecular simulations is to utilize the Dry MARTINI force field [111], which is based on the standard wet MARTINI force field but excludes the aqueous phase. Dry MARTINI utilizes the same bead type as the standard MARTINI force field, but includes adjustment to the bonded and non-bonded interactions to account for the effects of water. It should be noted, however, that since this type of force field is even coarser than the classic MARTINI force field, the results obtained from these MD simulations should therefore be considered qualitative. The use of the Dry MARTINI force field also allows for the simulations that are orders of magnitude larger than those simulated in water.

There are, however, some limitations to be considered when using Dry MARTINI force field. The bonded and non-bonded interactions have been modified, resulting in increased interactions of polar beads to mimic hydrophobic effects and decreased

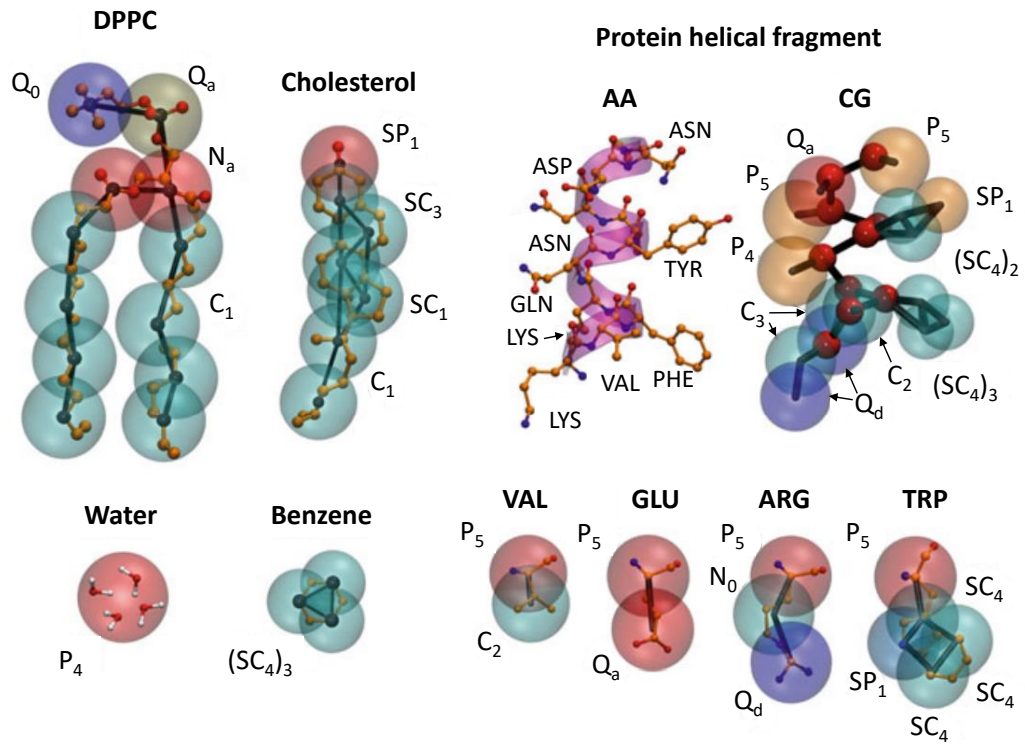

Fig. 2.3 Examples of MARTINI mapping, where the CG beads are reported in transparency in correspondence to the all atom (AA) models. The systems reported are DPPC, cholesterol, water, benzene, a protein helical fragment, and a few amino acids (valine, glutamic acid, arginine, and tryptophan). Figure adapted from Ref. [110], replicated under the permission of *Springer Nature Limited*

interactions of polar and charged particles to account for the implicit screening effect of water molecules. It is also important to note that Dry MARTINI can only be used to study systems in water solutions, as the interactions with water are always taken into account as an implicit solvent [111].

Nevertheless, the primary advantage of Dry MARTINI is the acceleration of MD simulation, particularly for systems in which water molecules occupy a large portion of the simulation box, such as in studies of micelles. In these cases, speed-up factors of up to two orders of magnitude have been observed.

2.3.3 Minimalistic models

Minimalistic models are defined with top-down approaches and represent exclusively a specific configuration of the system to be studied. In this thesis, minimalistic models are utilized as toy models to explore the system before the development of finer CG models. In fact, since minimalistic resolution is lower compared to the MARTINI-based models, they allow computing faster simulations and observing phenomena that occur at higher time-scales. In this regard, minimalistic models are described by interacting spheres, where bonded and non-bonded interactions are tuned in order to observe specific dynamics behaviors.

2.4 Molecular dynamics

Molecular Dynamics (MD) simulations are based on the resolution of Newton's equation of motion that allows to study the movement of every atom in a molecular system over time. These simulations can provide detailed information about molecular behavior at the atomic level, such as protein folding or the addition or removal of a ligand. In MD simulations, atoms are represented as beads and bonds among them are modeled as springs. By adjusting certain parameters, such as the size of the beads and the stiffness of the springs, it is possible to accurately replicate the molecular system to be studied.

After assigning initial positions and velocities to each particle, a first step of energy equilibration is needed. Once the system has equilibrated, the simulation can be extended for a specified amount of time, and the properties of interest can be measured. In this way, it is possible to obtain microscopic level information, such as the formation of hydrogen bonds, strength of interactions, etc., that may not be observable at the macroscopic level in real experiments.[112]

In atomistic models, each atom is represented by a particle. The motion of a particle i with mass m_i can be described by Newton's equation of motion as:

$$m_i \ddot{\mathbf{r}}_i(t) = \mathbf{f}_i \tag{2.4}$$

where $\mathbf{f}_i$ is the force acting on the molecule i. Thus, considering a system composed by N molecules interacting through forces, the motion will be described

by N sets of similar equation. Different algorithms have been proposed to solve Eq.2.4, one of the simplest is the Verlet algorithm. The position of a particle i at time $t+\Delta t$ can be expressed in terms of its position, velocity, and acceleration at a time t, through the Taylor series expansion:

$$\mathbf{r}_i(t+\Delta t) \approx \mathbf{r}_i(t) + \Delta t \dot{\mathbf{r}}_i(t) + \frac{1}{2}\Delta t^2 \ddot{\mathbf{r}}_i(t) \tag{2.5}$$

that can also be written as:

$$\mathbf{r}_i(t+\Delta t) \approx \mathbf{r}_i(t) + \Delta t \mathbf{v}_i(t) + \frac{\Delta t^2}{2m_i}\mathbf{F}_i(t) \tag{2.6}$$

where $\mathbf{F}_i(t)$ is equal to the opposite of the derivative of the potential energy $\mathscr{V}$ ($\mathbf{F}_i(t) = -\partial\mathscr{V}/\partial\mathbf{r}_i$), and can also contain external forces that can be applied to the system, as temperature, pressure, etc. In the same way, it is also possible to obtain for the expansion at $t-\Delta t$:

$$\mathbf{r}_i(t-\Delta t) = \mathbf{r}_i(t) - \Delta t \mathbf{v}_i(t) + \frac{\Delta t^2}{2m_i}\mathbf{F}_i(t) \tag{2.7}$$

Adding the Eqs.2.6 and 2.7 it is possible to obtain a velocity-independent scheme:

$$\mathbf{r}_i(t+\Delta t) = 2\mathbf{r}_i(t) - \mathbf{r}_i(t-\Delta t) + \frac{\Delta t^2}{m_i}\mathbf{F}_i(t) \tag{2.8}$$

Eq.2.8 is the Verlet algorithm, in which, given a set of initial position and initial velocities, Eq.2.6 can be used to obtain a set of coordinate. Subsequently, Eq.2.8 can be used to generate a trajectory of arbitrary length. Verlet algorithm only generates the positions, to obtain the velocities the following formula should be used:

$$\mathbf{v}_i(t) = \frac{\mathbf{r}_i(t+\Delta t) - \mathbf{r}_i(t-\Delta t)}{2\Delta t} \tag{2.9}$$

However, MD simulations only allow the control of microscopic properties of the system. In order to compare simulation results with the experimental observation, it is essential to regulate the macroscopic properties, such as temperature and pressure. Therefore, according to the Gibbs' concept, an ensemble is a collection of systems that share common macroscopic properties, as total energy, temperature, and volume.

While the evolution of every system is described by the microscopic laws of motion from different initial conditions, meaning that at every time step the system is described by a distinct microscopic state.[113] Ensembles can be defined for several thermodynamic situations:

- The Canonical ensemble (NVE) corresponds to an isolated system, thus with fixed volume V, energy E, and number of atoms N
- The Isothermal-Isobaric ensemble (NVT) corresponds to a closed system where the number of atoms N, the volume V, and the temperature T are fixed
- The Gran Canonical ensemble (μVT) corresponds to an open system with constant chemical potential μ, volume V, and temperature T
- The Microcanonical ensemble (NPT) characterized by constant number of atoms N, pressure P and temperature T

However, the resolution of the equations of motion is extremely time-consuming, and depends on the number of atoms present in the system studied. Therefore, one way to reduce the computational time of MD simulations is to study a system that is as small as possible, while still being large enough to avoid discontinuities in the potential energy calculation and to prevent the finite-size effects. If the system is too large, periodic boundary conditions (PBC) can be used to approximate an infinite system with a small part, called unit cell. In PBC, when a particle reaches one side of the unit cell, it reappears on the opposite side with the same velocity. The unit cell is surrounded by the copies in all directions. In this way, each particle interacts with its neighbors, even if they are on the opposite side of the simulation box. This approach is important because it allows the thermodynamic properties, such as temperature, pressure, and density, to be preserved. It is worth nothing that the cutoff radius chosen for non-bonded interactions should be shorter than half the size of the unit cell, in order to avoid particles interacting with themselves.

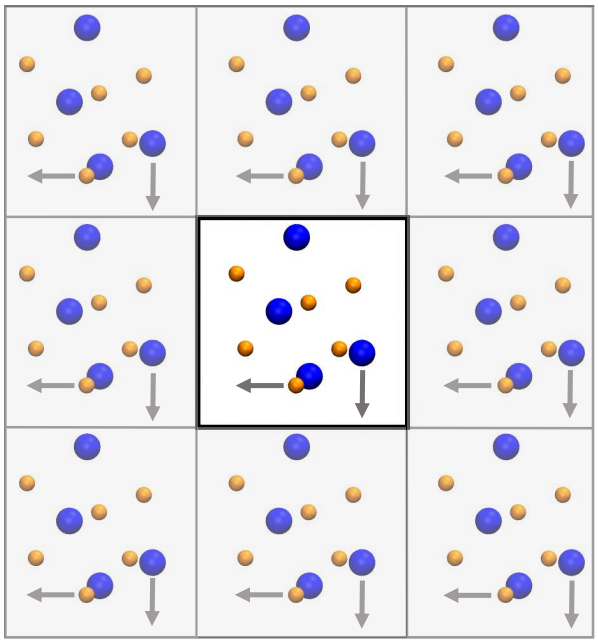

Fig. 2.4 Periodic boundary conditions (PBC)

2.5 Enhanced sampling

It is worth noting that the results of MD simulations are only valid if the system being simulated is ergodic over the duration of the simulation, meaning that the system has explored all the possible states in a statistically uniform and random manner. However, these configurations are often separated by high energy barriers that can only be crossed through rare, high enough fluctuations, or, in other cases, the diffusion of the system in the configuration space may be slow. In most cases, the sampling of classical MD is unsatisfactory, and even more severe, it is difficult to check (if not simulating forever). In either of these scenarios, a significant amount of computational time may be necessary to obtain a sufficient sample of configurations for statistical analysis. To address this issue, several methods have been proposed, including biased simulation approaches and metadynamics.

2.5.1 Biased simulations

Enhanced sampling simulations are often utilized to accelerate the sampling of the configurational space or to study the free energy surface (FES) of a system.

However, in some cases, the primary focus of enhanced simulations may not be the FES itself, but rather the study of a particular phenomenon without considering the energy barriers involved. To achieve this, biased simulations can be used to effectively guide the system to overcome energy barriers and explore the phase space in a more efficient manner, simply by applying a directional force as a bias. For example, Koner *et al.* [114] utilized umbrella sampling calculations [115] to tune the intermolecular interactions in order to obtain an intertwining of organic nanotubes consistent with experimental results. Alternatively, replica exchange MD simulations can be utilized to investigate the different assembled configurations of proteins in explicit solvent.[116]

2.5.2 Metadynamics

The metadynamics method involves the use of an external (Gaussian) bias potential to accelerate the sampling of the configuration space. The bias is applied to a selected number of degree of freedom, known as collective variables (CVs) with the ultimate goal of reconstructing the free energy surface (FES) as a function of the chosen CVs.

The history-dependent bias potential, which is a function of the CVs, consists of a sum of Gaussians deposited on the system trajectory in the CVs space in order to discourage the system from revisiting configurations that have already been sampled. In continuous direct metadynamics, the bias potential is continuously applied during the MD simulation. Letting S be the set of n functions of the microscopic coordinates R of the system:

$$S(R) = (S_1(R), ..., S_n(R)) \tag{2.10}$$

The bias potential at time t can be written as:

$$V_G(S,t) = \int_0^t dt' \omega exp\left(- \sum_{i=1}^{n} \frac{(S_i(R) - S_i(R(t')))^2}{2\sigma_i^2} \right) \tag{2.11}$$

where ω is the energy rate (the ratio of the height of the Gaussian and the deposition stride), and σ_i is the width of the Gaussian for the ith CV.

There are several advantages to use metadynamics in MD simulations: (i) it speeds up the sampling of rare events by forcing the system to move away from

local energy minima, (ii) it enables the system to explore reaction pathways, (iii) it does not require prior knowledge of the landscape, and (iv) if the simulation is run for a sufficient duration, it is possible to estimate the FES from the bias potential. Additionally, to further enhance the exploration of the configurational space, it is possible to conduct multiple parallel metadynamics MD simulations, known as multiple walkers simulations, in which each simulation contributes to the history-dependent bias potential.

However, metadynamics also has some limitations: (i) the bias potential does not converge to a constant value of the free energy in a single run, but rather oscillates around it, making it difficult to determine when to end the simulation; (ii) the selection of appropriate CVs can be challenging. The first issue can be addressed through the use of well-tempered metadynamics, in which the bias deposition rate decrease over the course of the simulation. In well-tempered metadynamics, the bias potential is described by a different expression:

$$V(S,t) = k_B \Delta T ln\left(1 + \frac{\omega N(S,t)}{k_B \Delta T}\right) \tag{2.12}$$

where $N(S,t)$ is the histogram of the S variables collected during the simulation, and ΔT is an input parameter with the dimension of temperature.

When selecting CVs in metadynamics, the following criteria should be considered: (i) the CVs should distinguish between the initial, final, and any intermediate state, (ii) the CVs should include all the slow modes of the system, and (iii) they should be kept to a minimum number. Because metadynamics involves a reduction in dimensionality, if the CVs do not adequately distinguish between different states in the simulation, the results may not contain valuable information. Slow CVs must be included to properly describe the transitions between configuration states, but it can be helpful to include some fast CVs to speed up the convergence of the simulation. Additionally, the convergence rate is also affected by the number of CVs chosen, so the number of CVs should be minimized in order to limit the dimensionality of the space being explored. Suitable CVs can be selected from a set of pre-implemented options in PLUMED [117–119], such as the number of contacts or distances, or they can be developed specifically for the system being studied.

2.6 Standard analysis of MD simulations

As previously mentioned, molecular models can be used to observe the dynamics behavior of the supramolecular materials, but also to characterize them from a structural and dynamic point of view. There are various calculations in literature that can be applied to the final trajectories to characterize the materials in different degrees of complexity. Typically, studies based on MD simulations contains a combination of them. This Thesis employs both standard and advanced analysis methods to describe the intrinsic dynamics of the stimuli-responsive materials under investigation.

The standard analyses in this study are performed using the Gromacs package, which is also the software utilized for conducting the MD simulations. For instance, the gyration radius is commonly employed to measure the dimensions of spherical systems such as micelles or nanoparticles. Alternatively, the solvent accessible surface area (SASA) can be utilized to measure the surface area exposed to the solvent (either implicit or explicit) and may correlate with the level of assembly in the system. The coordination number is often used to quantify the strength of the interactions between the monomers in assembled structures or aggregates with external species.

However, there may be phenomena that cannot be detected by these types of analyses or even by a combination of them. In such cases, it is necessary to consider more complex techniques to detect them.

2.7 Advanced analysis of MD simulations

Recent advances in computational power and techniques have made it possible to predict and classify models of target physical properties using a combination of MD simulations and machine learning (ML) algorithms. In particular, machine learning techniques can be used to explore and describe materials and their structures by extracting meaningful information and patterns from the simulations results. However, to improve the performance of the ML approaches, systems must be described by a limited number of variables, ideally different from the simple coordinates of the system – a system with N particles is described by $3N$ coordinates. Descriptors, which are functions of the coordinates of the system under consideration (such

as angles, coordination numbers), can provide a more compact description of the phenomena to be analyzed. The reliability of the results depends on the descriptor's ability to accurately represent the property of interest. However, selecting an appropriate descriptor can be challenging as there is not a single, universally applicable descriptor. [120]

Several dimensionality-reduction machine learning techniques have been developed to evaluate the collective dynamics behavior of complex chemical/molecular systems under both equilibrium and non-equilibrium conditions. The Smooth Overlap of Atomic Position (SOAP) [121] descriptor provides a high-dimensional description of molecular environments. This description, called "atomic-environment", is a high dimensional vector that stores all the information about a specific central reference atom. The technique involves the application of a Gaussian smoothed density profile at the selected reference site; the SOAP environment takes into account the contributions of other particles within a certain cutoff radius r_{cut}. Then, the SOAP power spectra can be calculated as:

$$\mathbf{p}(\mathbf{r})^{i}_{nn'l} = \pi \sqrt{\frac{8}{2l+1}} \sum_{m=-l}^{l} c^{i}_{nlm}(\mathbf{r}) * c^{i}_{n'lm}(\mathbf{r}) \tag{2.13}$$

where c^{i}_{nlm} are the expansion coefficients of the particle density surrounding the *i*th center. Additionally, this is the output that can be obtained from the SOAP calculation using the DScribe [122] package. Once obtained the measure of two environments corresponding to two different sites, it is possible to calculate a similarity measure within these environments, which is defined by a linear kernel of their density representation:

$$K^{SOAP}(i,j) = \rho_i(\mathbf{r}) \cdot \rho_j(\mathbf{r}) \propto \mathbf{p}_i \cdot \mathbf{p}_j \tag{2.14}$$

The similarity measure within two different environments corresponds to the dot product of the power spectra of the two sites. The local densities, represented by $\rho_i(\mathbf{r})$ and $\rho_j(\mathbf{r})$, are centered at the $i-th$ and $j-th$ sites, respectively, within the cutoff radius r_{cut}. Equation 2.14 can be also considered as a measure of the similarity between the two environments, with a value of K^{soap} that ranges from 0, indicating completely different environments, to 1, indicating matching environments. As a

result, the power spectra and the SOAP kernel can be used to define a similarity metric between two sites, known as the SOAP distance:

$$d^{SOAP}(i,j) = \sqrt{2 - 2 \cdot K^{SOAP}(i,j)} \propto \sqrt{2 - 2\mathbf{p}_i \cdot \mathbf{p}_j} \tag{2.15}$$

However, the output from the SOAP algorithm is a high-dimensional vector, which is too complex to be efficiently analyzed using machine learning techniques. Therefore, a Principal Component Analysis (PCA) can be utilized to reduce the number of components in the SOAP distance vector. PCA is an algorithm that reduces the dimensionality of the data by preserving the variation within the dataset.[123]

Once the number of variable has been reduced, the use of a ML approach, such as the Probability Analysis of Molecular Motif (PAMM) [124, 125], allows for the analysis of the results using a clustering technique. PAMM is a density-based clustering technique that recognizes molecular motifs in a system, such as defects, by studying the probability distribution of fragments observed in an atomistic simulation. The parameter space is divided into a sparse grid in order to reduce the dimensionality of the dataset and estimate the density using the Kernel-density estimation. The unsupervised cluster subdivision process, based on the quick-shift algorithm, starts from a random point in the grid and connects it to the nearest grid point at a higher probability density until a stopping criterion is reached. The next clusters are detected in the same way, avoiding points already assigned to a cluster. The distributions of the different clusters are then fitted in order to interpret the different modes and identify the different motifs in the system.

Recently, this approach permits to observe the internal dynamics in BTA fibers [86] and to classify different self-assembled materials based on their structure, stability, and dynamics [87]. This Thesis reports some examples of applications of this advanced methods, demonstrating its importance in the study of stimuli-responsive processes.

Chapter 3

Modeling autonomous chemotactic self-assembled nanoparticles that respond to surface gradients

*The work described in this Chapter has been published in the following paper: "C. Lionello, A. Gardin, A. Cardellini, D. Bochicchio, M. Shivrayan, A. Fernandez, S. Thayumanavan and G. M. Pavan. Toward chemotactic supramolecular nanoparticles: From autonomous surface motion following specific chemical gradients to multivalency-controlled disassembly. ACS Nano **2021**, 15, 16149–16161" [126], and has been adapted with permission of Creative Commons CC BY license.*

Abstract

Nature designs chemotactic supramolecular structures with the ability to selectively bind specific groups present on surfaces, autonomously scan them moving along density gradients, and react once encountering a critical concentration. These properties are crucial in several biological functions and therefore provide inspirations for designing artificial systems capable of similar bioinspired autonomous behaviors. One approach is to use soft molecular units that self-assemble in aqueous solution forming nanoparticles (NPs) that display specific chemical groups on their surface, enabling for multivalent interactions with complementarily functionalized surfaces.

However, a first challenge is to explore the behavior of these assemblies at sufficiently high-resolution to investigate the molecular factors controlling their behaviors.

Here, we demonstrate that by coupling coarse-grained (CG) molecular models and advanced simulation approaches, the (autonomous or driven) motion of self-assembled NPs on a receptor-grafted surface can be studied at sub-molecular resolution. In particular, we focus on self-assembled NPs composed of facially amphiphilic oligomers. We observe how tuning the multivalent interactions between the NP and the surface allows to control NP binding, its diffusion along chemical surface gradients, and ultimately, the NP reactivity at determined surface group densities. *In silico* experiments provide physical-chemical insights on key molecular features in the self-assembling units which determine the dynamic behavior and fate of the NPs on the surface: from adhesion, to diffusion, and disassembly. These findings offer a privileged perspective into the chemotactic properties of supramolecular assemblies, thus improving our knowledge on how to design new types of materials with bioinspired autonomous behaviors.

3.1 Introduction

Learning how to design new smart materials, with, for example, the capacity of cells to adapt their cellular activity, to respond to selective recognition/binding of ligands [127–131] in a controlled way would be of great interest [132–136]. A specific example is provided by leukocytes, which bind the surfaces of blood capillaries, roll and scan surface markers, slow down, stop, and release inflammatory signals. Such binding, rolling, and reacting capabilities are controlled by a complex interplay between protein-protein and protein-carbohydrate interactions at the interface.[137, 81, 138, 132–135]

While mimicking the complexity and autonomous precision of the immune system is a challenging task, imparting similar autonomous functionalities to synthetic materials (Figure 3.1) would be a significant breakthrough in many fields, including biomedicine, sensing, and adaptive materials. However, achieving this goal requires gaining a deeper understanding of the molecular factors that control the selective non-covalent interactions and the complex interplay between them at the interface. In particular, responsive nanoparticles (NPs) have shown binding capabilities associated with customized releasing of encapsulated cargos.[132–136]

Both monovalent and multivalent interactions has been exploited in the design of selective interactions. As examples, Liao et al. studied the correlation between monovalent labelling schemes on a gold NP and its diffusion rate on supported lipid bilayer membranes [139], while Overseem and coworkers investigated multivalent binding profiles of influenza virus on surfaces with receptor density gradients [140]. However, the rational design of chemotactic functional materials requires a level of observations that is difficult to achieve solely with experimental techniques. This is because tracking, tracing and observing the movement of small, soft NPs on surfaces at sufficiently high spatio-temporal resolution is challenging [141, 142], and gaining insights into the molecular factors and processes that govern NP chemotactic responsive behavior is even more complex, as it requires observing these materials in action at a submolecular resolution.

In this view, various molecular models and simulations approaches have been proposed to reach this goal. For instance, coarse-grained (CG) models have been used to study the adhesion and dynamics of minimalistic nanoparticles on ligand-functionalized surfaces [143–146], allowing the calculation of the number of interactions between the spherical NP and the surface receptors [146, 147]. A similar approach has been applied to monitor the rolling of a soft spherical cell model on surfaces under the presence of an external flow.[144] Alternatively, the diffusion profile of a rigid sphere on a cross-linked membrane has been largely investigated.[147–149] Specifically, variations of surface receptor density and multivalent interactions between NP and gel-like membrane were observed to have many effects on the diffusivity of the NP, eventually inducing NP trapping in high-density regions.[147, 149]

In order to design supramolecular assemblies that have the ability to selectively bind surfaces, autonomously scan them moving along chemical surface gradients, and trigger controlled dynamic responses, it is necessary to use finer-level molecular models. Finer-level molecular models, and in particular CG models with a resolution of $\sim$5 $\dot{A}$, coupled with advanced molecular simulations and analysis, have been adopted to study the dynamics and dynamic properties of supramolecular self-assemblies [132, 76, 150]. *In silico* simulations can provide a unique perspective into the response of supramolecular polymeric materials to different biorelevant stimuli, such as changes in temperature, salts, solvents, and light.[132, 80] All-atom molecular dynamics (AA-MD) simulations of protein-responsive assemblies have allowed the comparison of the self-assembly stability of NPs composed of soft amphiphilic oligomers bearing biotin ligands with specific and non-specific

interactions with complementary extravidin. In particular, it was demonstrated how specific binding events with the complementary protein were capable of destabilizing the assembled NPs [132].

Despite such interesting structural/energetic insights, it is worth noting that fascinating bioinspired properties such as chemotaxis have an intrinsically dynamic character, which encourages the study of the dynamic behavior of chemotactic assemblies at high (submolecular) resolution in search of molecularly relevant information on how to control them.

In this study, we propose a reverse multiscale modeling approach for the design of supramolecular NPs that exhibit autonomous chemotactic behavior. Our approach begins with a minimalistic coarse-grained (mCG) model of supramolecular NPs that can selectively bind groups present on surfaces, and uses classical and advanced simulations to study their dynamic chemotactic behavior. Focusing on a realistic example of supramolecular assemblies, we then increase the resolution of our models to a finer coarse-grained (fCG) level, and we explore molecular strategies for controlling the autonomous behavior of the responsive NPs on the surface. *In silico* modelling experiments finally show how to control the chemotactic properties and dynamic disassembly of the supramolecular NPs. This multiscale approach provides a flexible platform for the rational design of assembled structures with programmable autonomous chemotactic properties.

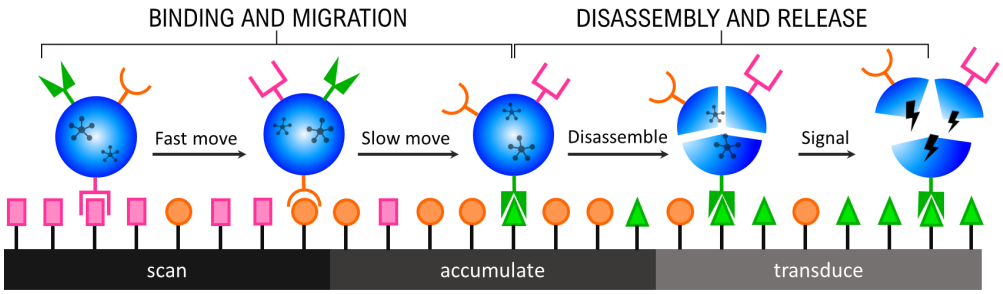

Fig. 3.1 Schematic representation of cells (e.g., leukocytes) that bind and autonomously roll/translocate on surfaces, scanning them and releasing (inflammatory) signals in the presence of high-densities of surface markers indicative of, e.g., an infection. Figure adapted from Ref. 126 with permission of Creative Commons CC BY license.

3.2 Computational approach

We developed coarse-grained molecular models of different scales-resolution to study the chemotactic response of several soft nanoparticles (NPs) on receptors-grafted surfaces. In particular, these models allow us to investigate the consequences of the variations in the monomer-monomer and monomer-receptors interactions on the behavior and stability of the assembled NP on the surface. All the MD simulations have been carried out using Gromacs software [151] patched with PLUMED [118], while the VMD visualization suite was used to display and render the simulated systems.

Minimalistic coarse-grained (mCG) model and simulation setup

We started by developing a minimalistic mCG model composed of three different bead types representing the monomers within the assembly, the guest particles contained inside the self-assembled NP, and the receptors grafted on the surface. The interactions within these beads were defined using a Lennard Jones (LJ) 12-6 potential setting the LJ parameters to σ = 0.47 nm and ε = 10 kJ mol^{-1}, for the monomer-monomer interactions ($\Delta Eass$) and to σ = 0.35 nm and ε = 40 kJ mol^{-1} for the monomer-receptor interaction ($\Delta Ebind$). This resulted in a $\Delta Eass/\Delta Ebind$ ratio of $\sim 1/4$ which is comparable to that of similar self-assembling oligomers containing a ligand that specifically binds to a complementary receptor protein (based on the avidin-biotin interaction) [132]. Additionally, a weakly 9-3 LJ attractive potential of 2.0 kJ mol^{-1} (20 times weaker than specific interactions) was added to the surface in order to mimic the weak non-specific interactions between the NP and the surface, and to prevent the NP to penetrate inside the surface in the receptor-free surface regions. The surface receptor CG beads were kept frozen during the simulations. The NP-surface system was then initially minimized using the steepest descent algorithm, and a leap-frog stochastic dynamics integrator was used for the production run. A Langevin dynamics was conducted using Coulomb and Van der Waals cutoffs of 1.1 nm, and a relative dielectric constant of ε_r = 15 (to implement electrostatic screening of the solvent, accordingly with the Dry MARTINI force field standards) [111]. All simulations using this model have been conducted at 300 K of temperature, in NVT conditions using a 20 fs timestep. Due to the anisotropic nature of the system, Periodic Boundary Conditions were considered only along x- and y-axis.

Metadynamics (MetaD) simulations were used to enhance the NP sampling of the surface. A MetaD bias was applied to the x- and y-distances (used as the collective variable, CV) of the NP center of mass respect to the origin of the system, depositing every 5000 steps Gaussian kernels of height 20 kJ/mol^{-1} and width of 1.0 for both variables.

All-atom (AA) and submolecular resolution (fCG) models

The self-assembling units considered herein are amphiphilic oligomers, characterized by a branched scaffold with three hydrophobic decyl chains, and three hydrophilic polyethylene glycol moieties (Figure 3.2b). Additional groups can then be added on the hydrophilic strands, for example, in this case, carboxylic acid groups (COOH groups) permit to functionalize the final aggregates. Therefore, monomers deprotonate in water at neutral pH providing a charge of -1e, -2e, or -3e, as shown in Figure 3.2b. The capability of these monomers to self-assemble into charged NPs able to bind positively charged surfaces is confirmed by the experimental results reported in Appendix A. The atomistic model of the oligomer was built with Avogadro [152] based on their chemical structure, which have been parametrized based on the General Amber Force Field (GAFF) [153], using Antechamber [154]. Consequently, the fine fCG models of the oligomers were built based on the MARTINI force field [105]. The bonded parameters have been optimized automatically to reproduce the bond, angle and dihedral distributions of the AA-MD simulations using Swarm-CG [85]. The non-bonded parameters have been optimized by choosing the appropriate MARTINI bead types in order to (i) reproduce the radius of gyration and the Solvent Accessible Surface Area (SASA) of the all-atom model seen in AA-MD simulations, and (ii) to reproduce the free-energy of dimerization between two oligomers in water obtained via metadynamics (AA-MetaD *vs.* CG-MetaD) simulations between two monomers (see Figure 3.3). For the best reliability, first a wet MARTINI-based CG model was created and optimized, which has been then used to optimize the Dry MARTINI-based CG model used for the simulations of Figures 3.7-3.12. The self-assembled NPs were then obtained by inserting 100 dry-CG monomers in a box and a classical MD simulation was run. The larger and more stable NP was found to be composed of 44 monomers and was used as a reference in all the simulations (Figure 3.2c). Ten CG beads were added inside the aggregate in order to represent guest particles, and their interaction was weak enough to allow for prompt monitoring of

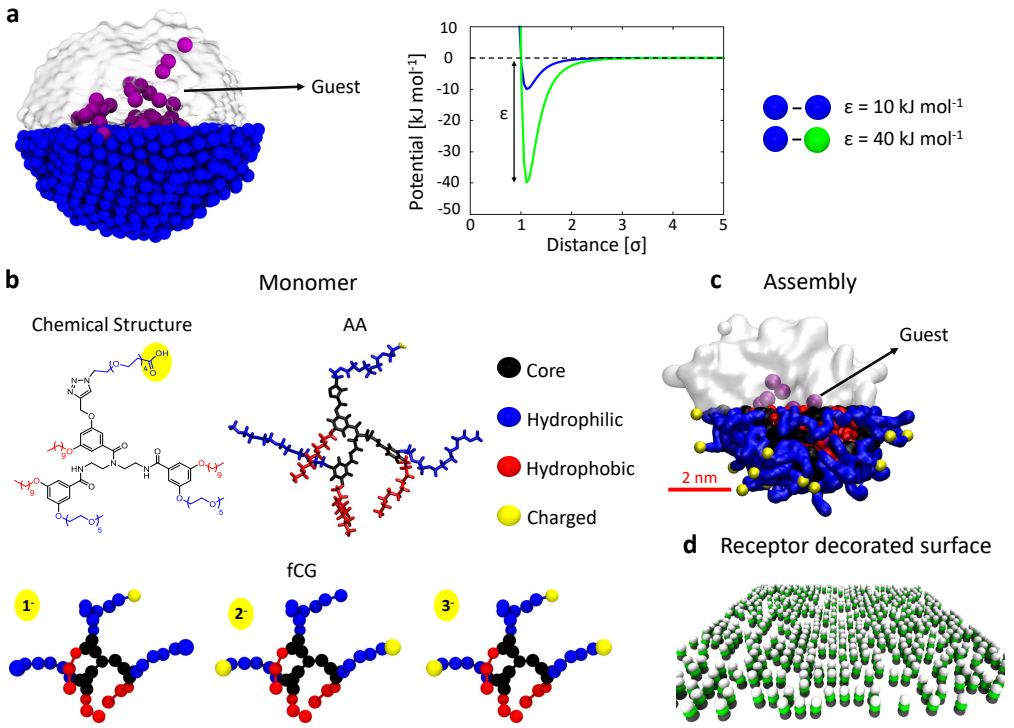

Fig. 3.2 Submolecular resolution of mCG and fCG models to study self-assembled NPs and their adhesion onto functionalized surfaces. **a** Minimalistic CG model of a supramolecular NP where blue beads indicate the self-assembled monomers and the violet beads reproduce an encapsulated guest, while the surface receptors are colored in green. The monomer-monomer and monomer-receptors interactions are tuned to reach the $\Delta Eass/\Delta Ebind$ ratio of $\sim 1/4$. **b-d** Finer CG models to study self-assembled NPs and their adhesion onto functionalized surfaces. (b) Chemical structure, all-atom (AA), and fine coarse-grained (fCG) models of facially amphiphilic monomers. These self-assembling units are composed of a branched core (in black), hydrophobic groups (red), and hydrophilic groups (red), which can be functionalized in different ways (i.e., with COO- charged groups, in yellow, in the example studied herein). (c) fCG model of a NP obtained via self-assembly of 44 oligomers in water. Guest fCG particles (in purple) are encapsulated in the NP and used to track guest release upon eventual NP disassembly. (d) fCG model of a surface functionalized with $+1$e charged groups (dark green CG beads are constrained in their position, while the topmost white ones carry a $+1$e charge). Figure adapted from Ref. 126 with permission of Creative Commons CC BY license.

their release in case of the NP's disassembly (σ = 0.43 nm and ε = 6.5 kJ mol^{-1}). The alkylamine groups on the surface were also modeled at the same resolution level based on the Dry MARTINI force field. In detail, the amino-groups are defined by three CG beads: a base one, grafted to the surface, a central CG bead, mimicking a carbon linker, and a charged hydrophilic head. To keep the receptor position fixed, the base CG beads of the receptor groups were kept frozen during the simulations.

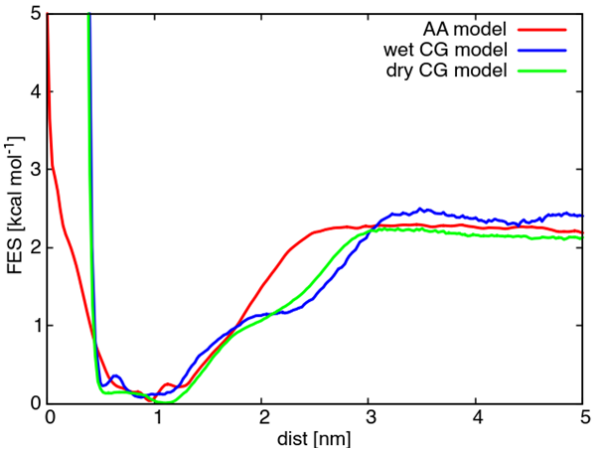

Fig. 3.3 Free Energy Surface (FES) of trimeric amphiphile dimerization obtained with well-tempered metadynamics technique. The validation of Coarse-Grained (CG) model (blue line) has been tuned on the all-atom (AA) profile (red line) as a function of the distance between the center of the two monomers. The distance variable refers to the COM distance (AA case) and the bead-to-bead distance (CG case) of the central residue of the standard monomer. Figure reproduced from Ref. 126 with permission of Creative Commons CC BY license.

fCG unbiased MD simulations

All fCG simulations were performed in implicit solvent, with a relative dielectric constant of ε_r = 15 to model the electrostatic screening of the solvent [111]. Explicit counter-ions were added to neutralize the system's charge. All CG-MD simulations of the fCG model were run in NVT conditions at T = 300 K. The systems were preliminary minimized using the steepest descent algorithm and a leap-frog stochastic dynamics integrator was then used for all unbiased MD production runs, using a 20 fs time step, and Coulomb and Van der Waals cutoffs of 1.1 nm. For the simulations regarding the static NP adhesion on different receptor density regions (as reported in Figure 3.7), three distinct NPs have been initially centered on top of four different 20 x 20 nm^2 surfaces, respectively, characterized by four different densities: $\rho 1$ = 0.034

rec/nm^2, $\rho 2$ = 0.09 rec/nm^2, $\rho 3$ = 0.64 rec/nm^2 and $\rho 4$ = 1 rec/nm^2. Each system was then equilibrated for 1 μs of CG-MD simulation.

Infrequent MetaD simulations for the study of NP unbinding

We ran 30 infrequent CG well-tempered MetaD simulations to obtain information on the characteristic timescale and the associated free energy barrier to be crossed in the system to detach a NP, represented by the fCG model and composed of -1e self-assembled oligomers, from a single surface receptor (Figure 3.9a). In these runs, as CV we used the number of contacts between the NP's charged beads and the surface receptor CG beads. We used a bias factor of 10, a Gaussian height of 1.2 kJ mol^{-1}, a deposition stride of 1 Gaussian every 50000 time step with a sigma of 0.5 nm. Simulations were terminated once the number of contacts was 0. The characteristic timescale for the event was then calculated from the Poissonian fit of the unbiased transition time distributions obtained from the 30 infrequent MetaD runs. The unbiased transition time (t) can be calculated from each individual MetaD run as:

$$t = t_{MetaD}\langle e^{\beta(V(s(R),t))}\rangle_{MetaD} \tag{3.1}$$

where $V(s(R),t)$ is the time dependent bias provided for the transition during the run, the exponential (brackets) is averaged over the MetaD run and β is kT^{-1}. The transition times (t) calculated from the MetaD runs were then used to build the transition probability distribution $P_{n\geq 1}$, namely the probability to observe at least one exchange event by time t:

$$P_{n\geq 1} = 1 - e^{-t/\tau} \tag{3.2}$$

where τ is the characteristic time for rare events. Figure 3.4 shows the exchange times collected from the individual runs. These fit well with Poissonian transition probability distributions $P_{n\geq 1}$. From the $P_{n\geq 1}$ distribution, it is then possible to calculate the characteristic timescale (TAU: τ) for the NP unbinding from a single/monovalent interaction with a surface receptor (Figure 3.9a).

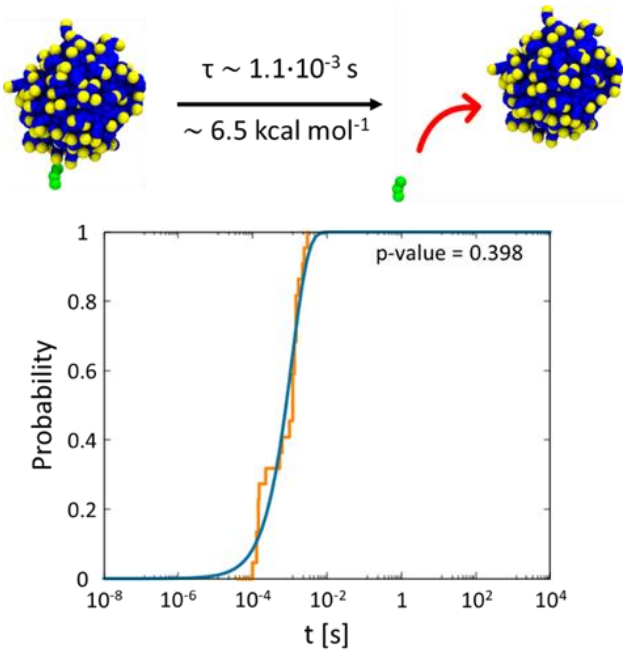

Fig. 3.4 Transition times extracted from the infrequent MetaD simulations. The plot reports the transition times collected from the replica infrequent MetaD simulations (orange segments), and the related Poissonian fitted distribution (in blue), for the detachment of the -1e charged fCG-NP from a single surface ligand (monovalent interaction). The analysis provides an estimated unbinding timescale of $\tau = 1.14 \cdot 10^{-3}$ s. Figure reproduced from Ref. 126 with permission of Creative Commons CC BY license.

Multiple-walker explorative CG-MetaD simulations

In the multiple-walker MetaD simulations, the surface was characterized only by the four central areas measuring 60 x 60 nm^2 (Figure 3.9b). Multiple-walker MetaD was used to explore in parallel 36 simulations of the same fCG system. The bias acted along the x- and y-distance of the NP's center of mass from the origin of the system. The bias was constructed by depositing every 500 CG-MD steps Gaussian kernels of height 1.2 kJ mol^{-1} and width of 0.1 for both variables. Repeating the simulations with or without using the Particle Mesh Ewald (PME) summation to treat long-range electrostatics provided consistent results, proving the general validity of the approach in exploring the chemotactic NP behavior on the surface.

In silico NP rolling and exfoliation experiments

We then built a surface model with dimension of $120x30$ nm^2, consisting of four consecutive regions with varying receptor densities: $\rho_0 = 0$ rec/nm^2, $\rho_1 = 0.12$ rec/nm^2, $\rho_2 = 0.52$ rec/nm^2, $\rho_3 = 1.12$ rec/nm^2, each measuring $30x30$ nm^2 (see Figure 3.11a). In these CG-MD simulations, we utilized the fCG model of NP and the CG-MD runs were carried out in NVT conditions at 300 K, with Coulomb and Van der Waals interactions modelled using a 1.1 nm cutoff. A constant force of $F = -100$ kJ/mol/nm was applied to the center of mass of the NP in these MD simulations, along the main x-axis of the surface (Figure 3.11a), in order to generate a pulling effect on the NP comparable to that one of a flux existing in the blood vessels (NP diffusion rate: $0.5 - 1$ cm/s) [155]. To prevent the NP from jumping far from the surface in the receptor-free region, a wall on z-axis was implemented using the PLUMED plugin at the center of mass of the NP at 5 nm with kappa=150.0 and exp=2.

3.3 Results and discussion

Chemotaxis of a supramolecular model nanoparticle

In order to understand the key principles to design synthetic chemotactic nanoparticles, it is crucial to observe the dynamic behavior of soft assemblies on receptor-grafted surfaces at high resolution. To this end, we have started by examining a minimalistic supramolecular NP model composed of self-assembling units (monomers) that are capable of establishing specific interactions with complementary functionalized receptors present on a surface (Figure 3.5a). The outcome of this adhesion is primarily determined by the competition between the intermolecular interactions of monomers within the assembly, referred as $\Delta Eass$, and the multivalent interactions with the surface, referred as $\Delta Ebind$. Specifically, $\Delta Ebind$ depends on the strength of the interaction between the monomers' ligands and the receptors on the surface, the number of receptors grafted on the surface, and the ability of the soft NP to adapt to the surface, thus maximizing the interactions within it, which also depends on $\Delta Eass$. The fate of the soft aggregate is determined by the balance between these two energies. When $\Delta Eass$ is much higher than $\Delta Ebind$, a rigid adhesion of the NP

on the surface occurs, while for $\Delta Eass$ being similar to $\Delta Ebind$, the NP is able to deform its shape, favoring an increase in the number of interactions with the surface. On the other hand, for $\Delta Eass$ much smaller than $\Delta Ebind$, the NP will disassemble due to the high number of interaction with the receptors. The main challenge is thus to understand how to balance these two energies through the use of coarse-grained molecular models (as in the example in Figure 3.5b).

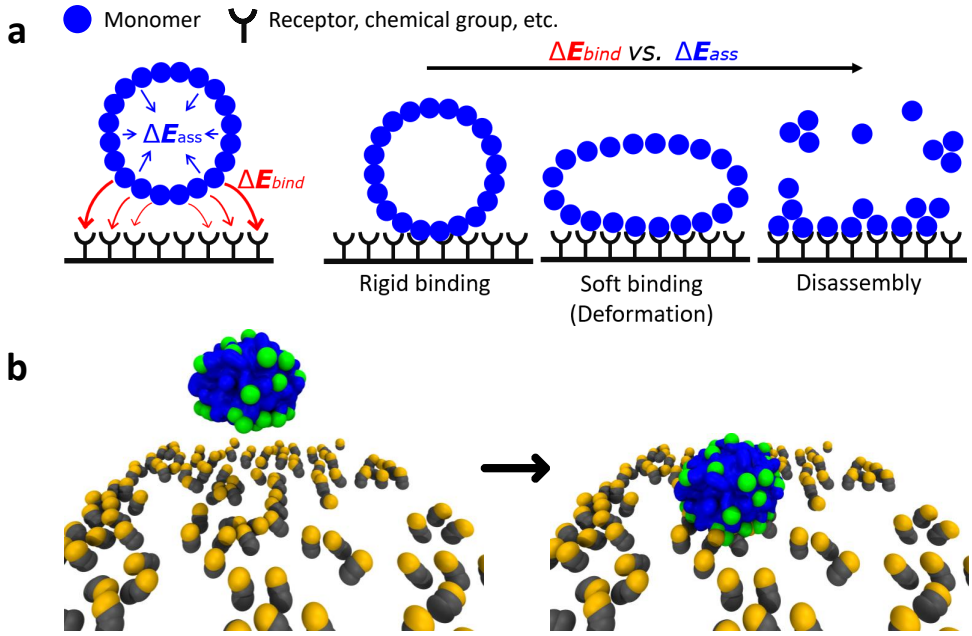

Fig. 3.5 Multivalent adhesion and chemotaxis in natural and synthetic assemblies. **a** Minimalistic Coarse-Grain (mCG) model of a self-assembled NP. When establishing a multivalent binding with a complementary functionalized surface, the NP's fate depends on the competition between the monomers-receptors interactions ($\Delta Ebind$: in red) and the monomer-monomer self-assembly energy ($\Delta Eass$: preserving the assembled structure, in blue). Whether the $\Delta Eass$ globally prevails, competes with the $\Delta Ebind$, or is dominated by the latter, would result in a rigid, soft adhesion, or even in the disassembly of the NP. **b** Example molecular model of a supramolecular NP (monomers colored in blue and green) before (left) and after adhesion (right) on a ligand-coated surface (ligands in gray, active binding groups in orange). Figure adapted from Ref. 126 with permission of Creative Commons CC BY license.

Minimalistic coarse-grained simulations

As a first case study, we consider a minimalistic CG (mCG) model that reproduces an assembled NP composed of 1925 CG beads, each of which representing one single monomer. The grafted surface was instead coated with single-bead receptors, and characterized by two different regions of distinct receptor density, namely the number of receptors in the lower density region being 1/64 that of the higher density region (as depicted in Figure 3.6). The Lennard-Jones (LJ) potential is utilized to model interactions between the different components of the system, obtaining a $\Delta Eass/\Delta Ebind$ ratio of $\sim$ 1/4 which is similar to that recently estimated for self-assembling oligomers containing a biotin ligand that specifically binds avidin [132]. To achieve this, we describe $\Delta Eass$ interactions using a 12-6 LJ potential, with σ = 0.47 nm and ε = 10 kJ mol^{-}1, while the monomer-receptor interactions, $\Delta Ebind$, are modeled with as σ = 0.35 nm and ε = 40 kJ mol^{-1}. The white areas of the surface represent regions of weak, non-specific interaction, modeled as a 9-3 LJ potential with ε = 2.0 kJ mol^{-1}, which is 20 times weaker than the monomer-receptor interaction. These simulations, however, have shown the tendency of the NP to rapidly bind a receptor on the surface, without the possibility to surf and scan the entire surface. In fact, the characteristic timescales to escape from the first NP-receptor interaction exceed the typical timescales accessible by classical CG-MD simulations (in this case in many systems), which for this reason results ineffective to study the dynamics of the system.

To overcome this limitation, one approach is to enhance the sampling of the system through biased simulations. We conducted metadynamics (MetaD) simulations that enhanced the motion of the NP on the surface. An energy bias was applied to the center of mass of the NP, activating changes in x- and y- coordinates, the plane of the surface, without any constriction along the z-direction. These variations of the NP position on the xy-plane promote a random walk on the surface, where the NP could either slide, translate, roll or in principle even bounce on/off the surface. CG-MetaD simulations highlight the tendency of the NP to move from low to high density regions and, in particular, to slide and diffuse on the less dense areas and to roll on the denser ones. Additionally, despite the absence of constriction along the z direction, the NP did not show any tendency to jump on the surface, neither in the receptor-free regions, due to non-specific interactions with the empty areas on the surface.

Even if the CG-MetaD simulations have been used exclusively with an explorative intention, they provide for the qualitative understanding of the NP's motion on a receptor-functionalized surface. In particular, the exploration depends on the Brownian motion at a thermalized regime, which promotes the random movement, and on the specific interactions in the different densities regions, which affects the residence time. However, it is important to notice that the only motion detected goes from the lower to the higher density regions, that is the consequence of the free energy of adhesion. Furthermore, when $\Delta Eass \ll \Delta Ebind$ and the simulated timescale is long enough, the probability of the NP to disassemble is higher than the one to escape from that region, this then means that the higher density regions can be considered as density traps.

Figure 3.6 reports the two different behaviors of the NP that have been observed. In low-density regions, the NP preserves its spherical shape during the diffusion process, even if in some cases, it loses some monomers due to the high interaction with the receptors. On the other hand, in the high-density region, the number of interactions with the surface increases, leading to a deformation of the NP that disassemble under the application of the MetaD potential. In this occasion, the release of the guest particles inserted into the NP, characterized by a weak interaction with the other beads, is observed. These simulations demonstrate that once the NP is on the region with the higher receptor density, despite the continuous application of the potential bias, the NP is not able to escape from it and disassemble. This suggests, that probably, even in a real system the NP can disassemble under the presence of external forces, releasing the cargo.

High-resolution insight into multivalent interactions

The results of previous mCG simulations have shown the crucial role of intermolecular interactions in the chemotactic mechanism. However, the resolution of the model does not allow a resolution fine enough to describe the chemical structure of existing systems. In order to gain a better understanding of how the $\Delta Eass$ affects the stability of the assembly, a finer CG (fCG) model permits to model both the NP and the surface with a $\sim 5\,\dot{A}$ resolution. This level of resolution allows for the study of, for example, the intermolecular interactions between the self-assembling units and multivalent interactions with the surface, enabling the understanding of the effects of the variations in the chemical structure of the single monomers. As a case

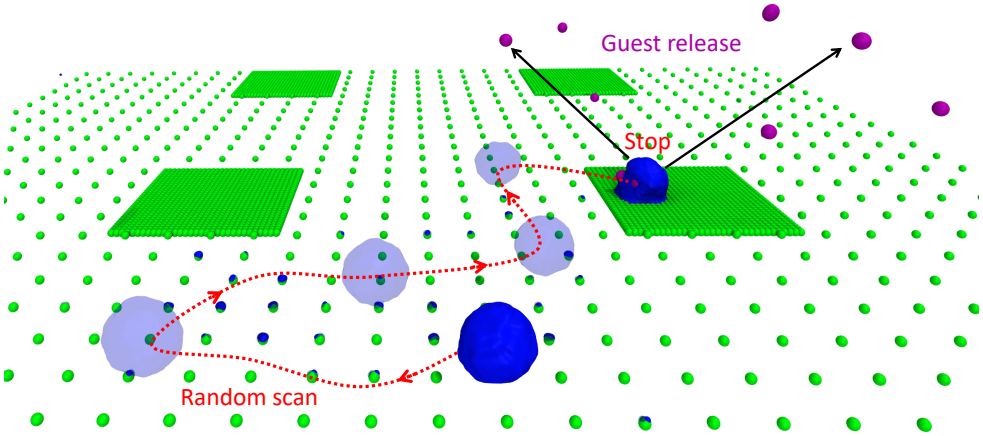

Fig. 3.6 Simulating the density-responsive behavior of chemotactic NPs using minimalistic models. Minimalistic mCG model of a supramolecular NP (blue CG beads: self-assembled monomers) with encapsulated guests (violet CG beads). In the surface model, two areas are distinguishable: with high and low receptor densities (green CG beads). In particular, the CG-MetaD trajectory (red dotted arrows) shows NP rolling and diffusion on the surface. Starting from a receptor-poor region, the NP randomly explores the surface during the CG-MetaD run, until reaching a receptor-rich region. Once the NP binds a receptor-rich region of the surface, the MetaD simulation suggests that the presence of a force continuously pulling the NP may induce NP disassembly over time, and the consequent release of the encapsulated guest particles (in violet). Figure adapted from Ref. 126 with permission of Creative Commons CC BY license.

example, in this work we considered facially amphiphilic oligomers, which form NPs in aqueous medium and are able to encapsulate hydrophobic guests.[132] Amphiphilic oligomers are particularly useful as both the hydrophilic and hydrophobic strands can be functionalized with specific chemical groups, enabling the binding to specific receptors ($\Delta Ebind$) in the first case or varying the stability of the final structure ($\Delta Eass$) in the second case.

The oligomers studied herein are characterized by a branched scaffold with three hydrophobic decyl chains, and three hydrophilic polyethylene glycol moieties (Figure 3.2b). Different chemical groups can then be grafted on the hydrophilic strands, which will be then exposed to the solvent after the self-assembly.[132, 156] In this case, the hydrophilic strands have been functionalized with carboxylic acid groups (COOH groups). These groups deprotonate in water at neutral pH providing a charge of -1e, -2e, or -3e to the oligomers, as shown in Figure 3.2b. Furthermore, experimental evidences demonstrate that these oligomers are able to self-assemble

into charged NPs able to bind positively charged surfaces. The information related to the experimental tests are exposed in the Appendix A.

The fCG, described by the dry MARTINI force field [105, 111], is obtained from the AA oligomer model already described in the computational approach paragraph. In particular, after an initial optimization of the bonded interactions through the Swarm-CG software [85], the non-bonded interactions are tuned to obtain a dimerization free-energy profile consistent with the atomistic results, as reported in Figure 3.3.[76, 157] Once obtained the fCG model, the most stable aggregate is made by 44 self-assembling oligomers. Additionally, in order to study the disassembly and release, we insert 10 beads into the self-assembled NPs to simulate an encapsulated cargo (Figure 3.2c). Finally, different surfaces are decorated with varying number of receptors, modeled as 3 CG beads, where the top one had a $+1$e charge and the bottom one was constrained in its position (Figure 3.2d).

Consequently, we conduct multiple simulations to investigate the adhesion strength of the NP on four different surfaces with varying receptor density, referred to as ρ_1, ρ_2, ρ_3, ρ_4, with the highest density corresponding to $\rho_4 = 1$ group/nm^2 (as shown in Figure 3.7). These simulations are used to examine the effects of variations in the ratio $\Delta Eass/\Delta Ebind$, as depicted in Figure 3.5a. The fCG-MD simulations reveal a strong correlation between the strength and the number of monomer-receptor interactions. In particular, to simulate rigid binding, deformation, and disassembly, three different NP surface charge densities are investigated, i.e. -44e, -88e, and -132e, respectively (see Figure 3.7)

The relationship between the stability of the NP and the number of interactions between the monomers and receptors is proven through the calculation of the number of contacts between the negatively charged beads of the oligomers and the positive beads of the surface receptors, as shown in Figure 3.8. The most extreme case, where one single monomer of the NP has a protonation state of -3e and was placed on the surface ρ_4, results in disassembly due to the maximum possible number of contacts, thus approximately 132. The correlation between the number of interactions with the surface was further supported by the experimental evidences reported in Figures A.1 and A.2 in the Appendix A.

The use of classical, unbiased fCG-MD simulations turn out to be effective exclusively in the study of the static binding of NPs on coated surfaces. However, the detachment of a charged bead from the surface requires timescales that cannot be

simulated with classical unbiased CG-MD simulations. To overcome this limitation, we again employed infrequent CG-MetaD simulations to estimate the characteristic timescale of this unbinding (according to similar setup as that used for mCG). These simulations reveal that it is necessary to overcome an energy barrier of $\sim$6.5 kcal mol^{-1} at room temperature, with an estimated time of $\sim$1.14 ms ($\sim 10^{11}$ simulation time steps, τ), as reported in Figures 3.4 and 3.9a. It should be noted that these systems are complex and variable, and thus, the data obtained should be interpreted qualitatively. However, the number of interactions considered in this analysis underestimate the real number of interaction existent between the NP and the surface. Therefore, in reality, the time of unbinding of the NP from a receptor covered surface should be longer compared to the one estimated herein.

In this context, MetaD simulations are employed to accelerate the movement of the NP by applying a gaussian-like bias potential on the xy position of the NPs' center of mass. Specifically, a larger surface is created with four distinct regions that featured varying densities of receptors. The NP is initially placed in a corner of the region with the lowest density of receptors (see Figure 3.9b-d). In addition, the NP's movement is confirmed and supported by experimental evidences (see Figures A.3 in Appendix A). Figures 3.9c-d display all the 36 trajectories and their temporal evolution, which demonstrate the tendency to move in a monodirectional path from lower to higher density regions. Despite the applied bias potential leading to a random motion of the NPs, they still exhibited a movement toward the center of the surface starting from the corner. Once the NPs reach the highest density areas, it is highly unlikely for them to escape, thus confirming the hypothesis of a molecular trap as previously observed in the mCG study.

To validate the observed behavior of NPs moving randomly on surfaces with homogeneous receptor density, we conduct two separate examples (as seen in Figure 3.10). The temporal-colored trajectories illustrate that as long as the nanoparticle is on a homogenous surface, it tends to randomly explore the surface. However, when the NP is placed on a surface with two different densities, it moves towards the region with the highest density and upon reaching it, the diffusion slows down due to an increase in the number of interactions. Based on these results, it can be concluded the NP will be observed most likely in that areas of high receptor density if $\Delta Eass > \Delta Ebind$, or will disassemble if $\Delta Eass < \Delta Ebind$.

The results obtained from both the minimalistic and the finer CG models indicate the same phenomenon, that is the autonomous diffusion of NPs from lower to higher density surfaces. This observation persists even if the two systems considered different types of intermolecular interactions, namely Van der Waals interaction in the first case, and electrostatic interactions in the second. It is noteworthy that the chemotactic response of NPs on coated surfaces can be designed and controlled by acting on the strength of the multivalent interactions established between the NPs and the higher/lower density regions of the surface during their motion.

In silico experiments of disassembly and release

As the previous MD simulations demonstrate, the exploration path of NPs on coated surfaces can be controlled. However, the disassembly and release of encapsulated guests have yet to be investigated. In this regard, an *in silico* experiment was developed utilizing the fCG models already discussed in the previous paragraph. A surface with four different receptor densities (from ρ_0, with no receptors, to ρ_3) was created (see Figure 3.11a), and a constant force was applied on the NP, simulating the effect of the flux present in blood vessels. This allowed to explore the NP motion on functionalized surfaces under external perturbation. The simulations revealed, in some cases, the disassembly of the NPs and release of cargo. The disassembly was quantified by measuring changes in the NPs' Solvent Accessible Surface Area ($\Delta SASA$).

This *in silico* study shows that an increase in the number of interactions between NPs and receptors leads to an increased exposure of the NPs to the solvent, even after the exfoliation of the NP (Figure 3.11b). The results also indicate that an increase in the number of charges on the oligomer surface results in earlier NP disassembly at lower surface densities of receptor groups (Figure 3.11b). Furthermore, by calculating the number of contacts between the oligomers and the guest particles, the percentage of guest release is determined as a function of the surface density of receptors, as shown in Figure 3.11c. These simulations demonstrate that by varying the number of charges on the NPs, it is possible to trigger the disassembly and release of cargo on different receptor densities, with significant percentages of guest release being higher than 20%.

However, as mentioned at the beginning of this section, the $\Delta Eass/\Delta Ebind$ ratio and the fate of the NPs, can be influenced not only by the variation of the number of negative charges on the surface of the NPs, thus acting on the $\Delta Ebind$, but also by the strength of the intermolecular interactions, thereby acting on $\Delta Eass$. To demonstrate that, as done for the case of thermo-responsive oligomers [158], we tuned the hydrophobicity of the NP, by modifying the chemistry of the oligomers' hydrophobic strands. Starting from the Original configuration of the oligomer (the one considered in the previous simulations and reported in Figure 3.12a), different chemical sequences are replaced to its C10 hydrophobic chains. In particular, considering the cases indicated in Figure 3.12b, Type-1 is obtained adding a CG-bead representing four carbon units (C14), while in Type-2 one halogenated carbon group (in orange) is added in order to increase the hydrophobicity of the oligomer. In Type-3 and Type-4 the last bead is replaced with phenyl and naphthyl functional groups respectively, affecting not only the $\Delta Eass$ but also the final shape due to a different rearrangement of these groups in the core of the NP.

We then replicated the same simulations already carried out for the Original configurations (then with -1e, -2e, -3e charges on the hydrophilic groups) and we compared the final results with the one in Figure 3.11b-c. In particular, Figure 3.12c shows the results obtained for the oligomers with charge -3e. Considering that Type-1, Type-3 and Type-4 are more hydrophobic than the Original configuration, the new designed NPs manifest a more stable behavior. In fact, Type-1 and Type-3 variants disassemble in the higher density surface (ρ_3), in other words, they require a higher number of interactions with the receptor beads to disassemble on ρ_2. Due to the high stability of the NP based on Type-4 oligomers, no disassembly is observed, as in this case $\Delta Eass$ is higher than $\Delta Ebind$ (as shown in Figure 3.12d). In case of Type-2 oligomer-based NP, the behavior shown is similar to the Original NP, as the bead added is less hydrophobic. The results related to the -1e and -2e NPs variants are reported in Figures A.4-A.5, Appendix A. These results demonstrate that the balance between $\Delta Eass$ and $\Delta Ebind$ can be controlled by acting on different parameters. To this regard, Figure 3.12d clearly shows how comparable behaviors in the system can be obtained with different NPs. While these cases change both in the hydrophobic groups and in the number of NP binding charges, thus variations acted both on $\Delta Eass$ and $\Delta Ebind$, the final balance of the two energies lead to the same fate of the NPs on the surface.

The kinetics of the stable NPs can be compared, as reported in Figure 3.12d, by evaluating the velocity and the Mean Square Displacement (MSD) in the regimes where the NPs maintain their integrity (Figure 3.13). Our analysis reveals that the motion of the NPs is influenced by the receptor density on the surface, the number of charges present on the NPs' surfaces, and on the stability of the NPs. As depicted in Figure 3.13, the diffusion of the NPs slows down when they are in higher density regions, as the number of oligomer-receptor interactions increases. The fCG-CG NPs exhibit a more sub-diffusive behavior, until the point where $\Delta Ebind$ becomes stronger than $\Delta Eass$, at which the disassembly of the NP is more likely to occur rather than diffusion. These simulations show how given the characteristics of a specific surface, different NPs can be rationally designed, in principle, to control the disassembly and the release of the encapsulated guest only after a certain density of groups is encountered in a functionalized region.

3.4 Conclusion

This work proposes a computational approach to investigate the chemotactic behavior of soft NPs through the combination of top-down and bottom-up multiscale molecular models and the use of advanced simulation approaches. By using minimalistic and finer molecular models, we examine the fundamental process behind the chemotactic behavior of various NPs. Initially, the effects of the competition between intermolecular interactions ($\Delta Eass$ energy) and monomer-receptor interaction ($\Delta Ebind$ energy) are investigated, as their balance controls the motion and fate of the NPs. Additionally, by utilizing a real case study based on oligomers self-assembly, we propose a chemical example for the creation of chemotactic-responsive systems. Moreover, variations in the NPs' charges or in the hydrophobic properties demonstrate to be useful to tune and control the interaction between the NP and the surface, including rolling, stopping, and in some cases, disassembly and guest release in targeted areas of the surface. Furthermore, *in silico* experiments provided insight into the stability of the customized structures, where, by knowing the characteristics of a target surface, and through the rational design of tailor NPs, controllable chemotaxis can be achieved in artificial molecular systems.

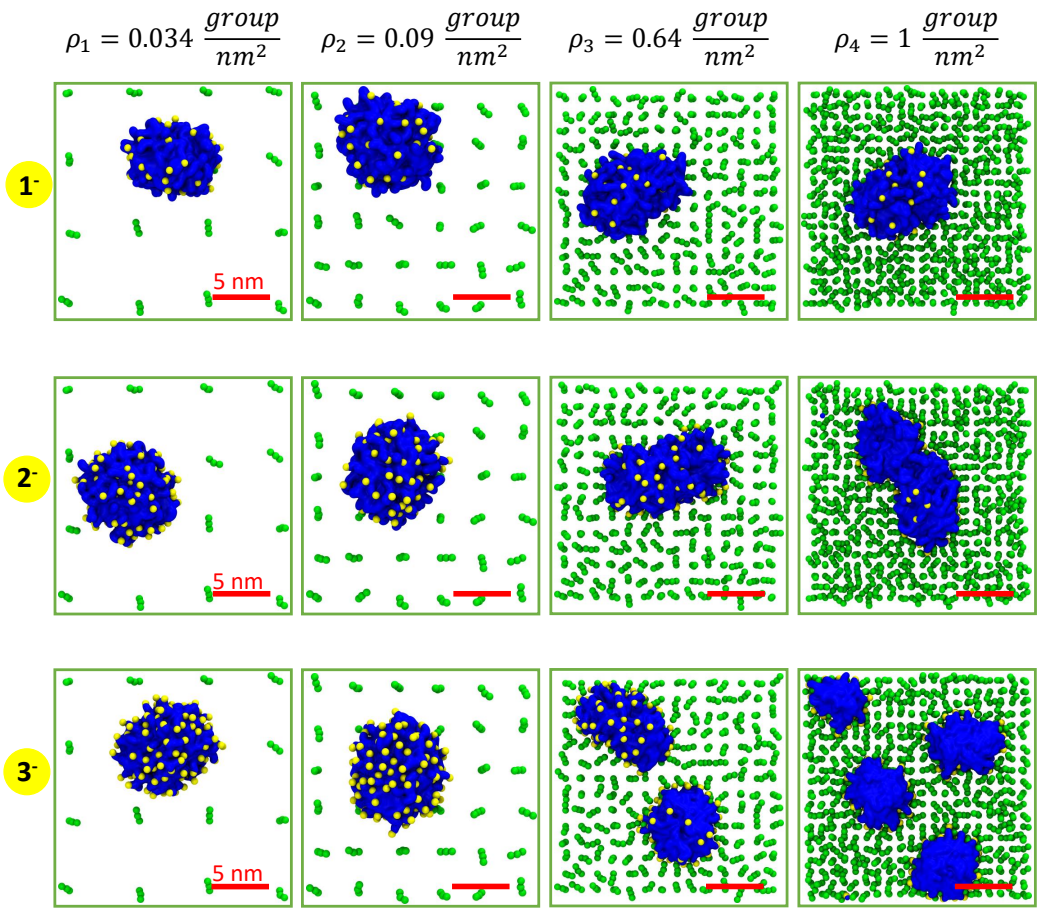

Fig. 3.7 CG-MD simulation of static NP adhesion to surfaces characterized by different densities of receptor groups. Snapshots taken after 1 μs of fCG-MD showing NP destabilization and disassembly upon adhesion may be observed while increasing the charge densities on the surface and on the NPs from -44e to -132e. Figure adapted from Ref. 126 with permission of Creative Commons CC BY license.

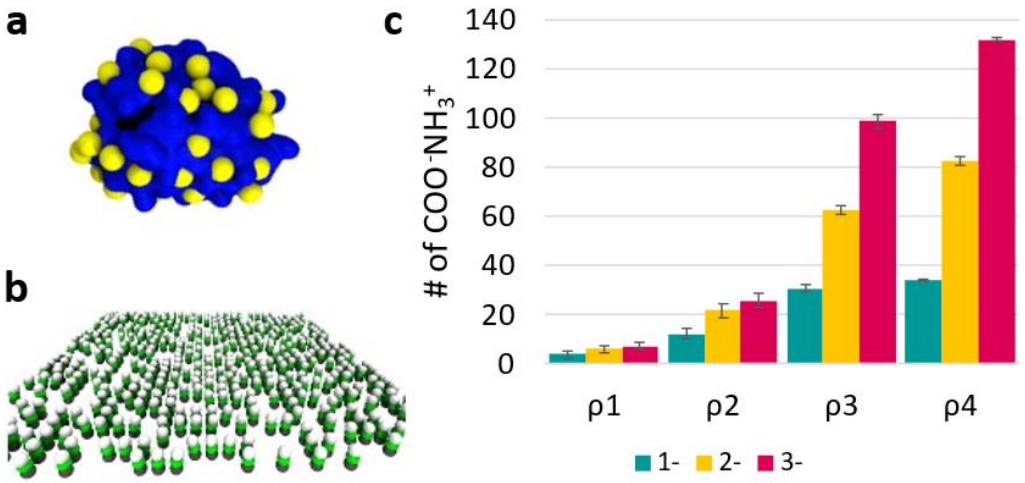

Fig. 3.8 (a) CG-MD simulation snapshot of a single self-assembled nanoparticle made of 44 trimeric amphiphiles validated as shown in Figure S1. Color code: charged beads are depicted in yellow, while blue beads represent the complementary monomer structure. (b) An example of ligands decorated surface. The charged beads are in white, while the remaining ligands are colored in green and gray. (c) Number of contacts between the NP charged beads and the surface ligand charged beads calculated in unbiased CG-MD simulations for different ligand concentrations (ρ_1, ρ_2, ρ_3, ρ_4) and protonation states (-1e, -2e, -3e). Figure reproduced from Ref. 126 with permission of Creative Commons CC BY license.

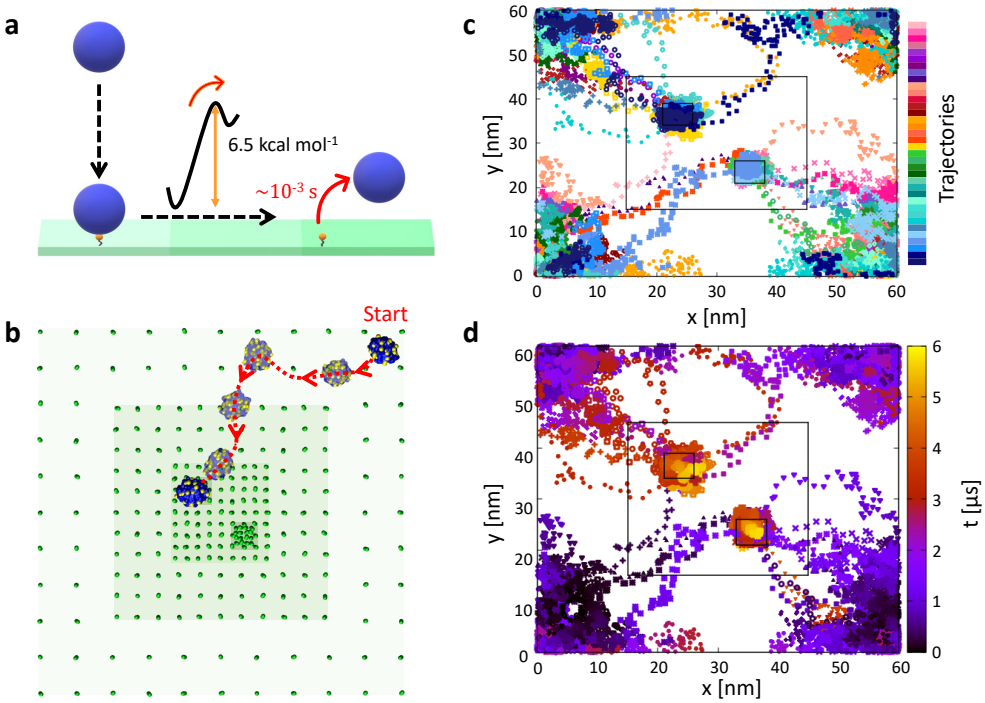

Fig. 3.9 Submolecular fCG models of NP chemotaxis. **a** Free-energy barrier (∼6-7 kcal mol^{-1}) and characteristic escape time scale ($\tau \sim 10^{-3}$ s CG) for fCG-NP unbinding from the surface in the case of a monovalent interaction. **b** Example of CG-MetaD trajectory extracted from the ensemble of panels **c** and **d**. **c** 36 trajectories of fCG-NPs on the surface from 36 multiple-walker CG-MetaD simulations (each color represents a different CG-MetaD run). **d** 36 multiple-walker CG-MetaD trajectories shown in panel **b**, colored based on the simulation time (dark blue to red and yellow). In all CG-MetaD runs, the fCG-NP is seen to move from the lowest to highest-receptor density regions on the surface over time. Figure reproduced from Ref. 126 with permission of Creative Commons CC BY license.

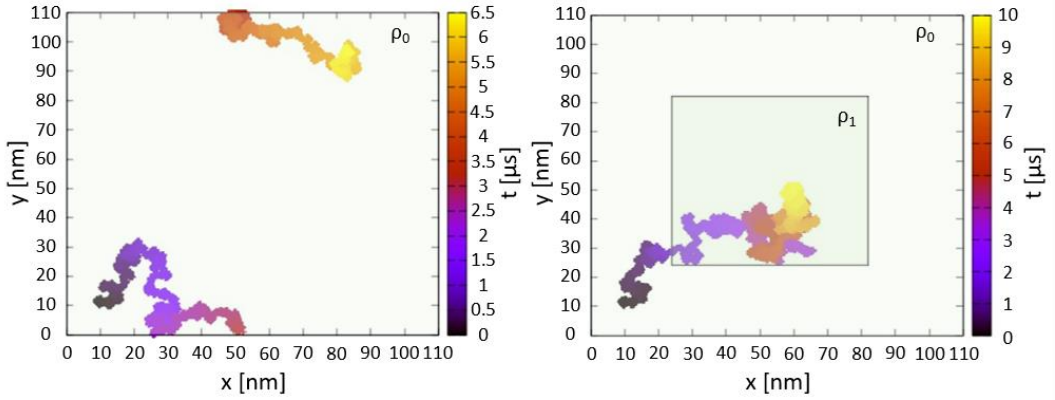

Fig. 3.10 CG-MetaD trajectories of fCG-NPs onto different surface models. Left: The fCG-NP moves randomly in 2D in the case where the density of surface receptor groups is low and uniform (ρ). Right: Motion of the NP onto a surface with two different, yet relatively low, receptor density regions (ρ_0 and a higher ρ_1). The NP motion becomes irreversible when it visits regions where the ρ is high enough to have $\Delta Ebind > \Delta Eass$. Figure reproduced from Ref. 126 with permission of Creative Commons CC BY license.

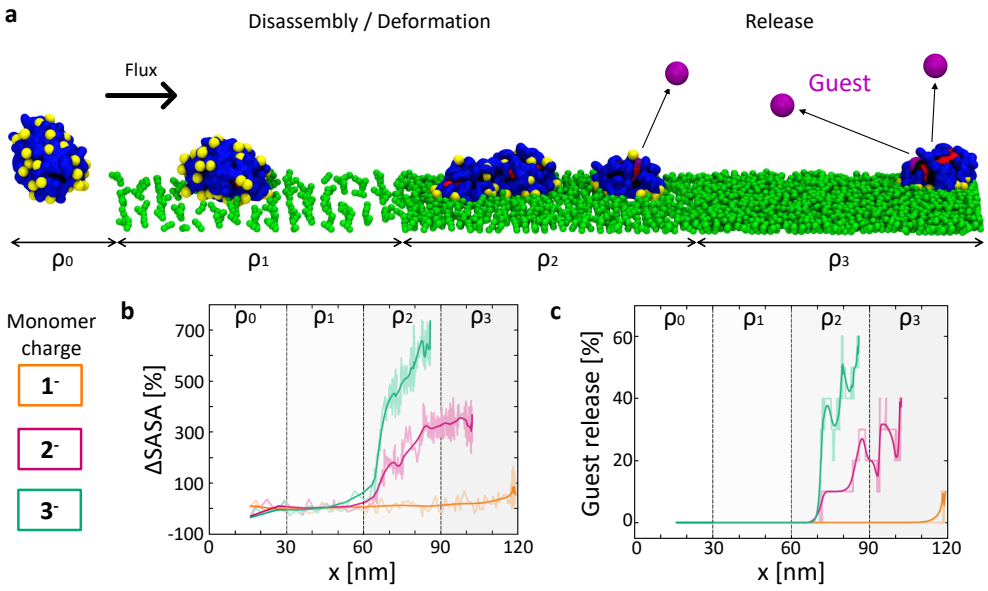

Fig. 3.11 *In silico* experiments of NP rolling, disassembling, and guest releasing in the presence of an external flux. **a** CG-MD simulation setup of tested NPs represented with a fCG model. **b,c** Monitoring NP disassembly and guest release. **b** Percentage variation of the NP SASA ($\Delta SASA$) for the NPs as a function of the oligomer charge. **c** Percentage of guest release as a function of the oligomer charge. Raw data are shown in transparent colors, solid trend lines are shown to guide the eye. Figure reproduced from Ref. 126 with permission of Creative Commons CC BY license.

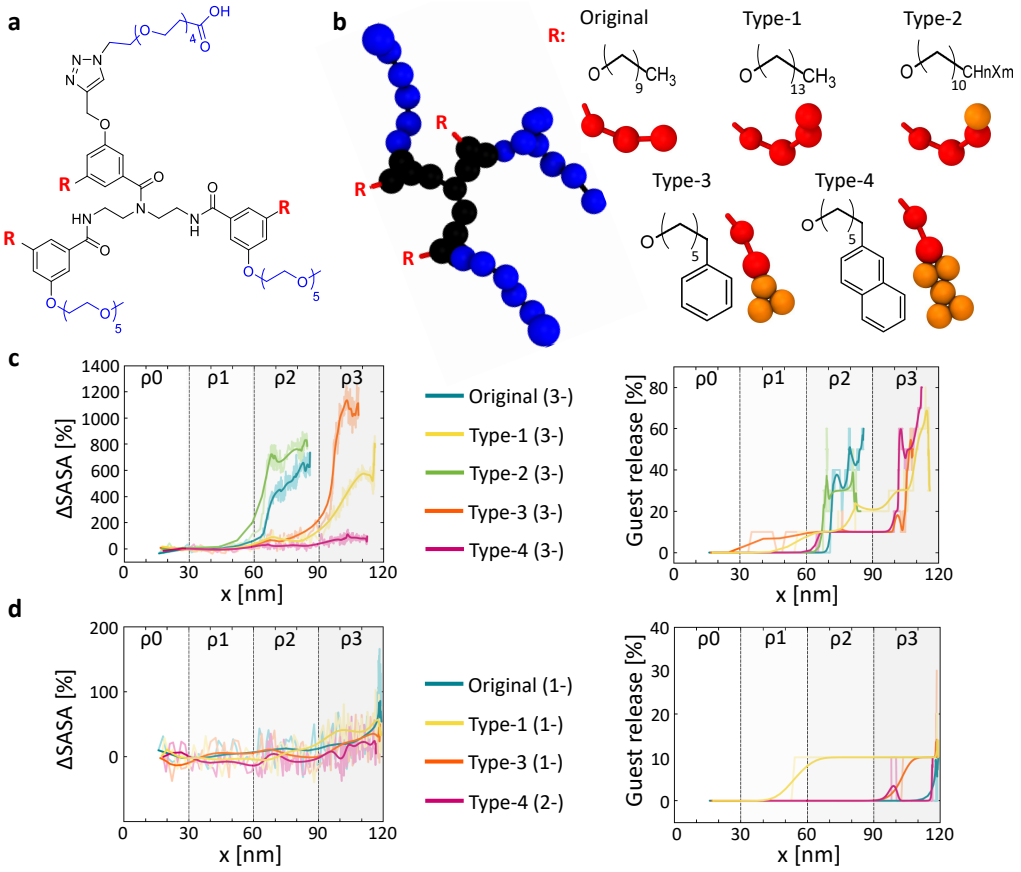

Fig. 3.12 Modulating the NP chemotaxis and responsiveness by tuning the hydrophobicity of the self-assembling units. **a** Original reference oligomer (C10 hydrophobic tails). **b** Hydrophobic groups of the Type-1, Type-2, Type-3, and Type-4 oligomer variants and their corresponding fCG models. **c** Comparison of $\Delta SASA$ (NP SASA variation) and percentage of guest release for NPs composed of the different trivalent (-3e) oligomer variants. Same data for the (-2e) NP variants are reported in Appendix A (see Figures A.4 and A.5). **d** Similar NP behaviors can be obtained by NPs composed of oligomer variants having a similar $\Delta Eass/\Delta Ebind$ balance. Raw data are shown in transparent colors, solid trend lines are shown to guide the eye. Figure reproduced from Ref. 126 with permission of Creative Commons CC BY license.

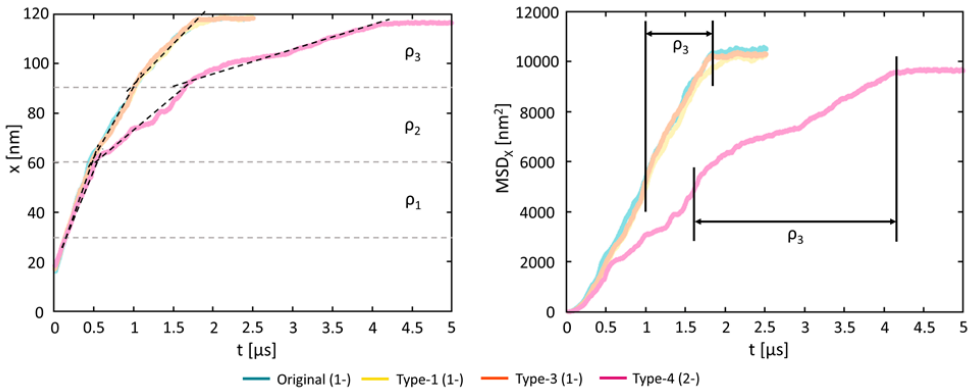

Fig. 3.13 X-position (x(t)) and x-Mean Square Displacement (x-MSD) of the fCG-NPs (Original, Type-1 (-1e), Type-3 (-1e), and Type-4 (-2e)) along the receptor-density-gradient surface displayed in Figure 3.11a of the main manuscript. The slope of the x(t) profiles represents the fCG-NP velocity along x direction. The data show that the higher is the receptor density on the surface (ρ), or the oligomer's charge (colored curves), the lower is the slope of the x(t) (black dotted lines): i.e., the fCG-NP motion on the surface becomes slower while the multivalent interactions between the NPs and the surface increase. Figure reproduced from Ref. 126 with permission of Creative Commons CC BY license.

Chapter 4

Into the dynamic of self-assembled micelles

The work contained in this Chapter has been published in the following paper: "A. Cardellini, M. Crippa, C. Lionello, S. P. Afrose, D. Das, G. M. Pavan. Unsupervised data-driven reconstruction of molecular motifs in simple to complex dynamic micelles. J. Phys. Chem. B ***2023****, 127, 2595–2608" [159], and has been adapted with permission of Creative Commons CC BY license.*

Abstract

The reshuffling mobility of molecular building blocks in self-assembled micelles is a key determinant of many interesting properties, from emerging morphologies and surface compartmentalization to dynamic reconfigurability and stimuli-responsiveness of these supramolecular soft particles. However, such complex structural dynamics is typically non-trivial to elucidate, especially for multi-component assemblies. Here, I describe a machine-learning approach that allow us to reconstruct the structural and dynamic complexity of mono- and bi-component surfactant micelles from high-dimensional data extracted from equilibrium molecular dynamics simulations. Unsupervised clustering of smooth overlap of atomic position (SOAP) data enables to identify, in a set of multi-component surfactant micelles, the dominant local molecular environments and to retrace their dynamics, in terms of exchange probabilities and transfer pathways of the constituent building-blocks. Provided a variety of mi-

celles, different in size and chemical nature, this approach can effectively recognize common molecular motives in an exquisitely agnostic, unsupervised way and to correlate them with the belonging species.

4.1 Introduction

The stability of a self-assembled materials depends not only on the external stimuli, but also from the internal ones. Numerous studies have evidenced that the internal reshuffling of building blocks and their arrangement into dynamic domains have a significant impact on the final properties of self-assembled architectures.[160–162] As an example, in supramolecular polymers, the rearrangement of the assembling units in a fiber, influenced by the presence of defective domains, affects the velocity of reorganization under the presence of specific stimuli.[163] Thus, it is crucial to comprehend the structural and dynamic environments present in soft assemblies for the rational design of self-assembling structures with controllable dynamic properties.[164, 165, 160, 166, 167]

The ability to control the levels of order/disorder, such as defects, in supramolecular materials allows for the control over fluid-like domains [87, 104] and their stability [168], activation of stimuli-responsive attitude [169], and acceleration of chemical reaction [88, 89]. Multi-component assemblies, in particular, are attracting significant attention because they offer the potential to create complex molecular features.[170, 169] For instance, surfactant-based micelles composed by different assembling units can be utilized to develop new supramolecular living structures.[88, 89, 171]

While several experimental techniques, such as Stochastic Optical Reconstruction Microscopy (STORM) [73], or Hydrogen/deuterium exchange (HDX) mass spectrometry [172], provide the ability to observe supramolecular assemblies with a resolution of $\sim$20–50 nm, the investigation of the intrinsic molecular mobility within them requires a submolecular resolution. All-atom (AA) and coarse-grained (CG) molecular dynamics (MD) simulations combined with machine learning approaches perfectly fit for this purpose, given their efficiency in the identification of molecular motifs in supramolecular assemblies, as demonstrated in recent works.[86, 87, 104]

In multi-component soft assemblies, the level of complexity is highly elevated due to the involvement of various self-assembling units in intermolecular interactions with other units and the solvent. Consequently, the prediction of the final structure and rearrangement of the building blocks can be challenging. To address this challenge, the combination of MD simulations and machine learning-based analysis is essential in understanding the correlation between the structural motives and chemical compounds. In this view, we propose a computational approach, based on the Smooth Overlap of Atomic Position (SOAP) and a clustering technique, to characterize the complexity of bi-component surfactant micelles, utilized as a representative case study, from both structural and dynamical point of view.

Initially, a minimalistic physical model was investigated to prove the arrangement of surfactants within micelles and validate the analysis protocol. Afterwords, the chemical structures presented in references 88, 89 were taken into consideration. The unsupervised analysis approach facilitated the recognition of several molecular environments within the bi-component micelles and their correlation to specific surfactant species. The procedure employed is intended to serve as a general method to investigate the global and microscopic structural and dynamical characteristics of complex multi-component self-assembled materials.

4.2 Computational approach

Minimalistic coarse-grained (mCG) model

The minimalistic CG (mCG) model describes two types of amphiphilic-like molecular building blocks, referred to as **R** and **B**, and represented with red and blue heads, respectively, in Figure 4.1a. These monomers are made of one bead for the heads and four beads for the tails (Figure 4.1a). Heads and tails are bonded through harmonic potentials to form a linear structure. The non-bonded interactions are described using Lennard-Jones (LJ) potentials. The LJ parameters have been adjusted in order to obtain the hydrophobic tails pointing inside the shell of hydrophilic heads. All parameters have been optimized by comparing them to an equivalent system simulated in explicit solvent, described by the standard MARTINI force field parameters (see Figure 4.1).[105] The utilization of the implicit solvent enhanced the reshuffling surfactants within micelles.

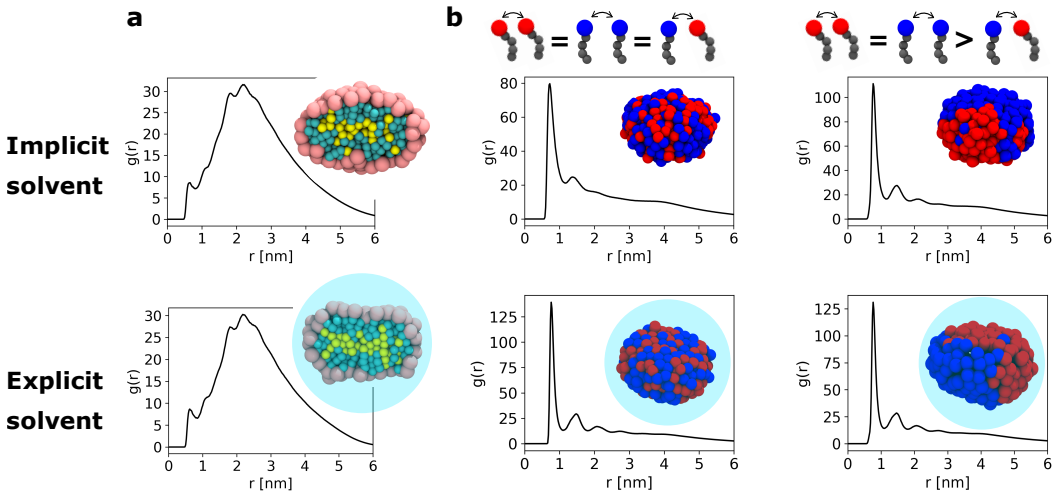

Fig. 4.1 Parametrization of the mCG model. **a** Radial distribution functions (g(r)) of the head beads (pink) respect to the geometric center of the last tail beads (yellow), both in implicit (top) and explicit (bottom) solvent model. **b** Radial distribution functions (g(r)) of the heads distribution around the core of each micelle in case of completely mixed (left) and compartmentalization (right) regime among red and blue surfactants. g(r)s are compared in implicit (top) and explicit (bottom) solvent models. Figure reproduced from Ref. 159 with permission of Creative Commons CC BY license.

The models in Figure 4.2a-c, top, have $\sigma_{RR} = 0.7\,\text{nm}$ and a reduced $\sigma_{BB} = 0.47\,\text{nm}$. The ε_{RB} determining the depth of the LJ interaction potential for the inter-species hetero-interaction energy between **R** and **B** heads was kept constant in all mCG systems ($\varepsilon_{RB} = 0.5\,\text{kJ mol}^{-1}$), while the intra-species homo-interaction (*i.e.*, ε_{RR} and ε_{BB}) was varied to promote mixing ($\varepsilon_{\mathbf{RR}} = \varepsilon_{\mathbf{BB}} = 0.5\,\text{kJ mol}^{-1}$), segregation ($\varepsilon_{\mathbf{RR}} = \varepsilon_{\mathbf{BB}} = 4\,\text{kJ mol}^{-1}$), or an intermediate behavior ($\varepsilon_{\mathbf{RR}} = 4\,\text{kJ mol}^{-1}$ and $\varepsilon_{\mathbf{BB}} = 0.5\,\text{kJ mol}^{-1}$). It is worth noting that, the properties of tail beads were kept constant for all the case studies and were identical in both **R** and **B** molecules. Specifically, for each mCG tail bead $\sigma_{tail} = 0.47\,\text{nm}$, while $\varepsilon_{tail} = 5\,\text{kJ mol}^{-1}$, defining both the intra- and inter-species interactions.

mCG-MD simulations

All CG-MD simulations of the minimalistic model were carried out using the Gromacs software [173] in NVT conditions at $T = 300\,\text{K}$. The dimensions of the simulation box were set to $20 \times 20 \times 20\,\text{nm}^3$, and the simulations have been con-

ducted in periodic boundary conditions. In all mCG micelle models, the number of molecules is $N_R = 100$ and $N_B = 100$ surfactant molecules.

After a brief preliminary minimization, the MD simulations were performed in implicit-solvent through Langevin dynamics, using the stochastic dynamics (*sd*) integrator, where the parameter tau-t= 0.1 ps accounts for both the friction of the solvent and thermal fluctuations of the system. The time step was set at $\Delta t = 40$ fs, and the non-bonded interaction potentials were truncated and shifted at a cutoff distance of 1.2 nm. For each simulation of self-assembly, at least 20 µs of CG-MD were performed, sampling the conformations every 1 ns. Only the equilibrium part of each trajectory, corresponding to the last 5 µs, was considered for analysis, as all simulations were initiated with randomly dispersed configurations. For the mixed system (**RR=BB=RB**), we performed a longer simulation of 40 µs, keeping always the last 5 µs for the analysis, as representative of the equilibrium of the system.

The CG-MD simulations of the control model in explicit solvent were carried out in NPT conditions, utilizing the *md* integrator, with a time step of $\Delta t = 40$ fs. The equilibrated part of the trajectories is 5 µs long and the conformations were sampled every 1 ns. The temperature of the system was maintained constant through the use of the velocity rescaling thermostat [174], with a time constant of $\tau_T = 1$ ps and a coupling temperature of $T = 300$ K. Pressure was kept constant using the Parrinello-Rahman barostat [175], with a time constant of $\tau_p = 8$ ps and a reference pressure of $p = 1$ bar.

All-atom (AA) and finer coarse-grained models (fCG)

All-atom models (AA) of the surfactants of Figure 4.3a were built in Avogadro [152] and parametrized using the OPLS-AA force field [176]. Van der Waals interactions were modeled using Lennard-Jones potential (LJ) with a cutoff of 1 nm. Electrostatic interactions at short range were calculated by summing the contributions of all particles within a 1 nm cutoff, while long-range interactions were evaluated using Particle-Mesh Ewald (PME) summation in Fourier space [177]. To generate the CG models, the AA surfactants were first solvated in a cubic box of 5nm filled with explicit SPC/E water molecules [178]. Then, a production run was conducted for 10 ns in NPT ensemble [174]. Using the AA-MD trajectories as a reference, the bond, angle, and dihedral distributions of the CG beads were optimized using the

Swarm-CG tool [85], following the four-to-one mapping typical of the MARTINI force field [105]. The non-boded interactions among the beads were described using the standard MARTINI 2.2 force-field [105] in explicit water.

AA and fCG-MD simulations

The AA-MD simulations of each surfactant were conducted through several steps, including a total energy minimization and two equilibration steps to achieve $T = 300\,\mathrm{K}$ and $p = 1$ bar. The first equilibration was performed in NVT ensemble for $100,\mathrm{ps}$, using the `v-rescale` thermostat [179] with a time constant of $\tau_T = 0.1,\mathrm{ps}$. The second equilibration was conducted in NPT ensemble for the same duration, using the Parrinello-Rahman barostat [175] with a time constant of $\tau_p = 2,\mathrm{ps}$. After the equilibration of the thermodynamic conditions, an additional 5 ns of production run was performed in the NPT ensemble, utilizing the Nose-Hoover thermostat [180] ($\tau_T = 0.4\,\mathrm{ps}$) and the Parrinello-Rahman barostat [175] ($\tau_p = 8\,\mathrm{ps}$).

The self-assembly CG-MD simulations were conducted using the MARTINI parametrization in explicit solvent [105]. No-polarizable-type P4-MARTINI beads have been used to model the explicit solvent, without any ionic strength. The dimensions of the simulation box were $L_x = 20.0\,\mathrm{nm}$, $L_y = 20.0\,\mathrm{nm}$, and $L_z = 20.0\,\mathrm{nm}$ in the x-, y-, and z-directions, respectively. The number of water beads in the box was ranging from 55000 to 60000 to keep a constant pressure while varying the surfactant concentration. The simulation protocol consisted of an initial 50.0 ns of equilibration run to thermalize the system at $p = 1.0\,\mathrm{bar}$ and $T = 300\,\mathrm{K}$, using the v-rescale thermostat [174] ($\tau_T = 2\,\mathrm{ps}$) and Berendsen barostat [181] ($\tau_p = 12\,\mathrm{ps}$). During the subsequent $10\,\mu\mathrm{s}$ of production run, the system was maintained at $p = 1.0\,\mathrm{bar}$ and $T = 300\,\mathrm{K}$, using the v-rescale thermostat and the Parrinello Rahman barostat [175]. A time-step of 20 fs was used to integrate Newton's equations of motion, and short-range interactions were truncated at 1.2 nm. The simulations were conducted using periodic boundary conditions in all the three dimensions. All simulations have been performed using Gromacs [173].

Unsupervised Machine Learning of molecular motifs

SOAP analysis

To investigate the internal molecular (surfactant) organization and dynamics within micelles, an accurate representation of the molecular environment surrounding each surfactant head is needed. SOAP vectors offer a high-dimensional data-driven classification of molecular environments that has been recently proven useful to classify molecular environments and classify assemblies based on those. In the case of these micelles, SOAP vectors [121] were calculated for the center of mass (COM) of each surfactant head in the equilibrated MD trajectories. At each frame of the CG-MD simulation, SOAP describes the local distribution and structural organization of surfactant head COMs within a specific cut-off radius. The equilibrated CG-MD micelle trajectories (last 5 µs and 3 µs for the mCG and fCG models, respectively) were extracted every 10 ns and analyzed using the DScribe package [122].

Dimensionality Reduction and unsupervised PAMM clustering

The dimensionality reduction of the SOAP vectors was carried out through Principal Component Analysis (PCA), by using TwoNN algorithm [182] and retain the first 5 Principal Components (PCs) in order to obtain at least 80% of total cumulative variance of our dataset, as reported in Table 4.1. For visualization purpose, only the first two PCA components of the 5-dimensional-dataset were plotted in Figures, 4.2a,b,c, 4.4a,c,e (left), 4.6a,e and 4.7a,e. The PCA algorithm was trained on the complete SOAP dataset, which included the SOAP vectors of the compared micelles.[87, 86]. Unsupervised clustering of the SOAP data was performed using the Probabilistic Analysis of Molecular Motifs (PAMM) clustering algorithm.[125, 86] The parameters used for computing the SOAP-based vectors, and for performing the PCA and PAMM clustering analyses, are outlined in Table 4.1.

Starting from results of the clustering analysis, we established the inter-conversion diagrams for each micelle by counting the total number of transitions between clusters in each frame along the equilibrated CG-MD trajectories. The conditional transition probabilities for each micelle were calculated by normalizing the results over the total number of transitions originating from the considered cluster. The population diagrams were obtained by averaging the distribution of clusters over

the analyzed trajectories. Finally, we evaluated the suitability of this unsupervised approach by determining the composition of each cluster by examining the specific amphiphile species it contained.

Table 4.1 Parameters set in the unsupervised machine-learning analysis. Note that D is the SOAP vector dimension computed for the relative `cut-off`. nPC and *var* are the number of principal components and variance regarding the dimensionality reduction analysis (PCA), respectively. *Ngrid* and *fs* are the number of grid points and a localization parameter of the anisotropic multivariate Gaussian, respectively.

	SOAP		PCA		PAMM	
	`cut-off` $[\dot{A}]$	*D*	*nPC*	*var %*	*Ngrid*	*fs*
mCG (fig 4.2)	30	324	5	88.5	2500	0.2
fCG (fig 4.4)	40	324	5	90.1	200	0.2
fCG (fig 4.6)	50	324	5	87.9	3800	0.2
fCG (fig 4.7)	50	324	5	87.9	3800	0.2

4.3 Results and discussion

Physical factors controlling bi-component micelles

The first part of this Chapter reports a case study of the minimalistic coarse-grained (mCG) model of a bi-component self-assembled micelle. This model was designed to examine the key factors that control the structure and dynamics of the micelle, as well as to validate the use of machine learning in the analysis. The model, depicted in Figure 4.1, represents the surfactant monomer as a five-beads amphiphile, where four smaller beads constitute the hydrophobic tails and are kept constant throughout all mCG studies, and one large bead simulate the hydrophilic head. The non-covalent interactions between the surfactants are modeled using a Lennard Jones (LJ) potential, whose parameters are present in the Computational approach section. The LJ parameters are set to result in a self-assembled micelle structure, where the solvophobic tails are directed inward and the solvophilic head are located on the surface of the micelle (see Figure 4.1). As it is an implicit solvent model, all the interactions between the different monomer and the solvent are accounted for in the description of the non-bonbed interaction and are controlled by the stochastic dynamics.

The mCG model of 200 surfactants is diversified into two different species, represented by 100 **R** and 100 **B** (colored red and blue in Figure 4.2a-c, top), to obtain bi-component micelles. The diversity between the two species is modeled in two different ways: (i) by modulating the homo and hetero head-head intermolecular interactions, and (ii) by changing the size of the amphiphile heads. Both of these approaches imitate the changes in the heads of two different surfactant species, resulting in molecules differentiated in size and physical-chemical affinities. While in real systems, changing surfactant species means altering both (i) and (ii), herein we took advantage from the flexibility of the mCG model to independently investigate the effects of interaction energy (i) and head size (ii), in order to reach a better understanding of the key factors driving either uniform mixing of the two species or their complete segregation into distinct domains within the micelle.

For example, we consider the impact of geometrical factors on the final assembled structure by varying the dimensions of the head beads, which can have different intermolecular interactions (Figure 4.2a-c, top). To this end, the radius of the **B** amphiphile head was decreased in order to obtain the ratio $\sigma_R/\sigma_B = 1.49$, while keeping unchanged the radius of the **R** head (Figure 4.2a-c). The structural and dynamic properties of the assembled micelles are investigated through a machine learning approach based on the SOAP descriptor. The SOAP vectors, which are centered on the head bead, enable the detection of the local molecular environments surrounding every surfactant. The SOAP spectrum of each surfactant then characterizes the degree of order and disorder of the surfactant heads within the micelle during the last 5 μs of the equilibrated mCG trajectories. The large SOAP dataset obtained (100000 SOAP spectra: 200 SOAP spectra, one for each surfactant, at each of the 500 sampled time steps) provides insights into the structural arrangement and order of the surfactants heads, as well as the rearrangement of the monomers within the micelle.[87, 86] The PAMM clustering method [125], applied on the PCA dimensionality-reduced SOAP dataset, and reported in Figure 4.2, detects three main clusters: the cyan cluster located on the bottom and topmost flat regions of micelles, and the gray and fuchsia clusters distributed in the less dense corona surrounding the micelles. The monitoring of the cluster during the MD simulations permits the evaluation of the rearrangement probabilities of surfactants to transient from one environment to another one, by estimating the transition rates. In particular, the interconversion diagrams (Figure 4.2, bottom) demonstrate the stability of the cyan cluster, with a probability range of $\sim 68-88\%$ for a cyan surfactant to remain in

its cluster. Meanwhile, the transition probability to the gray domain is unfavorable (below $\sim 3\%$), and the transition to the fuchsia cluster ranges from $\sim 10-29\%$. Increased intermixing is observed between the gray and fuchsia clusters in all cases.

The results obtained by regulating the intermolecular interactions raises interesting considerations regarding the correlation between the structural environments identified through the data-driven analysis and the distribution of surfactant species in those environments. In the case where LJ $\varepsilon_{RR} = \varepsilon_{BB} = \varepsilon_{RB}$,the distribution of the species is not uniform in the cluster (see histograms in Figure 4.2a, bottom), as, in particular, the cyan domains are populated up to $\sim 80\%$ by the **B** surfactants. Although a mixed configuration of the species was expected, with smaller head groups of the **B** surfactants, surrounding larger ones (**R** surfactants), a kind of phase separation occurred (see histograms in Figure 4.2a, bottom). This configuration is likely due to the combination of two mechanisms: the **B** surfactants, with the smallest sigma, tend to self-aggregate rather than surround the **R** heads, and the topological properties of **B** tend to favor a double layer organization, leading to arrangements in more flattened regions on the micelle surface. Alternatively, the example in Figure 4.2b shows a compartmentalization, where the cyan and gray clusters contain more than 95% of either **B** or **R** surfactants, respectively, as confirmed by the transition diagrams. The last example in Figure 4.2c, which is a more realistic model, highlights a closer correspondence between physical/structural micelle domains (SOAP clusters) and surfactant species (**B** or **R**).

The system depicted in Figure 4.2b highlights the challenges present in the prediction of the exact configuration and structural rearrangement of self-assembling monomers by simply providing the topological and force field details. The internal reorganization of the system is influenced by a combination of several aspects, making the identification of a predominant behavior challenging. These difficulties motivate the need for a more versatile, flexible, and transferable analysis approach that can unveil the structural and dynamic nature of diverse aggregate without any prior knowledge of their species. Such approach has the potential to be highly beneficial in the analysis of chemically-relevant, high-resolution models of realistic molecular systems where greater chemical detail is preserved.

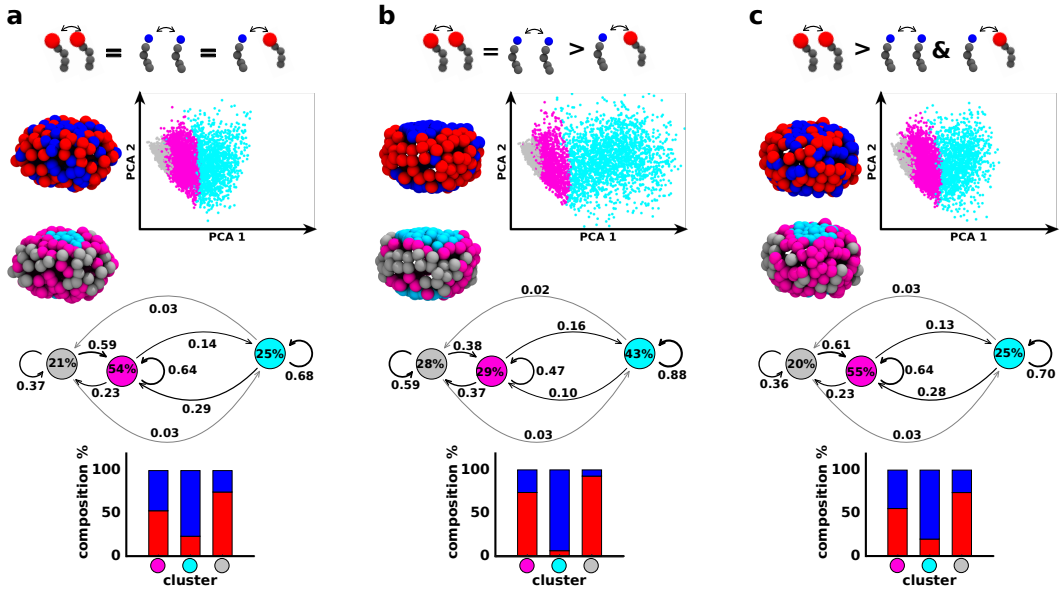

Fig. 4.2 Minimalistic mCG models and unsupervised ML analysis of complex micelles with different surfactant head sizes and variable inter-surfactant interactions. (a) Partial **R** and **B** amphiphile mixing is obtained for LJ $\varepsilon_{RR} = \varepsilon_{BB} = \varepsilon_{RB}$; (b) a net compartmentalization of **R** and **B** is observed at $\varepsilon_{RR} = \varepsilon_{BB} > \varepsilon_{RB}$; (c) an intermediate mixing/segregation is captured for $\varepsilon_{RR} > \varepsilon_{BB}$ and $\varepsilon_{RR} > \varepsilon_{RB}$.(a-c) Top: Equilibrium mCG-MD snapshots of various micelles made of **R** and **B** surfactants having LJ $\sigma_R/\sigma_B = 1.49$ (left); projection of the SOAP-dataset PCA on the first two Principal Components (right). Three SOAP clusters are identified: gray, magenta, and cyan. (a-c) Center: Equilibrum mCG-MD micelle snapshots showing the SOAP clusters distribution, and their dynamic inter-conversion diagrams (percentage cluster populations inside the coloured circles, normalized transition probabilities on the arrows connecting the various clusters). (a-c) Bottom: SOAP-cluster compositions in terms of **R** and **B** amphiphiles. Figure reproduced from Ref. 159 with permission of Creative Commons CC BY license.

Into the dynamics of realistic bi-component micelles

We considered a realistic example, the bi-component micelles reported in Ref. 88, where n-stearoyl L-histidine (**H**) self-assemble with either p-nitrophenyl ester of n-stearoyl L-phenylalanine (**F-NP**) and p-nitrophenyl ester of n-stearoyl L-histidine (**H-NP**) amphiphiles. In this Chapter, the first system will be referred as **SYS A** and the second system as **SYS B**, as shown in Figure 4.5a,b. Furthermore, based on experimental evidences, it is known that the self-assembly of **F-NP** and **H** leads to various complex configurations, which enable and enhance catalytic reaction between different surfactants at specific concentrations.[88, 89]

We characterized the different monomers using a finer coarse-grained (fCG) description, based on the MARTINI force field [105, 111]. The models are reported in Figure 4.3a, where red and blue colors are selected to distinguish the head beads belonging to diverse surfactant species within a single micelle. The self-assembled configuration was obtained starting with a dispersed solution (Figure 4.3b-d) of the equal amounts of **H** and **F-NP** monomers at different concentrations, 200, 310, or 400 surfactants in total, in explicit water. A fCG-MD simulation of 10 µs was performed to reach an equilibrated system, with the last 3 µs considered for the analysis. Some representative snapshots are shown in Figure 4.3c,d, including the final configuration for the case with 310 and 400 surfactants.

The snapshots of the final configurations reveal that the rearrangements of the amphiphiles depends strongly on the nature and orientation of the smaller micelles, resulting in a different self-assembled configurations. Since these model-systems represent a zoom close to the micelle, the concentration is higher than the Critical Micelle Concentration (CMC) [88], making it unlikely to observe surfactants in the monomeric form. The SOAP and PAMM analyses conducted herein (see 4.4) followed the same protocol presented for the minimalistic models in Figure 4.2.

The SOAP and PAMM analysis resulted in the detection of three different clusters, which are represented by the colors yellow, magenta and light blue in Figure 4.4. The projection of the first two principal components, shown in the interconnection diagrams of Figure 4.4a,c,e, reveal differences in the signal caused by the varying dimensions of the micelles. The yellow cluster represents surfactants located in the corona region, which contains the highest percentage of surfactants, ranging from 48% to 79%. At the same time, the light blue cluster identifies an internal domain sparsely populated (2% and 13%), and is present only in micelles with 310 and 400 monomer units. It is also never exposed to the solvent. The surfactants in the light blue cluster are encapsulated within the micelle in a double-layer configuration. The magenta cluster is the connection between the other two clusters, and represent the flatter top and bottom of the compressed micelles (Figures 4.4a-d), especially in the case with 310 surfactants. The inter-conversion diagrams shown at the bottom of Figure 4.4a,c,e, demonstrate that all the identified clusters are dynamically persistent, with probabilities higher than 86% (except for the magenta cluster in Figure 4.4a, b). The transition between the different clusters is infrequent, leading to limited mobility of the monomers, which maintain their surrounding in the configuration within a micelle. Although the dynamics in these fCG micelles is slower than in

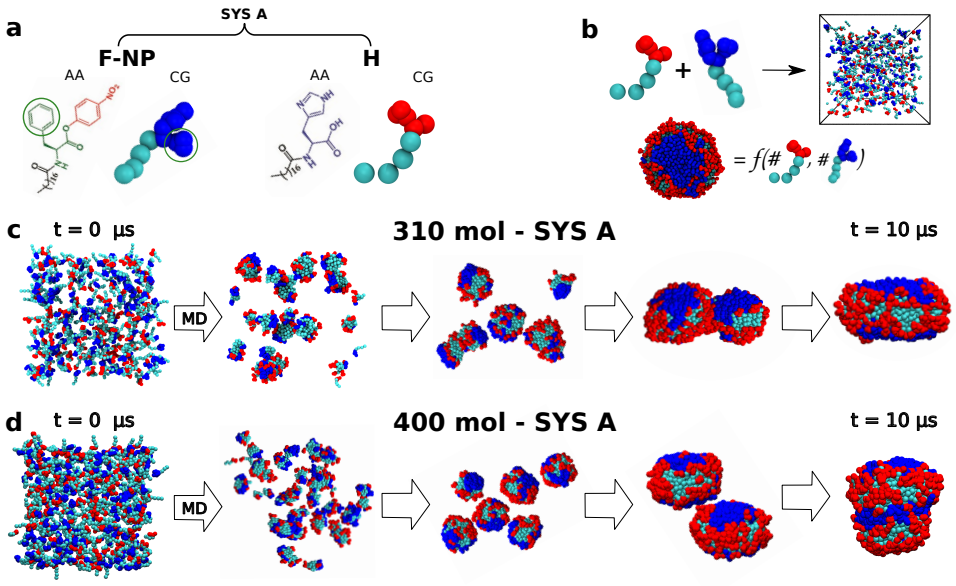

Fig. 4.3 Finer chemically-relevant bi-component micelle models. (a) Chemical structures (AA) and fine coarse-grained (fCG) models of **SYS A** surfactants: p-nitrophenyl ester of n-stearoyl L-phenylalanine, **F-NP** and n-stearoyl L-histidine, **H**. (b) Increased size micelles made of 200, 310, or 400 surfactants, respectively, have been obtained *via* self-assembly of an equal number of red and blue surfactants during fCG-MD simulations. (c-d) Representative snapshots of 10 μs self-assembly fCG-MD simulations to form two example of **SYS A** micelles containing 310 (c) and 400 (d) surfactants in total. Figure reproduced from Ref. 159 with permission of Creative Commons CC BY license.

the minimalistic one, they still exhibit internal dynamic complexity. The histograms in Figures 4.4b,d,f, which report the population of surfactants in different clusters, indicate that the yellow and magenta clusters are predominantly composed of **H** (red) and **F-NP** (blue) surfactants, respectively, with limited infiltration of secondary species. On the other hand, the light blue cluster is entirely made up of **F-NP** amphiphiles, indicating a structural reconfiguration of the micelles in which the light blue surfactants are encapsulated within the aggregate at a certain concentration. Both the histograms and the inter-conversion diagrams highlight that the exchange of **F-NP** (blue) surfactants from the light-blue to the yellow clusters is possible only through an intermediate transition involving the magenta domains, while the transition in the other direction is highly unlikely.

Subsequently, we conducted an investigation into an additional system, referred to as **SYS B**, with a reduced diversity between the two monomers, as the chemical structure of the hydrophilic heads is more similar than in **SYS A** (see Figure 4.5a,

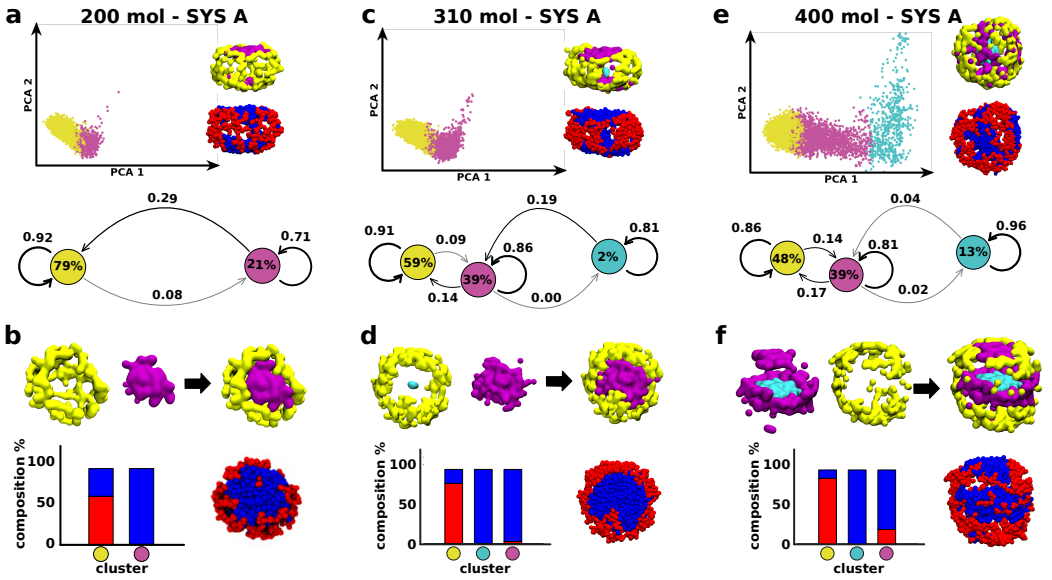

Fig. 4.4 SOAP dataset clustering of **SYS A** micelles containing 200 (a,b), 310 (c,d), or 400 (e,f) surfactants in total. (a,c,e) Top: PCA projections of the SOAP datasets on the first two Principal Components with the side view representation of micelles according to both the cluster identification and the molecular species details at fCG-MD time = 10 μs (a,c) and 9.3 μs (e). Bottom: Cluster inter-conversion diagrams, reporting (i) the surfactant populations per-cluster (percentages inside the colored circles), (ii) the normalized probabilities for surfactants to remain within a given cluster (arrows starting/ending from/to the same colored circle), and (iii) the transition probabilities towards a different cluster (arrows connecting diverse colored circles) in the time-interval of the analysis (dt = 10 ns). (b,d,f) Top: Equilibrium fCG-MD snapshots of micelles at 10 μs showing the decomposition in SOAP-detected clusters. Bottom left: bar plot of the percentage composition per-cluster in terms of red and blues amphiphiles. Bottom right: Equilibrium fCG-MD snapshots of micelles at 10 μs showing the molecular species distinction. Figure reproduced from Ref. 159 with permission of Creative Commons CC BY license.

b). This system exhibits a more pronounced reshuffling of surfactants compared to **SYS A**. As previously mentioned, the bi-component micelles were composed of 50% **H-NP** plus 50% **H** (see Figure 4.5b) and were simulated with the same methodology applied for **SYS A**. The differences between the two systems, i.e., the variations in the compartmentalization of the monomer units, are made evident by the calculation of the radial distribution functions (g(r)) and the coordination number (Figure 4.5a, b). The radial distribution functions were calculated between the hydrophilic heads of **H** monomer and the center of mass of hydrophobic tails, which represent the micelle core. The radial distribution function reveals a high probability of encountering red (**H**) surfactant heads in **SYS A** located approximately

3.5 nm from the micelle core, indicating a more localized spatial distribution in the corona region of the micelles (with diameter ranges from 7 and 8 nm). Conversely, in **SYS B**, the radial distribution functions display a more mixed rearrangement of red (**H**) surfactant heads, which are detected both in the external corona region (roughly at r = 3.5 nm) and in the top and bottom-most domains ($1nm < r < 2nm$) of flatten micelles. The evaluation of the number of contacts (Figure 4.5a,b) is higher for **SYS B** micelles, confirming the mixed configuration within the two surfactants. The results obtained are then validated through the machine learning analysis, comparing the results of **SYS A** and **SYS B** micelles composed of 200 (Figure 4.6) and 310 (Figure 4.7) surfactants.

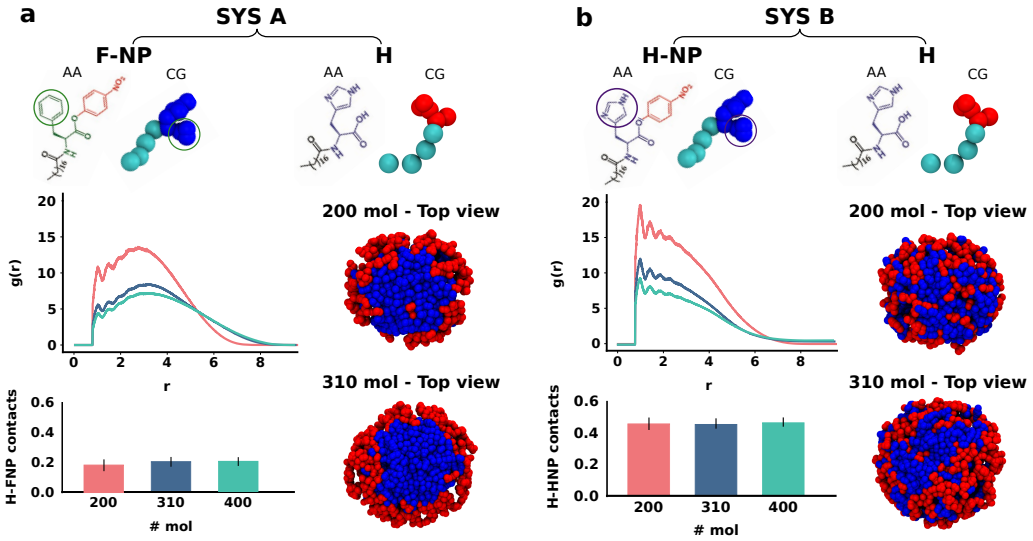

Fig. 4.5 Finer chemically-relevant bi-component micelle models of both **SYS A** and **SYS B** systems. (a-b) Top: Chemical structures (AA) and fine coarse-grained (CG) models of p-nitrophenyl ester of n-stearoyl L-phenylalanine, **F-NP** (a), n-stearoyl L-histidine, **H**(a,b), and p-nitrophenyl ester of n-stearoyl L-histidine **H-NP** (b). Although the same color code, **F-NP** and **H-NP** have distinct non-covalent parameters for those beads mapping chemically diverse rings highlighted in green and purple circle. (a-b) Center: Radial distribution function, g(r), between the hydrophilic heads of **H** monomer and the center of mass of hydrophobic tails representing the micelle core. Pink, blue, and cyan g(r) profiles correspond to 200, 310, 400 surfactant micelles, respectively. (a-b) Bottom: Percentage of **FNP** - **H** and **HNP** - **H** couple contacts in **SYS A** (a) and **SYS B** (b), respectively. Figure reproduced from Ref. 159 with permission of Creative Commons CC BY license.

The SOAP and PAMM analysis, as presented in Figures 4.6b,f and 4.7b,f, conducted in both **SYS A** and **SYS B** systems, identifies three main clusters: green, gray, and pink, ordered from the most populated to the least populated. Furthermore, the

population of the pink cluster increases with an increase in the number of surfactants composing the micelles, ranging from $\sim 1-2\%$ to $\sim 11-15\%$ (as shown in Figures 4.6 and 4.7). Both systems exhibit the absence of transitions between the pink and the green clusters, which confirms the presence of distinct environments within the micelles. The structure of the micelles are composed of a pink cluster in the topmost region, surrounded by a gray region, and an external green corona (side and top views of the micelles of Figure 4.7c,g).

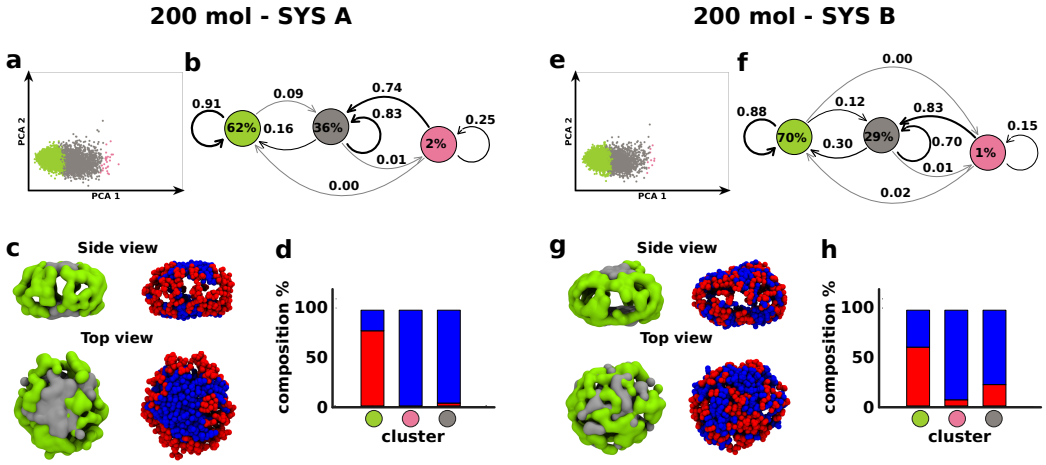

Fig. 4.6 Effect of chemical diversity on the structural and dynamical features of bi-component micelles. Data obtained from equilibrated fCG-MD simulations of 200-amphiphile micelles in case of **SYS A** (left) and **SYS B** (right) systems. (a,e): PCA projections of the SOAP datasets on the first two Principal Components. (b,f): cluster inter-conversion diagrams, reporting (i) the surfactant populations per-cluster (percentages inside the colored circles), (ii) the normalized probabilities for surfactants to remain within a given cluster (arrows starting/ending from/to the same colored circle) or (iii) the transition probabilities towards a different cluster (arrows connecting diverse colored circles) in the time-interval of the analysis (dt = 10 ns). (c,g): Equilibrium fCG-MD snapshots showing the SOAP-detected clusters (left) and the distribution of red and blue surfactant heads (right) in the micelles. (d,h): Population histograms showing the surfactant composition in each detected SOAP-cluster in terms of red and blues amphiphiles. Figure reproduced from Ref. 159 with permission of Creative Commons CC BY license.

However, the results show some differences between the two systems. Generally, the probability of a surfactant staying within a cluster in **SYS B** is lower compared to that in **SYS A**. Alternatively, the transitions between different clusters are higher in **SYS B** as compared to **SYS A**. This is due to higher reshuffling capability of the

two species present in **SYS B**. In addition, from the population histograms in Figures 4.6d,h and 4.7d,h, it is evident that the SOAP clusters in **SYS A** are mostly composed by only one of the surfactant species. The green cluster is made up of $\sim 80-95\%$ red surfactants, while the gray and the pink environments contain almost exclusively blue surfactants. In contrast, the clusters in **SYS B** are more heterogeneous, as the green cluster in 200 mol-**SYS B** system is composed of $\sim 60\%$ and $\sim 40\%$ of red and blue surfactants, while the gray environment in 310 mol-**SYS B** contains $\sim 70\%$ blue surfactants and $\sim 30\%$ red surfactants. It is worth mentioning that the clustering analysis is dependent on the dataset in which the classification is carried out. As a result, minor variations in the clustering may arise when comparing the molecular motives of the same micelle that are included in different starting datasets (as seen in Figures 4.4, 4.6, and 4.7). In other words, the identification of internal structural domains is not absolute, but always relative to a collection of assemblies (dataset).

In conclusion, the machine learning approach presented in this Chapter has demonstrated the correlation between physically and structurally different clusters and their composition in terms of surfactant species even in this finer CG models. By combining the results from Figures 4.4-4.6-4.7 with those obtained for the minimalistic mCG models in Figure 4.2, the critical factors that control the structural and dynamic complexity of amphiphile micelles can be identified. The topological differences between the surfactant molecules and intermolecular interaction are found to be key drivers of surfactant rearrangement in the micelle, resulting either compartmentalization or complete mixing. Furthermore, the SOAP-based machine learning analysis provides quantitative insights by reconstructing collective structural motives and uncovering dominant dynamic pathways in terms of transient and residence probabilities among different environments in bi-component micelles. Moreover, the realistic molecular systems (Figures 4.4-4.6-4.7) provide evidence of the impact of even minor molecular variations among the two species. This focus the attention on both the structural and energetic properties of the self-assembling units in influencing the obtainment of an intermixed or segregated final structure. In this regard, the machine learning approach proposed is able to recognize such perturbations, even when small differences among the amphiphiles result in diverse molecular behaviors in the assembly.

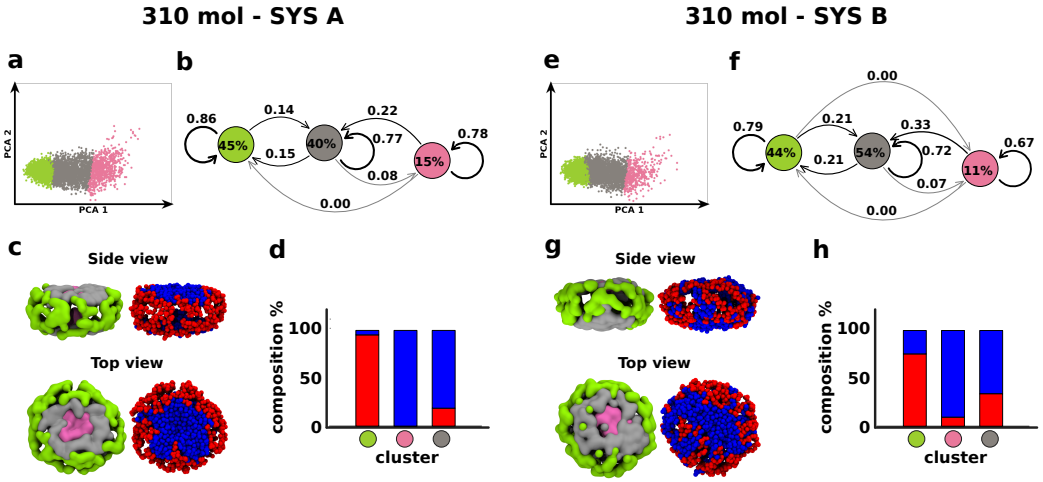

Fig. 4.7 Effect of chemical diversity on the structural and dynamical features of bi-component micelles. Data obtained from equilibrated fCG-MD simulations of 310-amphiphile micelles in case of **SYS A** (left) and **SYS B** (right) systems. (a,e): PCA projections of the SOAP datasets on the first two Principal Components. (b,f): cluster inter-conversion diagrams, reporting (i) the surfactant populations per-cluster (percentages inside the colored circles), (ii) the normalized probabilities for surfactants to remain within a given cluster (arrows starting/ending from/to the same colored circle) or (iii) the transition probabilities towards a different cluster (arrows connecting diverse colored circles) in the time-interval of the analysis (dt = 10 ns). (c,g): Equilibrium fCG-MD snapshots showing the SOAP-detected clusters (left) and the distribution of red and blue surfactant heads (right) in the micelles. (d,h): Population histograms showing the surfactant composition in each detected SOAP-cluster in terms of red and blues amphiphiles. Figure reproduced from Ref. 159 with permission of Creative Commons CC BY license.

4.4 Conclusion

The comprehension of the structural and dynamic complexity of multi-component self-assembling systems is a complicate challenge. In this Chapter we presented an unsupervised machine learning approach to examine the structural and dynamic behavior of bi-component micelle models. By combining SOAP descriptors and unsupervised clustering (PAMM) with finer chemically-relevant and minimalistic physical models, we observe the principal factors that regulate the rearrangement of surfactants in dynamic self-assembled micelles.

The unsupervised machine learning approach used herein has proved to allow for the reconstruction of the structural and dynamic features of multi-component

micelles. The analysis detects assembled domains with conformational differences, such as flat and compact *vs.* toroidal less-dense domains in slightly compressed micelles. This method enables the identification of dominant structural environments on micelles, the estimation of their stability, and the resolution of the dynamic exchange of the self-assembling monomers among the identified clusters. As a result, a comprehensive picture of the micelles is obtained, including their structural density, and pathways for exchange and reshuffling of self-assembling molecules within them.

We also evaluated the sensitivity of the unsupervised analysis proposed herein in correlating structural motives with different molecular species based solely their arrangement and movement within the self-assembled micelle. From our results, the formation of structural domains (clusters) in a micelle, which relies on different physical features, does not necessarily depend on the segregation of the molecular species. Instead, these may be simply a result of how the assembling units aggregate in certain conditions. In structurally non-uniform micelles, surfactants can intermix almost completely in all regions of the micelle as long as they are similar enough to cross-interact. On the contrary, different amphiphile species tend to separate in different micelle environments if the co-assembled species differ in topology and intermolecular interactions. The comparison between fCG and mCG evidences the role played by the geometrical features and details of the molecular building blocks, as the molecular structure encodes different shape recognitions and different intermolecular interactions in the building blocks.

In conclusion, the unsupervised data-driven analysis approach presented in this Chapter represents a high-potential method for reconstructing and understanding the structural and dynamical complexity of soft self-assembled micelles, as well as for investigating the key factors that can influence their complex behavior.

Chapter 5

Emergent supramolecular conductive behaviors in colloidal superlattices

The work contained in this Chapter has been published in the following paper: "C. Lionello, C. Perego, A. Gardin, R. Klajn and G. M. Pavan. Supramolecular semiconductivity through emerging ionic gates in ion-nanoparticle superlattices. ACS Nano ***2023****, 17, 275-287" [183], and has been adapted with permission of Creative Commons CC BY license.*

Abstract

The self-assembly of nanoparticles driven by small molecules or ions may produce colloidal superlattices with properties evocative of those of metals or semiconductors. However, how much the properties of such supramolecular crystals actually resemble those of atomic materials often remains unclear. Herein, coarse-grained molecular simulations demonstrate how a behavior evocative of that of electronic semiconductors may arise even on a higher scale in a colloidal superlattice. In particular, we focus on gold nanoparticles functionalized with positively charged groups that self-assemble into FCC crystals through the mediation of citrate counterions. *In silico* ohmic experiments show to what extent the dynamically diverse behavior of the counterions in different superlattice domains permits the opening of conductive ionic gates above certain levels of applied electric fields. The observed binary conductive/non-conductive behavior is reminiscent of that of conventional

semiconductors, while, at a supramolecular level, crossing the "band gap" requires a sufficient electrostatic stimulus to break the electrostatic interactions and make ions diffuse throughout the superlattice's cavities.

5.1 Introduction

Colloidal superlattices, which are based on the assembly of functionalized nanoparticles (NPs) [184–195], have been receiving considerable attention due to the ease of controlling the NPs' self-assembly into different supramolecular crystalline or quasi-crystalline architectures [196–201, 184, 202–206]. There have been various methods proposed to control the self-assembling process, such as the rational design of NP shape and surface chemistry [207–212], manipulation of the self-assembling process [213, 193, 100], or utilization of molecular binding units. The use of molecular binding units includes, for instance, NPs functionalized with DNA strands [207, 214–219, 91], and the utilization of electrostatic interactions. In particular, the employment of electrostatic interactions has been of interest, as they permit the realization of binary lattices [208, 220–222], homo-NP superlattices [100, 223–225], or supramolecular fibers [226]. The final properties of a colloidal superlattice are not only dependent on the interactions within the NPs and their organization [227, 228, 225, 229], but also on the presence and the behavior of the mediating species [97, 226, 230, 98, 231, 232, 99, 100]. Supramolecular materials have garnered significant interest due to their plasmonic, magnetic, and electrical properties [233–236], but especially because they are considered as larger-scales analogs of atomic crystals, with NPs serving as superatoms [237–242]. Despite the presence of various methods for controlling the formation of the supercrystals [221, 243, 244, 100, 225], the factors underlying the emergence of collective properties remain an unresolved challenge.

Recent studies have shown the utilization of DNA interactions to create various superstructures that mimic the conformations of metallic lattices.[90–96] The NPs composing the crystal structure are referred to as atom equivalents, and the smaller species responsible for the assembled structure are referred to as superelectron equivalents. The movement of these superelectrons within the synthetic lattice, similar to the movement of electrons in metals, has been demonstrated through a combination of experimental evidences and molecular simulations.[90–96, 245] Similarly,

aggregates of gold NPs functionalized with positively charged (11-mercaptoundecyl)-*N,N,N*-trimethylammonium (TMA) groups, in the presence of Cl^- ions were found to have semiconductive properties, which could be useful for the realization of new conductive materials.[97–99] Another study looked at the self-assembly of TMA-NPs, which represent the atom analogs (AAs) driven by the presence of various types of anions, such as citrate (CIT) and ATP. This study was carried out both from the static and dynamic perspective, allowing for an exploration of the motility of the CIT ions, which were considered as electron analogs (EAs).[100]

In this context, a number of hierarchical scale analogies have been drawn between supramolecular lattices and atomic lattices due to the observed motion of EAs in AA superlattices, particularly in the realm of semiconductors where a notable charge transport of EAs components has been observed through the lattice defects in superionic crystals [246–250]. However, the precise characteristics of metals, semiconductors, and superionic conductors are difficult to be observed in supramolecular crystals. The study presented in this Chapter aims to use coarse-grained (CG) molecular simulations to examine the underlying features of EA motion and conductivity. The supramolecular lattice studied is the FCC lattice composed of TMA-NPs and CIT ions, as discussed in Ref.[100] In particular, an *in silico* approach is developed to investigate the lattice's ohmic properties under the application of an external electric field. Through this method, the differences in ion-driven conduction compared to the classical metallic conductivity are highlighted, while at the same time, similarities with semiconductive materials are revealed. The use of CG models with a resolution around $< 5\,\dot{A}$ enables the investigation of the mechanism behind ionic conduction, providing further insights towards controlling the emergent properties of colloidal supercrystals.

5.2 Computational approach

Coarse-grained molecular dynamics simulation protocol

The coarse-grained (CG) models of TMA-Au NPs and citrate ions, both in explicit and in implicit solvent, were developed from the all-atom (AA) simulations of TMA-Au NP subsections in citrate-rich water solvent, as outlined in Ref. 100. The AA model was parametrized with Amber force field [153] and minimized in

explicit solvent. Subsequently, starting from the AA trajectories, the CG model was parametrized with the MARTINI force field [105] in explicit solvent. The study presented herein employs the CG model in implicit solvent, built upon the dry MARTINI force field description.[111] The use of these models permits the investigation of the submolecular dynamics of complex supramolecular aggregates, as well as to reach the relevant sizes and timescales that characterize their collective, macroscopic behavior.[76, 77, 100] It should be noted, however, that the information obtained from these models is to be considered solely qualitative, even though the results can still be used to compare the system's dynamics under various external conditions and to provide indicative trends of the resulting dynamic behavior.

Every considered system was made of four TMA-Au NPs and 1072 citrate^{3-} anions. The single TMA-Au NP was defined by a gold core of diameter ~ 7.4 nm, composed of 12527 beads that interact via Lennard-Jones interactions and organized in an FCC lattices. The NP was coated with a shell of 804 positively (+1) charged TMA ligands bound to the NP surface via harmonic potentials of length 0.395 *nm* and force constant $k = 1.0 \times 10^4$ kJmol^{-1}nm^{-2}, modeled, according to the MARTINI CG scheme, with 13 beads each (Figure 5.1a). The citrate anions, added to neutralize the total charge of the systems, are modeled as three CG beads each carrying one negative charge, resulting in a total of $-3e$ charge (Figure 5.1a). In accordance with the experimental observation of Ref. 100, the NPs were arranged in the simulation box to form an FCC lattice (see Figure 5.1b). The NPs were positioned at the same distance observed in the self-assembling process reported in Ref. 100. The resulting CG-MD simulation cell had an initial size of $L_x = L_y = L_z = 14.35$ nm. By applying periodic boundary conditions (PBC) in all directions, an infinite superlattice was modeled, although some residual finite size effects may not be entirely excluded due to the limited size of the cell (Figure 5.3).

All CG molecular dynamics (CG-MD) simulations were performed using the Gromacs software [151], integrating the dynamics of the CG particles via Langevin equations of motion. Initially, a 20 *ns* NVT simulation was run to thermalize the system at either $T = 300$ K or $T = 333$ K. During this equilibration phase, a stochastic temperature coupling time of $\tau_T = 2$ ps was used. Subsequently, a 100 ns of NPT simulation was conducted to allow the crystal to equilibrate at a constant pressure of $p = 2 \times 10^{-6}$ bar via the Berendsen barostat method [181] with a pressure coupling time of $\tau_p = 10$ ps and temperature coupling time of $\tau_T = 2$ ps. Finally, the same NPT scheme was employed to perform 20 μs-long production

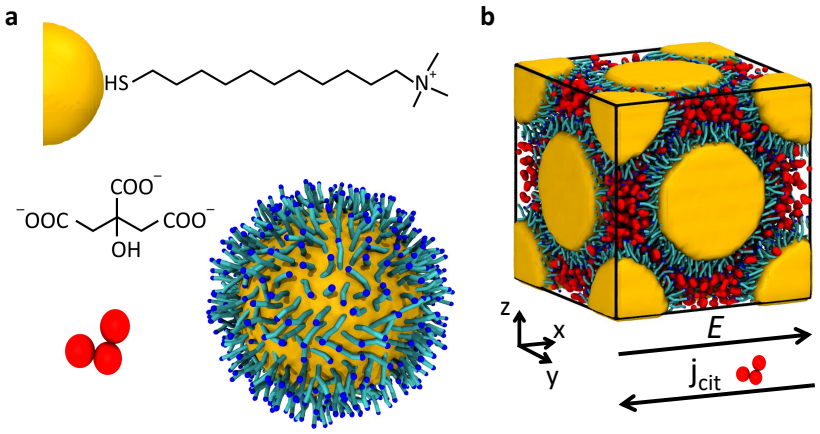

Fig. 5.1 Coarse-grained molecular model of TMA-Au NPs and citrate ions. **a** Chemical formulas of the positively charged TMA ligands, negatively charged CIT ions, and CG models of one CIT (red) and one TMA-NP (d = 7.4 nm, yellow) decorated with 804 charged TMA ligands (cyan; terminal charges in blue). **b** CG model of the unitary FCC cell in the superlattice, with Au-NPs colored yellow, TMA ligands colored blue, and citrate ions colored red. The direction of the application of the electric field E is also evidenced. Figure adapted from Ref. 183 with permission of Creative Commons CC BY license.

runs at either $T = 300$ K or $T = 333$ K and $p = 2 \times 10^{-6}$ bar. A 20-fs integration time-step, which is standard in MARTINI models [105], was used. In the CG-MD simulations with the external field, a constant, uniform electrostatic field along the x-direction was applied with different values of the amplitude E, ranging from 0.005 V nm^{-1} to 0.11 V nm^{-1}. The stability of the FCC lattice was not compromised up to $E = 0.11$ V nm^{-1}, but given the limited size of the system, it cannot be excluded that other crystal structures are more favorable than the FCC structure at high values of E. Sampling these out-of-equilibrium crystal rearrangements with our model is prohibitive. Nonetheless, the assumption that the crystal remains in the FCC structure, even under intense electrostatic fields, should not affect the general purpose of our analyses, which is to observe a supramolecular semiconductive-like behavior.

Study of citrates' dynamics

In order to characterize in detail the structure and dynamics of the citrates within the lattice model, several analyses were carried out. Firstly, the average displacement of

the anions in the x-direction was determined over the simulation time. The positions of all citrates in each simulated systems (with varying T and E) were averaged at each time-step and any discontinuities in the ion path due to PBC were removed to accurately determine their total movement. Based on the average displacement of citrates, the ionic current density was calculated as $j = Nqv_d$, where N represents the number density of the citrates, their charge being $q = -3e$, and v_d is the average drift velocity. From the ionic current density, the resistivity of the material can be estimated as $\rho = |E/j|$.

To gain further insight into the dynamics of the citrates, the SOAP analysis was utilized to differentiate between different molecular states populated by the anionic species.[251, 87] We computed the SOAP descriptors for each CIT ion by examining the relative spatial displacement of the CIT ions within a specified SOAP cutoff (rcut). At every sampled MD step we computed the SOAP spectra of each center of mass of all citrate ions. The SOAP spectra served as a fingerprint descriptor of the level of order/disorder in the displacement of the surrounding CITs' centers of mass within the cutoff. We performed this SOAP analysis using the Python package DScribe[122], using `rcut` = 65 Å (`rcut` = 65 Å was found to be the best compromise between computational cost and the level of detail/information), and `nmax`,`lmax` = 8.

We computed the SOAP vectors of every citrate ion, for all the collected CG-MD trajectories, with a sampling stride of dt = 50 ns, generating a comprehensive dataset of SOAP information associated to the citrates at different temperature (T = 300 and 333 K) and electrostatic field (E ranging from 0.005 V nm^{-1} to 0.11 V nm^{-1}) conditions. To rationalize this high-dimensional dataset, we applied a clustering algorithm to identify the most probable molecular states of the anions. The dimensionality of the data was reduced using Principal Component Analysis (PCA), performed using the Python package Scikit-Learn [252], and retaining only the first three principal components. The resulting three-dimensional descriptors were then processed using the Probabilistic Analysis of Molecular Motif (PAMM) unsupervised clustering scheme.[125] This allowed to classify all the sampled configurations of the citrates in the crystal into three different states: citrates at the interface between the two NPs (blue in all figures), those in the octahedral cavities (red), and those in the tetrahedral cavities (cyan). The molecular motif classification allowed to quantify the population of the three different states, as well as the probability of transition between them (along the collected CG-MD trajectories), providing information on

the structure and dynamics of the citrates under different temperature and electrostatic drive conditions.

5.3 Results and discussion

This Chapter focuses on the investigation of a colloidal superlattice composed of positively charged TMA-NPs self-assembled into an FCC lattice in presence of negatively charged trivalent CIT ions (Figure 5.2a).[100] Studies of all-atom and implicit-solvent CG models have shown that CIT ions play a crucial role in increasing the stability of the self-assembly of two TMA-NPs by overcoming their electrostatic repulsion.[100] Once the interactions within the TMA-NPs have been stabilized, the CIT ions were found to retain their dynamical properties (Figure 5.2c). A machine-learning approach was used to classify the CIT ions into three different environments based on the level of order/disorder in the environment surrounding them. The analysis - via unsupervised clustering and dimensionality reduction - distinguishes three main CIT environments, differing each other in their internal order and dinamicity. In Figure 5.2c, CIT ions at the interface between the two NPs are colored in blue, CIT ions interacting only with a single NP are colored in red. The analysis also reveals an intermediate layer (colored in green). It was observed that the ions at the interface are more static than those on the surface of a single NP, but the ionic environments are continuously exchanging the CIT ions, maintaining an equilibrium condition as seen in the interconnection plot of Figure 5.2c (right). The dynamics of this system and its hierarchy, with static TMA-NPs surrounded by dynamic small negatively-charged CIT ions, make it ideal for the study of ordered supramolecular lattices and their potential conducive properties.

We proposed an *ad hoc* ohmic *in silico* experiment developed to examine the correlation between the mobility of the EAs (i.e. CITs) in the superlattice and the conductive/non-conductive behavior of such supramolecolar lattices. Our experiment uses a CG model in implicit solvent to simulate an FCC lattice composed of four positively charged TMA-NPs replicated in three dimension through PBC to create an infinite lattice. 1072 $-3e$ CIT ions are added into the lattice to neutralize the charge of the NPs. A homogeneous directional electric E is applied along the x-direction to promote and track the diffusion of the CIT ions within the lattice (Figure 5.3: left and center). The recirculation of the ions in the system is facilitated by the PBC, meaning

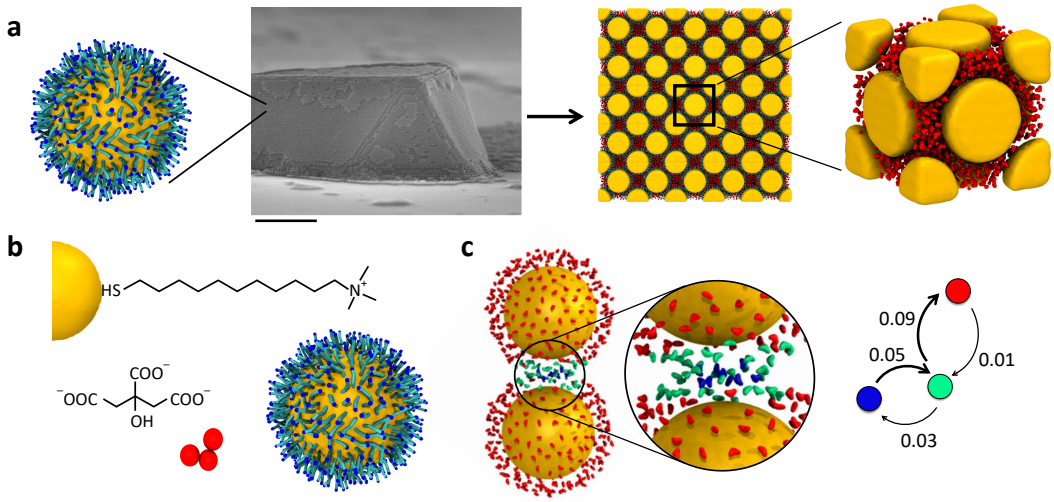

Fig. 5.2 NP-citrate colloidal superlattices and *in silico* ohmic experiments of ionic conductivity. **a** Trivalent citrate ions (CIT) driving the self-assembly of TMA-Au NPs into crystalline FCC superlattices in an aqueous solution (for experimental details, see Ref.100) Left: schematic representation of an Au NP. Center: a representative SEM image of a colloidal crystal coassembled from 7.4 nm TMA-Au NPs and citrate anions. Right: Au NPs colored as golden spheres, citrates colored in red. **b** Structural formulas of the positively charged TMA ligands and of the negatively charged CIT ions, and CG models of one CIT (red) and one TMA-NP (d = 7.4 nm, yellow) decorated with 804 charged TMA ligands (cyan; terminal charges in blue). **c** CG-MD simulation showing CIT ions mediating the interaction between two TMA-NPs (TMA ligands not shown for clarity). Unsupervised clustering of SOAP data extracted from the CG-MD simulation detects three different/distinct CIT environments.[100] CIT ions at the NP-NP interface are colored blue, CIT ions bound to one NP only - in red. The two CIT domains communicate by exchanging CITs *via* an intermediate green domain. Inset: detail of the CIT ions close to the NP-NP interface, colored based on their SOAP-detected cluster/state. Right: transition plot showing the dynamic interconnections between the SOAP environments. The numbers on the arrows are normalized transition probabilities (probability that one CIT in a given environment undergoes a transition into another in the time-interval used in the analysis).[100] Figure adapted from Ref. 183 with permission of Creative Commons CC BY license.

that once a CIT ion exits from one side of the simulation box, it is reinserted on the opposite side, mimicking an infinite source of CIT ions. Consequently, to investigate the effects of external perturbations on the mobility of ions and the conductive properties of the assembly, 20 μs production runs are conducted under various electric fields ranging from $E = 0$ (referred to as unperturbed case) to 0.11 V nm^{-1} at two different temperatures (T = 300 K and T = 333 K).

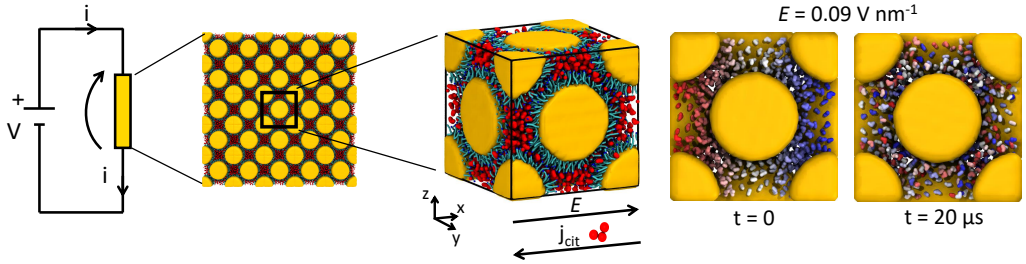

Fig. 5.3 Schematic representation of the MD approach. Left: scheme of the *in silico* ohmic experiments to study the ionic conductivity of the superlattices. Center: CG model of the bulk of an FCC TMA-NP superlattice (unitary FCC cell containing four TMA-NPs, and its replication in space): Au-NP in yellow, TMA ligands in blue, CIT in red. A uniform electric field (E) oriented along x direction is applied during the MD simulations, and the mobility of the CIT ions is systematically monitored for different E intensities. Example: motion of CITs during the MD simulation at $E = 0.09$ V nm^{-1}. The CIT ions are initially colored based on their x position (left, $t = 0$ μs): reshuffling of colors after $t = 20$ μs of MD (right) demonstrates reshuffling and diffusion of the CIT ions. Figure adapted from Ref. 183 with permission of Creative Commons CC BY license.

Once obtained the trajectories, we analyze the dynamics of CIT ions under different E intensities. For instance, as depict in Figure 5.3 (right), CIT ions are color-coded based on their x position at the beginning and after 20 μs of CG-MD under $E = 0.09$ V nm^{-1}. The final snapshot shows a global rearrangement of the anions along the simulation. Similarly, in Figure 5.4a, where the final snapshots are reported for $T = 300$ K and $E = 0$, $E = 0.01$ V nm^{-1}, and $E = 0.11$ V nm^{-1}, the CIT ions are colored based on their x-position. As all simulations start from the same configuration, variations in the coloring pattern in the final configurations reflect the variations in anions' diffusion along the E direction. By examining the final patterns, it is evident that weaker electric fields, such as $E = 0$ and $E = 0.01$ V nm^{-1}, have limited effects on the movements of CIT ions, while they increase with higher E intensities, such as $E = 0.09$ V nm^{-1} and 0.11 V nm^{-1}. A similar

behavior is observed at $T = 333$ K, where the thermal agitations also increase the motility of the ions (see Figure 5.4b).

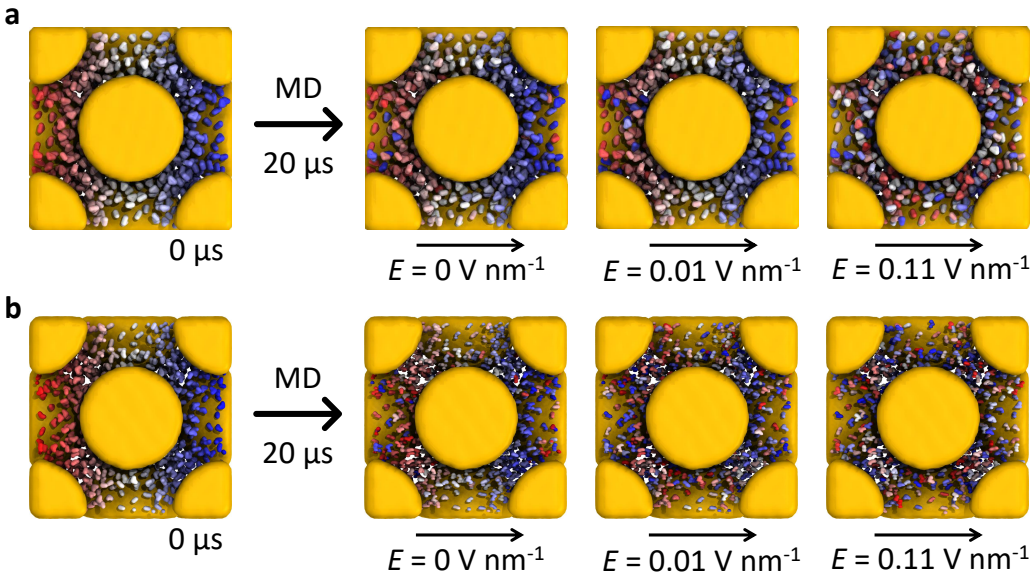

Fig. 5.4 Ionic motion in the colloidal crystal. Snapshots at the beginning (left) and after 20 μs of MD simulation (right) at **a** $T = 300$ K and **b** $T = 333$ K for different values of the electrostatic field, E (the initial configuration is identical in all simulations). CIT ions are colored according to their initial x position at the beginning of the MD ($t = 0$) in the simulation boxes, TMA groups are not shown for clarity. CIT diffusion along the x axis is proven by the red-white-blue color reshuffling at the end of the simulations. Figure adapted from Ref. 183 with permission of Creative Commons CC BY license.

To gain a more precise understanding of the diffusivity of the CIT ions, we calculated their average displacement along the x-direction during the simulations, as shown in Figure 5.5. It is important to note that all systems reach the equilibrium, as the x-displacement display a constant rate during the MD. After an initial transition phase, it is evident that CIT diffusion is enhanced by both increasing the electric field E intensity and temperature T. However, it is worth noting that the simulations utilize an approximated CG model in implicit solvent, meaning that eventual polarization effects in the solvent as a response of the electric field are not explicitly considered. As a result, the obtained results should be considered only qualitatively. However, despite such approximations, the results are neat.

From the $\langle x \rangle$-displacement, we calculated the ionic current as $j = Nqv_d$, where N is the number density of the CIT ions, $q = -3e$ is the CIT charge, and v_d is the average drift velocity (in x direction) measured in the simulations. The absolute

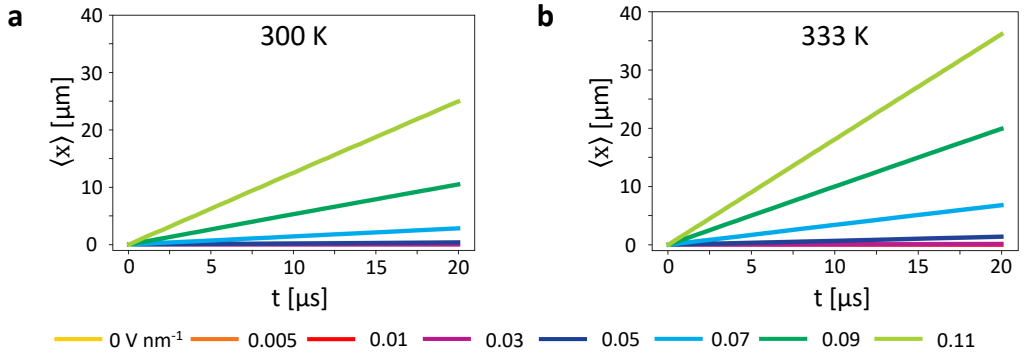

Fig. 5.5 Ionic conductivity of the colloidal crystal. **a** Average displacement of the CIT ions along x direction (direction of the applied E) at $T = 300$ K as a function of MD simulation time. Data are reported for different values of applied E (see color legend). **b** Same as **a** at $T = 333$ K. From the slope of the colored lines, it is possible to estimate the average current density j in all simulated cases. Figure adapted from Ref. 183 with permission of Creative Commons CC BY license.

values are figured in Figure 5.6a as a function of the applied electric field E. The calculation of the density current allows us to distinguish two regimes: the non-conducive regime, in which the ionic current is almost negligible (for E lower than $\sim 0.05-0.07$ V nm^{-1} at $T = 333-300$ K, respectively), and the conductive regime, where the increase in ionic current is almost proportional to the increase in E at higher electric fields. Consequently, from the density current and the intensities of E, we estimate the resistivity of the superionic lattice through the Ohm's law as $\rho = |E/j|$ (see Figure 5.6b), which decreased with increasing E. The combination of the two results from the calculation of j and ρ reveals a non-ohmic behavior of the lattice with respect to the CIT ions diffusion, which is in contrast to the typical characteristics of metals but more in line with semiconductors. The binary non-conductive/conductive behavior is reminiscent of electronic semiconductors, with the exception that in this superionic crystal, the conduction depends on CIT ions and intermolecular interactions. Specifically, it is the presence of intermolecular interactions between the CIT ions and TMA-NP that requires the application of an energy high enough to overcome the energy barrier and allow conduction in the superlattices. The results demonstrate that the minimum electric field required to activate the ionic hopping and conduction is $E \sim 0.05$ V nm^{-1}. Another difference compared to metallic materials is their dependence on temperature. In metals, an increase in the temperature results in a decrease in the conductive properties. However, in this case, the calculation of density current and resistivity reveals that

with increasing temperature, there is an increase in j and a decrease in ρ (as shown in Figure 5.6). These enhanced thermal vibrations provide extra energy to overcome the energy barrier. This aligns with the behavior of superionic conductors [246–248] where a rise in temperature leads to increase disorder and higher ion mobility through the sublattice. Although the results and the applied electric field intensity should be treated as qualitative due to the reference to a CG model, they demonstrate the presence of a conductive and non-conductive behavior dependent on temperature, which is similar to the behavior of semiconductors but on a larger scale. This is further confirmed by the resistivity values, which fall within the typical range of semiconductive materials (between $\sim 10^{-5}$ and $\sim 10^{5}\,\Omega\,\mathrm{m}$).

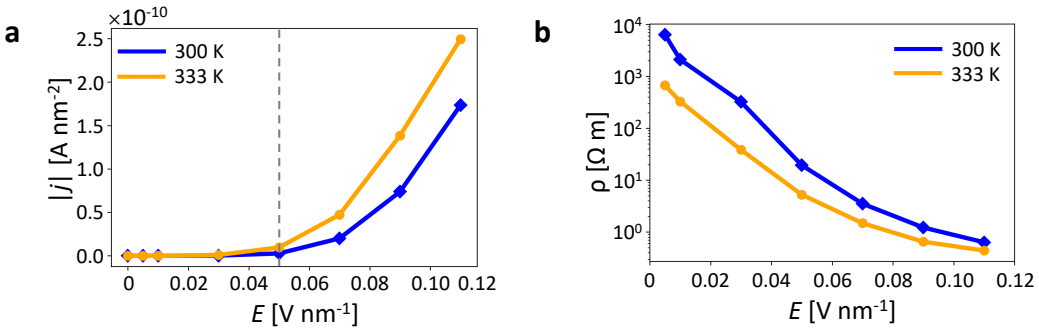

Fig. 5.6 Ionic conductivity of the colloidal crystal. **d** Current density j associated to the CIT diffusion along x as a function of T and E. As the E intensity overcomes a threshold value (vertical dashed line), the system switches from non-conductive to conductive regime. **e** Resistivity ρ associated to the CIT current, as a function of T and E. Figure adapted from Ref. 183 with permission of Creative Commons CC BY license.

These allow us to obtain insights into the macroscopic properties of the lattices. However, to gain a deeper understanding of the underlying mechanisms of the CIT conduction, it is essential to also observe the process at a microscopic level. Therefore, we aim to investigate the local phenomena controlling CIT diffusion, to determine if there are differences in the CIT motion or if some are more static than others. To this end, we employ a data-driven approach that has been recently applied to various supramolecular systems.[87, 251, 100] The SOAP analysis is performed to investigate the level of order or disorder in the ionic domains of the TMA-NPs FCC superlattice and the organization of the CIT ions within them. This is achieved by centering the SOAP vector [121, 253, 254] at the center of mass of each CIT ion in the lattice. The unsupervised clustering of the 428800 SOAP spectra (1072 SOAP spectra x 400 snapshots in every MD simulation), through the Probabilistic

Analysis of Molecular Motifs (PAMM) approach [125] allows for the examination of the high-dimensional information obtained from the SOAP analysis.

The PAMM analysis results identify three different clusters, represented by the colors red, blue and cyan in Figure 5.7b,c,g. The ions with the same color belong to the same cluster and are surrounded by a similar SOAP environment, while ions with different colors belong to different ionic environments. The blue color indicates the CIT ions at the interface between two TMA-NPs, the red color represents the CIT ions in the octahedral cavities in the FCC lattice, and the cyan color represents the ions in the tetrahedral cavities (as shown in Figure 5.7b,c,g). The high-dimensional SOAP data is reduced with Principal Component Analysis (PCA), allowing the visualization of the different environments. The first two Principal Components (PC) at $T = 300$ K and $T = 333$ K are shown in Figure 5.7d,h, where the three different colors represent the different SOAP-detected motifs identified by the PAMM analysis. It is important to note that the two CIT clusters occupying the tetrahedral and octahedral cavities are not in direct contact with each other, as they are separated by the CIT ions at the NP-NP interface.

At every time step considered, the motion of all CIT ions and the SOAP environment which they belong to, are detected using the SOAP analysis, enabling the reconstruction of dynamic complexity for each considered E and T. This analysis permits the calculation of the transition probability matrices (reported in Figure 5.7f,j) which define the average probability for a CIT ion to remain in its current SOAP environment (diagonal entries) or to pass through to another state (off-diagonal entries) in the time interval between two consecutive analyzed snapshots. Based on the calculated probabilities, it is possible to estimate the average transition rate for a CIT ion. For instance, the transition time of a CIT ion occupying octahedral cavities to the NP-NP interface environment at $T = 300$ K is approximately $\sim 0.002\,\mathrm{ns}^{-1}$, resulting in a transition timescale of $\sim 500\,\mathrm{ns}$. The numbers on the diagonal of the matrices reflect the stability of the clusters. In this study, the red cluster is the most dynamics, while the blue cluster is the most stable. CIT ions belonging to the blue cluster can be considered as the "glue" holding TMA-NPs self-assembled and also undergoing continuous ions exchange, as previously demonstrated in Ref. 100. Similar observations can be made for the system at $T = 333$ K (Figure 5.7j), where the internal dynamics are further enhanced. Finally, the transition matrices indicate that at $E = 0$, CIT ions cannot directly exchange between octahedral (red)

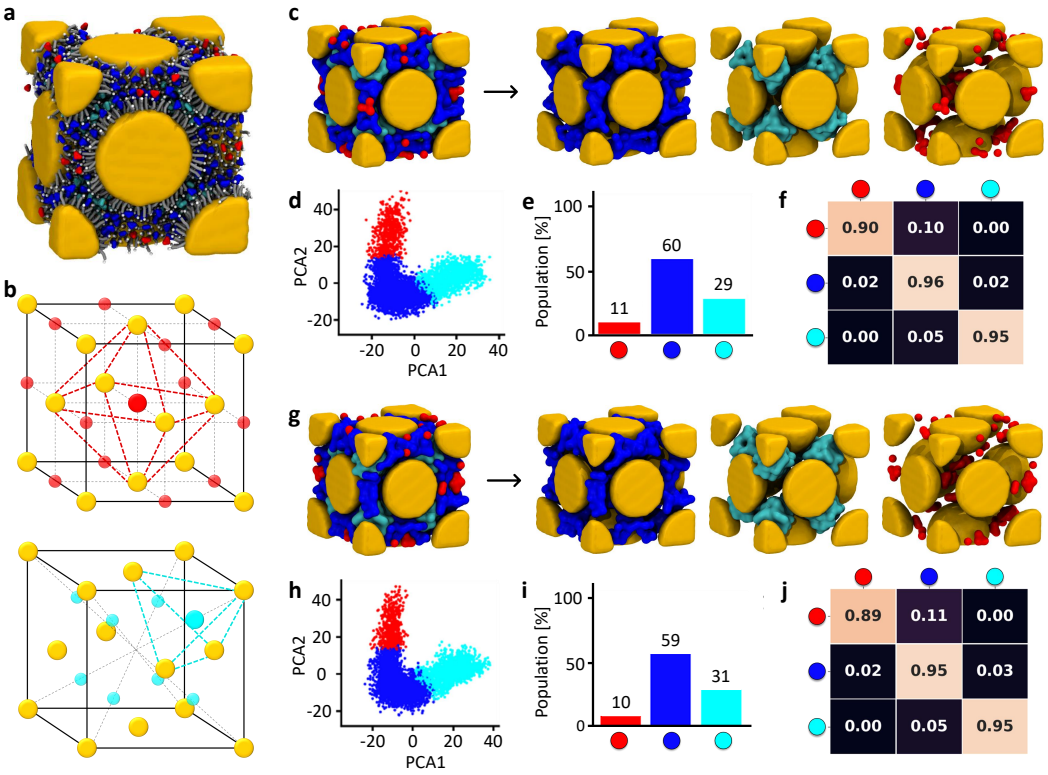

Fig. 5.7 Data-driven detection of dynamic ionic environments in the NP superlattice. **a** Snapshot of the superlattice system at $T = 300$ K and $E = 0$ (after 20 μs of MD simulation). Au NPs are colored yellow, TMA ligands in gray. CIT ions are colored (blue, red, or cyan) according to their detected SOAP state. **b** Cavities in the FCC superlattice: the octahedral cavities are identified in red (red dots: cavity centers, dashed red lines: cavity sides), the tetrahedral ones in cyan. **c-f** SOAP+PAMM analysis identifying the main CIT SOAP environments in the unperturbed systems ($E = 0$) at $T = 300$ K. **c** The SOAP+PAMM analysis detects three main CIT environments at $T = 300$ K: CIT ions at the NP-NP interface are colored in blue, and CIT ions in the tetrahedral cavities in cyan, CIT ions in the octahedral cavities in red. **d** Unsupervised clustering (PAMM) of the CIT SOAP data (PCA projection) allows identifying three main SOAP clusters, corresponding to the different CIT states/environments in the system. The clustering is performed on the first three PCs of the SOAP dataset; the projection on the first two PCs is shown. **e** Cluster population histogram. **f** Normalized transition probability matrix indicating the probabilities for a CIT in a given state to remain in that state (p_{ii}, diagonal entries) or to undergo a transition to another SOAP environment (p_{ij}, off-diagonal entries) in the time interval sampled during the analysis (in this case, d$t = 50$ ns). From the off-diagonal transition probabilities, one can also estimate the transition rates as $k_{ij} = p_{ij}/\mathrm{d}t$ and a characteristic transition timescale as $t_{ij} = k_{ij}^{-1}$. **g-j** SOAP+PAMM analysis for the unperturbed systems ($E = 0$) at $T = 333$ K. Figure reproduced from Ref. 183 with permission of Creative Commons CC BY license.

and tetrahedral (cyan) cavities, but can communicate indirectly *via* the more static interface domain (blue).

Subsequently, Figure 5.8 presents the results of simulations performed at $T = 300$ K. The final snapshots obtained from the MD simulations are shown in panels b and c under the absence and presence of high applied E, respectively. It is apparent that in the unperturbed state, the red and cyan clusters are separated within their respective cavities, while in the presence of high E, they appear to be rearranged. The quantitative data in the transition matrices (Figure 5.8d,e) supports this observation by illustrating two distinct regimes. On the one hand, for electric fields with intensities lower than $0.05\,\mathrm{V\,nm^{-1}}$, the systems exhibit similar behavior to the unperturbed case, suggesting that the electric field applied is not strong enough to activate the diffusion of CIT ions within the lattice. In this range, the supramolecular crystal displays non-conductive properties (Figure 5.6) and the probability of transition between red and cyan clusters is always zero, indicating that these two environments cannot directly exchange CIT ions. On the other hand, for electric fields with intensities equal or greater than $0.05\,\mathrm{V\,nm^{-1}}$, the dynamics of CIT ions in the lattice is enhanced, as indicated by a decrease in the diagonal probabilities and an increase in the off-diagonal ones. At 300 K for $E \geq 0.07\,\mathrm{V\,nm^{-1}}$, the blue cluster is the only SOAP state with a residence probability $\geq 50\%$, while the red and cyan clusters are purely transient states. This supports the assumption that the blue cluster plays a crucial role in maintaining the self-assembled configuration. The lattice was observed to become unstable and break apart with electric fields greater than $0.11\,\mathrm{V\,nm^{-1}}$. The population of the different clusters remains unchanged, with the CIT ions at the interface representing approximately 60% of the total population, the CIT ions in the tetrahedral representing approximately 30%, and the CIT ions in the octahedral cavities representing approximately 10% (see Figure 5.8).

The results demonstrate that the emergence of conductive properties in the lattice is related to the emergence of a direct dynamic communication between the clusters in the octahedral and tetrahedral cavities, as shown in the transition matrices that indicate an increase in the communication from 0 to $\sim 30\%$. This highlights the presence of ionic gates that enable the diffusion of CIT ions throughout the superionic lattice, giving the CIT ions in the cavities conductive properties. The CIT ions at the interface between the TMA-NPs play a crucial role in maintaining the integrity of the lattice. This phenomenon is similar to the differentiation of valence electrons and

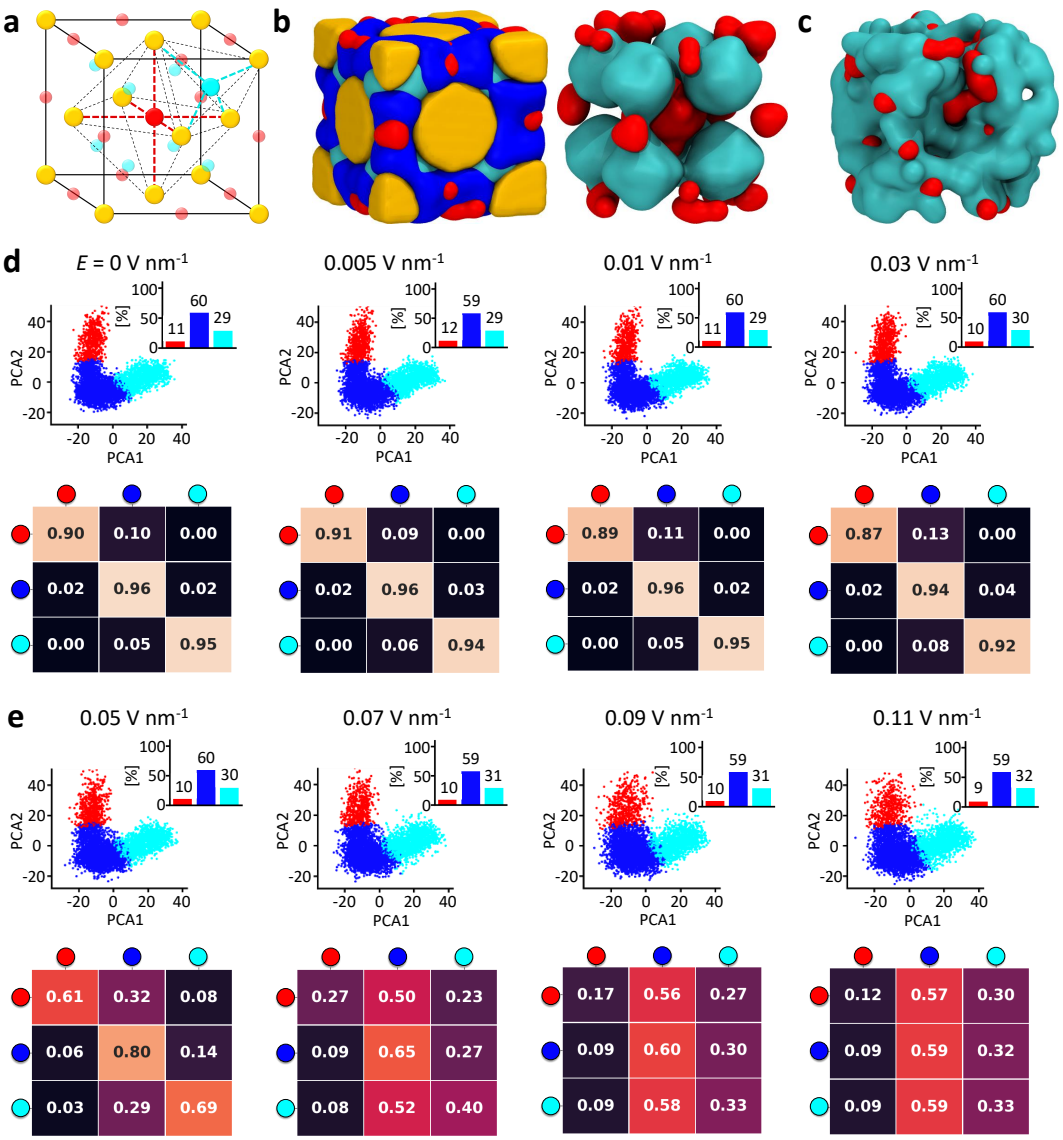

Fig. 5.8 Mechanism of ionic conduction in the NP superlattice at 300 K. **a** The octahedral and tetrahedral cavities in the FCC cell are indicated by red and cyan spheres, respectively. **b** TMA-NP superlattice: Au NP in yellow, TMA ligands not shown for clarity, CIT ions colored based on their SOAP state (left). Right: detail of the CIT ions in the tetrahedral (cyan) and octahedral (red) FCC cavities at $E = 0$. **c** Fusion between cyan and red CIT SOAP environments in the FCC lattice at $E = 0.11\,\mathrm{V\,nm^{-1}}$ (TMA-NPs and the blue cluster not shown for clarity). **d-e** Results of the SOAP+PAMM analysis of the superlattice simulation at $T = 300$ K for increasing intensities of E. SOAP clusters population histograms (top) and transition probability matrices (bottom) for all simulated cases. The analyses show how, at $T = 300$ K, and for $E < 0.05\,\mathrm{V\,nm^{-1}}$, all data are similar to the unperturbed case ($E = 0$), while for $E \geq 0.05\,\mathrm{V\,nm^{-1}}$ the CIT dynamics changes (supramolecular conduction). Figure reproduced from Ref. 183 with permission of Creative Commons CC BY license.

coordination sites in conductive materials (based on metal bonding), where some electrons are involved in forming the atomic bonds and others allow conductivity.

Our results demonstrate that such collective phenomena in NP superlattice cannot be explained by the properties of the individual CIT ions environments in the unperturbed systems, and are instead emergent behavior originating from the coordinated motions of ions in response to the applied stimulus (E). These findings highlight the importance of studying such complex molecular systems at high enough resolution to track the motion of individual ions and at a large enough scale to observe collective behaviors.[79]

Finally, the results from the SOAP and PAMM analyses at $T = 333$ K are presented in Figure 5.9. Overall, despite increased dynamics due to thermal vibrations, the mechanism behind the conductive properties is similar to that at $T = 300$ K. The snapshots in panels b and c show a similar arrangement of the CIT environments within the lattice, which retain a nearly constant population. The role of NP-NP interface ions in maintaining the stability of the structure is also evident. Furthermore, the emergence of conductive properties is accompanied by direct diffusion of CITs between the tetrahedral and octahedral cavities within the lattice. The only difference is that in this case, a weaker electric field of $0.03\,\mathrm{Vnm}^{-1}$ is required for CIT diffusion, suggesting that the breakage of intermolecular interactions is facilitated by thermal agitation. This is also opposite to the conduction of metals, where an increase in temperature hinders conduction.

5.4 Conclusion

The process of designing new controllable materials relies on the identification of analogies with existing, natural structures and the formulation of rules that can be applied at various length scales. In this regard, although superlattices may exhibit some analogies with atomic crystals, the differences in the driving forces utilized complicate the understanding of the similarities of their supramolecular properties with those of atomic crystals.

In this study, we proposed a computational approach to analyze the conductive behavior of supramolecular colloidal crystals composed of TMA-functionalized NPs (referred to as atom analogs) and CIT ions (referred to as electron analogs),

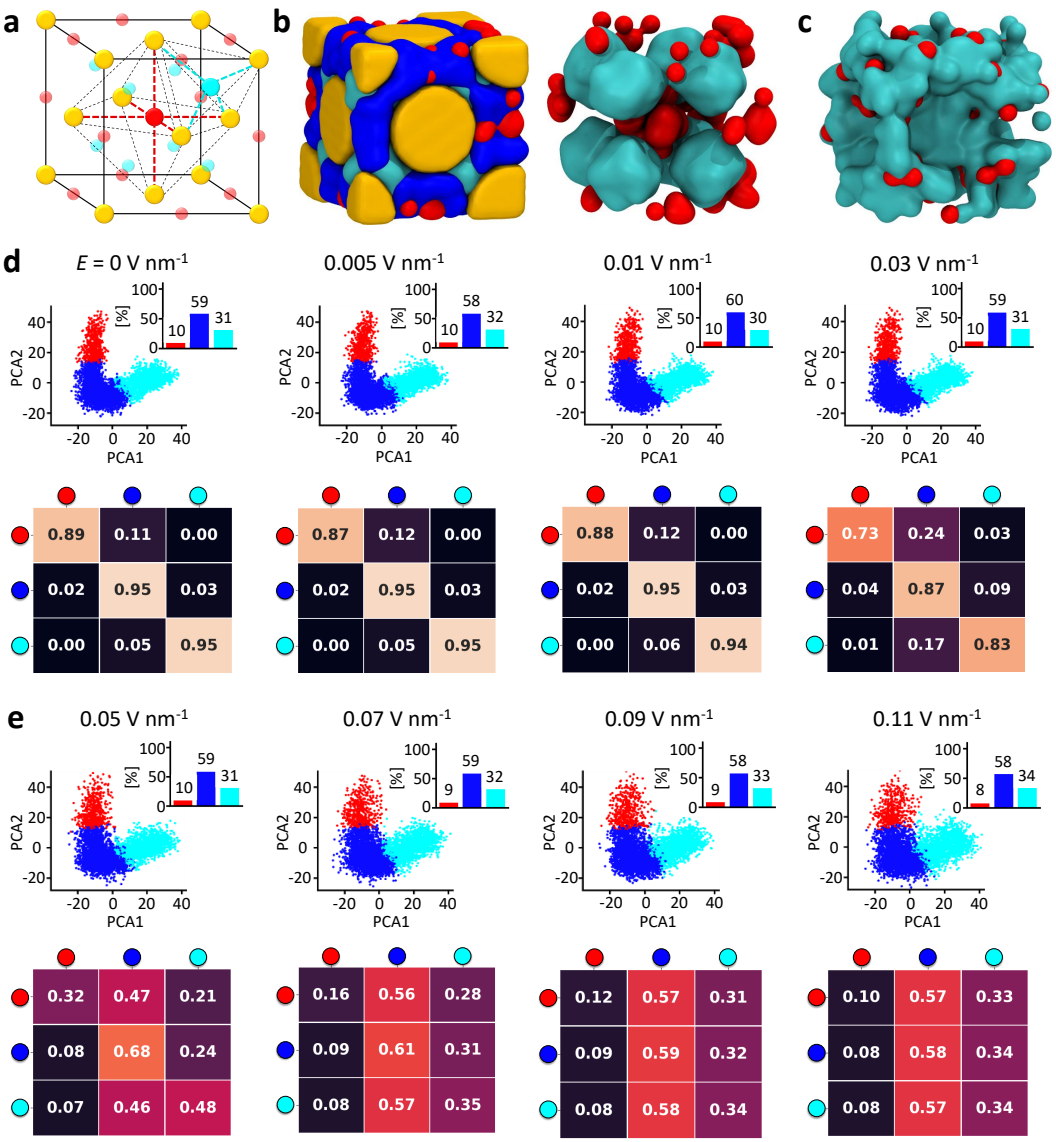

Fig. 5.9 Ionic conduction in the NP superlattice at 333 K. **a** The octahedral and tetrahedral cavities in the FCC cell (red and cyan spheres). **b** Left: TMA-NP superlattice (Au NP in yellow, TMA ligands not shown for clarity, CIT ions colored based on their SOAP state). Right: CIT ions in the tetrahedral (cyan) and octahedral (red) FCC cavities at $E = 0$ and $T = 333$ K. **c** Cyan and red CITs gating in the FCC lattice at $E = 0.11\,\mathrm{V\,nm^{-1}}$ (TMA-NPs and blue CITs not shown for clarity). **d-e** Results of the SOAP+PAMM analysis of the superlattice simulation at $T = 333$ K for increasing intensities of E. SOAP clusters population histograms (top) and transition probability matrices (bottom) for all simulated cases. The analyses show how, at $T = 333$ K, for $E < 0.03\,\mathrm{V\,nm^{-1}}$ all data are similar to the unperturbed case ($E = 0$), while for $E \geq 0.03\,\mathrm{V\,nm^{-1}}$ the CIT dynamics changes (supramolecular conduction). Figure reproduced from Ref. 183 with permission of Creative Commons CC BY license.

see Figures 5.2-5.3). The main difference with traditional conductive materials is that the current is carried by the CIT ions. Our aim was to establish an analogy between the motion of CIT ion within the lattice and the properties of conductors, semiconductors, and insulators. By utilizing CG molecular models, we were able to study the complexity of this system and gain insights into its behavior while preserving its physical features (Figures 5.2-5.3). Our results show that the lattice exhibits supramolecular semiconductive behavior, driven by the diffusion of the CIT ions under the influence of external electric fields (Figures 5.4-5.6). The *in silico* experiments demonstrate that a certain intensity of electric field is required to cross the energy "band gap" and activate the CITs diffusion (Figure 5.6a).

The machine-learning based approach proposed in this work identifies three distinct ionic environments in these NP superlattices, as shown in Figure 5.7. The CIT ions at the NP-NP interface are found to serve as bonding electron analogs, stabilizing the FCC lattice. On the other hand, CIT ions in the octahedral and tetrahedral cavities of the FCC lattice are found to be more dynamic and likely to act as electron analogs (Figures 5.8 and 5.9). The study of the system at the microscopic level reveals a correlation between the emergence of ionic conduction and the connection between the CIT ions in the octahedral and tetrahedral cavities.

Although here we used approximated molecular models and the results have thus a qualitative meaning, the MD simulations highlight that classical intermolecular interactions in colloidal supercrystals may produce complex emergent charge transport behaviors, similar to those typical of electronic materials. The method proposed herein allowed to gain a qualitative understanding of the ionic conductive properties such various colloidal superlattices. In this particular case, it led to the observation of a binary non-conductive/conductive behavior based on non-covalent interactions. This study also highlights the complexity of the supramolecular stimuli-responsive assemblies, and how the collective molecular behaviors resulting from such complexity can only be understood by studying the effect of the stimuli on large ensembles of interacting individual entities.

Chapter 6

Modeling temperature responsive assemblies

*The work described in this Chapter has been published in the following paper: "H. Liu, C. Lionello, J. Westley, A. Cardellini, U. Huynh, G. M. Pavan and S. Thayumanavan. Understanding functional group and assembly dynamics in temperature responsive systems leads to design principles for enzyme responsive assemblies. Nanoscale **2021**, 13, 11568-11575" [170] and has been adapted with permission from the Royal Society of Chemistry.*

Abstract

Thermo-responsive polymeric assemblies undergo phase transition (from complete miscibility to phase separation) in correspondence to the lower critical solution temperature (LCST). In order to investigate this phenomenon, herein, we examine the effects of temperature variations on self-assembled amphiphilic oligomers with molecular models and experimental observations. Molecular simulations prove that the dynamics of temperature-sensitive supramolecular assemblies is not only affected by the dehydration of oligoethylene glycol (OEG) motifs, but also by the thermally-promoted molecular motions. While both approaches detect a similar trend in the size variation of the assembly, as a consequence of the different temperatures applied.

6.1 Introduction

Thermo-responsive polymeric systems are widely investigated, as intermolecular interactions are particularly sensible to thermal stimuli.[52] There are two different types of thermo-responsive polymers (see Figure 1.9). The first type exhibits a lower critical solution temperature (LCST), rendering the polymers completely miscible in water when the temperature is below the LCST. The second type presents an upper critical solution temperature (UCST), resulting in complete miscibility in water when the temperature is above the UCST.[53] Therefore, the behavior of thermo-responsive polymers is dependent on the balance between polymer-polymer interactions and polymer-aqueous solution interactions.

Among polymeric assemblies that experience a phase change in correspondence to LCST [255–259], polymers composed of oligo- and poly-ethylene glycol, along with poly(N-alkylacrylamides) have been widely investigated due to their responsiveness at temperature above LCST, which results in the disruption of hydrogen bonds with water [260–264] and an increase in hydrophobicity [265, 266]. The temperature-induced phase change is always coupled to a sharp increase in hydrophobicity, connected with a change in the number of hydrogen bonds. However, recent studies have revealed that some oligoethyleneglycol (OEG) aggregates display a more subtle morphological transition at temperatures below the LCST, named sub-LCST transition, where the sizes of the assemblies significantly varies.[267] Unfortunately, the mechanism behind the sub-LCST behavior is still unclear and is dependent on both on the type of OEG-based amphiphiles and on the chain length.[268–270] The variations in temperature also have an impact on the internal dynamics of the assembly. While an increase in temperature should enhance the dynamics of the nanoassembly [271–273], the relationship is inverse in case of sub-LCST behavior where the increase in the hydrophobicity freeze the molecular assemblies at higher temperature.[267]

The purpose of this study was to comprehend the influence of temperature variations on amphiphilic assemblies when small hydrophobic patches were exposed on the hydrophilic surface of the assemblies, as depicted in Figure 6.1. In this regard, experimental observations were complemented by molecular dynamics simulations, providing an analysis of the effects of temperature on the structural dynamics of these complex, self-assembled systems.

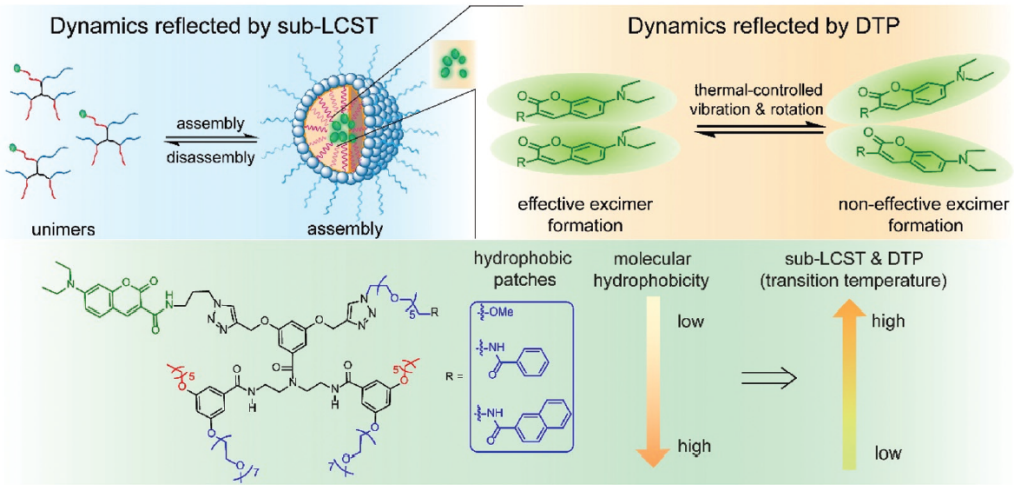

Fig. 6.1 Schematic presentation of the assembly dynamics reflected by sub-LCST and dynamic transition point (DTP) and their relationship with the molecular hydrophobicity. Due to their amphiphilic nature, the oligomers presented herein tend to aggregate into excimer configurations in water. Figure reproduced from Ref. 170 with permission from the Royal Society of Chemistry.

6.1.1 Experimental context

In this study, the focus is on thermo-responsive oligomers, which are low molecular weight polymer analogs with a limited number of repeating units, whose physical properties are dependent on the length of the chain.[274] The considered amphiphilic oligomers containing 7-diethylaminocoumarin are synthesized through a multistep procedure in which the intermediates are isolated and purified prior to proceed with the next step [274]. The first synthesized amphiphilic oligomer is EG7-C6-Ph (Figure 6.2), whose amphiphilicity is modulated by functionalizing it with hydrophilic and hydrophobic chains. The EG7-C6-Ph oligomer has a diethylenetriamine backbone, where the terminal amino moieties are substituted with amphiphilic benzamides, and the hydrophobic parts are based on hexyl (C6), while the hydrophilic parts are based on heptaethylene glycol (EG7). The hydrophobic side of the molecule, which contains both the 7-diethylaminocoumarin fluorophore moiety and a phenyl group (Ph), is functionalized with an amphiphilic benzamide.

To study the effects of changes in hydrophobicity, the Ph group is then substituted with various small hydrophobic patches, and the other case studies are shown in Figure 6.2. The final oligomer is synthesized by adding the amphiphilic block to the

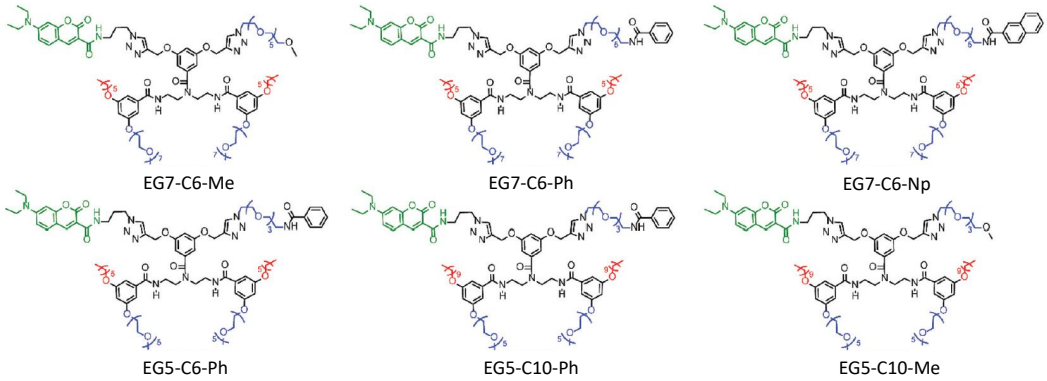

Fig. 6.2 Structures of amphiphilic oligomers investigated in this study. Figure adapted from Ref. 170 with permission from the Royal Society of Chemistry.

diethylenetriamine core, and labeling it with the coumarin moiety through a click chemistry reaction.

Experimentally, the temperature-dependent behavior of the assemblies is studied by observing variations in the fluorescence signal. The amphiphilic assemblies exhibit two fluorescence emission peaks with maxima at 479 nm and 536 nm, which correspond to the fluorescence of aminocoumarin when it is in monomer and excimer conformation, respectively (as shown in Figures 6.1 and 6.3a). The total fluorescence intensity of both peaks decreases with the increase of the temperature due to the rise in nonradiative decay. Of particular interest is the observation of the ratio between the monomer (I_M) and excimer (I_E) radiation, which exhibits two distinct trends based on the temperature applied (as depicted in Figure 6.3b). Specifically, the I_M/I_E ratio decreases from T = 5 to T = 30 °C and increases from T = 30 to T = 65 °C. Since the excimer emission is an indication of the proximity of two fluorophore moieties within the nanoassembly, a decrease in the I_M/I_E ratio signifies the presence of a tighter assembly. The decrease in the I_M/I_E ratio between 5 and 30 °C is a result of the increase in the hydrophobic behavior of the oligomers due to the disruption of hydrogen bonds within the OEG moieties and water, leading to a more compact assemblies and higher excimer formation. On the other hand, between 30 and 65 °C, the increase in temperature promotes the molecular motion, resulting in more dynamic assemblies, less excimer formation, and a gradual increase in the I_M/I_E ratio. This is confirmed by the variations in the dimension of the assemblies shown in Figure 6.3c.

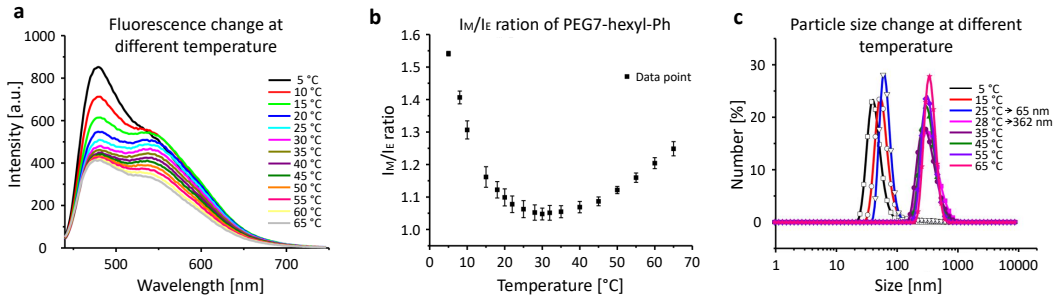

Fig. 6.3 Experimental characterization of EG7-C6-Ph-constituted assemblies: **a** fluorescence of the assemblies at different temperature. **b** I_M/I_E ratio versus temperature. **c** Particle sizes at different temperature. Figure adapted from Ref. 170 with permission from the Royal Society of Chemistry.

However, the resolution that is possible to reach experimentally techniques does not allow obtaining molecular-level insights into the responsive behavior. Molecular simulations may be useful to this end. The utilization of molecular models enables tracking of interactions between the aggregate and water, allowing quantification of variations in the hydrophobicity of the building blocks. Coarse-grained (CG) models described by the MARTINI force field are characterized by a resolution 5 $\dot{A}$, which permits the observation of self-assembly processes and interaction with water molecules. The simulations of these CG models require a high computational cost. Thus, as a proof of concept, our study focused on the investigation of the excimer based on EG7-C6-Ph monomers at three different temperatures: the LCST, one below the LCST, and one above the LCST.

6.2 Materials and methods

All-Atoms Molecular Dynamics (AA-MD) protocol

The all atom (AA) models of each oligomer were realized in Avogadro [152], and the simulations in water were performed with Gromacs 2018.6 software [151]. The system was firstly subjected to minimization, followed by 100 ps thermalization simulation in the NVT ensemble at a temperature of 300 K using the V-resale algorithm [179]. The thermalization was followed by a 100 ps NPT equilibration to reach a pressure of 1 bar through the Berendsen barostat method [181]. Lastly, a longer production of 100 ns was carried out in NPT conditions, utilizing the Nose-

Hoover thermostat [180] and the Parrinello-Rahman barostat [175] to maintain the temperature and pressure at 300 K and 1 bar, respectively. All simulations were carried out with a time step of 2 fs, the standard time step for AA simulations.

Coarse-Grained Molecular Dynamics (CG-MD) protocol

The coarse-grained (CG) models, which were based on the MARTINI force field [105], were derived from the previously obtained AA trajectories and parametrized using the Swarm-CG software [85] (as shown in Figure 6.4). A preliminary aggregate

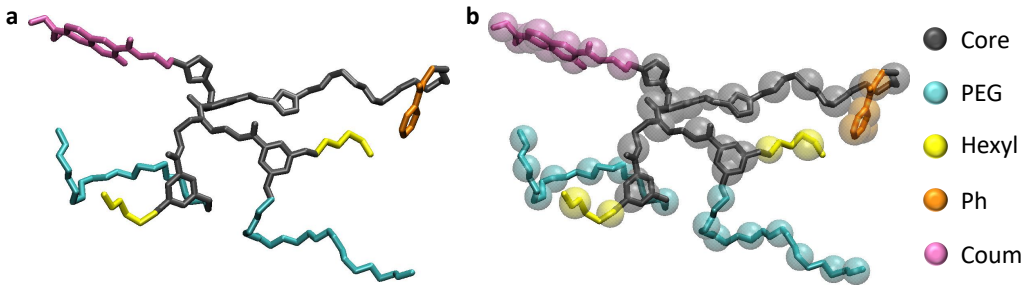

Fig. 6.4 **a** All-atom (AA) and **b** coarse-grained (CG) molecular models of EG7-C6-Ph. Figure adapted from Ref. 170 with permission from the Royal Society of Chemistry.

was generated with a simulation in vacuum at 303 K, where 50 monomers were randomly placed in a 100 nm^3 simulation box (as shown in Figure 6.5), with periodic boundary conditions in all the three dimensions. This aggregate was then placed in a simulation box filled with explicit water molecules described by the MARTINI force field, and the entire system was equilibrated in water at 303 K. After the equilibration, simulations were run at 283 K, 303 K, and 333 K. It is worth noting that for the system at 283 K, 10% of the water beads were replaced with anti-freezing MARTINI water particles to prevent water freezing. The CG MD simulations were conducted at 1 atm using the V-rescale thermostat [179] and Berendsen barostat [181] with isotropic pressure scaling, with a compressibility of $4.5 * 10^{-5}$ MPa^{-1} and coupling time constants of 1 ps and 2 ps for the V-rescale and Berendsen coupling schemes, respectively. For the CG-MD simulations in water, the electrostatic and van der Waals cutoff were fixed at 1.1 nm. All the GC-MD simulations were run in Gromacs [151].

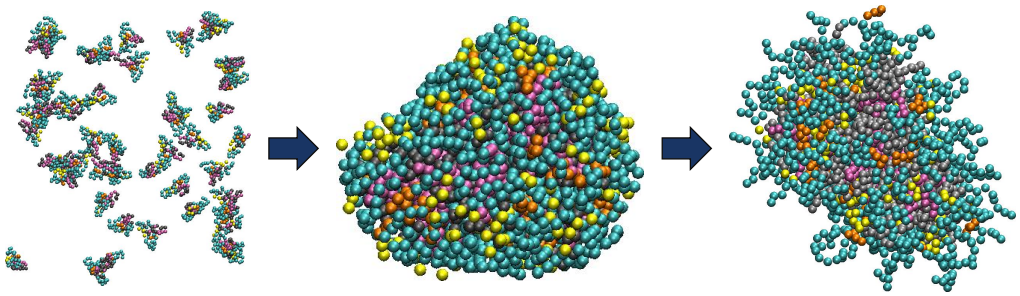

Fig. 6.5 CG-MD snapshots of 50 EG7-C6-Ph monomers (most left side) and the corresponding self-assembly in water (most right side). Figure reproduced from Ref. 170 with permission from the Royal Society of Chemistry.

6.3 Results and discussion

To study the effects of the variations of temperature on the oligomer-based assemblies at the macroscopic level, we developed all-atom (AA) and coarse-grained (CG) models of the amphiphilic oligomer of Figure 6.4. The CG model was parametrized according to the MARTINI force field [105] and optimized for the best agreement with the AA model using the Swarm-CG software [85]. Initially, we placed 50 amphiphilic monomers in a simulation box in vacuum to obtain a preliminary assembly (Figure 6.5, center), that, once simulated in water, rearranged the hydrophilic and hydrophobic chains properly (Figure 6.5, right). In particular, as depicted in Figure 6.6, the hydrophilic OEG chains (PEG) were directly exposed to the solvent, while the more hydrophobic groups of the oligomers were contained in the central part of the aggregate. Subsequently, we carried out molecular dynamics (MD) simulations at 10 °C, 30 °C, and 60 °C of the EG7-C6-Ph assembly in explicit solvent, using the Gromacs software [151].

The radius of gyration (R) has been calculated from the MD trajectories, and used as a metric to indicate the variations in the structure and compactness of assemblies and their subgroups under different temperatures (as reported in Figure 6.7). We specifically calculate the R values of the global assemblies (R_a), as well as the hexyl (R_{hexyl}), coumarin (R_{Coum}), and PEG (R_{PEG}) groups of the oligomers. In Figure 6.7a, the ratio of R for the various groups and the entire assembly is reported in order to gain insights into the arrangement of the assembled structures. A ratio of R/R_a higher than 1 suggests that the groups are situated on the surface of the assembly and thus

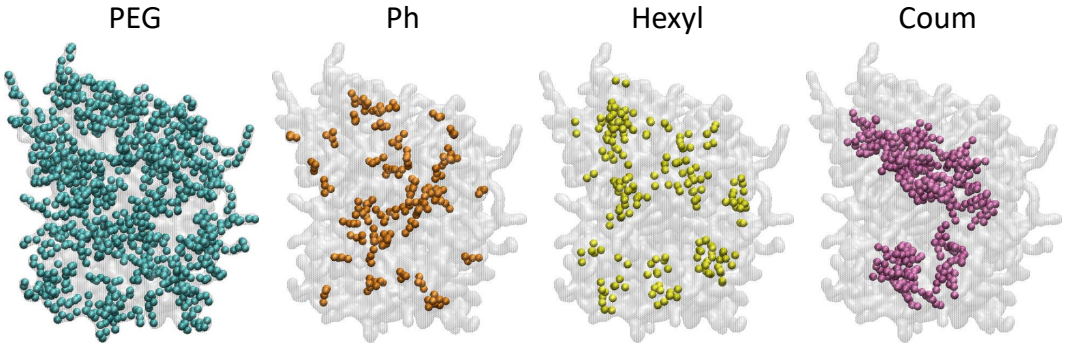

Fig. 6.6 CG-MD snapshot of the self-assembled EG7-C6-Ph monomers where the CG beads of the PEG, R3 (Ph), hexyl, and Coumarin groups are colored in cyan, orange, yellow, and purple, respectively. As expected, the hydrophilic chains (PEG) are directly exposed to the solvent, while the more hydrophobic branches (Ph, Hexyl, and Coum) are oriented toward the interior of the excimer. Figure adapted from Ref. 170 with permission from the Royal Society of Chemistry.

exposed to the solvent, while a ratio of R/R_a lower than 1 indicates that the groups are embedded in the interior of the assembly. Consequently, tracking the R/R_a ratio at different temperatures enables the detection of structural rearrangements resulting from variations in temperature. The ratios R_{hexyl}/R_a and R_{Coum}/R_a, which are both lower than 1, demonstrate the hydrophobic nature of these groups by occupying the inner region of the assembly and avoiding the interactions with water. Alternatively, the value of R_{PEG}/R_a higher than 1 confirms the hydrophilic nature of PEG chains and their arrangement on the exterior of the aggregate. On the other hand, Figure 6.7b displays the R_a values of the assemblies simulated at the three different temperatures. It can be seen that the gyration radius of the assembly at 30 °C is lower than at 10 °C and 60 °C, a trend which is consistent with the fluorescence results depicted in Figure 6.3b and the hypotheses of PEG dehydration and thermally-promoted molecular motion. Therefore, the decrease in the gyration radius at 30 °C is directly linked to the breakage of the hydrogen bonds within water, resulting in a more hydrophobic and compact assembly. At the same time, the increase in R_a at higher temperature is driven by the increase in the thermal vibrations.

Subsequently, we calculated the number of interactions between the CG-beads representing the PEG chains and water, as depicted in Figure 6.8b. At T = 10 °C the number of PEG-water interactions is higher than at the other two temperatures, thereby highlighting the hydrophilic properties of PEG at lower temperature. Simul-

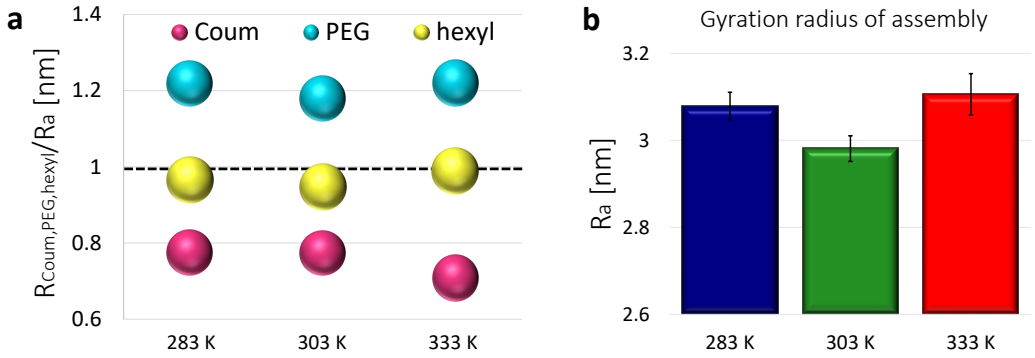

Fig. 6.7 CG-MD snapshot of the self-assembled EG7-C6-Ph monomers where the CG beads of the PEG, R3 (Ph), hexyl, and Coumarin groups are colored in cyan, orange, yellow, and purple, respectively. Figure adapted from Ref. 170 with permission from the Royal Society of Chemistry.

taneously, both the decrease in the PEG-PEG contact reported in Figure 6.8a and the increase in interactions between the hydrophobic chains in the oligomer and the water molecules (as shown in Figure 6.8c) indicate the swelling of the assemblies at T = 60 °C. An increase in the temperature from 30 °C to 60 °C results in a higher probability of water molecules penetrating the assembly due to the thermal-induced motion of the oligomer. As a consequence, the coumarin groups are more in contact with water molecules, as shown in Figure 6.8e. In fact, at T = 60 °C, the coumarin groups are arranged in a more compact manner in order to reduce interactions with water beads, as also evidenced by the reduction in the R_{Coum}/R_a ratio in Figure 6.7a.

6.4 Conclusion

Thermo-responsive polymers are widely investigated for their abilities to undergo conformational or phase change in correspondence to the lower critical solution temperature (LCST). One example is the behavior of poly-ethylene glycol based aggregates below the LCST, which become more hydrophobic at high temperature and exhibit changes in size.

In this work, we investigated the behavior of EG7-C6-Ph assemblies both with computational and experimental methods, by varying temperatures. In particular, molecular dynamics simulations, and especially coarse-grained molecular models, are employed to study both the variations in size and hydrophobicity. The calcula-

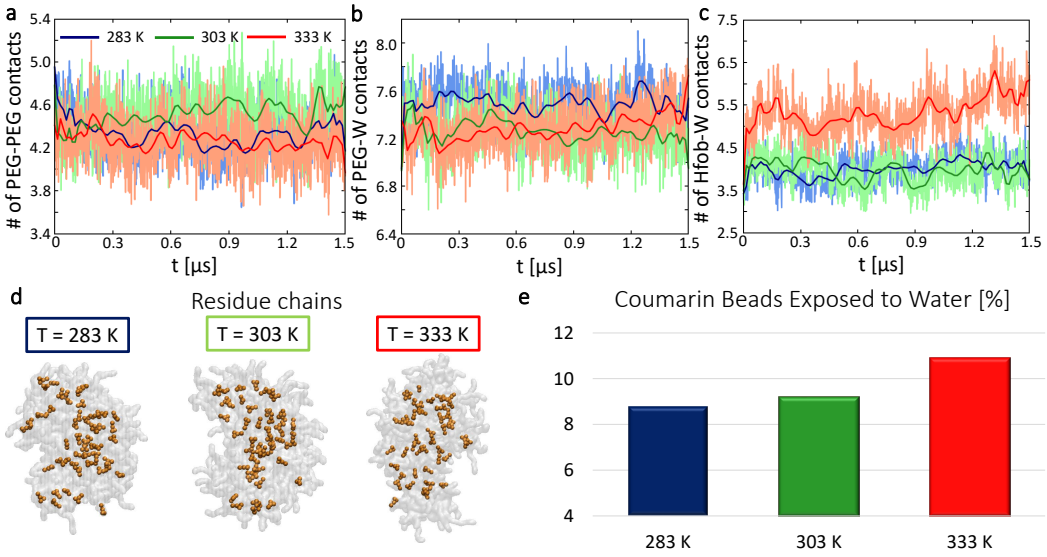

Fig. 6.8 Number of contacts between **a** PEG-PEG beads, **b** PEG and water, **c** hydrophobic groups and water for EG7-C6-Ph, calculated from the equilibrated trajectories. From 283 K to 303 K there is a slight increase in the number of PEG-PEG contacts and decrease in PEG-water contacts. This indicates that the 283 K assembly is more hydrated and hydrophilic than the 303 K assembly. From 303 K to 333 K there is a decrease in the number of PEG-PEG contacts because the structure vibrates more, and, therefore, it is less tightly packed, while there is no significant difference in the number of PEG-water contacts. The increase of hfob-water contacts and decrease of PEG-PEG contact from 303 K to 333 K indicate the swelling of assemblies. **d** CG-MD snapshots of assembly at 283 K, 303 K, and 333 K. The residual beads modelling the phenyl groups are highlighted in orange. **e** Percentage of coumarin beads exposed to water over the total number of NP assembly beads. The enhancement of temperature leads to a higher water penetration inside the NP core, thereby increasing the percentage of coumarin surface accessible to the solvent. Figure reproduced from Ref. 170 with permission from the Royal Society of Chemistry.

tions of the gyration radius show the trend of size changes, and highlight a decrease in interactions between the hydrophilic chains of the oligomers and water molecules, leading to increased hydrophobicity of the nanoassembly above the LCST. Furthermore, the swelling of the aggregates is observed at higher temperatures, indicated by the increase in both size and number of water molecules penetrating the assembly. At the same time, experimental evidences have detected the size transition by analyzing the fluorescence spectrum of the aminocoumarin chain in both monomer and excimer conformation, confirming the hypotheses of variations in the hydrophobicity of the aggregates.

In conclusion, the use of molecular models provide valuable insights into the interactions between the oligomers and water, which is essential for understanding the thermo-responsiveness of poly-ethylene glycol based aggregates.

Chapter 7

Modeling microtubule-based GTP-responsive nanocapsules

The work described in this chapter has been published in the following paper: "N. Uchida, A. Kohata, K. Okuro, A. Cardellini, C. Lionello, E. A. Zizzi, M. A. Deriu, G. M. Pavan, M. Tomishige, T. Hikima and T. Aida. Reconstitution of microtubule into GTP-responsive nanocapsules. Nature Commun. ***2022****, 13, 5424" [275], and has been adapted with permission of Creative Commons CC BY license.*

Abstract

With the purpose of developing drug nanocarriers, the utilization of nanocapsules that can disassemble in response to guanosine triphosphate (GTP) can be a solution to efficiently treat diseases caused by cancer and RNA viruses. GTP is, in fact, present at high levels in such diseased tissues. Here, I discuss modeling results that have been obtained in the context of a comprehensive study on the rearrangement of microtubules into a nanocapsule that selectively responds to GTP. When the tubulin monomer from microtubule is incubated at 37 °C with a mixture of GTP and nonhydrolysable GTP*, a tubulin nanosheet forms. Upon the addition of photoreactive molecular glue to the resulting dispersion, the nanosheet is transformed into a nanocapsule. Computational simulations allowed to obtain results useful to complement the experiments, allowing to gain insights into the effects of interactions between the glue molecules and tubulin-based assemblies.

7.1 Introduction

The selection of the most suitable building blocks for the realization of drug delivery carriers is crucial to ensure that the carrier disassembles in response to endogenous receptors overexpressed in diseases cells.[276–284] Adenosine triphosphate (ATP) has been considered as a potential option as endogenous receptor due to its high presence in cancer tissues [278–282, 285], however, its high concentration in healthy cells (>1 mM [286]) makes it challenging to control the release of ATP-based delivery systems. An alternative option is the use of guanosine triphosphate (GTP), which plays a fundamental role in various biological processes [287–300], such as cell division [287], nucleotide synthesis [288], and cell signaling [289]. GTP is extensively consumed in cell division processes as tubulin heterodimer (THD), and the assembled configuration (microtubule, MT), utilizes it as energy source to continuously polymerize and depolymerize.[290–295] Alternatively, GTP is also involved in the replication of RNA viruses [301–304], as coronaviruses. GTP is therefore present in certain diseased cells (1.5-4.5 mM [305]), i.e. in rapid proliferating cancer cells [306], and in RNA virus-infected cells [307], while in healthy cells, the concentration of GTP is instead negligible, minor than 0.3 mM [308]. In this regard, the development of GTP-responsive devices may help in treatment of diseases caused by cancer and RNA viruses. This case study focuses on the development of a nanocapsule ($^{CL}\mathrm{NC}_{GTP/GTP*}$ shown in Figure 7.1c), that responds to GTP.

The nanocapsule realized herein consists of tubulin heterodimer (THD), which are composed of α-tubulin, colored green in Figure 7.1a, and β-tubulin, colored cream. Both the components are capable of binding to GTP. When the α-tubulin unit is bound to GTP, it cannot be hydrolyzed or substitute with other nucleoside phosphates. On the other hand, when GTP is attached to the β-tubulin unit, it can be hydrolyzed into GDP. As a consequence, in this study, the GTP units are replaced with GTP*, a nonhydrolysable GTP analogue (guanylyl 5'-α,β-methylenediphosphonate), resulting in the formation of THD_{GTP*}. Both THD_{GTP} and $THD_{GTP}{}^{*}$ self-assemble at 37 °C into microtubules MT_{GTP} and $MT_{GTP}{}^{*}$, respectively (as shown in Figure 7.1b).[309, 310] The depolymerization of MT_{GTP} results in the formation of THD_{GDP}, while, since GTP* is non-hydrolyzable, $\mathrm{MT}_{GTP}{}^{*}$ does not depolymerize into $THD_{GDP}{}^{*}$.

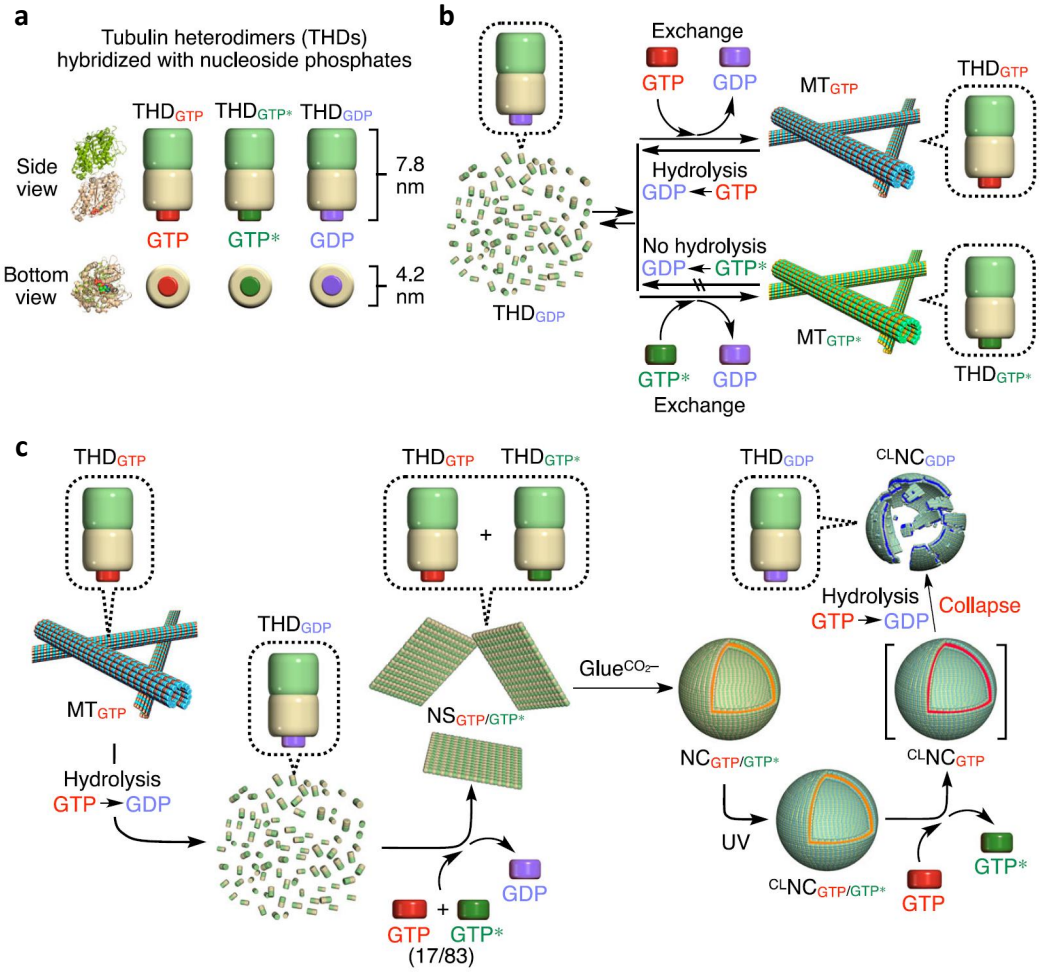

Fig. 7.1 Strategy used to prepare THD-based GTP-responsive ${}^{CL}NC_{GTP/GTP*}$. **a** Schematic illustrations of tubulin heterodimers (THDs) hybridized with GTP (THD_{GTP}), its non hydrolysable analogue GTP* (THD_{GTP*}), and GDP (THD_{GDP}) at its β-tubulin unit. **b** Schematic illustration of two self-assembling modes of THD into microtubules (MTs). MT_{GTP} depolymerizes into THD_{GDP} upon GTP hydrolysis. THD_{GDP} rehybridizes with GTP after a GTP treatment, facilitating the formation of MT_{GTP}. In contrast, MT_{GTP*} does not undergo depolymerization. **c** Schematic illustration of the multistep procedure for the synthesis of cross-linked nanocapsules (${}^{CL}NC_{GTP}$/GTP*) from MT_{GTP}. MT_{GTP} is depolymerized into THD_{GDP}, which is incubated with a mixture of GTP* (83mol%) and GTP (17mol%) to form nanosheet NC_{GTP}/GTP*. Upon treatment with $Glue^{CO_2-}$, $NS_{GTP/GTP*}$ is transformed into spherical nanocapsules ($NC_{GTP/GTP*}$), which are further exposed to UV light, affording ${}^{CL}NC_{GTP}$/GTP*. Upon the addition of GTP, ${}^{CL}NC_{GTP}$/GTP* collapses through the conformational change of the THD units induced by GTP hydrolysis. Figure adapted from Ref. 275 with permission of Creative Commons CC BY license.

The combination of a specific molar ratio of THD_{GTP}/THD_{GTP*} results in the formation of leaf-like two-dimensional nanosheets (NS) instead of MT, as depicted in Figure 7.1c. Furthermore, the presence of glue molecules [311–313] causes the NS to rearrange into a spherical nanocapsule, referred to as $^{CL}NC_{GTP/GTP^*}$ (Figure 7.1c), which can contains, for example, an anticancer drug. In this work, we study the formation of $^{CL}NC_{GTP/GTP^*}$ in the presence of $Glue^{CO_2-}$ at both at the microscopic and molecular resolution through the combination of experimental and computational approaches.

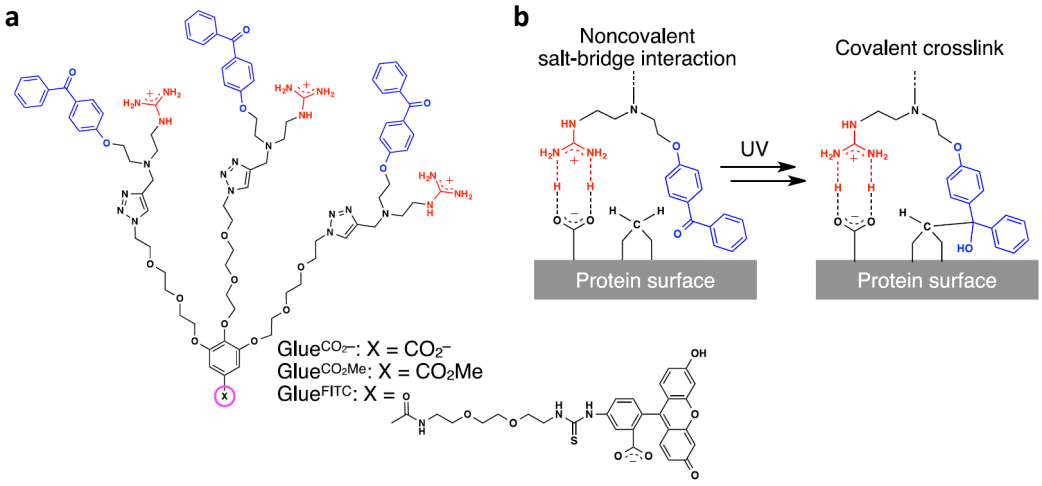

Fig. 7.2 Representation of the glue molecules utilized to stabilize the $^{CL}NC_{GTP/GTP*}$. **a** Molecular structures of photoreactive molecular glues ($Glue^{CO_2-}$, $Glue^{CO2-Me}$, and $Glue^{FITC}$) bearing three guanidinium ions (Gu^+) and benzophenone (BP) groups at their periphery and CO_{2-}, CO_2 Me, and FITC groups at the focal core. **b** The molecular glue covalently binds to the protein surface at its photoexcited BP groups after the noncovalent adhesion via a Gu^+/oxyanion multivalent salt-bridge interaction. Figure adapted from Ref. 275 with permission of Creative Commons CC BY license.

7.1.1 Experimental context

Experimentally, the procedure for synthesizing $NC_{GTP/GTP*}$ from MT_{GTP} is shown in Figure 7.1c, with a specific example provided in Figure 7.3a. The first step consists in the cooling of the 1,4-piperazinediethanesulfonic acid (PIPES) buffer (pH 6.8) solution of MT_{GTP} (5.8 mg ml^{-1}, shown in Figure 7.3c) at 4 °C for 3 h to achieve complete depolymerization into THD_{GDP}, as depicted in Figure 7.3d. The resulting monodisperse feature of THD_{GDP} is confirmed by the dynamic light scattering (DLS)

analysis displayed in Figure 7.3b, blue line. Subsequently, the THD_{GDP} solution 0.3 mg ml^{-1} is added to a PIPES buffer solution containing 17 mol% GTP and 83 mol% GTP* (300 μM in total) at 37 °C for 30 minutes. During this step, THD_{GDP} is transformed into THD_{GTP} and THD_{GTP*} through the conversion GDP → GTP and GDP → GTP*, which aggregate into 5 nm thick $NS_{GTP/GTP*}$, as reported in Figures 7.3e,f. It is important to note that the concentration of GTP* must be controlled to obtain $NS_{GTP/GTP*}$, as in case of GTP and GTP* mixtures containing up to 70 mol% of GTP*, the THD has low probability to self assemble. On the other hand, if the content of GTP* is above 85 mol%, the THD self-assembles mainly into MT rather than NS. The optimal THD_{GTP}/THD_{GTP*} molar ratio to obtain NS is therefore in the range of 70-85 mol%. By utilizing the 83 mol% of THD_{GTP*}, nuclear magnetic resonance (NMR) spectroscopy in DMSO reveals the presence of 65 mol% of THD_{GTP*} in the $NS_{GTP/GTP*}$ obtained. Finally, $NS_{GTP/GTP*}$ is incubated in PIPES buffer containing $Glue^{CO_2-}$ for 30 min at 37 °C to produce the $NC_{GTP/GTP*}$ shown in Figure 7.3g. The transformation from NS to NC is evidenced by the increase in hydrodynamic diameter from 56 nm to 660 nm, shown in green and orange in Figure 7.3b. Additionally, the transmission electron microscopy (TEM) demonstrates that the $NC_{GTP/GTP*}$ is effectively a hollow sphere (Figure 7.3g).

However, $NC_{GTP/GTP*}$ are unstable in albumin or serum in buffer, indicating that the assembly is not stable enough to be utilized as a drug delivery carrier. The use of $Glue^{CO_2-}$, which contains multiple benzophenone (BP) groups, is crucial to bind and stabilize the structure. BP groups, under photoexcitation, form covalent bonds with the adhering proteins (Figure 7.2b). Fluorescent analysis demonstrates the photoreactivity of $Glue^{CO_2-}$ with the $NC_{GTP/GTP*}$ assembling units. To test the stability of the NC in the presence of $Glue^{CO_2-}$, $NC_{GTP/GTP*}$ in a PIPES buffer solution is exposed to UV light for two minutes. Both TEM (Figure 7.3h) and DLS profiles (Figure 7.3b) show that the cross-linked (CL) $^{CL}NC_{GTP/GTP*}$ maintains the spherical shape and remains intact even after the incubation in albumin or serum, demonstrating the crucial role of the $Glue^{CO_2-}$ in stabilizing the capsule. However, the exact location of the $Glue^{CO_2-}$ molecules on the $^{CL}NC_{GTP/GTP*}$ is not clear. To gain insights into this interaction, we perform all-atom molecular dynamics simulations.

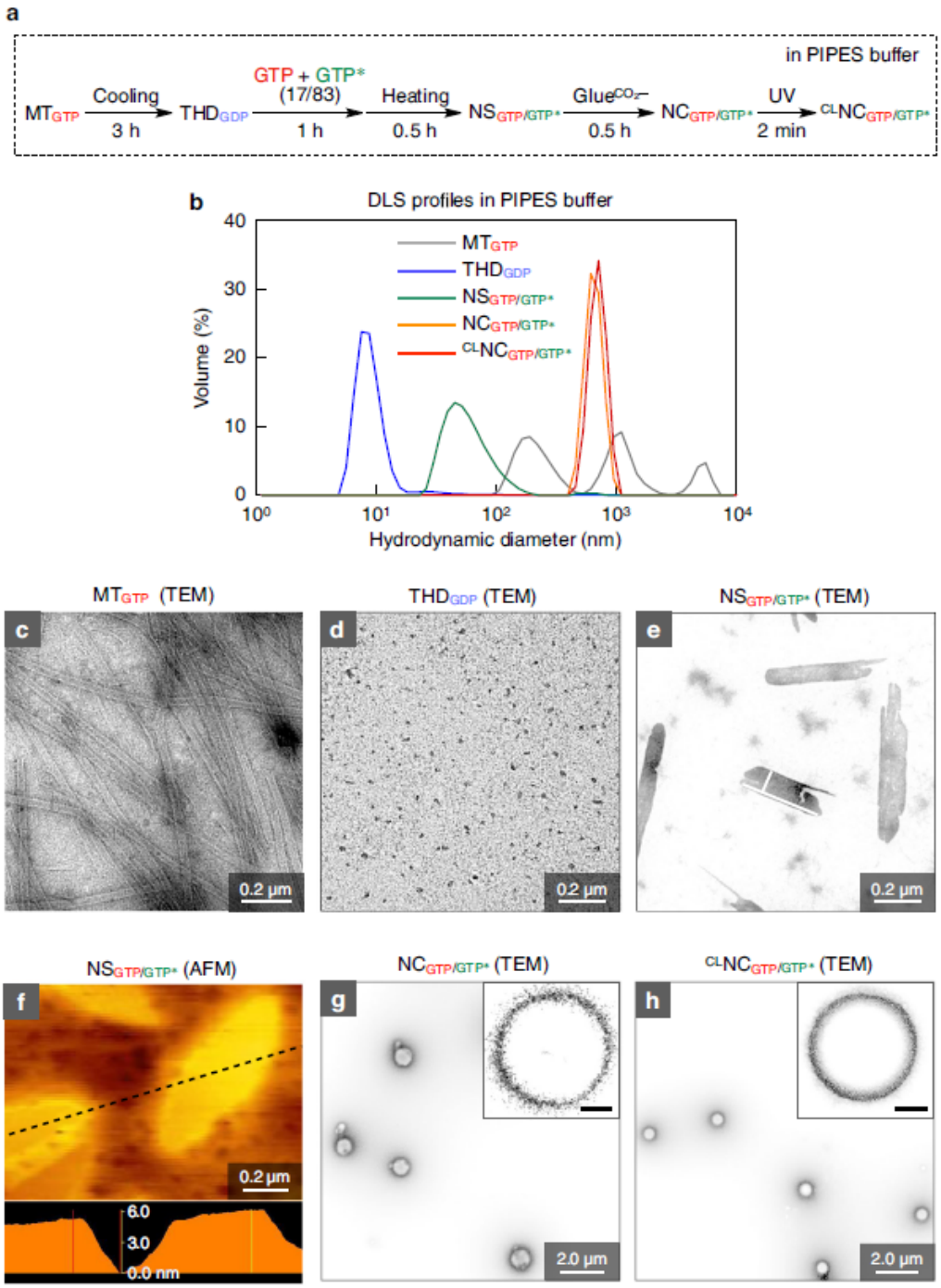

Fig. 7.3 Reconstitution of MT into $^{CL}NC_{GTP/GTP*}$. **a** A typical procedure for the preparation of $^{CL}NC_{GTP/GTP*}$. **b** DLS profiles of MT_{GTP} (gray), THD_{GDP} (blue), $NS_{GTP/GTP*}$ (green), $NC_{GTP/GTP*}$ (orange), and $^{CL}NC_{GTP/GTP*}$ (red) in PIPES buffer. **c–e** TEM images of MT_{GTP} (5.8 mg ml^{-1}; c), THD_{GDP} (0.3 mg ml^{-1}; d), and $NS_{GTP/GTP*}$ (0.3 mg ml^{-1}; e). **f** AFM image of $NS_{GTP/GTP*}$ (0.3 mg ml^{-1}) and its height profile. **g,h** TEM images of $NC_{GTP/GTP*}$ (13 μg ml^{-1}; g) and $^{CL}NC_{GTP/GTP*}$ (13 μg ml^{-1}; h). All TEM samples were negatively stained with uranyl acetate. Inset scale bars, 250nm. Figure reproduced from Ref. 275 with permission of Creative Commons CC BY license.

7.2 Material and methods

We have carried out molecular dynamics (MD) simulations to investigate the role of Glue$^{CO_2-}$ molecules while self-assembling to the THD$_{GTP*}$. All the MD simulations were performed using AmberTools [153], Gromacs software [151], and Visual molecular Dynamics (VMD) package.

Equilibration of Glue$^{CO_2-}$ in aqueous solution

The all-atom molecular model of Glue$^{CO_2-}$ was created in Avogadro [152] and parametrized using the general Amber force field (GAFF) [314]. The molecule was positioned in a simulation box filled with explicit TIP3P water molecules [315], considering the periodic boundary conditions in the three directions. Subsequently, three chloride and one sodium counterions were added into the solution to achieve an ionic strength of 0.15 M. The system was then minimized and pre-thermalized at 37 °C through 1 ns of NVT simulation. Consequently, a 200 ns MD simulation was carried out in NPT conditions at a temperature of 37 °C and pressure of 1 atm with a 2 fs time step and a cut-off of 1.2 nm.

Development of Glue$^{CO_2-}$ and THD$_{GTP*}$ models

The [THD$_{GTP*}$]$_3$ configuration, corresponding to three laterally assembled THD, was extracted from the Protein Data Bank (PDB) structure of THD$_{GTP*}$ (PDB code: 3J6E) [316]. Missing residues were compensated with the one from another THD structure (PDB code: 1TUB) [317] to form a complete model of [THD$_{GTP*}$]$_3$. Two systems were then generated from this model: one composed by [THD$_{GTP*}$]$_3$ and 30 randomly placed pre-equilibrated Glue$^{CO_2-}$ molecules within the simulation box, and the other one composed solely of [THD$_{GTP*}$]$_3$ as a control. The periodic boundary conditions were considered in all the three directions for both systems. The simulation boxes were then filled with explicit TIP3P water molecules [315] and a number of counterions necessary to neutralize the systems. The microtubule topology was treated by the AMBER99-ILDN force field [318].

Adhesions of Glue$^{CO_2-}$ onto THD$_{GTP*}$

The THD$_{GTP*}$ systems were first minimized and then pre-thermalized at 300 K through 1 ns NVT and 1 ns NPT simulations, with THD$_{GTP*}$ atoms restrained with a position restraint of 1000 kJ mol^{-1} nm^{-2}. During these preliminary phases, the systems reached the temperature of 37 °C and the correct solvent density (1 atm of pressure). To allow the Glue$^{CO_2-}$ molecules to approach the THD$_{GTP*}$, 20 ns of NVT simulation was carried out at 37 °C, maintaining THD$_{GTP*}$ at a fixed position. Subsequently, all restraints were removed in 200 ns of NPT production at 37 °C and 1 atm. Both electrostatic and Van der Waals interactions were treated within a 1.2 nm cutoff radius and Lennard-Jones interactions were described using the Particle-Mesh Ewald method [177] with 1.2 nm cutoff. The V-rescale thermostat [179] was employed with a coupling time step of 0.1 ps, whereas the Parrinello-Rahman barostat [175] was considered with a coupling time step of 5.0 ps. From the equilibrated phase of the MD trajectories, various analyses were conducted. The effect of Glue$^{CO_2-}$ adhesion on THD$_{GTP*}$ hydrophobicity and total solvent-accessible surface area was detected using the Gromacs *gmx sasa* tool [319]. On the other hand, the variations in electrostatic potentials on the THD$_{GTP*}$ surface induced by the presence of Glue$^{CO_2-}$ were investigated through the Adaptive Poisson-Boltzmann Solver (APBS) software package [320].

Interactions of Glue$^{CO_2-}$

After this preliminary phase, we investigated the strength of Glue$^{CO_2-}$ interactions by calculating the radial distribution function *g(r)* between key groups in glue and tubulin assemblies (nanosheets). In particular, high and sharp peaks at short distances r in the *g(r)* profile highlights a high probability of finding groups in proximity to each other during the simulations, indicating therefore strong and persistent interactions. On the contrary, the absence of evident peaks in the g(r) profile, or peaks minor than one, indicate negligible interactions (see Figure 7.7a). The radial distribution functions were calculated specifically between the Gu$^+$ groups of Glue$^{CO_2-}$ and the anionic amino acids (aspartic acid and glutamic acid) of THD$_{GTP*}$, the Gu$^+$ groups of Glue$^{CO_2-}$ and the OH groups of neutral amino acids (serine, threonine, and tyrosine) of THD$_{GTP*}$, and the CO_2-groups of Glue$^{CO_2-}$ and the cationic amino acids (lysine and arginine) of THD$_{GTP*}$. Additionally, g(r) were calculated to examine the

nature of Glue$^{CO_2-}$-to-Glue$^{CO_2-}$ interactions, in particular we calculated the g(r) for CO_2- vs. Gu^+ groups present in the Glue$^{CO_2-}$ molecules in the simulated systems.

7.3 Results and discussion

In order to investigate the adhesion of Glue$^{CO_2-}$ molecules on the tubulin assembly (nanosheet), we conducted molecular dynamics (MD) simulations utilizing all-atom models. It is worth noting that tubulin NS are generally 0.04 μm^2 wide and 4.2 nm thick, consequently the NC$_{GTP/GTP*}$, characterized by $\sim$6.2 μm^2 of surface area and 50 nm thickness, is composed by at least 1000 pieces of NS$_{GTP/GTP*}$. Because of these sizes, it is not feasible to simulate the entire NC with molecular models. Thus, we have focused on analyzing the effects of the formation of salt-bridge interactions between 30 Glue$^{CO_2-}$ molecules and three laterally assembled THD$_{GTP*}$ units ([THD$_{GTP*}$]$_3$) as a model for NS. The [THD$_{GTP*}$]$_3$ model was obtained by merging of two models present in the protein data bank (PDB codes: 3J6E and 1TUB) and is shown in Figure 7.4a. Furthermore, we parametrized a Glue$^{CO_2-}$ molecule, which exhibits the tendency to assume a globular conformation in water and a hydrodynamic diameter of 1.5 nm (Figure 7.4b and Figure B.1 in B).

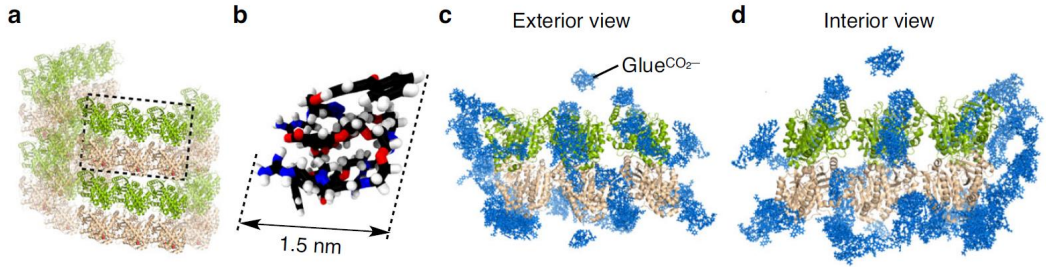

Fig. 7.4 Snapshots of the all-atom models of the [THD$_{GTP*}$]$_3$ and Glue$^{CO_2-}$ molecules. **a** Three laterally assembled THD$_{GTP*}$ units ([THD$_{GTP*}$]$_3$) in MT$_{GTP*}$ as a partial model of NS. **b** An equilibrated MD snapshot of Glue$^{CO_2-}$. **c, d** The outer (c) and inner (d) views of [THD$_{GTP*}$]$_3$ hybridized with 30 equivalents of Glue$^{CO_2-}$. Figure adapted from Ref. 275 with permission of Creative Commons CC BY license.

The adhesion of 30 Glue$^{CO_2-}$ equivalents (reported in Figure 7.4c,d) on the surface of the [THD$_{GTP*}$]$_3$ increases its hydrophobic nature (Figure 7.5a,b) due to the neutralization of the surface charge by the presence of the charged Glue$^{CO_2-}$. This is also confirmed by the estimation of the solvent accessible surface area of

$[THD_{GTP*}]_3$, where the percentage of hydrophobic surface exposed to the solvent increases from 48% in absence of $Glue^{CO_2-}$ to 57%, as depicted in Figure 7.5c.

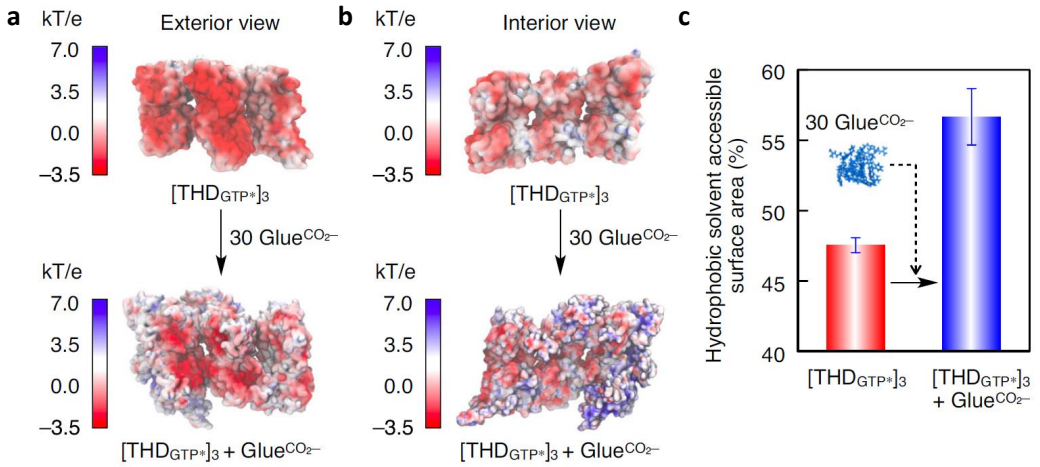

Fig. 7.5 Estimation of the electrostatic surface potential and hydrophobic solvent-accessible surface area of $[THD_{GTP*}]_3$ in presence and absence of $Glue^{CO_2-}$. The outer **a** and inner **b** views of $[THD_{GTP*}]_3$ with its electrostatic surface potential in the absence (upper) and presence (lower) of 30 equivalents of hybridized $Glue^{CO_2-}$. Negative and positive potential areas are colored in red and blue, respectively. **g** The percentage of hydrophobic solvent-accessible surface area in the absence (47.5 ± 0.5; red) and presence (56.7 ± 2.0; blue) of 30 equivalents of hybridized $Glue^{CO_2-}$. Bars represent mean values $\pm$ SD from 2000 data points. Figure adapted from Ref. 275 with permission of Creative Commons CC BY license.

Additionally, the adhesion of $Glue^{CO_2-}$ onto $[THD_{GTP*}]_3$ influences the conformation of $[THD_{GTP*}]_3$ by flattening the NS (Figure 7.6a). In particular, the angle distribution highlights an increase in the angle from $\sim 154^\circ$ characteristics of the native structure up to $\sim 156^\circ$ in presence of glue molecules, colored red and blue, respectively, in Figure 7.6b. Nonetheless, it is worth noting that even after the adhesion of $Glue^{CO_2-}$ equivalents, the $[THD_{GTP*}]_3$ maintains a certain level of flexibility (Figure 7.6b).

Lastly, we investigated the adhesion sites by calculating the radial distribution functions g(r) of the charged groups in $Glue^{CO_2-}$ and the amino acid residues of $[THD_{GTP*}]_3$ (as shown in Figure 7.7a), considering the hypotheses that the CO_2-groups in acid and glutamic acid interact with the Gu+ groups in $Glue^{CO_2-}$, and the cationic groups in lysine and arginine interact with the CO_2- group in $Glue^{CO_2-}$. On the one hand, the analysis confirms that the Gu+ groups in $Glue^{CO_2-}$ are located close to the CO_2- groups on the $[THD_{GTP*}]_3$ surface (depicted in blue in Figure

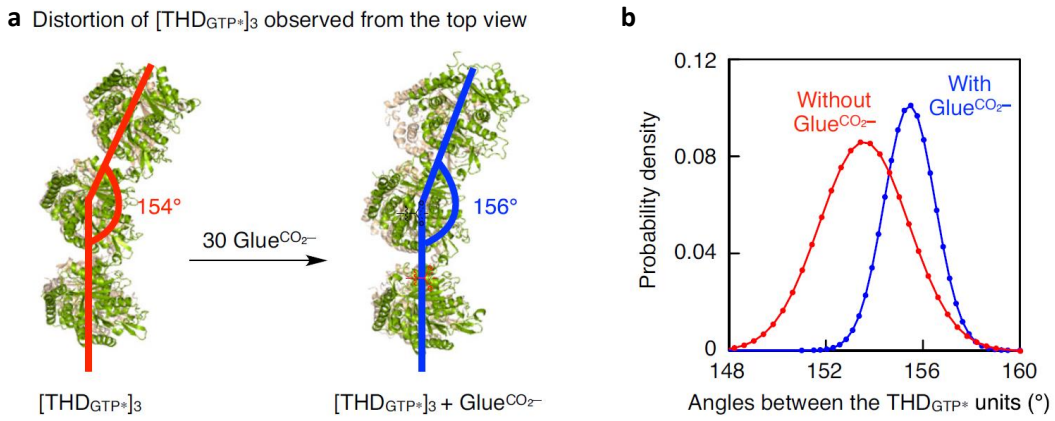

Fig. 7.6 Variations in bending capabilities of $THD_{GTP*}]_3$ in presence and absence of $Glue^{CO_2-}$.$[THD_{GTP*}]_3$ observed from the top view **a** and its angle distributions **b** in the absence (red) and presence (blue) of 30 equivalents of hybridized $Glue^{CO_2-}$. Figure adapted from Ref. 275 with permission of Creative Commons CC BY license.

7.7a), while are not present near the polar but non-ionic hydroxyl groups in serine, threonine, and tyrosine (Figure 7.7a, gray). On the other hand, the g(r) data does not reveal the interaction between the CO_2- group of $Glue^{CO_2-}$ and the cationic groups on the $[THD_{GTP*}]_3$ surface (as shown in Figure B.2 in Appendix B). Therefore, the g(r) confirms that there is interaction between the Gu+ and CO_{2-} groups of the $Glue^{CO_2-}$ molecules through salt-bridge interactions (as shown in red in Figure 7.7a), leading to the formation of a dense Gu+/CO_{2-} salt-bridged polymeric network on the $[THD_{GTP*}]_3$ surface (see Figure 7.7b). It is exactly this interaction that may promote and stabilize the curvature of the $NS_{GTP/GTP*}$ in the formation of $NC_{GTP/GTP*}$, as also demonstrated experimentally in references 321, 322.

7.4 Conclusion

In this Chapter, we have studied, through all-atom molecular models, how the presence of glue molecules can deform and stabilize a tubulin-based assembly. The final aggregate can be then utilized to realize a possible nanocarrier to treat cancer or virus-infected cells by taking advantage of the biocompatibility of tubulin heterodimers (THD) and of the over expression of guanosine triphosphate (GTP) in diseased tissues. In particular, in presence of GTP, or a nonhydrolysable GTP analogue (guanylyl 5'-α,β -methylenediphosphonate, GTP*), THD_{GTP*} and THD_{GTP} monomers poly-

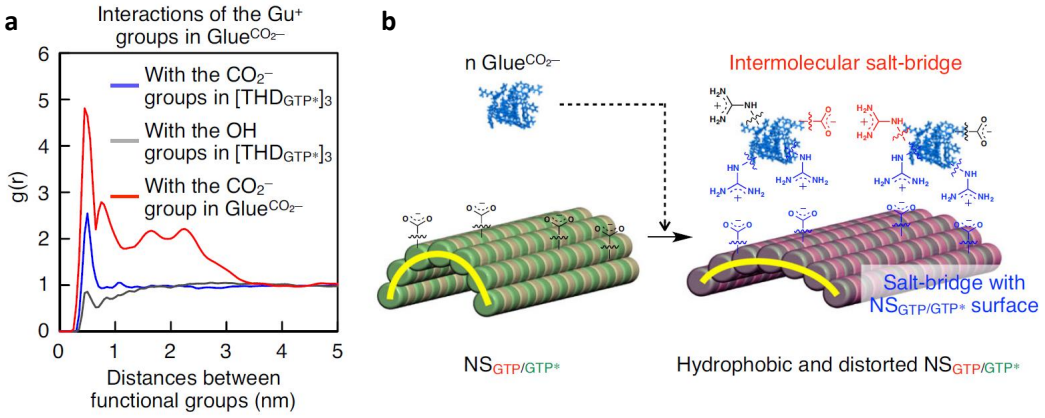

Fig. 7.7 Insights in the disposition of Glue$^{CO_2-}$ onto the surface of THD$_{GTP*}$. **a** Radial distribution functions g(r) of the Gu$^+$ groups in Glue$^{CO_2-}$ with carboxylates (blue) and non-ionic hydroxyl groups (gray) on the $[THD_{GTP*}]_3$ surface, and the carboxylate at the focal core of Glue$^{CO_2-}$ (red). **b** Schematic illustration of a possible adhesion event of Glue$^{CO_2-}$ onto NS$_{GTP/GTP*}$ and its effects on the features of NS$_{GTP/GTP*}$. The Gu$^+$ groups in Glue$^{CO_2-}$ form a salt bridge with carboxylates on the NS$_{GTP/GTP*}$ surface and at the focal core of Glue$^{CO_2-}$, and the Glue$^{CO_2-}$-based polymeric network thus formed through this process increases the hydrophobicity of the NS$_{GTP/GTP*}$ surface, making NS$_{GTP/GTP*}$ more flatten. Figure adapted from Ref. 275 with permission of Creative Commons CC BY license.

merizes into tubulin nanosheets (NS$_{GTP/GTP*}$). Additionally, by exploiting the glue molecules technology, and, in particular, utilizing the Glue$^{CO_2-}$, NS$_{GTP/GTP*}$ rearrange into a nanocapsule-like configuration, named NC$_{GTP/GTP*}$, which stabilizes after a photo-induced cross-linking within the glue molecules (^{CL}NC$_{GTP/GTP*}$).

In this context, experimental evidences allow to monitor all the step to obtain the ^{CL}NC$_{GTP/GTP*}$ by testing the variations in shape and sizes through different analyses (i.e., Dynamic Light Scattering, Transmission Electron Microscopy, Atomic Force Microscopy). In parallel, all-atom molecular dynamics simulations gain insights into the intermolecular interactions between the Glue$^{CO_2-}$ molecules and three lateral assembled THD$_{GTP*}$. The analyses at the molecular resolution demonstrate the effects of this adhesion on the hydrophobicity and flexibility of the $[THD_{GTP*}]_3$, and the location of the Glue$^{CO_2-}$ on the tubulin surface.

These results have allowed the realization of a ^{CL}NC$_{GTP/GTP*}$ nanocarrier that disassembles in correspondence of high densities of GTP releasing the encapsulated drug.

Chapter 8

Conclusions

Self-assembled materials are ordered or disordered aggregates of molecules connected *via* intermolecular bonds. As a consequence of these non-covalent interactions, self-assembled materials are characterized by intrinsic dynamics that, in some cases, allow the materials to respond and adapt to external stimuli. Therefore, stimuli-responsive materials demonstrated great potential in the development of advanced smart materials by allowing for precise control over the supramolecular structure and properties. However, the designing process of the self-assembling units is discouraged by the difficulties in predicting and controlling the properties of the final aggregates. In this regard, molecular modeling and simulations provide a significant support in comprehending the physical-chemical mechanisms that control the self-assembling processes. In particular, molecular models permit the observation of the responsive process at a molecular level, which cannot be achieved through experimental approaches.

This PhD Thesis presents and discusses studies that employ molecular dynamics (MD) simulations and advanced techniques to gain a deeper understanding of the design of new responsive materials and to further comprehend phenomena detected through experimental analyses. All-atom (AA), and, in particular, coarse-grained (CG) models have proven to be extremely useful in the exploration of the dynamics of self-assembled systems and their stimuli-responsive properties. For example, as evidenced in the study of the motion of soft nanoparticles (NPs) on various receptor-functionalized surfaces. We demonstrate how properties, such as chemotacticity or semiconductivity, may emerge even in self-assembling materials. The chemotactive

behavior of NPs was found to be controlled by the multivalent interactions (energy of assembly and energy of binding) to control the disassembly on selective surfaces. This confirms the importance of rational design in successfully controlling and predicting the behavior of soft NPs on specific surfaces. Subsequently, we examine the dynamic complexity of bi-component micelles by varying the structural and energetic properties of the second components. In the case of similar components, where intermixed interactions are as favored as homo interactions, the two species are more reshuffled in the micelle compared to the case in which differences in the intermolecular interactions encourage a more separated configuration. It is interesting to note that such unique properties emerge in these materials thanks to their supramolecular character. Similarly, through the same approach, CG-MD simulations and machine learning-based analyses reveal to be necessary to deeply understand the response of self-assembled materials to certain stimuli. The application of various electric fields on face-centered cubic lattices composed by TMA-NP and citrate ions causes an increase in the diffusion of the smaller species. The calculation of density current reveals a semiconductive behavior, indicating that ionic conduction is only permitted by overcoming a certain energy barrier. This is also supported by the SOAP and PAMM analyses, which identify the two local environments responsible for the emergence of conduction.

Consequently, the same techniques, especially all-atom (AA) and CG models, have been employed to two experimental systems. Through CG-MD simulations, we investigate the impact of temperature variations on the size and hydrophobicity of amphiphilic aggregates, obtaining outcomes consistent with the experimental findings. Specifically, CG-MD results confirm that an increase in the temperature above the LCST leads to an increase in the hydrophobicity of the assembly. Meanwhile, the use of AA-MD simulations allows for the exploration of the intermolecular interactions between tubulin heterodimers and the glue molecules used to stabilize the nanocapsule. These simulations demonstrate the formation of salt bridge interactions with the surface of the tubulin nanosheets, affecting their flexibility and neutralizing their surface charge.

In conclusion, this Thesis encompasses various computational approaches aimed to deeply understand the phenomena underlying the responsiveness of several materials at a submolecular level, demonstrating the flexibility of these methods. Moreover, the results that I have collected during my PhD highlight the crucial role of molecular models and simulations in the rational design of new smart materials, leading to

a more efficient optimization of intermolecular interactions in the development of controllable self-assembled materials.

References

[1] J.-M. Lehn. *Supramolecular Chemistry*. Wiley, 1995.

[2] J.-M. Lehn. Supramolecular chemistry—scope and perspectives molecules, supermolecules, and molecular devices(nobel lecture). *Angew. Chem. Int. Ed. in English*, 27(1):89–112, 1988.

[3] G. Singh, H. Chan, A. Baskin, E. Gelman, N. Repnin, P Král, and R. Klajn. Self-assembly of magnetite nanocubes into helical superstructures. *Science*, 345(6201):1149–1153, 2014.

[4] M. Albrecht. Supramolecular chemistry—general principles and selected examples from anion recognition and metallosupramolecular chemistry. *Sci. Nat.*, 94(12):951–966, 2007.

[5] C. Fasting, C. A. Schalley, M. Weber, O. Seitz, S. Hecht, B. Koksch, J. Dernedde, C. Graf, E.-W. Knapp, and R. Haag. Multivalency as a chemical organization and action principle. *Angew. Chem. Int. Ed.*, 51(42):10472–10498, 2012.

[6] K. S. Mali and S. De Feyter. Principles of molecular assemblies leading to molecular nanostructures. *Philos. Trans. R. Soc. A*, 371(2000):20120304, 2013.

[7] A. C. Mendes, E. T. Baran, R. L. Reis, and H. S. Azevedo. Self-assembly in nature: using the principles of nature to create complex nanobiomaterials. *Wiley Interdiscip. Rev.: Nanomed. Nanobiotechnology*, 5(6):582–612, 2013.

[8] S. Imai, M. Takenaka, M. Sawamoto, and T. Terashima. Self-sorting of amphiphilic copolymers for self-assembled materials in water: Polymers can recognize themselves. *J. Am. Chem. Soc.*, 141(1):511–519, 2018.

[9] J. Hamacek, M. Borkovec, and C. Piguet. A simple thermodynamic model for quantitatively addressing cooperativity in multicomponent self-assembly processes – part 1: Theoretical concepts and application to monometallic coordination complexes and bimetallic helicates possessing identical binding sites. *Chem. Eur. J.*, 11(18):5217–5226, 2005.

[10] J. Hamacek, M. Borkovec, and C. Piguet. A simple thermodynamic model for quantitatively addressing cooperativity in multicomponent self-assembly processes—part 2: Extension to multimetallic helicates possessing different binding sites. *Chem. Eur. J.*, 11(18):5227–5237, 2005.

[11] A. Rao, S. Roy, V. Jain, and P. P. Pillai. Nanoparticle self-assembly: From design principles to complex matter to functional materials. *ACS Appl. Mater. Interfaces*, 2022.

[12] M. Antonietti and S. Förster. Vesicles and liposomes: A self-assembly principle beyond lipids. *Adv. Mater.*, 15(16):1323–1333, 2003.

[13] R. Chhabra, J. Sharma, Y. Liu, S. Rinker, and H. Yan. DNA self-assembly for nanomedicine. *Adv. Drug Deliv. Rev.*, 62(6):617–625, 2010.

[14] S. Winkler, S. Szela, P. Avtges, R. Valluzzi, D. A. Kirschner, and D. Kaplan. Designing recombinant spider silk proteins to control assembly. *Int. J. Biol. Macromol.*, 24(2-3):265–270, 1999.

[15] S. Zhang. Emerging biological materials through molecular self-assembly. *Biotechnol. Adv.*, 20(5-6):321–339, 2002.

[16] G. Askarieh, M. Hedhammar, K. Nordling, A. Saenz, C. Casals, A. Rising, J. Johansson, and S. D. Knight. Self-assembly of spider silk proteins is controlled by a pH-sensitive relay. *Nature*, 465(7295):236–238, 2010.

[17] D. A. Cisneros, C. Hung, C. M. Franz, and D. J. Muller. Observing growth steps of collagen self-assembly by time-lapse high-resolution atomic force microscopy. *J. Struct. Biol.*, 154(3):232–245, 2006.

[18] F. H. Silver, J. W. Freeman, and G. P. Seehra. Collagen self-assembly and the development of tendon mechanical properties. *J. Biomech.*, 36(10):1529–1553, 2003.

[19] J. G. Rouse and M. E. Van Dyke. A review of keratin-based biomaterials for biomedical applications. *Materials*, 3(2):999–1014, 2010.

[20] C Conde and A. Cáceres. Microtubule assembly, organization and dynamics in axons and dendrites. *Nat. Rev. Neurosci.*, 10(5):319–332, 2009.

[21] K. A. Johnson and G. G. Borisy. Kinetic analysis of microtubule self-assembly in vitro. *J. Mol. Biol.*, 117(1):1–31, 1977.

[22] Monnard-P. A. and D. W. Deamer. Membrane self-assembly processes: Steps toward the first cellular life. *Anat. Rec.*, 268(3):196–207, 2002.

[23] P. J. G. Butler. Self–assembly of tobacco mosaic virus: the role of an intermediate aggregate in generating both specificity and speed. *Philos. Trans. R. Soc. Lond., B, Biol. Sci.*, 354(1383):537–550, 1999.

[24] A. Klug. The tobacco mosaic virus particle: structure and assembly. *Philos. Trans. R. Soc. Lond., B, Biol. Sci.*, 354(1383):531–535, 1999.

[25] C. Wang, L. Fu, Z. Hu, and Y. Zhong. A mini-review on peptide-based self-assemblies and their biological applications. *Nanotechnology*, 33(6):062004, 2021.

[26] J. D. Hartgerink, E. Beniash, and S. I. Stupp. Peptide-amphiphile nanofibers: A versatile scaffold for the preparation of self-assembling materials. *Proc. Natl. Acad. Sci. U.S.A.*, 99(8):5133–5138, 2002.

[27] Q. Zhang, P. Zhang, S. Jian, J. Li, F. Li, X. Sun, H. Li, Y. Zeng, Y. Zeng, S. Liang, P. Chen, and Z. Liu. Drug-bearing peptide-based nanospheres for the inhibition of metastasis and growth of cancer. *Mol. Pharm.*, 17(9):3165–3176, 2020.

[28] K. Kornmueller, I. Letofsky-Papst, K. Gradauer, C. Mikl, F. Cacho-Nerin, M. Leypold, W. Keller, G. Leitinger, H. Amenitsch, and R. Prassl. Tracking morphologies at the nanoscale: Self-assembly of an amphiphilic designer peptide into a double helix superstructure. *Nano Res.*, 8(6):1822–1833, 2015.

[29] F. Pan, X. Zhao, S. Perumal, T. A. Waigh, J. R. Lu, and J. R. P. Webster. Interfacial dynamic adsorption and structure of molecular layers of peptide surfactants. *Langmuir*, 26(8):5690–5696, 2009.

[30] U. Khoe, Y. Yang, and S. Zhang. Self-assembly of nanodonut structure from a cone-shaped designer lipid-like peptide surfactant. *Langmuir*, 25(7):4111–4114, 2008.

[31] Y. Kimura, T. Terashima, and M. Sawamoto. Self-assembly of amphiphilic random copolyacrylamides into uniform and necklace micelles in water. *Macromol. Chem. Phys.*, 218(18):1700230, 2017.

[32] S. Cantekin, T. F. A. de Greef, and A. R. A. Palmans. Benzene-1, 3, 5-tricarboxamide: a versatile ordering moiety for supramolecular chemistry. *Chem. Soc. Rev.*, 41(18):6125, 2012.

[33] S. M. C. Schoenmakers, A. J. H. Spiering, S. Herziger, C. Böttcher, R. Haag, A. R. A. Palmans, and E. W. Meijer. Structure and dynamics of supramolecular polymers: Wait and see. *ACS Macro Lett.*, 11(5):711–715, 2022.

[34] B. Wu, L. Liu, L. Zhou, J. R. Magana, M. M. R. M. Hendrix, J. Wang, C. Li, P. Ding, Y. Wang, X. Guo, I. K. Voets, M. A. Cohen Stuart, and J. Wang. Complex supramolecular fiber formed by coordination-induced self-assembly of benzene-1, 3, 5-tricarboxamide (BTA). *J. Colloid. Interface Sci.*, 608:1297–1307, 2022.

[35] G. Ouyang, L. Ji, Y. Jiang, F. Würthner, and M. Liu. Self-assembled möbius strips with controlled helicity. *Nat. Commun.*, 11(1), 2020.

[36] S. Saha, I. Regeni, and G. H. Clever. Structure relationships between bis-monodentate ligands and coordination driven self-assemblies. *Coord. Chem. Rev.*, 374:1–14, 2018.

[37] S. Pullen, J. Tessarolo, and G. H. Clever. Increasing structural and functional complexity in self-assembled coordination cages. *Chem. Sci.*, 12(21):7269–7293, 2021.

[38] N. Ahmad, A. H. Chughtai, H. A. Younus, and F. Verpoort. Discrete metal-carboxylate self-assembled cages: Design, synthesis and applications. *Coord. Chem. Rev.*, 280:1–27, 2014.

[39] O. Yanshyna, M. J. Białek, O. V. Chashchikhin, and R. Klajn. Encapsulation within a coordination cage modulates the reactivity of redox-active dyes. *Commun. Chem.*, 5(1), 2022.

[40] C. Ngai, B. da Camara, C. Z. Woods, and R. J. Hooley. Size- and shape-selective catalysis with a functionalized self-assembled cage host. *J. Org. Chem.*, 86(18):12862–12871, 2021.

[41] J. W. Steed and J. L. Atwood. *Supramolecular chemistry*. John Wiley & Sons, 2022.

[42] A. Sorrenti, J. Leira-Iglesias, A. J. Markvoort, T. F. A. de Greef, and T. M. Hermans. Non-equilibrium supramolecular polymerization. *Chem. Soc. Rev.*, 46(18):5476–5490, 2017.

[43] J. H. van Esch, R. Klajn, and S. Otto. Chemical systems out of equilibrium. *Chem. Soc. Rev.*, 46(18):5474–5475, 2017.

[44] S. Yoshida, M. Takinoue, E. Iwase, and H. Onoe. Dynamic transformation of self-assembled structures using anisotropic magnetized hydrogel microparticles. *J. Appl. Phys.*, 120(8):084905, 2016.

[45] M. D. Hager, P. Greil, C. Leyens, S. van der Zwaag, and U. S. Schubert. Self-healing materials. *Adv. Mater.*, 22(47):5424–5430, 2010.

[46] P. Song, H. Qin, H.-L. Gao, H.-P. Cong, and S.-H. Yu. Self-healing and superstretchable conductors from hierarchical nanowire assemblies. *Nat. Commun.*, 9(1), 2018.

[47] J. Du, Z. Wang, Z. Wei, J. Yao, and H. Song. An environmental friendly self-healing coating with silane/ce-ZSM-5 zeolite structure for corrosion protection of aluminum alloy. *Surf. Coat. Technol.*, 436:128290, 2022.

[48] S. Amador-Vargas, M. Dominguez, G. León, B. Maldonado, J. Murillo, and G. L. Vides. Leaf-folding response of a sensitive plant shows context-dependent behavioral plasticity. *Plant Ecol.*, 215(12):1445–1454, 2014.

[49] Q. Wang, G. R. Gossweiler, S. L. Craig, and X. Zhao. Cephalopod-inspired design of electro-mechano-chemically responsive elastomers for on-demand fluorescent patterning. *Nat. Commun.*, 5(1), 2014.

[50] M.W. Urban. *Stimuli-Responsive Materials: From Molecules to Nature Mimicking Materials Design*. Royal Society of Chemistry, 2019.

[51] F. Ofridam, M. Tarhini, N. Lebaz, É. Gagnière, D. Mangin, and A. Elaissari. pH-sensitive polymers: Classification and some fine potential applications. *Polym. Adv. Technol.*, 32(4):1455–1484, 2021.

[52] M. A. Ward and T. K. Georgiou. Thermoresponsive polymers for biomedical applications. *Polymers*, 3(3):1215–1242, 2011.

[53] A. Bordat, T. Boissenot, J. Nicolas, and N. Tsapis. Thermoresponsive polymer nanocarriers for biomedical applications. *Adv. Drug Deliv. Rev.*, 138:167–192, 2019.

[54] Y. Zhou, S. Wang, J. Peng, Y. Tan, C. Li, F. Y. C. Boey, and Y. Long. Liquid thermo-responsive smart window derived from hydrogel. *Joule*, 4(11):2458–2474, 2020.

[55] W. Du, X. Liu, L. Liu, J. W. Y. Lam, and B. Z. Tang. Photoresponsive polymers with aggregation-induced emission. *ACS Appl. Polym. Mater.*, 3(5):2290–2309, 2021.

[56] X. Yan, F. Wang, B. Zheng, and F. Huang. Stimuli-responsive supramolecular polymeric materials. *Chem. Soc. Rev.*, 41(18):6042, 2012.

[57] P. Singh, B. Youden, A. Carrier, K. Oakes, M. Servos, R. Jiang, S. Lin, T. D. Nguyen, and X. Zhang. Photoresponsive polymeric microneedles: An innovative way to monitor and treat diseases. *J. Control. Release*, 353:1050–1067, 2023.

[58] E. Yarali, M. Baniasadi, A. Zolfagharian, M. Chavoshi, F. Arefi, M. Hossain, A. Bastola, M. Ansari, A. Foyouzat, A. Dabbagh, M. Ebrahimi, M. J. Mirzaali, and M. Bodaghi. Magneto-/ electro-responsive polymers toward manufacturing, characterization, and biomedical/ soft robotic applications. *Appl. Mater. Today*, 26:101306, 2022.

[59] C. Ma, S. Wu, Q. Ze, X. Kuang, R. Zhang, H. J. Qi, and R. Zhao. Magnetic multimaterial printing for multimodal shape transformation with tunable properties and shiftable mechanical behaviors. *ACS Appl. Mater. Interfaces*, 13(11):12639–12648, 2021.

[60] Q. Zhang, Y. Zhang, Y. Wan, W. Carvalho, L. Hu, and M. J. Serpe. Stimuli-responsive polymers for sensing and reacting to environmental conditions. *Prog. Polym. Sci.*, 116:101386, 2021.

[61] X. Zeng, K. Yang, C. Huang, K. Yang, S. Xu, L. Wang, P. Pi, and X. Wen. Novel pH-responsive smart fabric: From switchable wettability to controllable on-demand oil/water separation. *ACS Sustain. Chem. Eng.*, 7(1):368–376, 2018.

[62] H. T. Hoang, S.-H. Jo, Q.-T. Phan, H. Park, S.-H. Park, C.-W. Oh, and K. T. Lim. Dual pH-/thermo-responsive chitosan-based hydrogels prepared using "click" chemistry for colon-targeted drug delivery applications. *Carbohydr. Polym.*, 260:117812, 2021.

[63] L. Yang, Y. Zhan, R. Yu, J. Lan, J. Shang, B. Dou, H. Liu, R. Zou, and S. Lin. Facile and scalable fabrication of antibacterial CO_2-responsive cotton for ultrafast and controllable removal of anionic dyes. *ACS Appl. Mater. Interfaces*, 13(2):2694–2709, 2021.

[64] S. Fan, J. Chen, C. Fan, G. Chen, S. Liu, H. Zhou, R. Liu, Y. Zhang, H. Hu, Z. Huang, Y. Qin, and J. Liang. Fabrication of a CO2-responsive chitosan aerogel as an effective adsorbent for the adsorption and desorption of heavy metal ions. *J. Hazard. Mater.*, 416:126225, 2021.

[65] T. J. Quill, G. LeCroy, D. M. Halat, R. Sheelamanthula, A. Marks, L. S. Grundy, I. McCulloch, J. A. Reimer, N. P. Balsara, A. Giovannitti, A. Salleo, and C. J. Takacs. An ordered, self-assembled nanocomposite with efficient electronic and ionic transport. *Nat. Mater.*, 22(3):362–368, 2023.

[66] X. Tian, P. Wang, T. Li, X. Huang, W. Guo, Y. Yang, M. Yan, H. Zhang, D. Cai, X. Jia, F. Li, B. Xu, T. Ma, C. Yan, and H. Lei. Self-assembled natural phytochemicals for synergistically antibacterial application from the enlightenment of traditional chinese medicine combination. *Acta Pharm. Sin. B*, 10(9):1784–1795, 2020.

[67] Deepak, Z. Mallick, U. Sarkar, D. Mandal, and R. K. Roy. Synergetic h-bonding and c-t interaction-mediated self-assembled structure results in a room-temperature ferroelectric material exhibiting electric field-induced dipole switching and piezo- and pyroelectric energy conversion. *Chem. Mater.*, 35(8):3316–3328, 2023.

[68] R. Wang, X. Yan, B. Ge, J. Zhou, M. Wang, L. Zhang, and T. Jiao. Facile preparation of self-assembled black phosphorus-dye composite films for chemical gas sensors and surface-enhanced raman scattering performances. *ACS Sustain. Chem. Eng.*, 8(11):4521–4536, 2020.

[69] A. Milsom, A. M. Squires, B. Woden, N. J. Terrill, A. D. Ward, and C. Pfrang. The persistence of a proxy for cooking emissions in megacities: a kinetic study of the ozonolysis of self-assembled films by simultaneous small and wide angle x-ray scattering (SAXS/WAXS) and raman microscopy. *Faraday Discuss.*, 226:364–381, 2021.

[70] S. K. Brar, N. Wangoo, and R. K. Sharma. Enhanced and selective adsorption of cationic dyes using novel biocompatible self-assembled peptide fibrils. *J. Environ. Manage.*, 255:109804, 2020.

[71] K. Chen, X. Yan, J. Li, T. Jiao, C. Cai, G. Zou, R. Wang, M. Wang, L. Zhang, and Q. Peng. Preparation of self-assembled composite films constructed by chemically-modified MXene and dyes with surface-enhanced raman scattering characterization. *Nanomaterials*, 9(2):284, 2019.

[72] S.-W. Kuo. Hydrogen bonding mediated self-assembled structures from block copolymer mixtures to mesoporous materials. *Polym. Int.*, 71(4):393–410, 2021.

[73] L. Albertazzi, D. van der Zwaag, C. M. A. Leenders, R. Fitzner, R. W. van der Hofstad, and E. W. Meijer. Probing exchange pathways in one-dimensional aggregates with super-resolution microscopy. *Science*, 344(6183):491–495, 2014.

[74] A R Leach. *Molecular modelling*. Prentice-Hall, London, England, September 1996.

[75] N. A. Saleh, H. Elhaes, and M. Ibrahim. Design and development of some viral protease inhibitors by QSAR and molecular modeling studies. In *Viral Proteases and Their Inhibitors*, pages 25–58. Elsevier, 2017.

[76] D. Bochicchio and G. M. Pavan. From cooperative self-assembly to water-soluble supramolecular polymers using coarse-grained simulations. *ACS Nano*, 11(1):1000–1011, 2017.

[77] D. Bochicchio and G. M. Pavan. Effect of concentration on the supramolecular polymerization mechanism via implicit-solvent coarse-grained simulations of water-soluble 1,3,5-benzenetricarboxamide. *J. Phys. Chem. Lett.*, 8(16):3813–3819, 2017.

[78] D. Bochicchio, M. Salvalaglio, and G. M Pavan. Into the dynamics of a supramolecular polymer at submolecular resolution. *Nat. Commun.*, 8(1):1–11, 2017.

[79] M. Crippa, C. Perego, A. L. de Marco, and G. M. Pavan. Molecular communications in complex systems of dynamic supramolecular polymers. *Nat. Commun.*, 13:2162, 2022.

[80] A. Torchi, D. Bochicchio, and G. M Pavan. How the dynamics of a supramolecular polymer determines its dynamic adaptivity and stimuli-responsiveness: structure–dynamics–property relationships from coarse-grained simulations. *J. Phys. Chem. B*, 122(14):4169–4178, 2018.

[81] D. Bochicchio, S. Kwangmettatam, T. Kudernac, and G. M. Pavan. How defects control the out-of-equilibrium dissipative evolution of a supramolecular tubule. *ACS Nano*, 13(4):4322–4334, 2019.

[82] R. Montis, L. Fusaro, A. Falqui, M. B. Hursthouse, N. Tumanov, S. J. Coles, T. L. Threlfall, P. N. Horton, R. Sougrat, A. Lafontaine, G. Coquerel, and A. D. Rae. Complex structures arising from the self-assembly of a simple organic salt. *Nature*, 590(7845):275–278, 2021.

[83] S. Datta, Y. Kato, S. Higashiharaguchi, K. Aratsu, A. Isobe, T. Saito, D. D. Prabhu, Y. Kitamoto, M. J. Hollamby, A. J. Smith, R. Dalgliesh, N. Mahmoudi, L. Pesce, C. Perego, G. M. Pavan, and S. Yagai. Self-assembled poly-catenanes from supramolecular toroidal building blocks. *Nature*, 583(7816):400–405, 2020.

[84] C. Lochenie, A. Insuasty, T. Battisti, L. Pesce, A. Gardin, C. Perego, M. Dentinger, Wang D., G. M. Pavan, A. Aliprandi, and L. De Cola. Solvent-driven chirality for luminescent self-assembled structures: experiments and theory. *Nanoscale*, 12(41):21359–21367, 2020.

[85] C. Empereur-Mot, L. Pesce, G. Doni, D. Bochicchio, R. Capelli, C. Perego, and G. M. Pavan. Swarm-cg: Automatic parametrization of bonded terms in martini-based coarse-grained models of simple to complex molecules via fuzzy self-tuning particle swarm optimization. *ACS Omega*, 5:32823–32843, 2020.

[86] P. Gasparotto, D. Bochicchio, M. Ceriotti, and G. M. Pavan. Identifying and tracking defects in dynamic supramolecular polymers. *J. Phys. Chem. B*, 124(3):589–599, 2019.

[87] A. Gardin, C. Perego, G. Doni, and G. M. Pavan. Classifying soft self-assembled materials via unsupervised machine learning of defects. *Commun. Chem.*, 5(1), 2022.

[88] S. P. Afrose, S. Bal, A. Chatterjee, K. Das, and D. Das. Designed negative feedback from transiently formed catalytic nanostructures. *Angew. Chem.*, 131(44):15930–15934, 2019.

[89] S. P. Afrose, C. Ghosh, and D. Das. Substrate induced generation of transient self-assembled catalytic systems. *Chem. Sci.*, 12:14674–14685, 2021.

[90] M. Girard, S. Wang, J. S. Du, A. Das, Z. Huang, V. P. Dravid, B. Lee, C. A. Mirkin, and M. Olvera de la Cruz. Particle analogs of electrons in colloidal crystals. *Science*, 364(6446):1174–1178, 2019.

[91] C. R. Laramy, M. N. O'Brien, and C. A. Mirkin. Crystal engineering with DNA. *Nat. Rev. Mater.*, 4(3):201–224, 2019.

[92] Y. Lin and M. Olvera de la Cruz. Sublattice melting in binary superionic colloidal crystals. *Phys. Rev. E*, 101(3):032603, 2020.

[93] A. Ehlen, H. Lopez-Rios, and M. Olvera de la Cruz. Metallization of colloidal crystals. *Phys. Rev. Mater.*, 5(11):115601, 2021.

[94] H. Lopez-Rios, A. Ehlen, and M. Olvera de la Cruz. Delocalization transition in colloidal crystals. *J. Phys. Chem. C*, 125(1):1096–1106, 2021.

[95] S. Wang, S. Lee, J. S. Du, B. E. Partridge, H. F. Cheng, W. Zhou, V. P. Dravid, B. Lee, S. C. Glotzer, and C. A. Mirkin. The emergence of valency in colloidal crystals through electron equivalents. *Nat. Mat.*, 21:580–587, 2022.

[96] H. F. Cheng, S. Wang, and C. A. Mirkin. Electron-Equivalent Valency through Molecularly Well-Defined Multivalent DNA. *J. Am. Chem. Soc.*, 143(4):1752–1757, 2021.

[97] H. Nakanishi, D. A. Walker, K. J. M. Bishop, P. J. Wesson, Y. Yan, S. Soh, S. Swaminathan, and B. A. Grzybowski. Dynamic internal gradients control and direct electric currents within nanostructured materials. *Nat. Nanotechnol.*, 6(11):740–746, 2011.

[98] Y. Yan, S. C. Warren, P. Fuller, and B. A. Grzybowski. Chemoelectronic circuits based on metal nanoparticles. *Nat. Nanotechnol.*, 11(7):603–608, 2016.

[99] X. Zhao, L. Yang, J. Guo, T. Xiao, Y. Zhou, Y. Zhang, B. Tu, T. Li, B. A. Grzybowski, and Y. Yan. Transistors and logic circuits based on metal nanoparticles and ionic gradients. *Nat. Electron.*, 4(2):109–115, 2021.

[100] T. Bian, A. Gardin, J. Gemen, L. Houben, C. Perego, B. Lee, N. Elad, Z. Chu, G. M. Pavan, and R. Klajn. Electrostatic co-assembly of nanoparticles with oppositely charged small molecules into static and dynamic superstructures. *Nat. Chem.*, 13(10):940–949, 2021.

[101] O. Silakari and P. K. Singh. Fundamentals of molecular modeling. In *Concepts and Experimental Protocols of Modelling and Informatics in Drug Design*, pages 1–27. Elsevier, 2021.

[102] Y. Gu and M. Li. Molecular modeling. In *Handbook of Benzoxazine Resins*, pages 103–110. Elsevier, 2011.

[103] M. A. González. Force fields and molecular dynamics simulations. *École thématique de la Société Française de la Neutronique*, 12:169–200, 2011.

[104] R. Capelli, A. Gardin, C. Empereur-mot, G. Doni, and G. M. Pavan. A data-driven dimensionality reduction approach to compare and classify lipid force fields. *J. Phys. Chem. B*, 125(28):7785–7796, 2021.

[105] S. J. Marrink, H. J. Risselada, S. Yefimov, D. P. Tieleman, and A. H. de Vries. The MARTINI force field: coarse grained model for biomolecular simulations. *J. Phys. Chem. B*, 111(27):7812–7824, 2007.

[106] S. J. Marrink and D. P. Tieleman. Perspective on the martini model. *Chem. Soc. Rev.*, 42(16):6801, 2013.

[107] C. Peter and K. Kremer. Multiscale simulation of soft matter systems – from the atomistic to the coarse-grained level and back. *Soft Matter*, 5(22):4357, 2009.

[108] C. Peter and K. Kremer. Multiscale simulation of soft matter systems. *Faraday Discuss.*, 144:9–24, 2010.

[109] P. C. T. Souza, R. Alessandri, J. Barnoud, S. Thallmair, I. Faustino, F. Grünewald, I Patmanidis, H. Abdizadeh, B. M. H. Bruininks, T. A. Wassenaar, P. C. Kroon, J. Melcr, V. Nieto, V. Corradi, H. M. Khan, J. Domański, M. Javanainen, H. Martinez-Seara, N. Reuter, R. B. Best, I. Vattulainen, L. Monticelli, X. Periole, D. P. Tieleman, A. H. de Vries, and S. J. Marrink. Martini 3: a general purpose force field for coarse-grained molecular dynamics. *Nat. Methods*, 18(4):382–388, 2021.

[110] X. Periole and S. J. Marrink. The martini coarse-grained force field. In *Methods in Molecular Biology*, pages 533–565. Humana Press, 2012.

[111] C. Arnarez, J. J. Uusitalo, M. F. Masman, H. I. Ingólfsson, D. H. de Jong, M. N. Melo, X. Periole, A. H. de Vries, and S. J. Marrink. Dry martini, a coarse-grained force field for lipid membrane simulations with implicit solvent. *J. Chem. Theory Comput.*, 11(1):260–275, 2014.

[112] D. Frenkel and S. Berend. *Understanding Molecular Simulations*. Academic Press, 2002.

[113] M. E. Tuckerman. *Statistical Mechanics: Theory and Molecular Simulations*. Oxford Graduate Texts, 2010.

[114] K. Koner, S. Karak, S. Kandambeth, S. Karak, N. Thomas, L. Leanza, C. Perego, L. Pesce, R. Capelli, M. Moun, M. Bhakar, T. G. Ajithkumar, G. M. Pavan, and R. Banerjee. Porous covalent organic nanotubes and their assembly in loops and toroids. *Nat. Chem.*, 14(5):507–514, 2022.

[115] Shankar Kumar, John M. Rosenberg, Djamal Bouzida, Robert H. Swendsen, and Peter A. Kollman. THE weighted histogram analysis method for free-energy calculations on biomolecules. i. the method. *J. Comput. Chem.*, 13(8):1011–1021, 1992.

[116] Till Siebenmorgen, Michael Engelhard, and Martin Zacharias. Prediction of protein–protein complexes using replica exchange with repulsive scaling. *J. Comput. Chem.*, 41(15):1436–1447, 2020.

[117] The PLUMED Consortium. Promoting transparency and reproducibility in enhanced molecular simulations. *Nat. Methods*, 16(8):670–673, 2019.

[118] G. A. Tribello, M. Bonomi, D. Branduardi, C. Camilloni, and G. Bussi. Plumed 2: New feathers for an old bird. *Comput. Phys. Commun.*, 185(2):604–613, 2014.

[119] M. Bonomi, D. Branduardi, G. Bussi, C. Camilloni, D. Provasi, P. Raiteri, D. Donadio, F. Marinelli, F. Pietrucci, R. A. Broglia, and M. Parrinello. Plumed: A portable plugin for free-energy calculations with molecular dynamics. *Comput. Phys. Commun.*, 180(10):1961–1972, 2009.

[120] M. A. Caro. Optimizing many-body atomic descriptors for enhanced computational performance of machine learning based interatomic potentials. *Phys. Rev. B*, 100:024112, 2019.

[121] A. P. Bartók, R. Kondor, and G. Csányi. On representing chemical environments. *Phys. Rev. B*, 87:184115, 2013.

[122] L. Himanen, M. O. J. Jäger, E. V. Morooka, F. Federici Canova, Y. S. Ranawat, D. Z. Gao, P. Rinke, and Foster A. S. Dscribe: Library of descriptors for machine learning in materials science. *Comput. Phys. Commun.*, 247:106949, 2020.

[123] M. Ringnér. What is principal component analysis? *Nat. Biotechnol.*, 26(3):303–304, 2008.

[124] P. Gasparotto and M. Ceriotti. Recognizing molecular patterns by machine learning: An agnostic structural definition of the hydrogen bond. *J. Chem. Phys.*, 141(17):174110, 2014.

[125] P. Gasparotto, R. H. Meißner, and Ceriotti M. Recognizing local and global structural motifs at the atomic scale. *J. Chem. Theory Comput.*, 14(2):486–498, 2018.

[126] C. Lionello, A. Gardin, A. Cardellini, D. Bochicchio, M. Shivrayan, A. Fernandez, S. Thayumanavan, and G. M. Pavan. Toward chemotactic supramolecular nanoparticles: from autonomous surface motion following specific chemical gradients to multivalency-controlled disassembly. *ACS nano*, 15(10):16149–16161, 2021.

[127] S. de Oliveira, E. E. Rosowski, and A. Huttenlocher. Neutrophil migration in infection and wound repair: going forward in reverse. *Nat. Rev. Immunol.*, 16(6):378–391, 2016.

[128] C. H. Stuelten, C. A. Parent, and D. J. Montell. Cell motility in cancer invasion and metastasis: insights from simple model organisms. *Nat. Rev. Cancer*, 18(5):296–312, 2018.

[129] X. Trepat, M. R. Wasserman, T. E. Angelini, E. Millet, D. A. Weitz, J. P. Butler, and J. J. Fredberg. Physical forces during collective cell migration. *Nature Physics*, 5(6):426–430, 2009.

[130] D. T. Tambe, C. C. Hardin, T. E. Angelini, K. Rajendran, C. Y. Park, X. Serra-Picamal, E. H. Zhou, M. H. Zaman, J. P. Butler, D. A. Weitz, J. J. Fredberg, and X. Trepat. Collective cell guidance by cooperative intercellular forces. *Nat. Mat.*, 10(6):469–475, 2011.

[131] P. Roca-Cusachs, R. Sunyer, and X. Trepat. Mechanical guidance of cell migration: lessons from chemotaxis. *Curr. Opin. Cell Biol.*, 25(5):543–549, 2013.

[132] D. A. Torres, M. Garzoni, A. V. Subrahmanyam, G. M. Pavan, and S. Thayumanavan. Protein-triggered supramolecular disassembly: Insights based on variations in ligand location in amphiphilic dendrons. *J. Am. Chem. Soc.*, 136(14):5385–5399, 2014.

[133] L. D. Zarzar and J. Aizenberg. Stimuli-responsive chemomechanical actuation: A hybrid materials approach. *Acc. Chem. Res.*, 47(2):530–539, 2013.

[134] S. N. Semenov, L. J. Kraft, A. Ainla, M. Zhao, M. Baghbanzadeh, V. E. Campbell, K. Kang, J. M. Fox, and G. M. Whitesides. Autocatalytic, bistable, oscillatory networks of biologically relevant organic reactions. *Nature*, 537(7622):656–660, 2016.

[135] J. Cui, D. Daniel, A. Grinthal, K. Lin, and J. Aizenberg. Dynamic polymer systems with self-regulated secretion for the control of surface properties and material healing. *Nat. Mat.*, 14(8):790–795, 2015.

[136] J. Liu, H. Xu, X. Tang, J. Xu, Z. Jin, H. Li, S. Wang, J. Gou, and X. Jin. Simple and tunable surface coatings via polydopamine for modulating pharmacokinetics, cell uptake and biodistribution of polymeric nanoparticles. *RSC Adv.*, 7(26):15864–15876, 2017.

[137] F. Xu, L. Pfeifer, S. Crespi, F. K.-C. Leung, M. C. A. Stuart, S. J. Wezenberg, and B. L. Feringa. From photoinduced supramolecular polymerization to responsive organogels. *J. Am. Chem. Soc.*, 143(15):5990–5997, 2021.

[138] I. Roy, S. Bobbala, R. M. Young, Y. Beldjoudi, M. T. Nguyen, M. M. Cetin, J. A. Cooper, S. Allen, O. Anamimoghadam, E. A. Scott, M. R. Wasielewski, and J. F. Stoddart. A supramolecular approach for modulated photoprotection, lysosomal delivery, and photodynamic activity of a photosensitizer. *J. Am. Chem. Soc.*, 141(31):12296–12304, 2019.

[139] Y.-H. Liao, C.-H. Lin, C.-Y. Cheng, W. C. Wong, J.-Y. Juo, and C.-L. Hsieh. Monovalent and oriented labeling of gold nanoprobes for the high-resolution tracking of a single-membrane molecule. *ACS Nano*, 13(10):10918–10928, 2019.

[140] N. J. Overeem, P. H. E. Hamming, M. Tieke, E. van der Vries, and J. Huskens. Multivalent affinity profiling: Direct visualization of the superselective binding of influenza viruses. *ACS Nano*, 15(5):8525–8536, 2021.

[141] Y. Yu, Y. Gao, and Y. Yu. "waltz" of cell membrane-coated nanoparticles on lipid bilayers: Tracking single particle rotation in ligand–receptor binding. *ACS Nano*, 12(12):11871–11880, 2018.

[142] R. W. Taylor, R. G. Mahmoodabadi, V. Rauschenberger, A. Giessl, A. Schambony, and V. Sandoghdar. Interferometric scattering microscopy reveals microsecond nanoscopic protein motion on a live cell membrane. *Nat. Photon.*, 13(7):480–487, 2019.

[143] M. Wang, S. R. Ravindranath, M. K. Rahim, E. L. Botvinick, and J. B. Haun. Evolution of multivalent nanoparticle adhesion via specific molecular interactions. *Langmuir*, 32(49):13124–13136, 2016.

[144] L. Lin and X. Zeng. Computational study of cell adhesion and rolling in flow channel by meshfree method. *Comput. Methods Biomech. Biomed. Engin.*, 20(8):832–841, 2017.

[145] G. Arya and A. Z. Panagiotopoulos. Log-rolling micelles in sheared amphiphilic thin films. *Phys. Rev. Lett.*, 95(18), 2005.

[146] T. Curk, J. Dobnikar, and D. Frenkel. Optimal multivalent targeting of membranes with many distinct receptors. *Proc. Natl. Acad. Sci. U.S.A.*, 114(28):7210–7215, 2017.

[147] V. E. Debets, L. M. C. Janssen, and A. Šarić. Characterising the diffusion of biological nanoparticles on fluid and cross-linked membranes. *Soft Matter*, 16(47):10628–10639, 2020.

[148] C. S. Korosec, L. Jindal, M. Schneider, I. C. de la Barca, M. J. Zuckermann, N. R. Forde, and E. Emberly. Substrate stiffness tunes the dynamics of polyvalent rolling motors. *Soft Matter*, 17(6):1468–1479, 2021.

[149] I. Palaia, A. Paraschiv, V. E. Debets, C. Storm, and A. Šarić. Durotaxis of passive nanoparticles on elastic membranes. *ACS Nano*, 15(10):15794–15802, 2021.

[150] M. D. M. Peri and C. Cetinkaya. Spherical nanoparticle–substrate adhesion interaction simulations utilizing molecular dynamics. *J. Adhes. Sci. Technol.*, 23(13-14):1723–1738, 2009.

[151] M. J. Abraham, T. Murtola, R. Schulz, S. Páll, J. C Smith, B. Hess, and E. Lindahl. Gromacs: High performance molecular simulations through multi-level parallelism from laptops to supercomputers. *SoftwareX*, 1:19–25, 2015.

[152] M. D. Hanwell, D. E Curtis, D. C. Lonie, T. Vandermeersch, E. Zurek, and G. R. Hutchison. Avogadro: an advanced semantic chemical editor, visualization, and analysis platform. *J. Cheminform.*, 4(1):1–17, 2012.

[153] J. Wang, R. M. Wolf, J. W. Caldwell, P. A. Kollman, and D. A. Case. Development and testing of a general amber force field. *J. Comput. Chem.*, 25(9):1157–1174, 2004.

[154] J. Wang, W. Wang, P. A. Kollman, and D. A. Case. Automatic atom type and bond type perception in molecular mechanical calculations. *J. Mol. Graph. Model.*, 25(2):247–260, 2006.

[155] E. N. Marieb and K. Hoehn. The muscular system. *Human Anatomy and Physiology, 9th edition. Boston, MA: Pearson Education*, pages 346–353, 2013.

[156] J. Gao, H. Wang, J. Zhuang, and S. Thayumanavan. Tunable enzyme responses in amphiphilic nanoassemblies through alterations in the unimer–aggregate equilibrium. *Chem. Sci.*, 10(10):3018–3024, 2019.

[157] D. Bochicchio and G. M. Pavan. Molecular modelling of supramolecular polymers. *Adv. Phys.: X*, 3(1):1436408, 2018.

[158] O. Munkhbat, M. Garzoni, K. R. Raghupathi, G. M. Pavan, and S. Thayumanavan. Role of aromatic interactions in temperature-sensitive amphiphilic supramolecular assemblies. *Langmuir*, 32(12):2874–2881, 2016.

[159] A. Cardellini, M. Crippa, C. Lionello, S. P. Afrose, D. Das, and G. M. Pavan. Unsupervised data-driven reconstruction of molecular motifs in simple to complex dynamic micelles. *J. Phys. Chem. B*, 127(11):2595–2608, 2022.

[160] Y. Cho, T. Christoff-Tempesta, S. J Kaser, and J. H. Ortony. Dynamics in supramolecular nanomaterials. *Soft Matter*, 17(24):5850–5863, 2021.

[161] Y. Cho, T. Christoff-Tempesta, D.-Y. Kim, G. Lamour, and J. H. Ortony. Domain-selective thermal decomposition within supramolecular nanoribbons. *Nat. Commun.*, 12(1):1–7, 2021.

[162] M. Wang, J. Wang, P. Zhou, J. Deng, Y. Zhao, Y. Sun, W. Yang, D. Wang, Z. Li, X. Hu, S. M. King, S. E. Rogers, H. Cox, T. A. Waigh, J. Yang, J. R. Lu, and H. Xu. Nanoribbons self-assembled from short peptides demonstrate the formation of polar zippers between β-sheets. *Nat. Commun.*, 9(1):1–11, 2018.

[163] L. Albertazzi, F. J. Martinez-Veracoechea, C. M. A. Leenders, I. K. Voets, D. Frenkel, and E. W. Meijer. Spatiotemporal control and superselectivity in supramolecular polymers using multivalency. *Proc. Natl. Acad. Sci. U. S. A.*, 110(30):12203–12208, 2013.

[164] T. Aida, E. W. Meijer, and S. I. Stupp. Functional supramolecular polymers. *Science*, 335(6070):813–817, 2012.

[165] M. J. Webber, E. A. Appel, E. W. Meijer, and R. Langer. Supramolecular biomaterials. *Nat. Mater.*, 15(1):13–26, 2016.

[166] J. D. Hartgerink, E. Beniash, and S. I. Stupp. Self-assembly and mineralization of peptide-amphiphile nanofibers. *Science*, 294(5547):1684–1688, 2001.

[167] C. J. Newcomb, T. J. Moyer, S. S. Lee, and S. I. Stupp. Advances in cryogenic transmission electron microscopy for the characterization of dynamic self-assembling nanostructures. *Curr. Opin. Colloid Interface Sci.*, 17(6):350–359, 2012.

[168] D. L. Pink, O. Loruthai, R. M. Ziolek, A. E. Terry, D. J. Barlow, M. J. Lawrence, and C. D. Lorenz. Interplay of lipid and surfactant: Impact on nanoparticle structure. *J. Colloid Interface Sci.*, 597:278–288, 2021.

[169] C. Perego, L. Pesce, R. Capelli, S. J George, and G. M. Pavan. Multiscale molecular modelling of atp-fueled supramolecular polymerisation and depolymerisation. *ChemSystemsChem*, 3(2):e2000038, 2021.

[170] H. Liu, C. Lionello, J. Westley, A. Cardellini, U. Huynh, G. M Pavan, and S Thayumanavan. Understanding functional group and assembly dynamics in temperature responsive systems leads to design principles for enzyme responsive assemblies. *Nanoscale*, 13(26):11568–11575, 2021.

[171] G. Ragazzon and L. J. Prins. Energy consumption in chemical fuel-driven self-assembly. *Nat. Nanotechnol.*, 13(10):882–889, 2018.

[172] X. Lou, R. P. M. Lafleur, C. Leenders, S. Schoenmakers, N. M. Matsumoto, M. B. Baker, J. L. J. Van Dongen, A. R. A. Palmans, and E.W. Meijer. Dynamic diversity of synthetic supramolecular polymers in water as revealed by hydrogen/deuterium exchange. *Nat. Commun.*, 8(1):1–8, 2017.

[173] B. Hess, C. Kutzner, D. van der Spoel, and E. Lindahl. GROMACS 4: Algorithms for Highly Efficient, Load-Balanced, and Scalable Molecular Simulation. *J. Chem. Theory Comput.*, 4(3):435–447, 2008.

[174] H. C. Andersen. Molecular dynamics simulations at constant pressure and/or temperature. *J. Chem. Phys.*, 72(4):2384–2393, 1980.

[175] M. Parrinello and A. Rahman. Polymorphic transitions in single crystals: A new molecular dynamics method. *J. Appl. Phys.*, 52(12):7182–7190, 1981.

[176] W. L. Jorgensen, D. S. Maxwell, and J. Tirado-Rives. Development and testing of the opls all-atom force field on conformational energetics and properties of organic liquids. *J. Am. Chem. Soc.*, 118(45):11225–11236, 1996.

[177] T. Darden, D. York, and L. Pedersen. Particle mesh ewald: An n log (n) method for ewald sums in large systems. *J. Chem. Phys.*, 98(12):10089–10092, 1993.

[178] H. J. C. Berendsen, J. R. Grigera, and T. P. Straatsma. The missing term in effective pair potentials. *J. Phys. Chem.*, 91(24):6269–6271, 1987.

[179] G. Bussi, D. Donadio, and M. Parrinello. Canonical sampling through velocity rescaling. *J. Chem. Phys.*, 126(1):014101, 2007.

[180] S. Nosé. A unified formulation of the constant temperature molecular dynamics methods. *J. Chem. Phys.*, 81(1):511–519, 1984.

[181] H. J. C. Berendsen, J. P. M. Postma, W. F. Van Gunsteren, A. R. H. J. Di Nola, and J. R Haak. Molecular dynamics with coupling to an external bath. *J. Chem. Phys.*, 81(8):3684–3690, 1984.

[182] E. Facco, M. d'Errico, A. Rodriguez, and A. Laio. Estimating the intrinsic dimension of datasets by a minimal neighborhood information. *Sci. Rep.*, 7(1):1–8, 2017.

[183] C. Lionello, C. Perego, A. Gardin, R. Klajn, and G. M. Pavan. Supramolecular semiconductivity through emerging ionic gates in ion–nanoparticle superlattices. *ACS Nano*, 17(1):275–287, 2023.

[184] M. A. Boles, M. Engel, and D. V. Talapin. Self-assembly of colloidal nanocrystals: From intricate structures to functional materials. *Chem. Rev.*, 116(18):11220–11289, 2016.

[185] D. E. Bergeron, P. J. Roach, A. W. Castleman, N. O. Jones, and S. N. Khanna. Al cluster superatoms as halogens in polyhalides and as alkaline earths in iodide salts. *Science*, 307(5707):231–235, 2005.

[186] M. Walter, J. Akola, O. Lopez-Acevedo, P. D. Jadzinsky, G. Calero, C. J. Ackerson, R. L. Whetten, H. Grönbeck, and H. Häkkinen. A unified view of ligand-protected gold clusters as superatom complexes. *Proc. Natl. Acad. Sci. U.S.A.*, 105(27):9157–9162, 2008.

[187] D. Vanmaekelbergh. Self-assembly of colloidal nanocrystals as route to novel classes of nanostructured materials. *Nano Today*, 6(4):419–437, 2011.

[188] K. Liu, Z. Nie, N. Zhao, W. Li, M. Rubinstein, and E. Kumacheva. Step-growth polymerization of inorganic nanoparticles. *Science*, 329(5988):197–200, 2010.

[189] G. Meng, N. Arkus, M. P. Brenner, and V. N. Manoharan. The free-energy landscape of cluster of attractive hard spheres. *Science*, 327(5965):560–563, 2010.

[190] A. Klinkova, H. Thérien-Aubin, R. M. Choueiri, M. Rubinstein, and E. Kumacheva. Colloidal analogs of molecular chain stoppers. *Proc. Natl. Acad. Sci. U.S.A.*, 110(47):18775–18779, 2013.

[191] K. Liu, A. Lukach, K. Sugikawa, S. Chung, J. Vickery, H. Therien-Aubin, B. Yang, M. Rubinstein, and E. Kumacheva. Copolymerization of Metal Nanoparticles: A Route to Colloidal Plasmonic Copolymers. *Angew. Chem. Int. Ed.*, 53(10):2648–2653, 2014.

[192] M. P. Boneschanscher, W. H. Evers, J. J. Geuchies, T. Altantzis, B. Goris, F. T. Rabouw, S. A. P. van Rossum, H. S. J. van der Zant, L. D. A. Siebbeles, G. Van Tendeloo, I. Swart, J. Hilhorst, A. V. Petukhov, S. Bals, and D. Vanmaekelbergh. Long-range orientation and atomic attachment of nanocrystals in 2D honeycomb superlattices. *Science*, 344(6190):1377–1380, 2014.

[193] M. Grzelczak, L. M. Liz-Marzán, and R. Klajn. Stimuli-responsive self-assembly of nanoparticles. *Chem. Soc. Rev.*, 48(5):1342–1361, 2019.

[194] C. Yi, H. Liu, S. Zhang, Y. Yang, Y. Zhang, Z. Lu, E. Kumacheva, and Z. Nie. Self-limiting directional nanoparticle bonding governed by reaction stoichiometry. *Science*, 369(6509):1369–1374, 2020.

[195] M. S. Lee, D. W. Yee, M. Ye, and R. J. Macfarlane. Nanoparticle Assembly as a Materials Development Tool. *J. Am. Chem. Soc.*, 144(8):3330–3346, 2022.

[196] C. B. Murray, C. R. Kagan, and M. G. Bawendi. Synthesis and characterization of monodisperse nanocrystals and close-packed nanocrystal assemblies. *Annu. Rev. Mater. Sci.*, 30(1):545–610, 2000.

[197] E. V. Shevchenko, D. V. Talapin, N. A. Kotov, S. O'Brien, and C. B. Murray. Structural diversity in binary nanoparticle superlattices. *Nature*, 439(7072):55–59, 2006.

[198] E. Auyeung, T. I. N. G. Li, A. J. Senesi, A. L. Schmucker, B. C. Pals, M. Olvera de la Cruz, and C. A. Mirkin. DNA-mediated nanoparticle crystallization into Wulff polyhedra. *Nature*, 505(7481):73–77, 2014.

[199] T. Paik, B. T. Diroll, C. R. Kagan, and C. B. Murray. Binary and ternary superlattices self-assembled from colloidal nanodisks and nanorods. *J. Am. Chem. Soc.*, 137(20):6662–6669, 2015.

[200] M. A. Boles and D. V. Talapin. Many-body effects in nanocrystal superlattices: Departure from sphere packing explains stability of binary phases. *J. Am. Chem. Soc.*, 137(13):4494–4502, 2015.

[201] M. Huang, C.-H. Hsu, J. Wang, S. Mei, X. Dong, Y. Li, M. Li, H. Liu, W. Zhang, T. Aida, W.-B. Zhang, K. Yue, and S. Z. D. Cheng. Selective assemblies of giant tetrahedra via precisely controlled positional interactions. *Science*, 348(6233):424–428, 2015.

[202] T. Udayabhaskararao, T. Altantzis, L. Houben, M. Coronado-Puchau, J. Langer, R. Popovitz-Biro, L. M. Liz-Marzán, L. Vuković, P. Král, S. Bals, and R. Klajn. Tunable porous nanoallotropes prepared by post-assembly etching of binary nanoparticle superlattices. *Science*, 358(6362):514–518, 2017.

[203] M. He, J. P. Gales, É. Ducrot, Z. Gong, G.-R. Yi, S. Sacanna, and D. J. Pine. Colloidal diamond. *Nature*, 585(7826):524–529, 2020.

[204] D. V. Talapin, E. V. Shevchenko, M. I. Bodnarchuk, X. Ye, J. Chen, and C. B. Murray. Quasicrystalline order in self-assembled binary nanoparticle superlattices. *Nature*, 461(7266):964–967, 2009.

[205] X. Ye, J. Chen, M. E. Irrgang, M. Engel, A. Dong, S. C. Glotzer, and C. B. Murray. Quasicrystalline nanocrystal superlattice with partial matching rules. *Nat. Mat.*, 16(2):214–219, 2017.

[206] K. S. Sugi, A. Maier, and M. Scheele. Emergent properties in supercrystals of atomically precise nanoclusters and colloidal nanocrystals. *Chem. Commun.*, 58:6998–7017, 2022.

[207] C. A. Mirkin, R. L. Letsinger, R. C. Mucic, and J. J. Storhoff. A DNA-based method for rationally assembling nanoparticles into macroscopic materials. *Nature*, 382(6592):607–609, 1996.

[208] A. M. Kalsin, M. Fialkowski, M. Paszewski, S. K. Smoukov, K. J. M. Bishop, and B. A. Grzybowski. Electrostatic Self-Assembly of Binary Nanoparticle Crystals with a Diamond-Like Lattice. *Science*, 312(5772):420–424, 2006.

[209] S. C. Glotzer and M. J. Solomon. Anisotropy of building blocks and their assembly into complex structures. *Nat. Mat.*, 6(8):557–562, 2007.

[210] P. F. Damasceno, M. Engel, and S. C. Glotzer. Predictive self-assembly of polyhedra into complex structures. *Science*, 337(6093):453–457, 2012.

[211] D. Frenkel. Order through entropy. *Nat. Mat.*, 14(1):9–12, 2015.

[212] Y. Geng, G. van Anders, P. M. Dodd, J. Dshemuchadse, and S. C. Glotzer. Engineering entropy for the inverse design of colloidal crystals from hard shapes. *Sci. Adv.*, 5(7):eaaw0514, 2019.

[213] A. Abelson, C. Qian, T. Salk, Z. Luan, K. Fu, J.-G. Zheng, J. L. Wardini, and M. Law. Collective topo-epitaxy in the self-assembly of a 3D quantum dot superlattice. *Nat. Mat.*, 19(1):49–55, 2020.

[214] F. A. Aldaye, A. L. Palmer, and H. F. Sleiman. Assembling Materials with DNA as the Guide. *Science*, 321(5897):1795–1799, 2008.

[215] D. Nykypanchuk, M. M. Maye, D. van der Lelie, and O. Gang. DNA-guided crystallization of colloidal nanoparticles. *Nature*, 451(7178):549–552, 2008.

[216] R. J. Macfarlane, B. Lee, M. R. Jones, N. Harris, G. C. Schatz, and C. A. Mirkin. Nanoparticle superlattice engineering with DNA. *Science*, 334(6053):204–208, 2011.

[217] Y. Wang, Y. Wang, D. R. Breed, V. N. Manoharan, L. Feng, A. D. Hollingsworth, M. Weck, and D. J. Pine. Colloids with valence and specific directional bonding. *Nature*, 491(7422):51–55, 2012.

[218] W. Liu, M. Tagawa, H. L. Xin, T. Wang, H. Emamy, H. Li, K. G. Yager, F. W. Starr, A. V. Tkachenko, and O. Gang. Diamond family of nanoparticle superlattices. *Science*, 351(6273):582–586, 2016.

[219] H. Lin, S. Lee, L. Sun, M. Spellings, M. Engel, S. C. Glotzer, and C. A. Mirkin. Clathrate colloidal crystals. *Science*, 355(6328):931–935, 2017.

[220] A. M. Kalsin, B. Kowalczyk, S. K. Smoukov, R. Klajn, and B. A. Grzybowski. Ionic-like Behavior of Oppositely Charged Nanoparticles. *J. Am. Chem. Soc.*, 128(47):15046–15047, 2006.

[221] A. M. Kalsin and B. A. Grzybowski. Controlling the Growth of "Ionic" Nanoparticle Supracrystals. *Nano Lett.*, 7(4):1018–1021, 2007.

[222] L. Wang, P.-A. Albouy, and M.-P. Pileni. Synthesis and self-assembly behavior of charged Au nanocrystals in aqueous solution. *Chem. Mater.*, 27(12):4431–4440, 2015.

[223] M. A. Kostiainen, P. Hiekkataipale, A. Laiho, V. Lemieux, J. Seitsonen, J. Ruokolainen, and P. Ceci. Electrostatic assembly of binary nanoparticle superlattices using protein cages. *Nat. Nanotechnol.*, 8(1):52–56, 2013.

[224] S. Kewalramani, G. I. Guerrero-García, L. M. Moreau, J. W. Zwanikken, C. A. Mirkin, M. Olvera de la Cruz, and M. J. Bedzyk. Electrolyte-Mediated Assembly of Charged Nanoparticles. *ACS Cent. Sci.*, 2(4):219–224, 2016.

[225] I. Coropceanu, E. M. Janke, J. Portner, D. Haubold, T. D. Nguyen, A. Das, C. P. N. Tanner, J. K. Utterback, S. W. Teitelbaum, M. H. Hudson, N. A. Sarma, A. M. Hinkle, C. J. Tassone, A. Eychmüller, D. T. Limmer, M. Olvera de la Cruz, N. S. Ginsberg, and D. V. Talapin. Self-assembly of nanocrystals into strongly electronically coupled all-inorganic supercrystals. *Science*, 375(6587):1422–1426, 2022.

[226] M. Garzoni, N. Cheval, A. Fahmi, A. Danani, and G. M. Pavan. Ion-Selective Controlled Assembly of Dendrimer-Based Functional Nanofibers and Their Ionic-Competitive Disassembly. *J. Am. Chem. Soc.*, 134(7):3349–3357, February 2012.

[227] M. V. Kovalenko, M. Scheele, and D. V. Talapin. Colloidal Nanocrystals with Molecular Metal Chalcogenide Surface Ligands. *Science*, 324(5933):1417–1420, 2009.

[228] J.-S. Lee, M. V. Kovalenko, J. Huang, D. S. Chung, and D. V. Talapin. Band-like transport, high electron mobility and high photoconductivity in all-inorganic nanocrystal arrays. *Nat. Nanotechnol.*, 6(6):348–352, 2011.

[229] J. Liao, L. Bernard, M. Langer, C. Schönenberger, and M. Calame. Reversible formation of molecular junctions in 2d nanoparticle arrays. *Adv. Mater.*, 18(18):2444–2447, 2006.

[230] V. Astachov, M. Garzoni, A. Danani, K.-L. Choy, G. M. Pavan, and A. Fahmi. In situ functionalization of self-assembled dendrimer nanofibers with cadmium sulfide quantum dots through simple ionic-substitution. *New J. Chem.*, 40(7):6325–6331, 2016.

[231] X. Zhao, B. Tu, M. Li, X. Feng, Y. Zhang, Q. Fang, T. Li, B. A. Grzybowski, and Y. Yan. Switchable counterion gradients around charged metallic nanoparticles enable reception of radio waves. *Sci. Adv.*, 4(10):eaau3546, 2018.

[232] X. Zhao, J. Guo, T. Xiao, Y. Zhang, Y. Yan, and B. A. Grzybowski. Charged Metal Nanoparticles for Chemoelectronic Circuits. *Adv. Mater.*, 31(45):1804864, 2019.

[233] J. Chen, A. Dong, J. Cai, X. Ye, Y. Kang, J. M. Kikkawa, and C. B. Murray. Collective dipolar interactions in self-assembled magnetic binary nanocrystal superlattice membranes. *Nano Lett.*, 10(12):5103–5108, 2010.

[234] C. Zhan, X.-J. Chen, J. Yi, J.-F. Li, D.-Y. Wu, and Z.-Q. Tian. From plasmon-enhanced molecular spectroscopy to plasmon-mediated chemical reactions. *Nat. Rev. Chem.*, 2(9):216–230, 2018.

[235] M. Haase and H. Schäfer. Upconverting Nanoparticles. *Angew. Chem. Int. Ed.*, 50(26):5808–5829, 2011.

[236] N. S. Mueller, Y. Okamura, B. G. M. Vieira, S. Juergensen, H. Lange, E. B. Barros, F. Schulz, and S. Reich. Deep strong light–matter coupling in plasmonic nanoparticle crystals. *Nature*, 583(7818):780–784, 2020.

[237] D. H. Son, S. M. Hughes, Y. Yin, and A. Paul Alivisatos. Cation exchange reactions in ionic nanocrystals. *Science*, 306(5698):1009–1012, 2004.

[238] H. Li, M. Zanella, A. Genovese, M. Povia, A. Falqui, C. Giannini, and L. Manna. Sequential cation exchange in nanocrystals: Preservation of crystal phase and formation of metastable phases. *Nano Lett.*, 11(11):4964–4970, 2011.

[239] K. R. Krishnadas, A. Baksi, A. Ghosh, G. Natarajan, A. Som, and T. Pradeep. Interparticle Reactions: An Emerging Direction in Nanomaterials Chemistry. *Acc. Chem. Res.*, 50(8):1988–1996, 2017.

[240] S. Wang, J. S. Du, N. J. Diercks, W. Zhou, E. W. Roth, V. P. Dravid, and C. A. Mirkin. Colloidal Crystal "Alloys". *J. Am. Chem. Soc.*, 141(51):20443–20450, 2019.

[241] S. Y. Park, A. K. R. Lytton-Jean, B. Lee, S. Weigand, G. C. Schatz, and C. A. Mirkin. DNA-programmable nanoparticle crystallization. *Nature*, 451(7178):553–556, 2008.

[242] M. R. Jones, N. C. Seeman, and C. A. Mirkin. Programmable materials and the nature of the DNA bond. *Science*, 347(6224):1260901, 2015.

[243] T. Cao, I. Szilagyi, T. Oncsik, M. Borkovec, and G. Trefalt. Aggregation of colloidal particles in the presence of multivalent co-ions: The Inverse Schulze–Hardy Rule. *Langmuir*, 31(24):6610–6614, 2015.

[244] Y. Li, M. Girard, M. Shen, J. A. Millan, and M. Olvera de la Cruz. Strong attractions and repulsions mediated by monovalent salts. *Proc. Natl. Acad. Sci. U.S.A.*, 114(45):11838–11843, 2017.

[245] Y. Lin and M. Olvera de la Cruz. Superionic colloidal crystals: Ionic to metallic bonding transitions. *J. Phys. Chem. B*, 126:6740–6749, 2022.

[246] S. Hull. Superionics: crystal structures and conduction processes. *Rep. Prog. Phys.*, 67(7):1233–1314, 2004.

[247] N. Kamaya, K. Homma, Y. Yamakawa, M. Hirayama, R. Kanno, M. Yonemura, T. Kamiyama, Y Kato, S. Hama, K. Kawamoto, and A. Mitsui. A lithium superionic conductor. *Nat. Mat.*, 10:682–686, 2011.

[248] Y. Wang, W. D. Richards, S. P. Ong, L. J. Miara, J. C. Kim, Y. Mo, and G. Ceder. Design principles for solid-state lithium superionic conductors. *Nat. Mat.*, 14:1026–1031, 2015.

[249] X. He, Y. Zhu, and Y. Mo. Origin of fast ion diffusion in super-ionic conductors. *Nat. Commun.*, 8(15893), 2017.

[250] P. Canepa, SH. Bo, G. Sai Gautam, B. Key, W. D. Richards, T. Shi, Y. Tian, Y. Wang, J. Li, and G. Ceder. High magnesium mobility in ternary spinel chalcogenides. *Nat. Commun.*, 8(1759), 2017.

[251] P. Gasparotto, D. Bochicchio, M. Ceriotti, and G. M. Pavan. Identifying and tracking defects in dynamic supramolecular polymers. *J. Phys. Chem. B*, 124(3):589–599, 2020.

[252] F. Pedregosa, G. Varoquaux, A. Gramfort, V. Michel, B. Thirion, O. Grisel, M. Blondel, P. Prettenhofer, R. Weiss, V. Dubourg, J. Vanderplas, A. Passos, D. Cournapeau, M. Brucher, M. Perrot, and E. Duchesnay. Scikit-learn: Machine learning in python. *J. Mach. Learn. Res.*, 12:2825–2830, 2011.

[253] S. De, A. P. Bartók, G. Csányi, and M. Ceriotti. Comparing molecules and solids across structural and alchemical space. *Phys. Chem. Chem. Phys.*, 18(20):13754–13769, 2016.

[254] E. A. Engel, A. Anelli, M. Ceriotti, C. J. Pickard, and R. J. Needs. Mapping uncharted territory in ice from zeolite networks to ice structures. *Nat. Commun.*, 9(1):2173, 2018.

[255] B. J. Rancatore, C. E. Mauldin, J. M. J. Fréchet, and T. Xu. Small molecule-guided thermoresponsive supramolecular assemblies. *Macromolecules*, 45(20):8292–8299, 2012.

[256] H. Wei, X.-Z. Zhang, H. Cheng, W.-Q. Chen, S.-X. Cheng, and R.-X. Zhuo. Self-assembled thermo- and pH responsive micelles of poly(10-undecenoic acid-b-n-isopropylacrylamide) for drug delivery. *J. Control. Release*, 116(3):266–274, 2006.

[257] P. Pan, M. Fujita, W.-Y. Ooi, K. Sudesh, T. Takarada, A. Goto, and M. Maeda. Thermoresponsive micellization and micellar stability of poly(*N*-isopropylacrylamide)-*b*-DNA diblock and miktoarm star polymers. *Langmuir*, 28(40):14347–14356, 2012.

[258] Karimi. M., P. S. Zangabad, A. Ghasemi, M. Amiri, M. Bahrami, H. Malekzad, H. G. Asl, Z. Mahdieh, M. Bozorgomid, A. Ghasemi, M. R. R. T. Boyuk, and M. R. Hamblin. Temperature-responsive smart nanocarriers for delivery of therapeutic agents: Applications and recent advances. *ACS Appl. Mater. Interfaces*, 8(33):21107–21133, 2016.

[259] V. Albright, A. Palanisamy, Q. Zhou, V. Selin, and S. A. Sukhishvili. Functional surfaces through controlled assemblies of upper critical solution temperature block and star copolymers. *Langmuir*, 35(33):10677–10688, 2018.

[260] Z. Al-Ahmady and K. Kostarelos. Chemical components for the design of temperature-responsive vesicles as cancer therapeutics. *Chem. Rev.*, 116(6):3883–3918, 2016.

[261] J. Dey, R. Ghosh, and R. D. Mahapatra. Self-assembly of unconventional low-molecular-mass amphiphiles containing a PEG chain. *Langmuir*, 35(4):848–861, 2018.

[262] M. M. Ali and H. D. H. Stöver. Well-defined amphiphilic thermosensitive copolymers based on poly(ethylene glycol monomethacrylate) and methyl methacrylate prepared by atom transfer radical polymerization. *Macromolecules*, 37(14):5219–5227, 2004.

[263] L. Hou and P. Wu. Microgels with linear thermosensitivity in a wide temperature range. *Macromolecules*, 49(16):6095–6100, 2016.

[264] K. Zheng, J. Ren, and J. He. Thermally responsive unimolecular nanoreactors from amphiphilic dendrimer-like copolymer prepared via anionic polymerization and cross metathesis reaction. *Macromolecules*, 52(17):6780–6791, 2019.

[265] D. Roy, W. L. A. Brooks, and B. S. Sumerlin. New directions in thermoresponsive polymers. *Chem. Soc. Rev.*, 42(17):7214, 2013.

[266] K. Kumbhakar, B. Saha, P. De, and R. Biswas. Cloud point driven dynamics in aqueous solutions of thermoresponsive copolymers: Are they akin to criticality driven solution dynamics? *J. Phys. Chem. B*, 123(51):11042–11054, 2019.

[267] J. M. Fuller, K. R. Raghupathi, R. R. Ramireddy, A. V. Subrahmanyam, V. Yesilyurt, and S. Thayumanavan. Temperature-sensitive transitions below LCST in amphiphilic dendritic assemblies: Host–guest implications. *J. Am. Chem. Soc.*, 135(24):8947–8954, 2013.

[268] K. R. Raghupathi, U. Sridhar, K. Byrne, K. Raghupathi, and S. Thayumanavan. Influence of backbone conformational rigidity in temperature-sensitive amphiphilic supramolecular assemblies. *J. Am. Chem. Soc.*, 137(16):5308–5311, 2015.

[269] G. M. Pavan, A. Barducci, L. Albertazzi, and M. Parrinello. Combining metadynamics simulation and experiments to characterize dendrimers in solution. *Soft Matter*, 9(9):2593, 2013.

[270] O. Munkhbat, M. Garzoni, K. R. Raghupathi, G. M. Pavan, and S. Thayumanavan. Role of aromatic interactions in temperature-sensitive amphiphilic supramolecular assemblies. *Langmuir*, 32(12):2874–2881, 2016.

[271] D.-W. Fu, W. Zhang, H.-L. Cai, Y. Zhang, J.-Z. Ge, R.-G. Xiong, and S. D: Huang. Supramolecular bola-like ferroelectric: 4-methoxyanilinium tetrafluoroborate-18-crown-6. *J. Am. Chem. Soc.*, 133(32):12780–12786, 2011.

[272] J. Liu and J. C. Conboy. Direct measurement of the transbilayer movement of phospholipids by sum-frequency vibrational spectroscopy. *J. Am. Chem. Soc.*, 126(27):8376–8377, 2004.

[273] P. Alam, N. L. C. Leung, Y. Cheng, H. Zhang, J. Liu, W. Wu, R. T. K. Kwok, J. W. Y. Lam, H. H. Y. Sung, I. D. Williams, and B. Z. Tang. Spontaneous and fast molecular motion at room temperature in the solid state. *Angew. Chem. Int. Ed.*, 58(14):4536–4540, 2019.

[274] G. Klaerner and R. Padmanabhan. Multi-step/step-wise polymerization of well-defined oligomers. In *Reference Module in Materials Science and Materials Engineering*. Elsevier, 2016.

[275] N. Uchida, A. Kohata, K. Okuro, A. Cardellini, C. Lionello, E. A. Zizzi, M. A. Deriu, G. M. Pavan, M. Tomishige, T. Hikima, and T. Aida. Reconstitution of microtubule into GTP-responsive nanocapsules. *Nat. Commun.*, 13(1), 2022.

[276] C. Sawyers. Targeted cancer therapy. *Nature*, 432(7015):294–297, 2004.

[277] M. Srinivasarao and P. S. Low. Ligand-targeted drug delivery. *Chem. Rev.*, 117(19):12133–12164, 2017.

[278] S. Biswas, K. Kinbara, T. Niwa, H. Taguchi, N. Ishii, S. Watanabe, K. Miyata, K. Kataoka, and T. Aida. Biomolecular robotics for chemomechanically driven guest delivery fuelled by intracellular atp. *Nat. Chem.*, 5(7):613–620, 2013.

[279] M. Naito, T. Ishii, A. Matsumoto, K. Miyata, Y. Miyahara, and K. Kataoka. Back cover: A phenylboronate-functionalized polyion complex micelle for ATP-triggered release of siRNA. *Angew. Chem. Int. Ed.*, 51(43):10904–10904, 2012.

[280] J. Deng and A. Walther. Atp-responsive and atp-fueled self-assembling systems and materials. *Adv. Mater.*, 32(42):2002629, 2020.

[281] A. Mishra, S. Dhiman, and S. J. George. Atp-driven synthetic supramolecular assemblies: from atp as a template to fuel. *Angew. Chem.*, 133(6):2772–2788, 2021.

[282] W.-C. Liao, C.-H. Lu, R. Hartmann, F. Wang, Y. S. Sohn, W. J. Parak, and I. Willner. Adenosine triphosphate-triggered release of macromolecular and nanoparticle loads from aptamer/dna-cross-linked microcapsules. *ACS nano*, 9(9):9078–9086, 2015.

[283] J. Mu, J. Lin, P. Huang, and X. Chen. Development of endogenous enzyme-responsive nanomaterials for theranostics. *Chem. Soc. Rev.*, 47(15):5554–5573, 2018.

[284] M. Karimi, A. Ghasemi, P. S. Zangabad, R. Rahighi, S. M. M. Basri, H. Mirshekari, M. Amiri, Z. S. Pishabad, A. Aslani, M. Bozorgomid, D. Ghosh, A. Beyzavi, A. Vaseghi, A. R. Aref, L. Haghani, S. Bahrami, and M. R. Hamblin. Smart micro/nanoparticles in stimulus-responsive drug/gene delivery systems. *Chem. Soc. Rev.*, 45(5):1457–1501, 2016.

[285] Y. Zhou, F. Tozzi, J. Chen, F. Fan, L. Xia, J. Wang, G. Gao, A. Zhang, X. Xia, H. Brasher, W. Widger, L. M. Ellis, and Z. Weihua. Intracellular atp levels are a pivotal determinant of chemoresistance in colon cancer cellsintracellular atp in cancer cell chemoresistance. *Cancer Res.*, 72(1):304–314, 2012.

[286] F. M. Gribble, G. Loussouarn, S. J. Tucker, C. Zhao, C. G. Nichols, and F. M. Ashcroft. A novel method for measurement of submembrane atp concentration. *J. Biol. Chem.*, 275(39):30046–30049, 2000.

[287] R. J. Shaw and L. C. Cantley. Ras, pi (3) k and mtor signalling controls tumour cell growth. *Nature*, 441(7092):424–430, 2006.

[288] N.-Y. Hsu, O. Ilnytska, G. Belov, M. Santiana, Y.-H. Chen, P. M. Takvorian, C. Pau, H. van der Schaar, N. Kaushik-Basu, T. Balla, C. E. Cameron, E. Ehrenfeld, F. J. M. van Kuppeveld, and N. Altan-Bonnet. Viral reorganization of the secretory pathway generates distinct organelles for rna replication. *Cell*, 141(5):799–811, 2010.

[289] A. Meshkini. Fine-tuning of the cellular signaling pathways by intracellular gtp levels. *Cell Biochem. Biophys.*, 70:27–32, 2014.

[290] T. Mitchison and M. Kirschner. Dynamic instability of microtubule growth. *Nature*, 312(5991):237–242, 1984.

[291] H. Aldaz, L. M. Rice, T. Stearns, and D. A. Agard. Insights into microtubule nucleation from the crystal structure of human γ-tubulin. *Nature*, 435(7041):523–527, 2005.

[292] J. W. J. Kerssemakers, L. E. Munteanu, L. Laan, T. L. Noetzel, M. E. Janson, and M. Dogterom. Assembly dynamics of microtubules at molecular resolution. *Nature*, 442(7103):709–712, 2006.

[293] A. Hoenger, E. P. Sablin, R. D. Vale, R. J. Fletterick, and R. A. Milligan. Three-dimensional structure of a tubulin-motor-protein complex. *Nature*, 376(6537):271–274, 1995.

[294] J. Avila. Microtubule functions. *Life Sci.*, 50(5):327–334, 1992.

[295] M. Dogterom and B. Yurke. Measurement of the force-velocity relation for growing microtubules. *Science*, 278(5339):856–860, 1997.

[296] A. C. Kruse, A. M. Ring, A. Manglik, J. Hu, K. Hu, K. Eitel, H. Hübner, E. Pardon, C. Valant, P. M. Sexton, A. Christopoulos, C. C. Felder, P. Gmeiner, J. Steyaert, W. I. Weis, K. C. Garcia, J. Wess, and B. K. Kobilka. Activation and allosteric modulation of a muscarinic acetylcholine receptor. *Nature*, 504(7478):101–106, 2013.

[297] B. K. Kobilka. G protein coupled receptor structure and activation. *Biochim. Biophys. Acta - Biomembr.*, 1768(4):794–807, 2007.

[298] A. P. Carter, W. M. Clemons, D. E. Brodersen, R. J. Morgan-Warren, B. T. Wimberly, and V. Ramakrishnan. Functional insights from the structure of the 30s ribosomal subunit and its interactions with antibiotics. *Nature*, 407(6802):340–348, 2000.

[299] J. Lin, M. G. Gagnon, D. Bulkley, and T. A. Steitz. Conformational changes of elongation factor g on the ribosome during trna translocation. *Cell*, 160(1-2):219–227, 2015.

[300] J. Cherfils and M. Zeghouf. Regulation of small gtpases by gefs, gaps, and gdis. *Physiol. Rev.*, 93(1):269–309, 2013.

[301] A. A. Van Dijk, E. V. Makeyev, and D. H. Bamford. Initiation of viral rna-dependent rna polymerization. *J. Gen. Virol.*, 85(5):1077–1093, 2004.

[302] D. Walsh and I. Mohr. Viral subversion of the host protein synthesis machinery. *Nat. Rev. Microbiol.*, 9(12):860–875, 2011.

[303] M. Kumar, H. Jayaram, R. Vasquez-Del Carpio, X. Jiang, Z. F. Taraporewala, R. H. Jacobson, J. T. Patton, and B. V. V. Prasad. Crystallographic and biochemical analysis of rotavirus nsp2 with nucleotides reveals a nucleoside diphosphate kinase-like activity. *Virol. J.*, 81(22):12272–12284, 2007.

[304] B. Hu, H. Guo, P. Zhou, and Z.-L. Shi. Characteristics of sars-cov-2 and covid-19. *Nat. Rev. Microbiol.*, 19(3):141–154, 2021.

[305] T. Inaoka and K. Ochi. RelA protein is involved in induction of genetic competence in certain *Bacillus subtilis* strains by moderating the level of intracellular GTP. *J. Bacteriol.*, 184(14):3923–3930, 2002.

[306] A. de S. Otero. Nm23/nucleoside diphosphate kinase and signal transduction. *J. Bioenerg. Biomembr.*, 32(3):269–275, 2000.

[307] D. F. Smee, B. L. Hurst, H. Egawa, K. Takahashi, T. Kadota, and Y. Furuta. Intracellular metabolism of favipiravir (t-705) in uninfected and influenza a (h5n1) virus-infected cells. *J. Antimicrob. Chemoter.*, 64(4):741–746, 2009.

[308] P. A. Smethurst and M. Griffin. Measurement of tissue transglutaminase activity in a permeabilized cell system: its regulation by ca2+ and nucleotides. *Biochem. J.*, 313(3):803–808, 1996.

[309] A. Desai and T. J. Mitchison. Microtubule polymerization dynamics. *Annu. Rev. Cell Dev. Biol.*, 13(1):83–117, 1997.

[310] H. Yajima, T. Ogura, R. Nitta, Y. Okada, C. Sato, and N. Hirokawa. Conformational changes in tubulin in GMPCPP and GDP-taxol microtubules observed by cryoelectron microscopy. *J. Cell Biol.*, 198(3):315–322, 2012.

[311] R. Mogaki, P. K. Hashim, K. Okuro, and T. Aida. Guanidinium-based "molecular glues" for modulation of biomolecular functions. *Chem. Soc. Rev.*, 46(21):6480–6491, 2017.

[312] N. Uchida, K. Okuro, Y. Niitani, X. Ling, T. Ariga, M. Tomishige, and T. Aida. Photoclickable dendritic molecular glue: Noncovalent-to-covalent photochemical transformation of protein hybrids. *J. Am. Chem. Soc.*, 135(12):4684–4687, 2013.

[313] Q. Wang, J. L. Mynar, M. Yoshida, E. Lee, M. Lee, K. Okuro, K. Kinbara, and T. Aida. High-water-content mouldable hydrogels by mixing clay and a dendritic molecular binder. *Nature*, 463(7279):339–343, 2010.

[314] G. Mukherjee, N. Patra, P. Barua, and B. Jayaram. A fast empirical gaff compatible partial atomic charge assignment scheme for modeling interactions of small molecules with biomolecular targets. *J. Comput. Chem.*, 32(5):893–907, 2011.

[315] W. L. Jorgensen, J. Chandrasekhar, J. D. Madura, R. W. Impey, and M. L. Klein. Comparison of simple potential functions for simulating liquid water. *J. Chem. Phys.*, 79(2):926–935, 1983.

[316] G. M. Alushin, G. C. Lander, E. H. Kellogg, R. Zhang, D. Baker, and E. Nogales. High-resolution microtubule structures reveal the structural transitions in $\alpha\beta$-tubulin upon gtp hydrolysis. *Cell*, 157(5):1117–1129, 2014.

[317] E. Nogales, S. G. Wolf, and K. H. Downing. Structure of the $\alpha\beta$ tubulin dimer by electron crystallography. *Nature*, 393(6681):191–191, 1998.

[318] V. Hornak, R. Abel, A. Okur, B. Strockbine, A. Roitberg, and C. Simmerling. Comparison of multiple amber force fields and development of improved protein backbone parameters. *Proteins: Structure, Function, and Bioinformatics*, 65(3):712–725, 2006.

[319] F. Eisenhaber, P. Lijnzaad, P. Argos, C. Sander, and M. Scharf. The double cubic lattice method: Efficient approaches to numerical integration of surface area and volume and to dot surface contouring of molecular assemblies. *J. Comput. Chem.*, 16(3):273–284, 1995.

[320] N. A Baker, D. Sept, S. Joseph, M. J. Holst, and J. A. McCammon. Electrostatics of nanosystems: application to microtubules and the ribosome. *Proc. Natl. Acad. Sci. U.S.A.*, 98(18):10037–10041, 2001.

[321] G. M. Pavan. Modeling the interaction between dendrimers and nucleic acids: a molecular perspective through hierarchical scales. *ChemMedChem*, 9(12):2623–2631, 2014.

[322] D. A. Walker, B. Kowalczyk, M. Olvera de la Cruz, and B. A. Grzybowski. Electrostatics at the nanoscale. *Nanoscale*, 3(4):1316–1344, 2011.

Appendix A

Supporting information related to Chapter 3

Structural illumination microscopy (SIM)

The quantification and rearrangement of trimeric assemblies on positively charged polylysine surfaces was carried out via Structural Illumination Microscopy (SIM). First, 1 mg of either 1, 2 or 3 COOH trimer was dissolved in 100 μL acetone. To this, a 1 mg/mL solution of DiD (1,1' - Dioctadecyl - 3,3,3',3' - Tetramethylindodicarbocyanine, 4 - Chlorobenzenesulfonate Salt) was loaded at 10 v/v%. 1 mL DI water was then added dropwise and stirred overnight to obtain trimeric assemblies dispersed in water and non-covalently encapsulating DiD dye. Solutions of the trimeric assemblies were then diluted to 0.05 mg/mL for SIM experiments. For experiments with SIM, a glass chamber setup was fabricated. Briefly, two pieces of clear double-sided tape of dimensions 1 cm x 3cm x 70 μm were placed on the polylysine functionalized glass slide 1 cm apart. A coverslip was then placed over the double-sided tape to form a thin chamber. For pH studies with SIM, 20 μL of the solution containing trimeric assemblies were injected into the glass chamber. For studies at neutral pH, 20 μL phosphate buffer at pH 7 was injected into the chamber and allowed to sit for 2 minutes. This was followed by a washing step to remove the buffer by injecting 75 μL DI water. Similarly, for studies at low pH, 20 μL phosphate buffer at pH 4 was injected into the chamber and allowed to sit for 2 minutes. This was followed by the washing step to remove the buffer by injecting 75 μL DI

water. Images were then captured, and the average number of particles counted using Nikon-NIS Elements. In Figure A.1, the fluorescent dots in the SIM experiments refer to the number of NPs bound to the surface. Figure A.1 shows that at neutral pH (pH = 7), because of the deprotonation of the COOH groups (into COO- groups), the number of NPs bound to the surface increases with the number of charged COO- terminal groups in the oligomer (increased multivalent binding interactions). This is quantified in the histograms in Figure A.2. The selective electrostatic nature of the binding is also experimentally proven by the pH-dependent experiments (see Figure A.1 going from neutral (a) to low pH (b)) the level of deprotonation and the number of COO- groups strongly decreases, reducing the strength of electrostatic binding and consequently the number of particles bound on the surface.

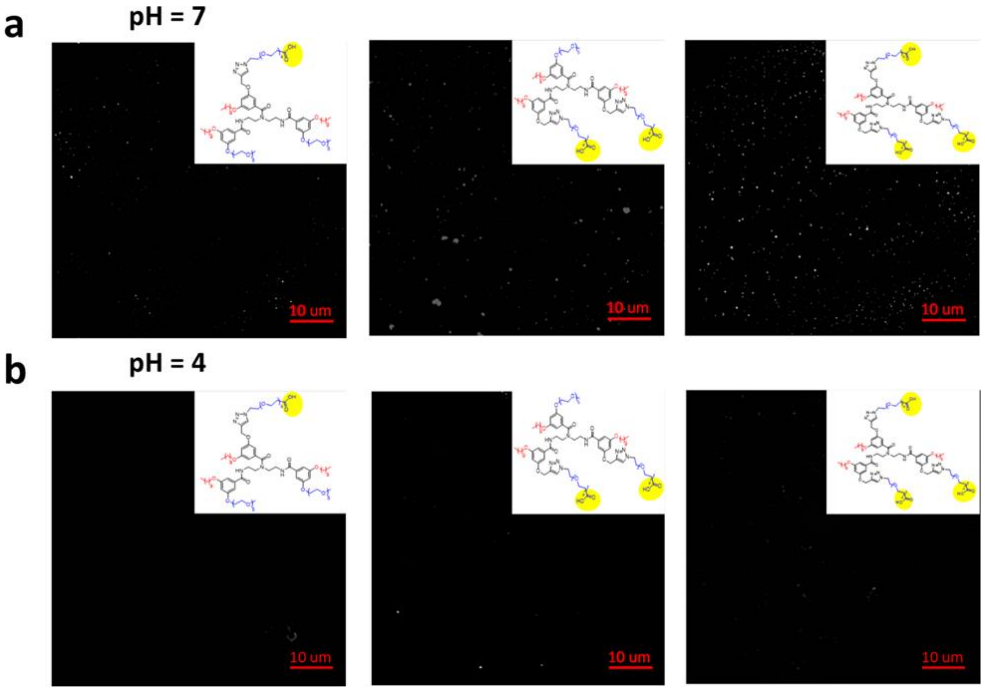

Fig. A.1 Structural Illumination Microscopy (SIM) images of a polylysine functionalized surface showing adhesion of 1-COOH, 2-COOH, 3-COOH trimeric assemblies at pH = 7 (a) and pH = 4 (b). White dots identify the surface bound NPs. Figure reproduced from Ref. 126.

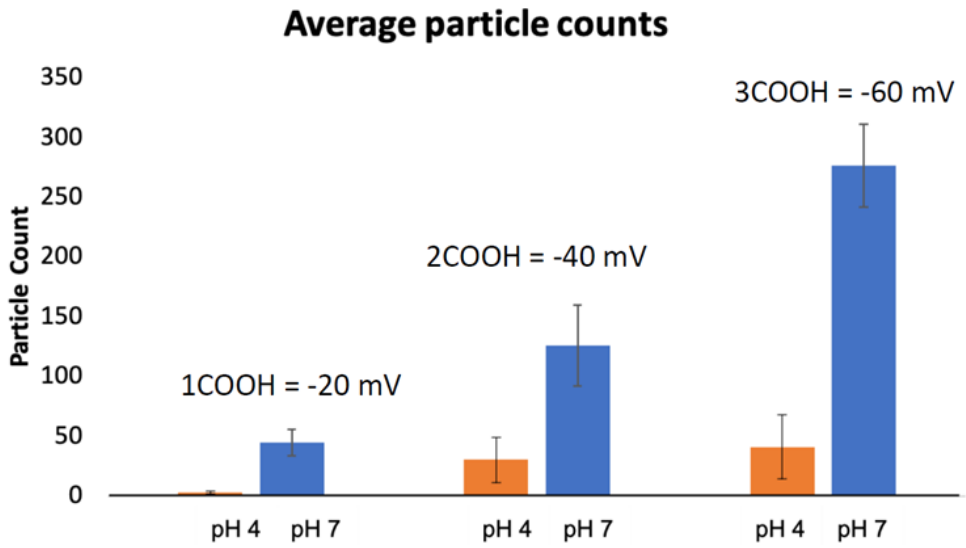

Fig. A.2 Quantification of trimeric assemblies on polylysine surfaces using SIM at pH = 7 and pH = 4. Increasing the multivalent interaction, the average particles adhered to the surface rise up in case of neutral pH, instead the average particle counts remain constant in case of pH = 4, remarking the increase of protonation of COO-terminal groups. Figure reproduced from Ref. 126.

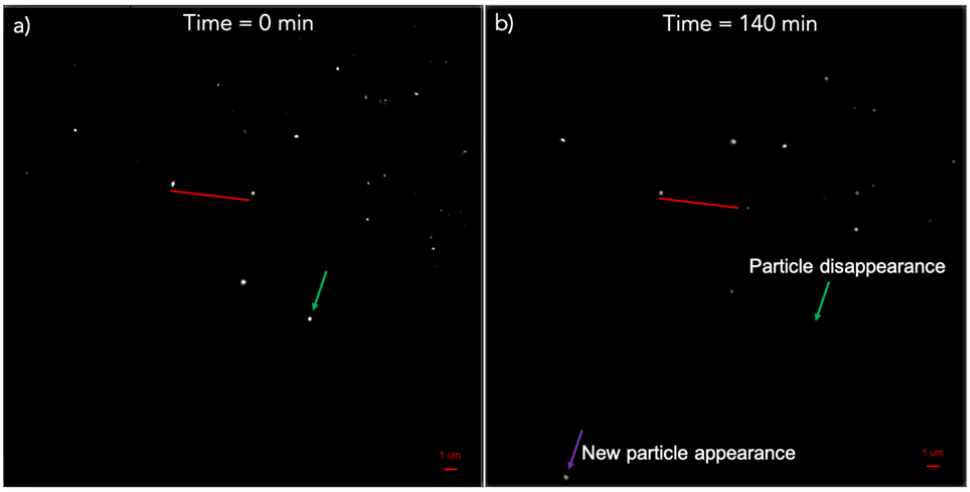

Fig. A.3 Structural Illumination Microscopy (SIM) images of a polylysine functionalized surface showing a) adhesion of 1-COOH trimeric assemblies at the start of the experiment and b) rearrangement of the trimeric assemblies as captured by the microscope after 140 minutes. Figure reproduced from Ref. 126.

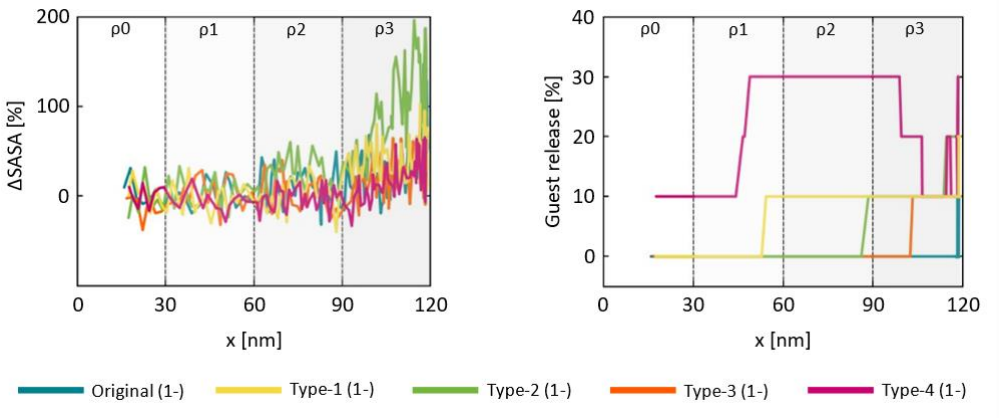

Fig. A.4 Comparison of Δ*SASA* (NP SASA variation) and percentage of guest release for NPs composed of the different trivalent (-1e) dendron variants. The CG models of Original, Type-1, Type-2, Type-3 and Type-4 residues are reported in Figure 3.12. Figure reproduced from Ref. 126.

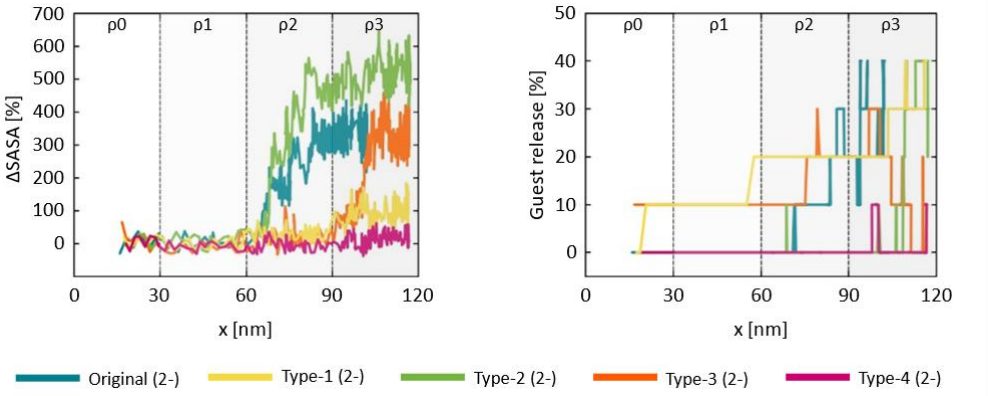

Fig. A.5 Comparison of Δ*SASA* (NP SASA variation) and percentage of guest release for NPs composed of the different trivalent (-2e) dendron variants. The CG models of Original, Type-1, Type-2, Type-3 and Type-4 residues are reported in Figure 3.12. Figure reproduced from Ref. 126.

Appendix B

Supporting information related to Chapter 7

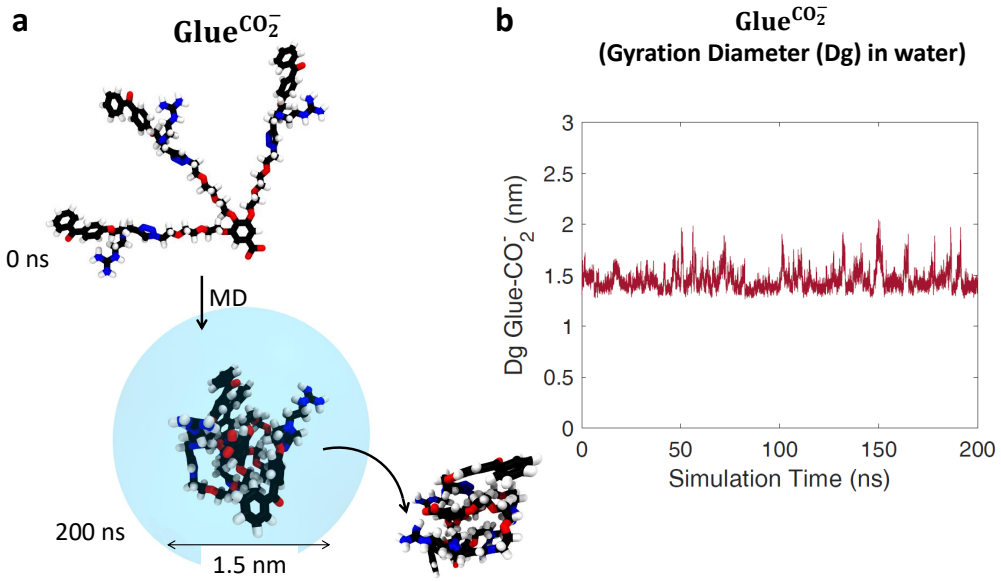

Fig. B.1 Conformation of a Glue$^{CO_2-}$ molecule in water. **a, b** Snapshots of GlueCO2– before (a) and after (b) the MD simulation. Nitrogen, oxygen, carbon, and hydrogen atoms of GlueCO2– are colored in blue, red, gray, and white, respectively. Water molecules and chloride anions are not shown explicitly. **c** Gyration diameter of GlueCO2– calculated along 200 ns by MD simulation. Figure adapted from Ref. 275.

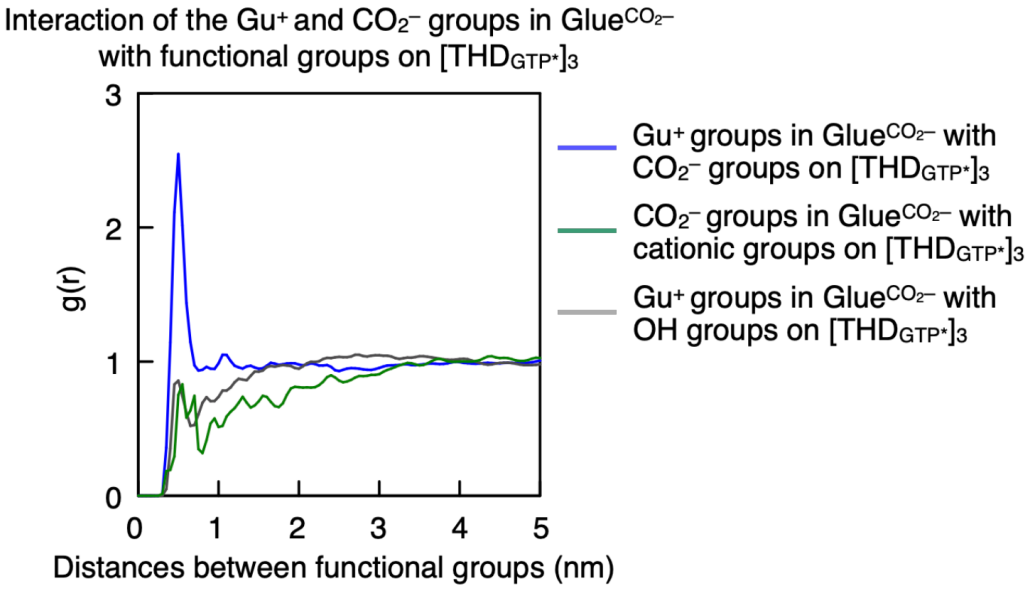

Fig. B.2 Radial distribution functions g(r) of the Gu+ groups in Glue$^{CO_2-}$ with CO_2- groups (blue) and nonionic hydroxyl groups (gray) on [THD$_{GTP*}$]$_3$, and the CO_2- group at the focal core of Glue$^{CO_2-}$ with cationic groups on [THD$_{GTP*}$]$_3$ (green). Figure reproduced from Ref. 275.